

University of Warwick institutional repository: <http://go.warwick.ac.uk/wrap>

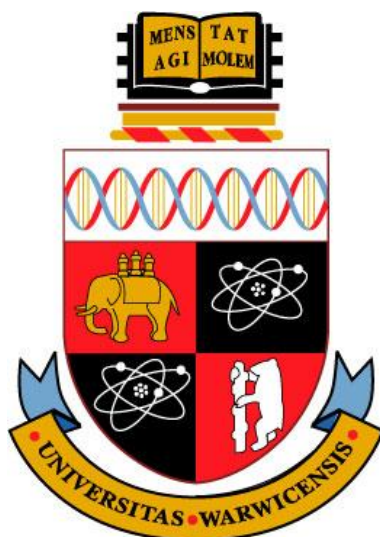
**A Thesis Submitted for the Degree of PhD at the University of Warwick**

<http://go.warwick.ac.uk/wrap/46892>

This thesis is made available online and is protected by original copyright.

Please scroll down to view the document itself.

Please refer to the repository record for this item for information to help you to cite it. Our policy information is available from the repository home page.



# **Crystal Growth and Dissolution of Gypsum and Analogous Materials: A Multi-Scale Approach**

**Michael Mburu Mbogoro**

A thesis submitted for the degree of Doctor of Philosophy

THE UNIVERSITY OF  
**WARWICK**

Department of Chemistry

September 2011

# Table of Contents

<b>Table of Contents</b> .....	<b>i</b>
<b>Acknowledgements</b> .....	<b>i</b>
<b>List of Figures</b> .....	<b>iii</b>
<b>List of Tables</b> .....	<b>xii</b>
<b>Declaration</b> .....	<b>xiii</b>
<b>Abstract</b> .....	<b>xv</b>
<b>Abbreviations</b> .....	<b>xvii</b>
<b>Glossary of Symbols</b> .....	<b>xix</b>
<b>Chapter 1 Introduction</b> .....	<b>1</b>
1.1. Gypsum Crystallography .....	1
1.2. Applications of Gypsum .....	4
1.2.1 Calcination.....	4
1.2.2 Building and Construction.....	5
1.2.3 Scaling and Weathering.....	6
1.2.4 Geochemistry .....	7
1.3. Crystal Growth/Dissolution Reactions .....	9
1.4. Crystal Growth Theory .....	10
1.4.1 Nucleation.....	10
1.4.2 Crystal Growth.....	14
1.4.3 Crystal growth Mechanisms.....	17
1.4.4 The Crystal Habit.....	18
1.5. Review of Gypsum Crystal Growth Studies .....	20
1.5.1 Bulk Crystal Growth Studies .....	20
1.5.2 Local Crystal Growth Studies.....	23
1.6. Crystal Dissolution Theory .....	24
1.7. Review of Gypsum Crystal Dissolution Studies .....	27
1.7.1 Bulk Crystal Dissolution Studies .....	27
1.7.2 Local Crystal Dissolution Studies.....	29
1.8. Analysis and Characterisation Techniques .....	31

1.8.1	Multi-Scale Approach.....	31
1.8.2	Bulk Techniques – The Channel Flow Cell (CFC).....	33
1.8.3	Local Techniques.....	35
1.9.	Thesis Aims.....	38
<b>Chapter 2 Experimental Procedures.....</b>		<b>46</b>
2.1.	Chemicals.....	46
2.2.	Etching of Crystal Surfaces .....	48
2.2.1	Etch Pit Visualisation and Analysis .....	50
2.3.	Channel Flow Cell (CFC) Studies.....	51
2.3.1	Preparation of Natural Samples .....	51
2.3.2	Polycrystalline Materials Modified with Humid-Creep Additives.....	51
2.3.3	Composite Phosphate Materials.....	52
2.3.4	Surface Roughness Normalisation for CFC Studies .....	53
2.3.5	Design of The CFC Unit.....	56
2.3.6	CFC Dissolution Procedure.....	58
2.4.	Micro-Crystal Growth Studies .....	59
2.4.1	Crystal Seeding Process.....	59
2.4.2	Crystal Growth Experiments .....	61
2.5.	Finite Element Method .....	63
<b>Chapter 3 Image Processing with Matlab .....</b>		<b>67</b>
3.1.	Introduction.....	68
3.2.	Method.....	72
3.2.1	Visualised Surfaces .....	72
3.2.2	Image Restoration via Batch Processing.....	73
3.3.	Graphical User Interfaces (GUIs).....	78
3.3.1	Images of Etched Gypsum Surfaces .....	78
3.3.2	Images of Etched Enamel Surfaces.....	82
3.4.	Discussion.....	87
3.5.	Conclusions.....	89

**Chapter 4 Bridging the Length Scales in Dissolution Kinetics: Macroscopic Fluxes, Mass Transport Effects & Direction-Specific Rates from Gypsum**

**Etch Pit Analysis ..... 92**

4.1.	Introduction.....	93
4.2.	Numerical Theory and Simulations.....	96
4.2.1	Model for Direction-Specific Dissolution Kinetics.....	97
4.3.	Results and Discussion.....	100
4.3.1	Morphological Etch Pit Analysis.....	100
4.3.2	Step Displacement Kinetics.....	103
4.4.	Direction-Specific Dissolution Kinetics.....	108
4.5.	Linking Microscopic and Macroscopic Dissolution Kinetics.....	111
4.6.	Conclusions.....	112

**Chapter 5 Intrinsic Kinetics of Gypsum and Calcium Sulphate Anhydrite  
Dissolution: Surface Selective Studies Under Hydrodynamic Control and**

**the Effect of Additives ..... 118**

5.1.	Introduction.....	119
5.2.	Experimental.....	122
5.3.	Mass Transport and Kinetic Modelling.....	123
5.3.1	Theory.....	123
5.3.2	Hydrodynamics.....	124
5.3.3	Convective-Diffusive Mass Transport.....	125
5.4.	Results and Discussion.....	127
5.4.1	Insights from Simulations.....	127
5.4.2	Dissolution Kinetics.....	130
5.5.	Conclusions.....	138

**Chapter 6 Dissolution Kinetics of Polycrystalline Calcium Sulfate-Based**

**Materials: Influence of Chemical Modification ..... 142**

6.1.	Introduction.....	143
6.2.	Theory and Kinetic Modelling.....	145
6.3.	Results and Discussion.....	146

6.3.1	Insights from Simulations.....	146
6.3.2	Surface Area Analysis .....	147
6.3.3	Surface Heterogeneity .....	149
6.3.4	Diffusion Layer Thickness .....	152
6.3.5	Dissolution Kinetics of Gypsum Modified with Humid-Creep Inhibitors 154	
6.3.6	Composite Materials .....	157
6.4.	Conclusions.....	161

**Chapter 7 Quantitative 3-D Visualisation of Gypsum Micro-Crystal Growth Kinetics Using AFM ..... 163**

7.1.	Introduction.....	164
7.2.	Experimental.....	167
7.3.	Characterisation of Seed Crystals.....	168
7.4.	Numerical Theory and Simulations.....	170
7.5.	Results and Discussions.....	173
7.5.1	Plane Specific Growth Rates .....	173
7.5.2	Effect of $r = (a_{Ca^{2+}}/a_{SO_4^{2-}})$ on Crystal Morphology .....	179
7.5.3	Step Motion on the Basal (010) Surface.....	180
7.5.4	Relationship Between Microscopic Fluxes, Macroscopic Growth Rates and Previous Kinetic Studies.....	185
7.6.	Conclusions.....	186

**Chapter 8 Conclusions..... 190**

# Acknowledgements

I would like to thank my supervisor Prof. Patrick R. Unwin for his guidance throughout the last four years. Your boundless energy and dedication has been truly inspiring. I only hope to have gleaned some of that brilliance.

I also thank Prof Julie Macpherson for her help and guidance. Your door has always been open to me and your frank advice has been invaluable to many areas of my work.

To Dr Massimo Peruffo, for teaching me the true meaning of *kaizen*: the relentless pursuit of, and elimination of weaknesses. Our frequent 'heated' exchanges on virtually all topics of conversation have ensured that I have gained a thorough and efficient approach to research. Most of all, I thank you for the selflessness with which you have given your time, particularly this last year.

The eclectic mix of personalities in the Electrochemistry and Interfaces Group has certainly been enjoyable. From those with whom I could share common frustrations and were eager to offer support, to those who by their nature, reminded me that occasional play is good for the soul. From quick coffee breaks, and ice-cream on the piazza, to pints at the Duck and balcony bbqs, it has been great!

To Laura, you have been a lifeline, when I truly needed it. You have always set the bar higher than most and yet you see no limits to your potential. Your love and support these last few years has been wonderful. I could not have done it without you.

To those outside the 'bubble' who have provided a much needed escape whenever necessary, thanks for keeping me sane.

Kūrīandũ a rūrīrī rwitũ,

Kwĩ Wainaina: Ūtũire wĩrutĩire mũno nĩ getha arĩa a nyinyi gũgũkĩra ta nĩ, mahote kūrĩkia gĩthomo kĩa. Nĩ ngũgũcokeria ngatho mũno nĩndũ igongona rĩaku nĩrĩatũmire mabataro maku macokio thutha mũno. Ndikariganĩrwo.

Kwĩ Wamoro: Ūrĩa wĩrutĩire ūtũũro waku wothe nĩgetha ūkinye harĩa ūrĩ nĩ ūhete gĩthomo kĩa hinya mũno. Ūnyonetie atĩ gũtirĩ ūndũ itangĩhota gwĩka ndĩna kĩoo. Kūrĩa guothe ūgakinya ūtũũroine waku-rĩ, nĩūrathimwo.

Kwĩ Nduta: Twarerirwo hamwe, na tũgĩthoma hamwe na ūgĩkorwo wĩ wambere gwĩtũ kuonia arĩangĩ njĩra na kwambĩrĩria mũciĩ waku. Ona wĩna mĩhango ya mũciĩ ūcio-rĩ, nĩwacokire gũcoka cukuru, na ūkĩrĩkia gĩthomo. Kūroneka atĩ gũtirĩ ūndũ we ūtangĩka ūtarĩ gũoya. Nĩ hinya ūcio waku wagũtoria hĩndĩ ya mathĩna na kũhingĩa maũndũ maritũ, ūngenagia mũno na ūkahe ūmĩrĩru. Nĩndagũcokeria ngatho nĩkũhingũra maitho.

Kwĩ Baba na Maitũ: Rĩu ingiuga atĩa tũndũ ndambĩrĩrĩa kũmũcokeria ngatho nĩ ibuku rĩngĩ ingĩandĩka. Kuma ndĩ mũnyinyi, nĩmũũndarĩite wega, na mũkanyonia mĩtũgo mĩega ya mĩtũrĩre. Nĩ muuhete hinya wa kuhingia maundu marĩa ndĩrĩrĩrie muno, mutakuhinyĩrĩria kana gwĩcĩria atĩ ndirĩ na uugĩ wa kũ-ũtoria. Gũtirĩ kūrĩa ingiakinyire itarĩ naũtheithio wanyu, mahoya manyu kana ona irathimo cianyu. Oo muthenya nĩ-njokagĩria mwathani ngatho nĩkuhe aciari mena wendo murikĩru na utathĩraga.

Kūrĩ arĩangĩ matana gwetũ-rĩ, mũtirĩganĩire. Kūrĩa guothe mũrĩ, nĩ ndamũcokeria ngatho na ndahoya mũtanahĩrwo nĩ mwanthani nĩgetha mũgĩe hinya wa kũmũtungata wega.

Nĩmũrathimwo mũrĩ othe.

# List of Figures

Figure 1.1: (a) Gypsum monoclinic prismatic morphology, (b) unit cell with the main crystallographic directions indicated and the interspaced H <sub>2</sub> O layer shown, and (c) the atomic structure of the (010) surface.....	2
Figure 1.2: Atomic stacking along the (a) [100] and (b) [001] directions.....	3
Figure 1.3: Humid creep of gypsum based plasterboard due to water uptake from atmosphere.....	6
Figure 1.4: Calcium sulphate scaling in oil pipe resulting in significant shrinkage of pipe capacity. <sup>32</sup> .....	7
Figure 1.5: Gypsum karst formation where (a) flowing river water dissolves gypsum deposits and (b) subsidence caused by dissolution of underwater gypsum beds. <sup>46</sup> .....	8
Figure 1.6: (a) Gibbs free energy diagram for crystal nucleation and (b) temperature dependence of the critical radius.....	12
Figure 1.7: Interplay between kinetics and thermodynamics of crystal growth. <sup>58</sup> .....	13
Figure 1.8: Fundamental steps involved in growth/dissolution at the crystal surface .....	15
Figure 1.9: Mononuclear growth as a source for birth-and-spread growth. ....	16
Figure 1.10: Polynuclear crystal growth. ....	16
Figure 1.11: Screw type dislocation in a simple cubic lattice.....	17
Figure 1.12: Typical sequence due to growth from a dislocation and AFM spiral growth image (bottom right). <sup>80</sup> .....	17
Figure 1.13: Simple cubic crystal showing different types of faces according to the periodic bond chain (PBC) theory. <sup>29</sup> .....	19

Figure 1.14: Scanning electron microscopy (SEM) images of (a) gypsum crystals grown in pure supersaturated solution and (b-c) grown in the presence of polyacrylate solutions. <sup>118</sup> .....	22
Figure 1.15: Typical features on a crystal surface. ....	25
Figure 1.16: Parallel surface processes contributing to crystal dissolution. ....	26
Figure 1.17: Dissolution etch pit as a source of stepwaves <sup>128</sup> .....	27
Figure 1.18: Relationship between different analytical techniques and the time (y-axis) and length (x-axis) scale under which crystal growth/dissolution is accessible. <sup>163</sup> .....	32
Figure 1.19: Typical channel flow cell schematic.....	34
Figure 1.20: Typical force curve illustrating deflection of the cantilever as a function of distance from the substrate.....	36
Figure 1.21: (a) Schematic of typical WLI. <sup>163</sup> and (b) interference fringes on an etched gypsum surface.....	37
Figure 2.1: (a) WLI micrograph of gypsum (010) surface after etching for 180 sec and (b) plot of cross-section across the surface between masked and reactive regions.....	50
Figure 2.2: WLI height images displaying the surface topography of polycrystalline gypsum samples before (a) and after (b) polishing. A plot of the height of surface data points is also shown (c) where the rougher surface exhibits a wider spread (black) compared to the smoother polished one (red).....	55
Figure 2.3: Illustration of (a) the two dimensional cross-section of the flow cell (not to scale), highlighting the crystal substrate which forms the base of the channel and the mixer in the outlet, (b) a photograph of a finished CFC unit where the scale bar is 10 mm and (c) schematic of the CFC design from several viewpoints, where the cell dimensions are in mm.....	57
Figure 2.4: Experimental set up used for CFC dissolution experiments.....	58

Figure 2.5: Silanisation of a glass substrate .....	60
Figure 2.6: DIC image of a silanised glass surface after a seeding process (~ 30 min) showing numerous crystals randomly distributed across the surface. The magnification of a small section (b) reveals well defined gypsum crystals exhibiting a monoclinic structure. Note that the formed crystals are of similar size (within ~ 10 %), indicating an instantaneous nucleation process. ....	61
Figure 2.7: A single etch pit undergoing a dissolution process is modelled by (a) describing the physical domain in the vicinity of the pit, where the numbers represent boundaries each governed by specific conditions, (b) a mesh made up of triangular nodes is generated over the entire domain with higher densities close to the active etch pit and (c) the FEM solution of the reaction-diffusion problem illustrated as a concentration profile.....	65
Figure 3.1: Sequence of operations performed on 3D images. ....	71
Figure 3.2: Typical WLI images reproduced using the in-house designed image processing package. (a) Etch pit on enamel surface and (b) etch pits on gypsum (010) surface. Note the tilt on the surface as denoted by the drastic colour change from the right-hand-side to the left-hand-side of the images as well as the missing pixels highlighted by the dark irregular areas close to the etch pit edges.....	73
Figure 3.3: (a) WLI micrograph of etch pits with (b) original cross-section (red) with missing pit data overlayed with a cross-section from a restored image where missing pixel values were replaced with a local average (green). ....	75
Figure 3.4: (a) 3D image of etch pit on enamel surface showing missing pixels and (b) etch pit after image restoration.....	76
Figure 3.5: Overlay of original (black) and tilt corrected (red) cross-section. ....	77
Figure 3.6: Graphical User Interface (GUI) designed to isolate the etch pits from the image background and determine etch pit measurements. ....	79
Figure 3.7: GUI image designed to extract height dependent etch pit dimensions where (a) is the input 3D image, (b) cross-	

sections across the surface and (c) cross-section through the image centroid.....	83
Figure 3.8: 3D surface plots of (a) a pre-processed etched enamel surface with a large central pit and (b) the result of user-defined smoothing to eliminate 'noise' while maintaining image integrity .....	85
Figure 3.9: Etch pit measurements at different pit depths. ....	86
Figure 3.10: Typical plot of etch pit length as a function of time, comparison between the Matlab IP package designed in-house (blue bars) and commercial IP software SPIP (red bars). ....	87
Figure 3.11: Comparisons between options and output from image analysis using (a) user-designed Matlab IP package and (b) typical commercial software .....	88
Figure 4.1: Schematic for etch pit analysis, in which a flat crystal surface is etched and dissolution is monitored by tracking the expansion of a characteristic etch pit and using complementary computer simulations to deduce dissolution kinetics, surface concentrations and mass transport effects. ....	95
Figure 4.2: (a) Simulation domain used for finite element simulations of plane (direction)- specific dissolution fluxes where the numbers represent the boundaries used in simulations (not to scale). (b) The simulated etch pit whose walls have been opened up for clarity, and (c) a typical etch pit with (d) the cross section along the pit length ([001] direction). The dashed line represents the approximation used for the pit geometry.....	98
Figure 4.3: Typical AFM micrographs of etch pits produced after etching the (010) gypsum surface in 0.2 M $\text{NaNO}_3$ solution for (a) 30 s, (b) 55 s, (c) 80 s , (d) 105 s and (e) the corresponding cross sectional profiles along the [001] direction for 25 s (black), 50 s (red), 75 s (blue) and 100 s (cyan). Note the evident anisotropy of step kinetics which results in etch pit elongation along the [001] direction. Pit depth corresponds to expansion in the [010] direction. ....	101
Figure 4.4: DIC micrographs of the (010) surface of gypsum showing matched halves after a 7 min etch in pure $\text{H}_2\text{O}$ . Note the correspondence of etch pits on the same mirror positions	

and that the area selected had a macroscopic scratch (bottom section) chosen deliberately to allow correlation of the mirror surfaces.....	103
Figure 4.5: Etch pit displacement as a function of etching time for the (010) gypsum surface (n=9) in solutions of 0.2 M NaNO <sub>3</sub> (black), 0.075 M Na <sub>2</sub> SO <sub>4</sub> (red), Ca(NO <sub>3</sub> ) <sub>2</sub> ·4H <sub>2</sub> O (blue) and pure H <sub>2</sub> O (green) for the (a) (010) face, (b) [001] and (c) [100] steps and the solid lines are linear fits to the experimental data.....	104
Figure 4.6: Typical simulated interfacial Ca <sup>2+</sup> and SO <sub>4</sub> <sup>2-</sup> concentration profile over the pit from a section of the overall pit (not to scale) close to the (100) face, after (a) 50 and (b) 100 s etches in pure H <sub>2</sub> O, and for comparison (c) an experimental etch pit formed after 100 s etch in pure H <sub>2</sub> O, acute angle (~62°). The magnification (a-b) highlights the change in surface concentration on the fast moving (100) face.....	110
Figure 4.7: Illustration describing the onset of dissolution at defect sites, where initially, the formed etch pits are isolated from their neighbours and show evidence of unimpeded high mass flux. With time, these pits grow to an extent that diffusional cross-talk is exhibited, with the consequence of establishing a planar diffusion profile at the inter-facial region.....	111
Figure 5.1: 2D representation of (a) the channel geometry used for finite element modelling simulations where the numbers represent the boundaries (edges) used in simulations (not to scale) and are described by equations 5.3 – 5.5, and (b) the velocity profile of solution within the flow cell for the case of $V_f = 0.167 \text{ cm}^3 \text{ s}^{-1}$ . The cell dimensions in (b) are in mm and were used throughout. ....	124
Figure 5.2: Illustration of (a) the CFC cross-section depicting the concentration for $V_f = 0.0083 \text{ cm}^3 \text{ s}^{-1}$ and $k_{\text{diss}} = 1 \times 10^{-3} \text{ cm s}^{-1}$ where dimensions are in mm, and (b) the corresponding interfacial concentration along the length of the channel for $V_f = 0.0083 \text{ cm}^3 \text{ s}^{-1}$ (black) and $V_f = 0.1649 \text{ cm}^3 \text{ s}^{-1}$ (red), with an applied rate constant $k_{\text{diss}} = 1 \times 10^{-3} \text{ cm s}^{-1}$ in each case. For comparison, the saturated solution concentration is shown (blue). ....	128

- Figure 5.3: (a) Simulated outlet concentrations and (b) mean surface flux,  $J_s$ , as a function of  $k_{\text{diss}}$  and  $V_f$ . The channel cell was characterised by the parameters shown in Figure 5.1(b)..... 129
- Figure 5.4: Typical DIC micrographs (scale bars 100  $\mu\text{m}$ ) of the (010) cleaved gypsum surface after etching in pure  $\text{H}_2\text{O}$  for (a) 90 s, (b) 10 min, (c) 30 min, and (d) the corresponding WLI micrograph after a 30 min etch, where the scale bar is 30  $\mu\text{m}$ ..... 131
- Figure 5.5: Cell outlet concentration as a function of flow rate for the dissolution of etched basal plane gypsum (red), edge plane gypsum (black) and anhydrite (blue) The solid line correspond to the best fits to the model with rate constant,  $k_{\text{diss}}$  ( $\text{cm s}^{-1}$ ) of  $6.0 (\pm 1.5) \times 10^{-4} \text{ cm s}^{-1}$ ,  $> 0.1 \text{ cm s}^{-1}$  and  $7.8 (\pm 1.3) \times 10^{-4} \text{ cm s}^{-1}$ , for basal plane gypsum, edge plane gypsum ( $c_{\text{eq}} = 11 \text{ mM}$  for gypsum) and anhydrite ( $c_{\text{eq}} = 16 \text{ mM}$ ) respectively. The simulation used other parameters stated in the text..... 132
- Figure 5.6: Outlet concentration as a function of flow rate for dissolution of the etched basal plane of gypsum in 5 mM solutions of l-tartaric acid (blue points), d-tartaric acid (green points), and STMP (black) and in pure  $\text{H}_2\text{O}$  (red). The solid lines correspond to the best fit rate constant,  $k_{\text{diss}}$  ( $\text{cm s}^{-1}$ ) predicted by simulations with values of  $6.0 (\pm 1.5) \times 10^{-4} \text{ cm s}^{-1}$  and  $1.3 (\pm 0.5) \times 10^{-4} \text{ cm s}^{-1}$  for pure  $\text{H}_2\text{O}$  and STMP, respectively, while l-tartaric and d-tartaric acids exhibit a similar rate constant of  $7.3 (\pm 2.0) \times 10^{-4} \text{ cm s}^{-1}$  (blue solid line)..... 134
- Figure 5.7: DIC micrographs of the (010) surface of gypsum (matched halves) after a 20 min etch in (a)  $\text{H}_2\text{O}$  and (b) 5 mM STMP. The two surfaces (a and b) are superimposed in (c) to show correspondence of etch pits on the surfaces. A cleaved gypsum surface etched for 20 min in 0.03 M  $\text{KNO}_3$  is shown in (d) for comparison. The scale bars are 300  $\mu\text{m}$ . WLI micrographs of pit morphology after etching for 20 min in (e)  $\text{H}_2\text{O}$  and (f) 5 mM STMP are also shown. The main crystallographic directions with respect to the etch pits formed on the (010) surface are indicated and the [010] direction normal to the surface..... 136
- Figure 6.2: Simulated outlet concentrations as a function of applied rate constant,  $k$ , and flow rate as predicted from finite element simulations, which are based on the parameters in Figure 6.1(a)..... 147

Figure 6.3: Typical SEM images from the backscattered electron detector (a) with the corresponding binarised image (b) of the gypsum control sample (1) and those impregnated with humid creep the additives: STMP (2), tartaric acid (3), boric acid (4) and gallic acid (5).the scale bar represents 50 $\mu\text{m}$ . .....	150
Figure 6.4: reactive surface area result from SEM image analysis, showing gypsum crystal (white) and resin (black). Error bars are based on 1 standard deviation. ....	151
Figure 6.5: Distance between active regions as a function of frequency on (a) gypsum control, and samples modified with; (b) STMP, (C) gallic acid, (d) tartaric acid and (e) boric acid .....	152
Figure 6.6: (a) Concentration profile within CFC highlighting cross sections taken across the channel height to measure the concentration profile of $\text{Ca}^{2+}$ ions at a fixed flux of $7 \times 10^{-9} \text{ mol cm}^{-2} \text{ s}^{-1}$ and (b) $V_f = 0.008 \text{ cm}^3 \text{ s}^{-1}$ and (c) $V_f = 0.167 \text{ cm}^3 \text{ s}^{-1}$ . ....	153
Figure 6.7: Plots of (a) $\text{Ca}^{2+}$ outlet concentration as a function of flow rate for the dissolution of polycrystalline gypsum impregnated with humid creep inhibitors. The solid lines correspond to best fits to the model with rate constants in $k$ ( $\text{mol cm}^{-2} \text{ s}^{-1}$ ) in the range of $8.6 (\pm 3.6) \times 10^{-9} \text{ mol cm}^{-2} \text{ s}^{-1}$ for all humid creep samples, and the samples were, gypsum control (black), STMP (green), tartaric acid (red), boric acid (blue), 3,4,5-trihydroxybenzoic acid (gallic acid) (pink) and STMP (green). These values were normalised with respect to surface area ( $\lambda$ ), to yield (b) the average surface fluxes $J_s$ of $1.3 (\pm 0.4) \times 10^{-8} \text{ mol cm}^{-2} \text{ s}^{-1}$ for the gypsum control, and $1.8 (\pm 0.3) \times 10^{-8} \text{ mol cm}^{-2} \text{ s}^{-1}$ , $1.0 (\pm 0.1) \times 10^{-8} \text{ mol cm}^{-2} \text{ s}^{-1}$ and $2.0 (\pm 0.6) \times 10^{-8} \text{ mol cm}^{-2} \text{ s}^{-1}$ and $7.4 (\pm 0.4) \times 10^{-9} \text{ mol cm}^{-2} \text{ s}^{-1}$ for the humid creep samples impregnated with tartaric acid, boric acid, 3,4,5-trihydroxybenzoic acid (gallic acid) and STMP, respectively. ....	155
Figure 6.8: Plots of outlet concentrations of calcium (blue) and phosphorous (red) as a function of flow rate for the phosphate binder samples where the Al: P ratio was (a) 0, (b) 0.1, (c) 0.2 and (d) 0.33. The solid lines correspond to the best fit to the model with fixed flux $k$ ( $\text{mol cm}^{-2} \text{ s}^{-1}$ ). Values for $k$ are shown in Table 4. ....	158

Figure 6.9: Plots of (a) dissolution fluxes, (b) dissolution fluxes normalised with respect to relative BET surface area and (c) dissolution fluxes normalised with respect to relative sample porosity. The rates of $\text{Ca}^{2+}$ (black) and $\text{PO}_4^{3-}$ (red) as a function of Al content for all binder composites are shown. The calcium fluxes from polycrystalline gypsum control (blue) are also shown. The relative porosity and BET surface areas are defined with respect to the values for the gypsum control.....	160
Figure 7.1: Typical Raman spectra acquired from analysing seed gypsum crystals.....	169
Figure 7.2: Typical AFM images of a grown gypsum crystal, (a) top view highlighting the dominant crystallographic directions and (b) showing crystal morphology.....	170
Figure 7.3: Simulation domain used for finite element simulations of plane-specific crystal growth fluxes. The numbers represent boundaries used in simulations (not to scale) and described in the text.....	172
Figure 7.4: Typical AFM height images (top view) of a seed crystal in $r = 1$ solution after growth for (a) 530 s, (b) 1215 s, (c) 2430 s and (d) 3645 s. The scale bar represents $2 \mu\text{m}$ .....	174
Figure 7.5: Crystal expansion of the principle planes; (100) (black), (001) (red) and the basal (010) surface (blue), as a function of time when grown in a stoichiometric ( $r$ ) growth solution.....	175
Figure 7.6: Summary plot of plane-specific growth fluxes to the (100) (black), (001) (red) faces and the basal (010) face (blue), as a function of solution stoichiometry ( $r$ ).....	176
Figure 7.7: AFM height images of crystals grown with $r$ values of (a-b) 0.133, (c-d) 1 and (e-f) 7.12 where (a), (c) and (e) are crystals initially and (b), (d) and (f) are after growth for ca. 1 hour. The scale bar represents $2 \mu\text{m}$ .....	180
Figure 7.8: (a) DIC image depicting a typical crystal in air with small areas on the basal (010) surface magnified via AFM to reveal (b) a growth hillock with a nucleation point in the centre, which acts as a source of steps. Image (c) is an area away from the source where fast moving steps parallel to the [100] direction have a large step spacing, with much more closely packed steps parallel to the [001]	

direction. Image (d) is close to the crystal edge where only steps parallel to the [001] direction are evident. Cross-sections in (c) and (d) are shown in (e) and (f), respectively, and serve to highlight a difference in step heights in the different regions of the crystal surface. .... 182

Figure 7.9: In-situ AFM height images showing steps parallel to the [001] direction on the (010) surface as a function of time, at (a) 300 s, (b) 770 s, (c) 1300 s and (d) 1830 s. A defect on the surface is also shown (black arrow) which is gradually filled in by moving steps. The cross-section in (a) is shown in (e), highlighting the step height and inter-step distance as well as the profile of the defect region. Image (f) plots the distance of three steps from the defect, as a function of time. .... 184

# List of Tables

Table 2.1: Composition of humid creep additive samples in 1mM solution .....	52
Table 2.2: Nominal compositions of composite samples.....	53
Table 4.1: Measured displacement velocities obtained from dissolution studies.....	105
Table 4.2: Summary of plane specific fluxes under different etchants.....	109
Table 5.1: Additives used for CFC dissolution studies on basal plane gypsum crystal .....	122
Table 6.2: WLI surfaces area ratio ( $\lambda$ ) prior to and after CFC measurements.....	148
Table 6.3: Theoretical flux predictions from simulations for composite binder materials .....	159
Table 7.1: Summary of all solutions used for growth experiments. ....	168
Table 7.2: Plane-specific surface concentrations for all r values.....	173
Table 7.3: Summary of all plane-specific displacement velocities.....	176

# Declaration

The work contained in this thesis is entirely original and my own my own work except for the following collaborations: finite element simulations carried out in Chapters 4 and 7 were performed by Dr. M. Peruffo, while those conducted in Chapter 5 were written by Dr M. Snowden. The synthetic polycrystalline materials used as substrates in the dissolution studies in Chapter 6 were prepared by Dr. R. Fisher. Some of the crystal growth experiments conducted in Chapter 7 were performed by E. L. Field.

I confirm that this thesis has not been submitted for any degree at another university.

Parts of this thesis have been included in the following publications:

1. C-A. McGeouch, M. A. Edwards, M. M. Mbogoro, C. Parkinson and P. R. Unwin, Scanning Electrochemical Microscopy as a Quantitative Probe of Acid-Induced Dissolution: Theory and Application to Dental Enamel, *Anal. Chem.*, **2010**, 82 (22), 9233-9328.
2. M. M. Mbogoro, M. E. Snowden, M. A. Edwards, M. Peruffo, and P. R. Unwin, Intrinsic Kinetics of Gypsum and Calcium Sulfate Anhydrite Dissolution: Surface Selective Studies under Hydrodynamic Control and the Effect of Additives *J. Phys. Chem. C*, **2011**, 115, 10147-10154.
3. R. Fisher, M. M. Mbogoro, M. E. Snowden, M. Joseph, J. Covington, P. R. Unwin and R. I. Walton, Dissolution Kinetics of Polycrystalline Calcium Sulfate-Based Materials: Influence of Chemical Modification, *Appl. Mater. Interfaces*, **2011**, 3 (9), 3528-3537.
4. M. M. Mbogoro, M. Peruffo, M. A. Edwards, and P. R. Unwin, A New holistic Approach to Dissolution Kinetics by Linking Direction-Specific

Microscopic Fluxes, Mass Transport Effects and Macroscopic Rates from Etch Pit Analysis: Application to Gypsum, *submitted to J. Phys. Chem. C.*

5. M. M. Mbogoro, M. Peruffo, E. L. Field, and P. R. Unwin, Quantitative 3-D visualization of micro-crystal growth kinetics using atomic force microscopy: Application to gypsum, *submitted to Cryst. Growth Design.*

# Abstract

This thesis is concerned with the growth and dissolution of gypsum and analogous crystalline materials, with the aim of understanding the kinetic and mechanistic processes at the mineral-solution interface. The research conducted was a collaborative project sponsored by Saint-Gobain Gypsum.

First, an image processing (IP) software package was developed to meet highly specialised IP needs and expedite the extraction of vital surface information from images produced in the growth and dissolution studies carried out in this thesis.

A simple but powerful morphological analysis of characteristic etch pit features formed on the basal plane of gypsum was proposed, to aid the determination of intrinsic dissolution kinetics. Limiting the study to short times produced microscopic active features, which exhibited high and quantitative mass transport rates. At early times, the reaction was surface controlled, with the edge planes dominating the process, revealing anisotropic step propagation kinetics. With time, an increased contribution from mass transport was observed, suggesting that at later times, the basal plane dominated reaction kinetics. Common ion effects indicated a greater impact of  $\text{Ca}^{2+}$  than  $\text{SO}_4^{2-}$  in reducing dissolution rates while inert ions enhanced dissolution in a direction-specific way. With this approach, microscopic phenomena were related to macroscopic measurements thus reconciling experimental length scales.

Dissolution of the basal (010) and edge (001) surfaces of gypsum and polycrystalline anhydrite, were probed at the bulk scale by coupling the channel flow cell (CFC) technique which displays high mass transport rates, with off-line spectrometric measurements of dissolved  $\text{Ca}^{2+}$ . Quantitative modelling of the diffusion-reaction within the CFC yielded a linear rate law for the dissolution process. Rates from the basal plane and anhydrite were found to be consistent with other bulk measurements, while the highly reactive edge plane exhibited

high rates indicating a transport-limited process. Sodium trimetaphosphate, a common humid-creep inhibitor was found to significantly retard basal plane dissolution rates. Further CFC studies were carried out on industrially-relevant, chemically modified  $\text{CaSO}_4$  based materials, using a simple flux approach. It was found that models proposing a dissolution-precipitation pathway as the mode of action of humid-creep inhibitors were less plausible than those proposing a surface binding pathway.

Finally, the influence of solution stoichiometry,  $r = (a_{\text{Ca}^{2+}} / a_{\text{SO}_4^{2-}})$  on the growth kinetics of microscopic gypsum crystals was determined at a constant supersaturation. Crystal growth was found to be entirely controlled by surface kinetics over the range of  $r$ , with the edge planes dominating the process. The highest lateral rates were found at  $r = 1$ , diminishing sharply at  $r \neq 1$ , and indicating strong plane-specific dependence on  $\text{Ca}^{2+}$  and  $\text{SO}_4^{2-}$  availability. Additionally, dramatic changes in the morphology of grown crystals were observed. Propagation of steps on the basal face revealed a complex polynuclear layer-by-layer growth process for this surface. Macroscopic growth rates compared well to previous bulk measurements indicating that the approach used provided a comprehensive multi-scale view of gypsum growth processes.

# Abbreviations

AFM	Atomic Force Microscopy
BCF	Burton Cabrera and Frank model
BET	Brunauer Emmet and Teller theory
CFC	Channel Flow Cell
CNT	Classical Nucleation Theory
EDXA	Energy dispersive X-Ray
FEM	Finite Element Modelling
GUI	Graphical User Interface
ICP-MS	Inductively Coupled Plasma-Mass spectrometry
ICP-OES	Inductively Coupled Plasma-Optical emission Spectrometry
IP	Image Processing
IS	Ionic Strength
KSV	Kossel Stranski and Volmer model
LCM-DIM	Laser Confocal-Differential Interference Contrast
Matlab	Mathematics Laboratory
MD	Molecular Dynamics
MSL	Micro-Stereo Lithography
NMR	Nuclear Magnetic Resonance
PBC	Periodic Bond Chain
QNM	Quantitative Nanomechanical Tapping
RDE	Rotating Disk Electrode
SECM	Scanning Electrochemical Microscopy
SEM	Scanning Electron Microscopy
<i>SPIP</i>	<i>Scanning Probe Image Processor</i>

SPM	Scanning Probe Microscopy
STM	Scanning Tunneling Microscopy
STMP	Sodium tri-metaphosphate
VSI	Vertical Scanning Interferometry
WLI	White Light Interferometry
XRD	X-ray Diffraction

# Glossary of Symbols

$\Delta G$	Free energy change
$\Delta g_s$	Free energy change per unit area
$\Delta g_v$	Free energy change per unit volume
$\mu$	Chemical potential
$2h$	CFC Channel height
$A_{pit}$	Etch pit surface area
$c_{eq}$	Concentration of $\text{CaSO}_4$ at equilibrium
$C_{eq}$	Concentration of free $\text{Ca}^{2+}$ at equilibrium
$C_{sat}$	Total Calcium concentration at equilibrium
$D$	Diffusion coefficient
$J_{[uvw], (hkl)}$	Direction-specific flux (or plane)
$J_n$	Nucleation rate
$J_o$	Intrinsic dissolution flux
$J_s$	Surface flux
$k_B$	Boltzmann Constant
$k_{diss}$	Dissolution rate constant
$k_f$	Rate constant for forward reaction
$k_r$	Rate constant for back reaction
$K_{sp}$	Solubility product
$k_t$	Mass transfer coefficient
$l$	Channel length
$l$	CFC Channel length
$l_p$	Characteristic pit dimension
$N$	Outward vector flux
$p$	Pressure
$r$	Solution ion ratio
$r^*$	Critical nucleus radius

$R$	Growth rate
$S$	Saturation state
$T$	Temperature
$t_{diff}$	Diffusion time
$v_{[uvw], (hkl)}$	Direction-specific step velocity (or plane)
$V_f$	Volume flow rate
$V_{pit}$	Etch pit volume
$w$	Channel width
$w$	CFC channel width
$\eta$	Dynamic viscosity
$\lambda$	Surface area ratio
$\rho$	Molar density
$\varphi$	Fraction of reactive surface area

# Chapter 1

## Introduction

The primary aim of this thesis is to investigate crystal growth and dissolution processes with particular emphasis on gypsum ( $\text{CaSO}_4 \cdot 2\text{H}_2\text{O}$ ). This chapter outlines the fundamental processes involved in crystal growth and dissolution and describes the associated thermodynamic and kinetic considerations. In addition, a critical review of gypsum growth and dissolution studies is provided and the need for a multi-scale approach which reconciles perceived discrepancies between local and bulk studies is highlighted. Finally the basic principles of some of the techniques used in this thesis are described.

### 1.1. Gypsum Crystallography

Gypsum ( $\text{CaSO}_4 \cdot 2\text{H}_2\text{O}$ ) is a crystal form of hydrated calcium sulphate and can be found in large quantities in underlying deposits.<sup>1</sup> The crystal structure of gypsum was first deduced by Atoji and Rundle<sup>2</sup> and later refined by Cole and Lancucki<sup>3</sup> using X-ray diffraction data. Gypsum exhibits a monoclinic prismatic structure (space group  $C2/c$ ) as shown in Figure 1.1 (a), and may be described as repeating layers of  $\text{Ca}^{2+}$  and  $\text{SO}_4^{2-}$  units perpendicular to the  $b$  axis.<sup>4</sup> The lattice parameters are;  $a = 5.679 \text{ \AA}$ ,  $b = 15.202 \text{ \AA}$ ,  $c = 6.522 \text{ \AA}$  while  $\alpha = \gamma = 90^\circ$ , and  $\beta = 118.43^\circ$ . A layer of  $\text{Ca}^{2+}$  is sandwiched between two  $\text{SO}_4^{2-}$  layers such that each  $\text{SO}_4^{2-}$  is tetrahedrally bound to four  $\text{Ca}^{2+}$  atoms<sup>4</sup> as observed in Figure 1.1(b). The arrangement is such that each plane of  $\text{Ca}^{2+}$  is between two  $\text{SO}_4^{2-}$  groups with  $\text{H}_2\text{O}$  molecules held between the  $\text{Ca}^{2+}$  and  $\text{SO}_4^{2-}$  units, linking the

$\text{SO}_4^{2-}$  planes through weak H-bonding. This arrangement allows for the perfect cleavage of (010) faces (Figure 1.1(c)) on gypsum crystals with a typical monolayer height of  $\sim 0.8$  nm comprising of a single  $\text{CaSO}_4$  bilayer.<sup>3</sup>

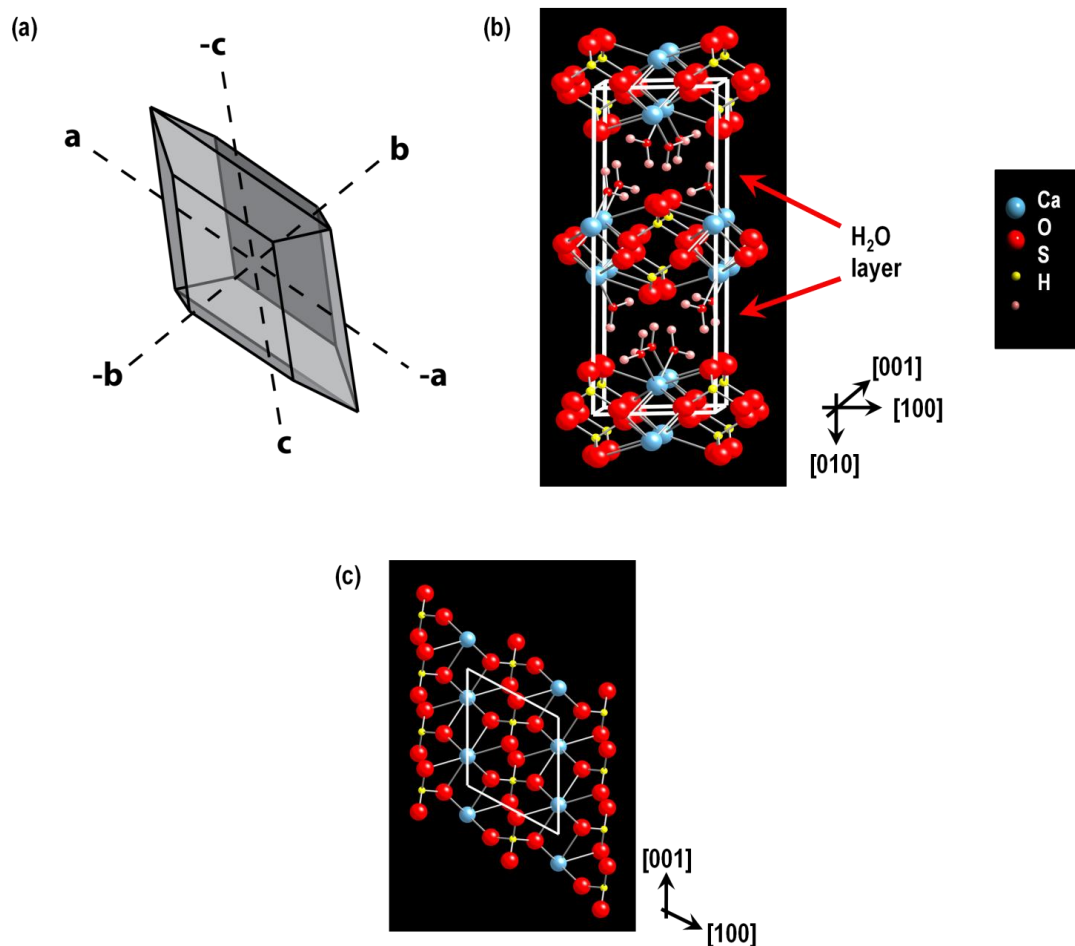


Figure 1.1: (a) Gypsum monoclinic prismatic morphology, (b) unit cell with the main crystallographic directions indicated and the interspaced  $\text{H}_2\text{O}$  layer shown, and (c) the atomic structure of the (010) surface.

The Periodic Bond Chains (PBCs) (see section 4.3 for further information) on gypsum crystal along the  $[100]$  and  $[001]$  directions are of significance particularly in gypsum growth and dissolution studies. Figure 1.2 illustrates the atomic arrangement in (a)  $[010]$  and (b)  $[001]$  monolayer steps

as well as (c) along the  $[100]$  direction. Atomic stacking follows a staggered arrangement of similar ions, i.e. from one Ca atom to a contiguous Ca atom, in  $[100]$  while in  $[001]$ , they lie directly on top of each other.<sup>4</sup> This atomic arrangement suggests that different faces may exhibit different reactivity when probing gypsum crystal growth / dissolution behaviour.

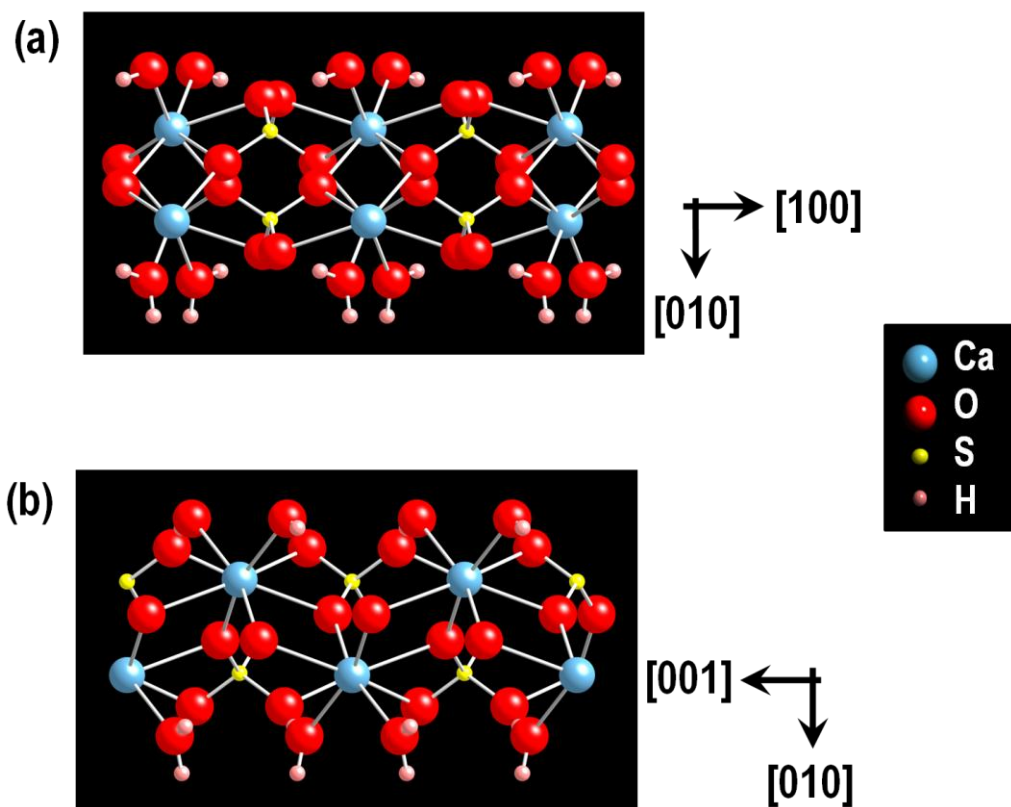


Figure 1.2: Atomic stacking along the (a)  $[100]$  and (b)  $[001]$  directions.

## 1.2. Applications of Gypsum

In addition to sedimentation, gypsum is also formed as a by product of nuclear power production.<sup>5-7</sup> Due to the physico-chemical properties exhibited by the mineral, gypsum is extensively used in the building and construction industry. The universal applications of gypsum based products have attracted huge demand as highlighted by global mining output of ~146 million metric tonnes in 2010.<sup>8</sup>

In addition, gypsum plays a role in the formation of mineral scaling and impacts the field of geochemistry. In this section, the role of gypsum in these fields will be discussed. The focus of the discussion will be the growth and dissolution of gypsum, which is the central theme connecting all these fields and applications and the topic of this thesis.

### 1.2.1 Calcination

One of the most popular applications of gypsum is in the manufacture of plaster products. Prior to the production of these materials, gypsum undergoes a calcination process which involves exposing it to elevated temperatures for prolonged periods.<sup>9</sup> Naturally, this process causes the expulsion of H<sub>2</sub>O from the crystalline matrix resulting in the decomposition of the crystal lattice structure and the formation of the meta-stable hemihydrate derivative (CaSO<sub>4</sub>·0.5H<sub>2</sub>O).<sup>10,11</sup> Further dehydration leads to the formation of anhydrite (CaSO<sub>4</sub>).<sup>12,13</sup> Phase transformation caused by the calcination process cause drastic changes to the mineral structure and consequently, to physico-chemical properties such as water resistance, flexural strength as well as durability.<sup>14</sup>

### 1.2.2 Building and Construction

Gypsum and its derivatives (anhydrite and hemi-hydrate) are typically used as additives in cement production in order to achieve optimum setting conditions which take advantage of quick hardening and high strength properties of gypsum. <sup>15,16</sup> However, in cement production, these derivatives are limited to internal use, as they are vulnerable to high levels of atmospheric humidity due to their hygroscopic nature. <sup>17</sup>

Gypsum is also widely used to manufacture plaster-board walls, where the susceptibility to high humidity environments is most striking. <sup>14,18</sup> During water uptake, humid creep occurs (Figure 1.3) where the plaster board increases in volume and expands thereby weakening the durability and strength of the plaster board. <sup>14,18</sup> Some studies suggest that humid creep is a consequence of a dissolution-precipitation mechanism involving a phase transformation from a gypsum derivative (hemi-hydrate or anhydrite) to gypsum crystal. <sup>19</sup> In order to understand the processes involved, and reduce the observed deleterious effects, various studies have investigated the role of additives on gypsum dissolution/crystallisation as well the reactivity of different gypsum faces under high humidity environments.<sup>20-22</sup>

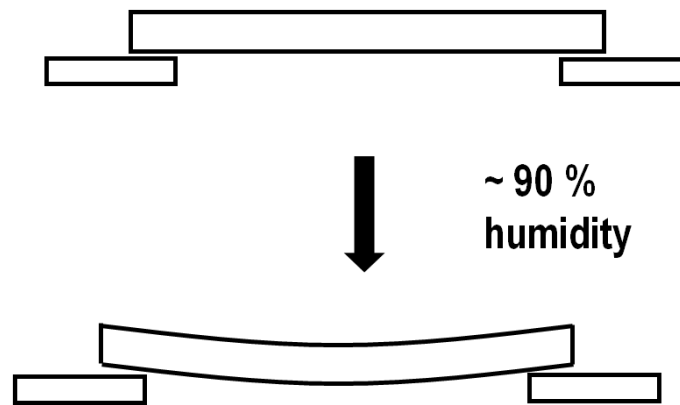


Figure 1.3: Humid creep of gypsum based plasterboard due to water uptake from atmosphere

### 1.2.3 Scaling and Weathering

Due to the ubiquity of gypsum building blocks ( $\text{Ca}^{2+}$  and  $\text{SO}_4^{2-}$  ions), the mineral is a dominant scalant and extensive studies have been carried out to investigate the factors which promote gypsum scaling and to find ways to suppress them.<sup>23-28</sup> Scaling occurs when water containing a substantial amount of dissolved ions forms precipitates on a surface due to a change in saturation (possibly due to evaporation of water close to these surfaces)<sup>28</sup>

Mineral scaling presents a pertinent problem in various areas. For instance, scaling in heat-exchange plants impedes the efficiency of thermal conduction<sup>23,31</sup> and in a similar way the performance of some household appliances (such as washing machines, dish washers, and electric kettles) due to scaling on heating elements.<sup>23,29</sup> In addition, it is a major challenge in industrial processes such as oil-extraction where precipitation on the inner surface of an oil pipeline can significantly impede the flux of fluids due to shrinkage of pipe capacity (Figure 1.4).<sup>7,30,31</sup>



Figure 1.4: Calcium sulphate scaling in oil pipe resulting in significant shrinkage of pipe capacity.<sup>32</sup>

Weathering occurs when crystal growth occurs in confined spaces such as pores and cracks in building materials and the resulting pressure due to small changes in volume can diminish structural integrity.<sup>33</sup> As a mineral used extensively in construction, the growth of gypsum crystallites in cements and other gypsum-based products can pose serious problems.<sup>34</sup> In order to counter this, some studies have attempted to understand the mechanisms of weathering in order to reduce the susceptibility of gypsum based materials.<sup>28,35-37</sup>

#### 1.2.4 Geochemistry

Large quantities of gypsum (and anhydrite) are found in both marine and continental deposits.<sup>38</sup> Compared to other sedimentary minerals such as carbonates, gypsum dissolution rates are relatively fast<sup>39-41</sup> and, as a consequence, extensive dissolution of these deposits can lead to the formation of karst features.<sup>21</sup> Karst formation (Figure 1.5) occurs due to dissolution of minerals from such underlying deposits and the subsequent removal of dissolved effluent by water (via underground streams and rain water).<sup>42</sup> Over

time, cavernous karsts may form causing the subsidence and collapse of overlying rock strata. This is particularly important in engineering ventures such as the construction of dams and reservoirs, where it is likely that the large volume of water held may tap into these mineral deposits and the subsequent dissolution may lead to significant devastation caused by flooding.<sup>1,43-45</sup>

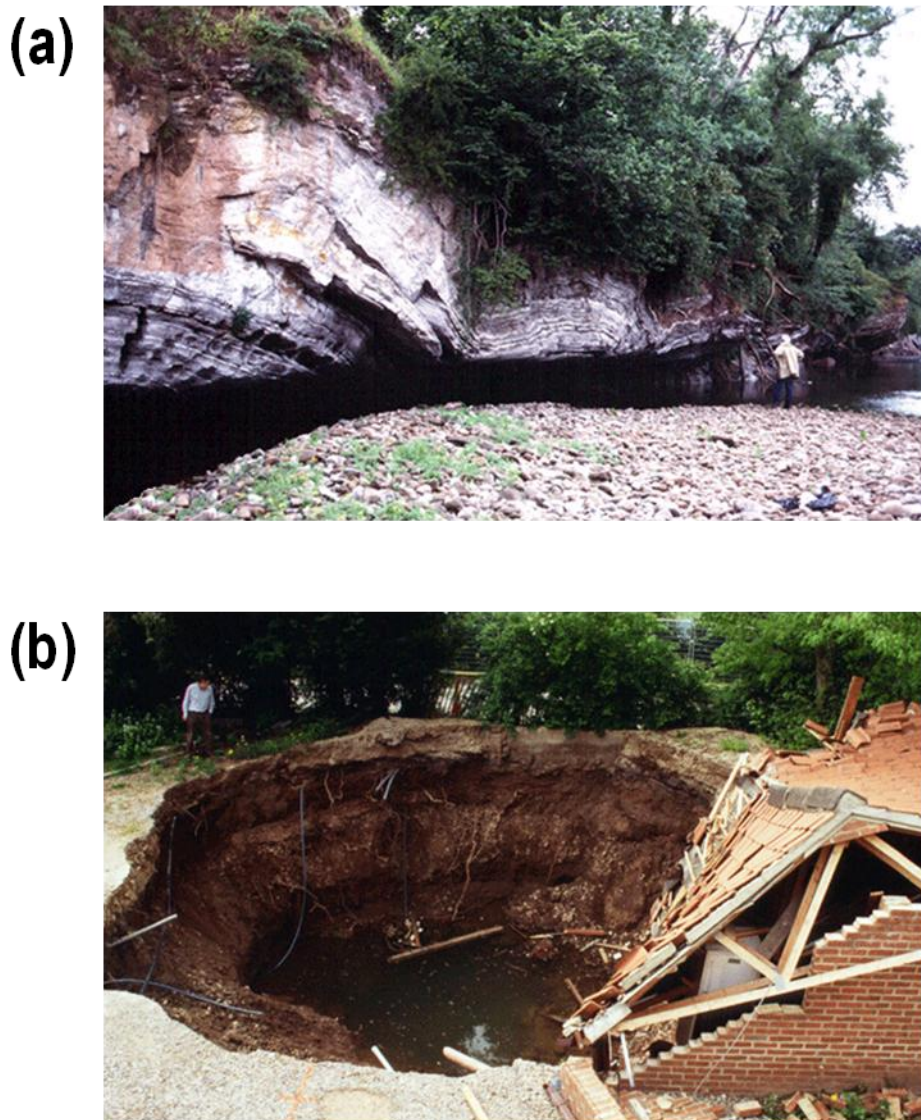
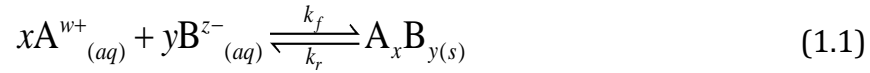


Figure 1.5: Gypsum karst formation where (a) flowing river water dissolves gypsum deposits and (b) subsidence caused by dissolution of underwater gypsum beds.<sup>46</sup>

### 1.3. Crystal Growth/Dissolution Reactions

The process of crystal growth and dissolution may be illustrated by the simple equation:



where  $\text{A}^{w+}$  and  $\text{B}^{z-}$  are reagent building blocks for the crystal  $\text{A}_x\text{B}_y$  and  $k_f$  and  $k_r$  represent the rate constants of the forward (nucleation and growth) and backward (dissolution) reactions, respectively. The saturation state,  $S$  is denoted by:

$$S = {}^{(w+z)}\sqrt{\frac{(a_A \times a_B)}{K_{sp}}} \quad (1.2)$$

where  $a$  is the activity of a reagent ion (A or B) and  $K_{sp}$  is the crystal solubility product. At equilibrium, the product of the activities is equal to the solubility product and  $S = 1$ . At this point, the forward and backward reactions have the same rate and thus, there is no net change in the system.

The formation of a new phase (either through crystal growth or dissolution), is represented by a deviation of the saturation state ( $S \neq 1$ ) or equivalently, a change in the chemical potential difference ( $\Delta\mu$ ) between the solution and the solid phase. When  $S < 1$  the system is undersaturated leading to dissolution and conversely, when  $S > 1$ , the system is supersaturated thereby promoting crystal growth. The extent of the deviation from equilibrium saturation is proportional to the thermodynamic driving force for the process. In thermodynamic terms, this driving force may be expressed as:

$$\Delta\mu = k_B T \ln \left[ \frac{(a_A \times a_B)}{K_{sp}} \right] \quad (1.3)$$

where  $k_B$  is the Boltzmann constant and  $T$  is the temperature. Taking the case of crystal growth as an illustrative case, a high level of supersaturation ( $S \gg 1$ ) corresponds to a large  $\Delta\mu$  and thereby a high driving force for nucleation/growth.<sup>47</sup> Equilibrium in this case is re-established via the formation of a solid crystalline phase, which continues until the dissolved ion concentration equals the solubility product and resulting in a reduction of the total free energy of the system.<sup>47</sup> The inverse argument applies in the case of crystal dissolution.

## 1.4. Crystal Growth Theory

### 1.4.1 Nucleation

Crystal nucleation is the process by which ions in the reagent phase arrange and aggregate to form a cluster of the product with a size that is thermodynamically stable.<sup>48</sup> Nucleation occurs primarily in two ways: *homogeneously* or *heterogeneously*. In the case of homogeneous nucleation, nuclei form in the bulk solution only, without the influence of a pre-existing solid phase<sup>47,49</sup> and usually occurs after an induction time which is governed by thermodynamics (system temperature, pressure etc) however, reaction kinetics play a significant role.<sup>29</sup> Alternatively, heterogeneous nucleation typically occurs on a pre-existing surface and is described below.

Homogeneous nucleation is well described by the Classical Nucleation Theory (CNT) as pioneered by the early works of Frenkel,<sup>50</sup> Turnbull and Fisher<sup>51</sup> as well as major contributions from Becker and Doring<sup>52</sup> and Volmer and Weber<sup>53</sup> and considers the energetics involved for the formation of a nucleus. The theory describes the forming nucleus as the result of collisions and aggregation of atoms into an ordered phase with a spherical shape (this shape

exhibits the lowest surface tension). The total free energy change ( $\Delta G$ ) of the nucleus formation is the sum of its volume and surface free energies<sup>29,47,54</sup> as described by:

$$\Delta G = -\left[\frac{4}{3}\pi r^3 \Delta g_v\right] + \left[4\pi r^2 \Delta g_s\right] \quad (1.4)$$

where  $r$  is the radius of the nucleus  $g_v$  is the free energy per unit volume and  $g_s$  is the free energy per unit area. A new stable solid phase has a much lower free energy than the prevailing supersaturated solution and therefore,  $\Delta G$  is negative. The volume free energy ( $\Delta g_v$ ) decreases with nucleus size, while the surface free energy ( $\Delta g_s$ ) increases with nucleus size (Figure 1.6(a)). As a consequence, the overall  $\Delta G$  increases with nucleus radius until it reaches a maximum ( $\Delta G^*$ ) at a certain nucleus radius, typically termed the critical radius,  $r^*$  and beyond this point, growth is favoured. Nuclei with radii smaller than  $r^*$  tend to dissolve back to ions.<sup>54</sup> Due to the activation barrier ( $\Delta G^*$ ), and the strong dependence on prevailing temperatures, (Figure 1.6(b)) homogeneous nucleation is likely to occur only at high supersaturation conditions ( $S \gg 1$ ) and consequently, is not typically observed in geological scales, where the saturation levels are closer to equilibrium ( $S = 1$ ).<sup>29</sup> Nuclei with radii smaller than  $r^*$  tend to dissolve back to ions.

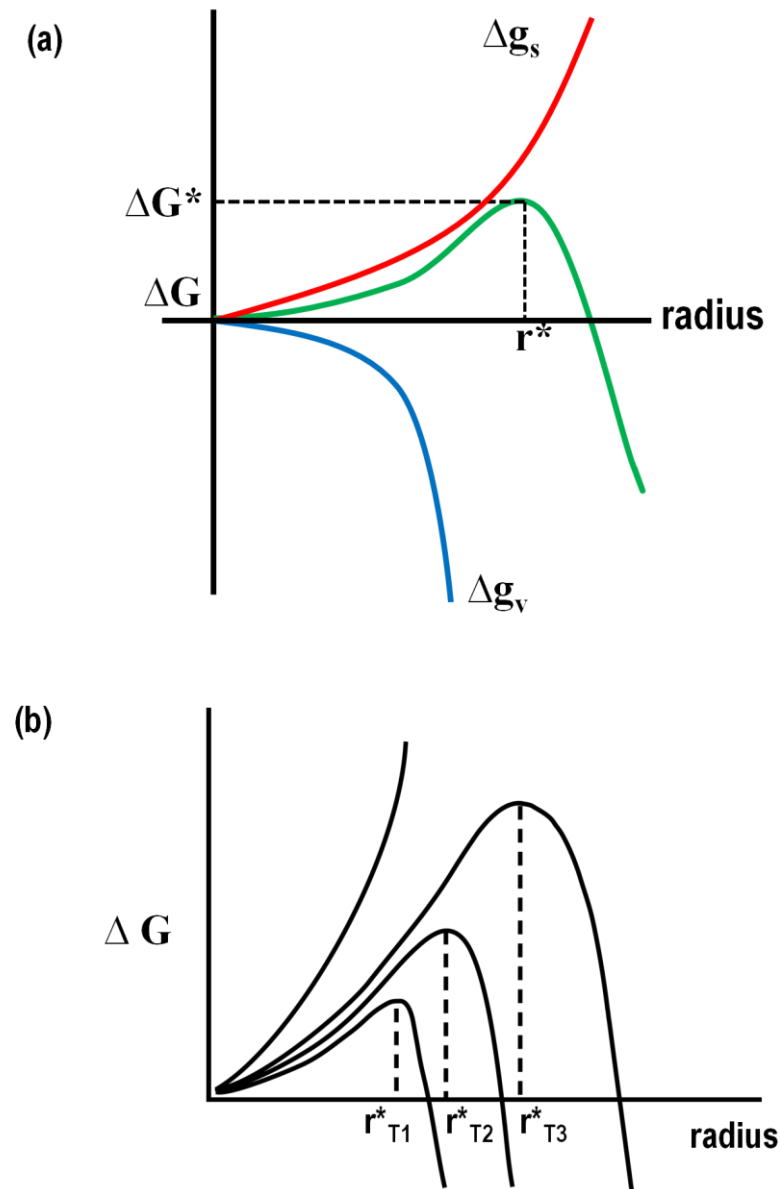


Figure 1.6: (a) Gibbs free energy diagram for crystal nucleation and (b) temperature dependence of the critical radius.

The nucleation rate,  $J$  follows an Arrhenius-type relation as described by:

$$J_n = A e^{\left(\frac{-\Delta G^*}{k_B T}\right)} \quad (1.5)$$

where  $A$  is a kinetic parameter related to the number of available nucleation sites on the nucleus.<sup>29</sup> A significant limitation of the CNT is that it assumes that the forming nucleus exhibits similar properties (such as interfacial

energy) to the bulk crystal.<sup>47</sup> However, the complex interplay between the kinetics and thermodynamics suggest the possibility of meta-stable clusters preceding the formation of the thermodynamically stable final crystalline phase.<sup>55</sup> These meta-stable phases give rise to polymorphism, where a kinetically favoured phase forms prior to reorganisation into a more thermodynamically stable polymorph (Figure 1.7).<sup>56-58</sup>

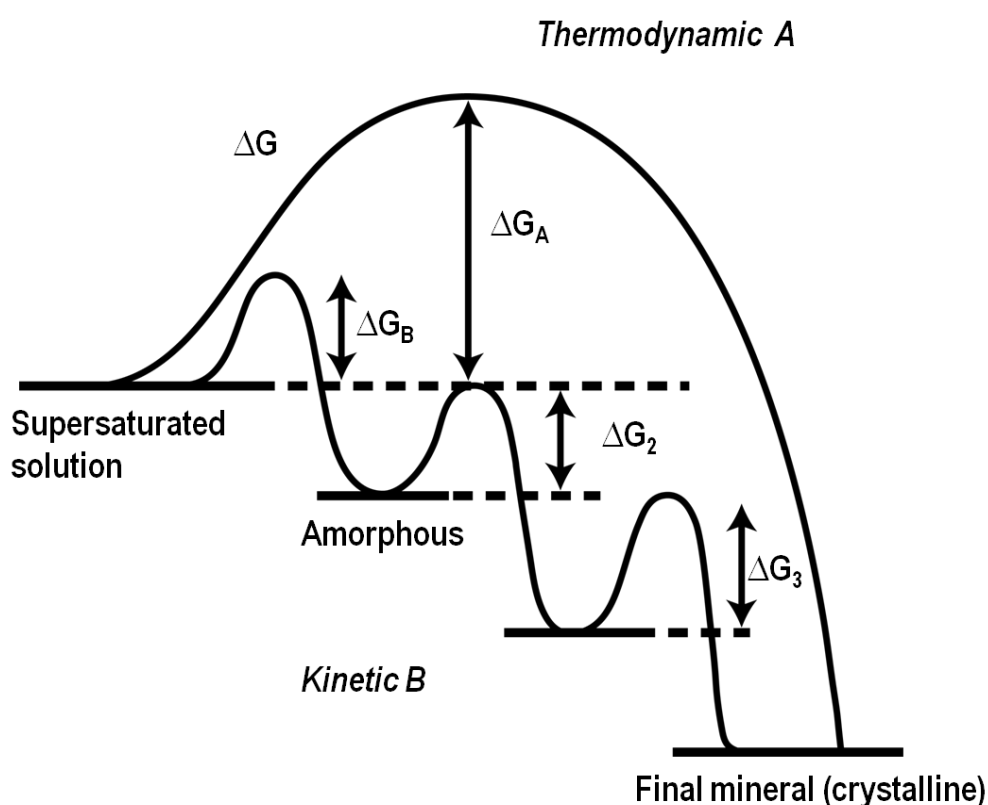


Figure 1.7: Interplay between kinetics and thermodynamics of crystal growth.<sup>58</sup>

Recent studies on crystal nucleation and growth have advanced our knowledge in this area considerably with some studies reporting the existence of complex nanosized precursors in organic biomineralisation.<sup>59,60</sup> More recently, Gebauer *et al.* observed these precursors in undersaturated solutions

close to equilibrium conditions, and formulated a possible alternative route to nucleation and subsequent crystal growth.<sup>61</sup>

Heterogeneous nucleation occurs when a new crystalline phase forms on an existing solid surface. Typically this occurs when the saturated media contains some solid impurities, or the crystalliser vessel has fissures, cracks or scratches which facilitate nucleation. The interfacial energy between a nucleus and a pre-existing solid surface is typically lower than that between a nucleus surface and the bulk media when homogeneously nucleation occurs.<sup>62-64</sup> The lower energy is due to the formation of stronger bonds between the ions which form the building blocks of the new crystalline phase and the solid surface compared to between these between the solvent and ions (solvation bonds). Stronger bonds lead to a smaller contribution of enthalpy to bond formation, thereby reducing the interfacial energy and thus the activation barrier to nucleation.<sup>63</sup>

The growth of these nuclei may be considered to grow in 2D or 3D depending on the nature of the surface and the initial shape of the nuclei. In the 2D case, only lateral growth occurs with the nuclei height remaining constant (*vide infra*).

#### **1.4.2 Crystal Growth**

Following the formation of stable nuclei, further attachment of new species leads to the formation of distinct ordered macroscopic surfaces through crystal growth. Growth kinetics may be considered to be governed by a sequence of steps: (i) mass transport of growth unit via diffusion through the bulk media, (ii) desolvation and adsorption onto the surface, (iii) diffusion of the growth unit across the surface and (iv) incorporation of growth unit onto an

energetically favourable site such as a kink or edge. (Figure 1.8). Processes i-ii are typically considered to be mass transport processes while iii-iv are surface processes. For dissolution models, the reverse sequence, i.e. iv-i applies. The rate of reaction is ultimately determined by the slowest of these steps.<sup>65,66</sup>

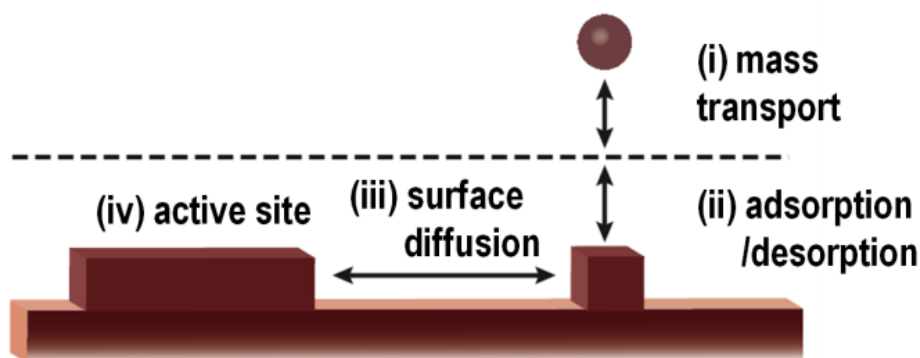


Figure 1.8: Fundamental steps involved in growth/dissolution at the crystal surface

Classical crystal growth models, as pioneered by the work of Volmer and Weber,<sup>53</sup> follows the adsorption of ions onto a planar surface via 2D nucleation which spreads to cover the entire surface thereby facilitating further growth (Figure 1.9). Polynuclear growth may also occur (Figure 1.10), which can cause the formation of defect sites which act as active sites. The Kossel, Stranski and Volmer (KSV) model suggests that incorporation of growth units into the crystal lattice occurs at these energetically favourable sites (kinks, steps, ledges).<sup>67-69</sup> According to the model, the incorporation of a growth unit at defect sites such as kinks involves binding at three points therefore presenting the most energetically favourable position. This is followed by an incorporation into steps then ledges, and finally the flat terrace where the adsorbing unit loses only one degree of freedom. Continuous growth eventually leads to a layer-by-layer

growth process and different rates of growth on different faces will determine the crystal macro-morphology.<sup>29</sup>

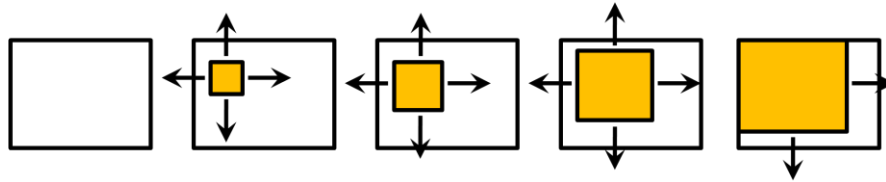


Figure 1.9: Mononuclear growth as a source for birth-and-spread growth.

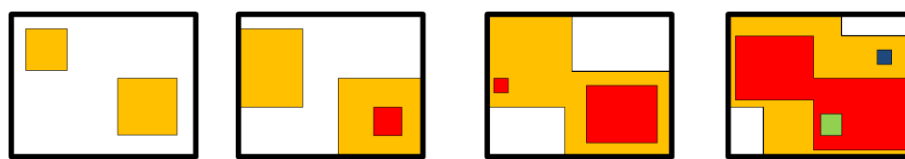


Figure 1.10: Polynuclear crystal growth.

Following the KSV model, Burton, Carbrera and Frank (BCF) asserted that the defect site from which kink sites emerge are screw dislocations which provide a more favourable site for nucleation than the planar surface.<sup>70,71</sup> A screw dislocation occurs during growth when rapid crystal growth or the incorporation of an impurity causes a mismatch on a contiguous layer (Figure 1.11).<sup>72</sup> They tend to propagate through the bulk crystal and creates a three dimensional spiral at the surface, which acts as an infinite source of steps (Figure 1.12). A dislocation is characterised by the Burger's vector which describes magnitude and direction of the atomic distortion around the dislocation.<sup>72</sup> The theoretical basis for describing crystal growth from a dislocation point as provided by the BCF model,<sup>73</sup> has since been validated by numerous microscopic studies.<sup>74-79</sup>

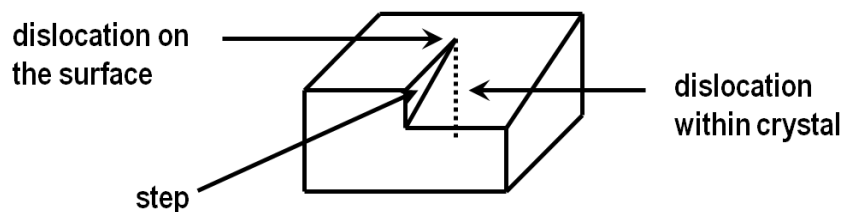


Figure 1.11: Screw type dislocation in a simple cubic lattice.

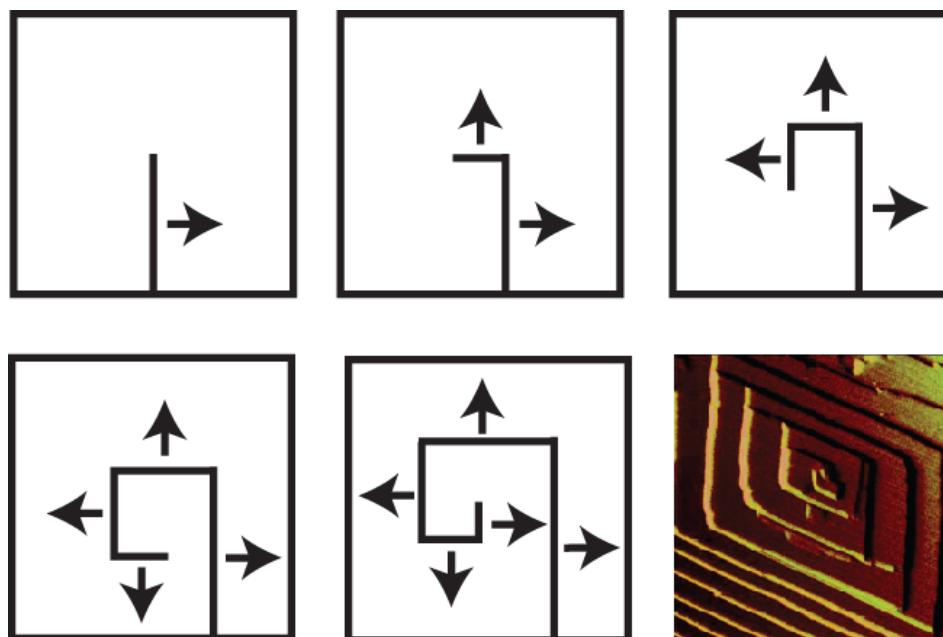


Figure 1.12: Typical sequence due to growth from a dislocation and AFM spiral growth image (bottom right).<sup>80</sup>

### 1.4.3 Crystal growth Mechanisms

Various crystal growth mechanisms relating the growth rate,  $R$  of an individual face, on the supersaturation conditions, for the different models described above. The BFC growth mechanism is assumed to be under transport-limited conditions.<sup>29</sup> At low supersaturation, below a critical value, the distance between contiguous steps is expected to be large and for this case, the rate of growth,  $R$ , follows a parabolic dependence on supersaturation, i.e.  $R \propto S^2$ .<sup>29</sup> In this case,  $R$  is considered to be independent of the diffusion boundary layer

thickness ( $\delta$ ) since the steps are isolated enough that their diffusion fields do not overlap and resulting in a significant amount of back-reaction (desorption of growth units back to bulk media) before eventual incorporation into the bulk crystal. On the other hand, at supersaturations higher than the critical value, a linear rate law,  $R \propto S$  is obtained, where the rate is inversely proportional to  $\delta$ . In this situation, the surface exhibits a high density of steps (and hence kinks) which facilitate fast adsorption and incorporation of growth units onto the surface.<sup>81</sup>

The birth-and-spread mechanism typically occurs at medium  $S$  where, nucleation (birth) occurs and growth (spread) proceeds at finite velocities,<sup>54</sup> resulting in a growth rate which depends on both the nucleation rate as well as the step velocity. This results in an exponential dependence of the growth rate on supersaturation:  $R \propto S^{5/6} \exp(S)$ .<sup>82</sup> At high  $S$ , (above critical value), the activation barrier to 2D growth is minimised, which reduces the requirement to attach to (typically more energetically favourable) kink sites and thus growth units may attach directly onto the terrace without further surface diffusion processes.<sup>29</sup> As a result, the surface roughens (so called kinetic roughening) in proportion to the increase in  $S$  and under these conditions,  $R$  depends linearly on  $S$ .

#### 1.4.4 The Crystal Habit

The description of a crystal in terms of its physical shape and appearance is termed the crystal habit. In growth and dissolution processes, the relationship between internal crystal structure and habit is fundamental to understanding the mechanisms through which crystals form. Bravais<sup>83</sup> was one of the first to associate the crystal habit with internal geometry and elucidate

the importance of certain crystal planes. Hartman and Perdok developed the periodic bond chain (PBC) theory which associates crystal geometry with bond energies.<sup>84,85</sup> In effect, one can segregate crystal faces in order of morphological importance as far as growth and dissolution processes are concerned (Figure 1.13). The PBC theory postulates that the *F* faces are flat at the molecular level and would grow either by 2D nucleation or via spiral growth from a dislocation. These faces have few kink sites which results in slow growth rates and consequently, they have significant influence on macroscopic crystal morphology. The *S* faces contain ledges with varying kink densities (depending on supersaturation, temperature e.t.c.), while *K* faces have numerous kink sites and therefore exhibit very fast growth kinetics.<sup>29</sup> Typically, the speed with which *K* faces grow means that steps on these faces are not observed under experimental time scales.

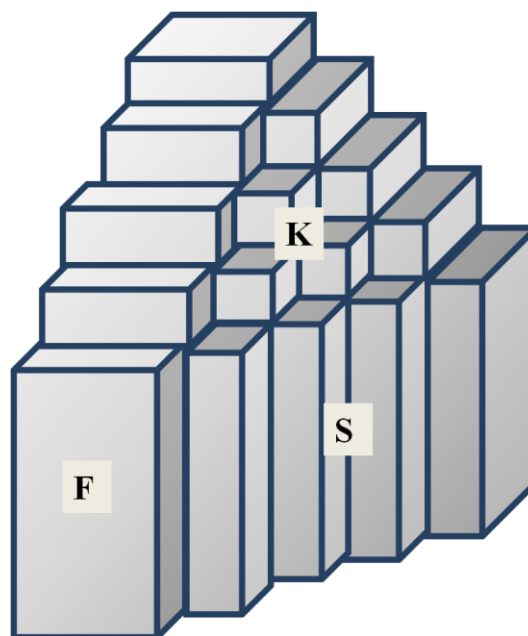


Figure 1.13: Simple cubic crystal showing different types of faces according to the periodic bond chain (PBC) theory.<sup>29</sup>

While the theories discussed above provide useful insights into crystal growth mechanisms, in real systems, the phenomenon involves the participation features on the entire crystal surface (kinks, ledges, terraces).

## **1.5. Review of Gypsum Crystal Growth Studies**

For a mineral which has been used for hundreds of years and applied to a vast array of fields, most early studies on gypsum were mainly concerned with the quantitative analysis of the physical properties of gypsum products.<sup>86-88</sup> Studies dedicated to understanding the mechanisms of gypsum crystal growth were not conducted extensively until the late 1950s.

### **1.5.1 Bulk Crystal Growth Studies**

The great majority of gypsum growth studies have been on the bulk scale which looks at macroscopic events and the factors which influence growth kinetics at this level. Several works have investigated nucleation kinetics and the influence of additives on the 'induction period' i.e. the period of time it takes to form a critical nucleus before crystal growth can occur. These include the early works by Shierholtz,<sup>89</sup> and later, by Nancollas and Liu<sup>90,91</sup> and others.<sup>92-94</sup> These studies found that additives significantly prolonged the induction time by retarding nucleation kinetics. On gypsum growth, works on suspensions or seeds was pioneered by Nancollas<sup>90,91,95-97</sup> who determined that growth kinetics followed 2<sup>nd</sup> order kinetics with respect to supersaturation. Later works have corroborated these findings.<sup>98-102</sup> Conversely, other studies have deduced rate laws which follow 1<sup>st</sup> order,<sup>89</sup> 3<sup>rd</sup> order<sup>103</sup> and even 4<sup>th</sup> order kinetics<sup>104</sup>. Recently, Witkamp *et al.*<sup>105</sup> deduced that the growth rate law varies from 2<sup>nd</sup>

order at low supersaturation in water, to 3<sup>rd</sup>-5<sup>th</sup> as ionic strength and supersaturation increase, potentially reconciling the discrepancies observed between previous bulk studies. Due to the vastly different experimental set ups and generally poorly defined mass transport conditions there is debate in whether the rate determining factor is diffusion control,<sup>89,98</sup> or surface control.<sup>90,95,101,106-108</sup> In addition, there is debate on the mechanism of growth, with some researchers suggesting a polynuclear 2D 'birth and spread' mechanism<sup>95,97,101,104,108</sup> while others, reporting that growth follows the spiral dislocation model.<sup>90,109</sup> Studies by Van Rosmalen *et al.*,<sup>56</sup> and Christoffersen *et al.*,<sup>52</sup> suggested a combination of both 2D 'birth and spread' and spiral growth models, depending on the saturation state and nature of defects on the crystal surface.

Due to the dominance of gypsum as a scalant, numerous studies have been focused on the effect of various scale inhibitors on gypsum growth. Inhibitors studied include; simple ions such as  $\text{NH}_4^+$ ,  $\text{NO}_3^-$ <sup>110,111</sup> and  $\text{Cl}^-$  salts<sup>92,93,111,112</sup> and numerous complex organic compounds such as polyacrylics,<sup>113,114</sup> phosphonates,<sup>91,101,114-117</sup> carboxylates<sup>94,101</sup> and copolymers.<sup>94,114</sup> In addition to retarding nucleation kinetics (*vide supra*), the general consensus is that these inhibitors operate by adsorbing on to growth sites (typically kinks and edges) thereby blocking the incorporation of growth units on the crystal surface.<sup>94</sup> For most of these studies, the incorporation of additives on the crystal surfaces, results predictably in a change in the morphology of grown crystals (Figure 1.14).

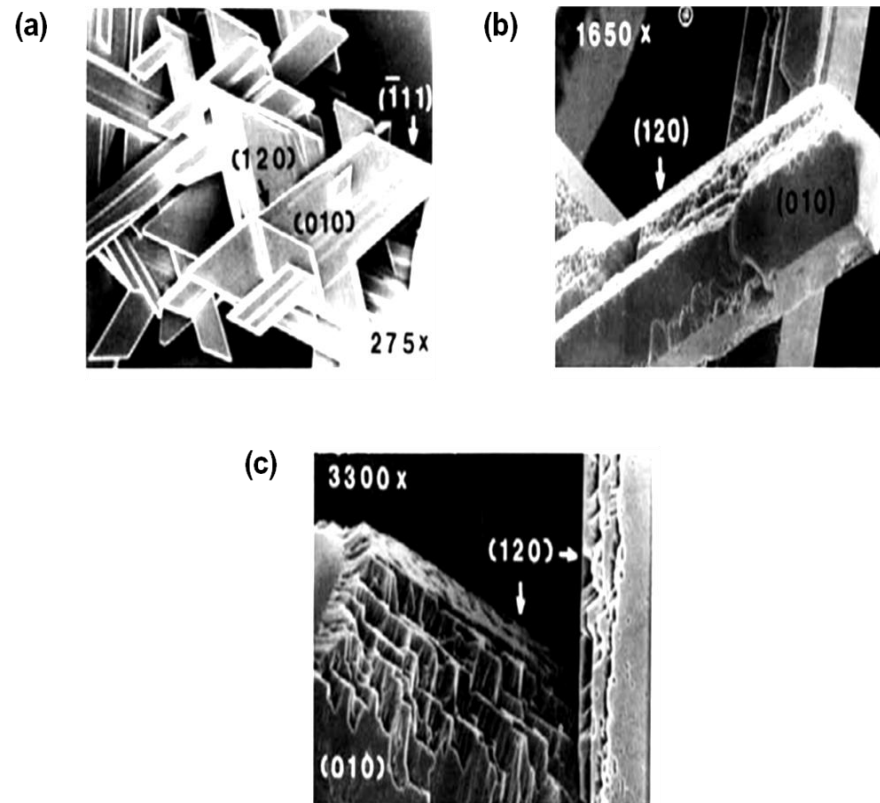


Figure 1.14: Scanning electron microscopy (SEM) images of (a) gypsum crystals grown in pure supersaturated solution and (b-c) grown in the presence of polyacrylate solutions.<sup>118</sup>

While macroscopic studies and the rates deduced therein are vital to our understanding of mineralisation mechanisms, they yield little information on the local processes at the crystal surface. As these eventually give rise to the macroscopically observed events, fundamental understanding of these processes is imperative. Therefore, in order to gain insights into gypsum growth kinetics, probing these local processes may provide a bridge between the vastly different perspectives of the macroscopic and the micro to nanoscale. To this end, various studies have been carried out and are discussed below.

### 1.5.2 Local Crystal Growth Studies

Compared to bulk studies, studies probing gypsum growth at a microscopic level has only gained momentum recently. This is primarily due to recent technological advances made through the invention of high resolution microscopy techniques such as atomic force microscopy (AFM) and white light interferometry (WLI) thereby revolutionising the way researchers probe surfaces.

Early work with a local perspective was carried out by Goto and Ridge<sup>109</sup> who investigated crystal growth from gypsum cleaved along the (010) plane via simple computer simulations. They reported a growth mechanism via the spiral growth model. Furthermore, growth was dominated by the displacement of the [001] and [100] steps. Recently, several *in situ* AFM studies by Bosbach *et al.*,<sup>111,116,119,120</sup> were carried out to investigate the growth on the (010) gypsum surface at close to equilibrium conditions ( $S \sim 1$ ). They reported a layer-by-layer growth mechanism with no evidence of spiral dislocations. In addition, they suggested a diffusion controlled growth process based on observing slower growth at sites of high step density compared to sites exhibiting isolated steps. Surface nuclei morphology was constrained to the [100] and [001] directions laterally and exhibited highly anisotropic displacement, following the trend:  $v_{[100]} \ll v_{[001]}$ , where  $v$  is the step displacement velocity in a particular direction. Step height was a few monolayers high ( $\sim 1$  nm) possibly as a consequence of the cleavage process. More recently, Van Driessche *et al.* corroborated a 2D layer-by-layer growth mechanism by studying the growth kinetics on cleaved (010) gypsum surfaces by combining *in situ* AFM with laser

confocal differential interference contrast microscopy (LCM-DIM).<sup>121</sup> This led them to suggest a mixed control as the dominant kinetic regime for this process.

While AFM has advanced the study of crystal growth at the local level, it has certain limitations, such as the range of scan speeds which can be successfully executed before one begins to lose imaging resolution.<sup>122</sup> This limitation is most relevant when visualising growth/dissolution phenomena under far from equilibrium conditions where step displacement velocities may be faster than the maximum cantilever raster speed attainable by the AFM set up. To this end, most AFM studies compensate for this by limiting experimental conditions to a range of supersaturations close to equilibrium conditions. In this way, the low driving force would yield step displacement velocities that can be accessed via AFM. Alternatively, some studies apply other techniques such as LCM-DCM<sup>121</sup> which allow for higher supersaturation conditions to be explored while others choose to work under *ex situ* conditions where the reaction may be monitored via time-dependent 'snapshots'.

## 1.6. Crystal Dissolution Theory

Whereas crystal growth has been studied extensively and corresponding growth theories developed in great detail, crystal dissolution has received much less attention despite its importance in a wide array of fields.<sup>123,124</sup> The thermodynamic driving force for dissolution is undersaturation ( $S < 1$ ), characterised by the principles outlined in Figure 1.8. Similar to crystal growth, dissolution starts preferentially at sites on the crystal surface which exhibit excess energy such as dislocations, kinks, edges and ledges over the planar

terrace (Figure 1.15). However, at extremely high undersaturation (and therefore a high driving force for dissolution), homogeneous nucleation at the perfect planar terrace is likely to occur as well in addition to the aforementioned defect sites.<sup>47</sup> The importance of considering the surface morphology is highlighted when one considers the factors that influence overall dissolution kinetics.

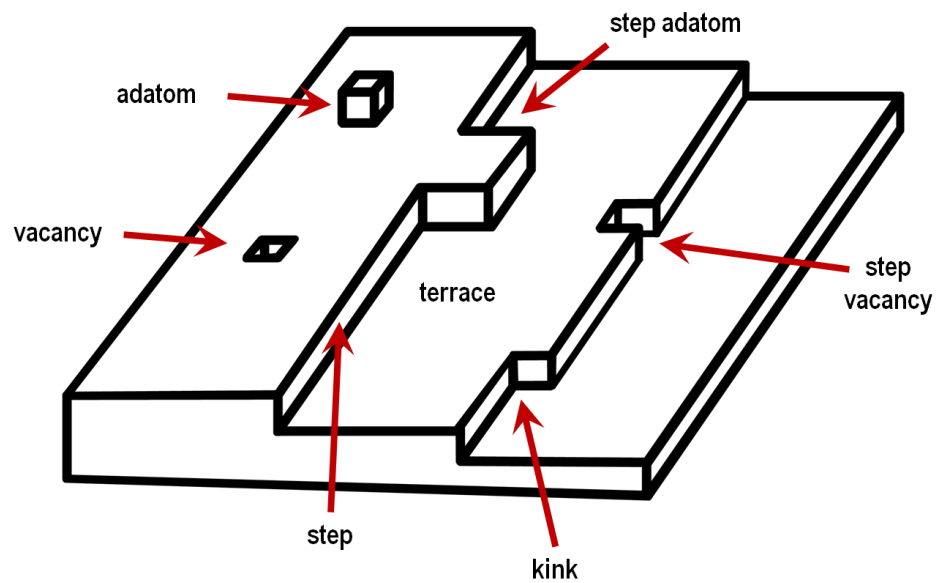


Figure 1.15: Typical features on a crystal surface.

Although each of these sites contributes to the dissolution of the crystal, the relative amount contributed differs greatly from one site to another as summarised in Figure 1.16.<sup>125</sup> Furthermore, these relative rates are dependent on the magnitude of the driving force.

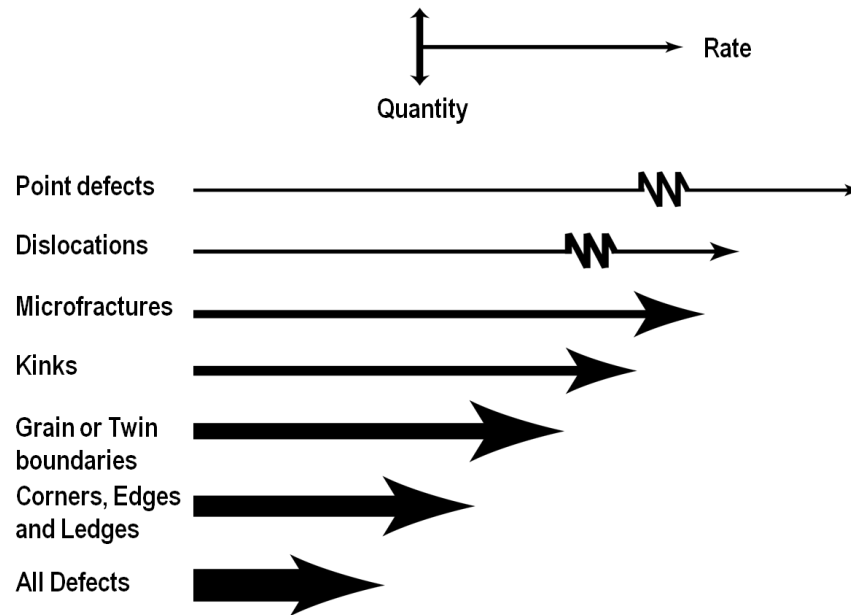


Figure 1.16: Parallel surface processes contributing to crystal dissolution.

Inspired by the development of the seminal BCF theory (*vide supra*), which describes dislocation-driven crystal growth (spiral growth), Cabrera and Levine<sup>126,127</sup> applied similar principles to crystal dissolution. In a similar way to crystal nucleation theory, at a critical driving force ( $\Delta G_{crit}$ ) typically under medium to high undersaturation conditions, the strain field of a dislocation opens up creating a hole with an increasing radius and forms a stable etch pit above a critical radius ( $r_{crit}$ ).<sup>126,127</sup> The formation is followed by a spiral dissolution mechanism, which provides an unlimited source of steps through which dissolution step waves can propagate (Figure 1.17).<sup>128</sup> Conversely, at close to equilibrium conditions, the size of the critical radius required to open the defect site is large and the thus etch pit nucleation is unfavourable.<sup>47</sup> Under these conditions, dissolution is largely characterised by dissolution at steps and edges rather than by etch pit formation.<sup>47</sup>

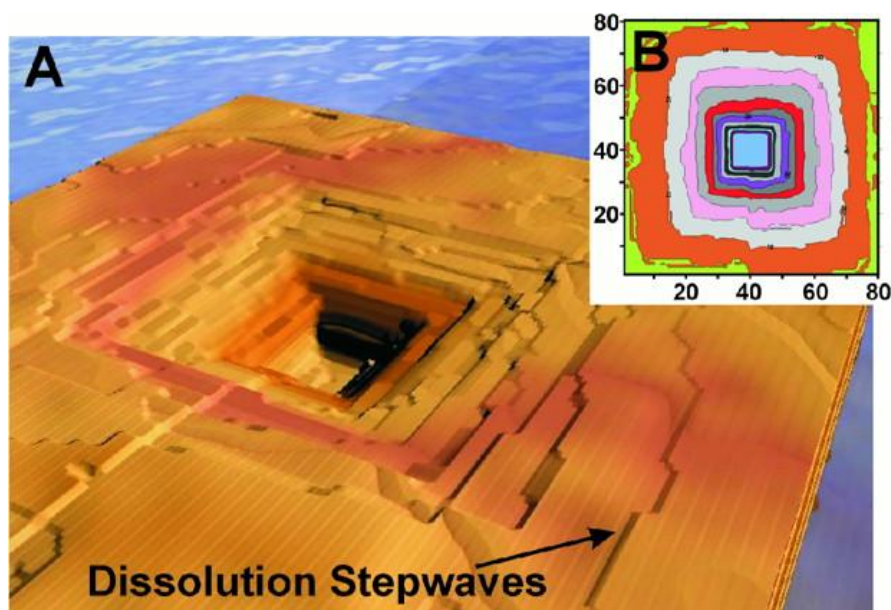


Figure 1.17: Dissolution etch pit as a source of stepwaves <sup>128</sup>

Recently, there has been an attempt to further develop crystal dissolution theories which reflect the dependence of dissolution rates on different undersaturation states <sup>123,124,128,129</sup> as well as independently express rate laws which are not necessarily analogous to those deduced for crystal growth studies as has been done in the past. <sup>124,130</sup> Furthermore, with the application of sophisticated complementary computer models which simulate crystal dissolution at the molecular level, the validity of proposed theories can be weighed against empirical observations. <sup>128,131</sup>

## 1.7. Review of Gypsum Crystal Dissolution Studies

### 1.7.1 Bulk Crystal Dissolution Studies

Analogous to crystal growth studies, bulk dissolution studies have been focused on the macroscopic events rather than the processes occurring at the crystal surface. For most studies, the reaction was monitored by estimating the

change in concentration of chemical species (such as dissolved  $\text{Ca}^{2+}$ ) via a number of ways; including electrochemical methods, mass spectrometry and titrimetry<sup>132</sup>. Deduction of dissolution rates and governing rate laws was typically carried out based on the time evolution of these concentration changes and the nature of prevailing mass transport conditions.<sup>40</sup> Some studies have applied well defined mass transport conditions by exploiting the rotating disk (RD) set up<sup>41,133-135</sup> or the channel flow cell (CFC) technique<sup>39</sup> while others have used suspensions<sup>136,137</sup> in batch or column set ups.<sup>138-142</sup> Due to this large variation in experimental methods and analytical techniques, there is a debate in the literature about the governing rate laws and rate determining processes. To this end, some studies claim that gypsum dissolution is a transport controlled process;<sup>133,136,137,140,143,144</sup> while others some assert a mixed control regime.<sup>41,134,135</sup> As expected, these studies yield equally divergent rate laws depending on experimental conditions (distance from equilibrium) with some suggesting 1<sup>st</sup> order kinetics<sup>39,41,136,145-148</sup> while others suggest 2<sup>nd</sup> order kinetics<sup>144</sup> and even zero order kinetics.<sup>133</sup>

An early study by Barton and Wilde<sup>133</sup> used the RD setup up with pelletised synthetic gypsum samples. While the experimental set up allows for well defined mass transport conditions, the use of polycrystalline samples introduced complications with regards to surface area changes and porosity during dissolution and in addition, the possibility of turbulence as an influential factor. Liu and Nancollas,<sup>136</sup> tracked gypsum dissolution from a stirred suspension and monitored concentration changes via a  $\text{Ca}^{2+}$  selective electrode. However, the mass transport conditions were poorly defined and the study assumed that for the case of an individual suspended crystal, dissolution

occurred in such a way that there was no change in the crystal's geometry, i.e. dissolution rate was the same in all directions. Since then various studies have corroborated the findings from these two studies in terms of deduced rate laws and/or the rate determining processes.

The implications of such divergent methods and experimental set ups was recently analysed by Colombani,<sup>40</sup> who collated and reviewed various earlier studies (including one of his own) and asserted that the essential difference between these was their mass transport condition (*vide infra*).

### 1.7.2 Local Crystal Dissolution Studies

Recently, attention has been focused on local surface behaviour in a similar way to crystal growth experiments, where high resolution local techniques such as AFM,<sup>149,150</sup> scanning electrochemical microscopy (SECM)<sup>151-155</sup> and vertical scanning interferometry (VSI)<sup>128,131,156,157</sup> have been exploited (*vide infra*). In these studies, the dissolution process is tracked via the evolution of the crystal surface at a microscopic/molecular level; deducing kinetics from analysing the surface retreat both normal to the surface and in the lateral directions.

Early local studies on gypsum dissolution relied on optical microscopy, probably because at the time, it was one of the best *in situ* methods used to obtain high resolution imaging of the process. These works were pioneered by Kasai *et al.*<sup>158</sup> and followed more recently by Raju<sup>159-161</sup> who observed the formation of rhombohedral etch pits. Raju asserted that these etch pits emerged from both screw and edge dislocation sites as evidenced from correspondence of etch pits produced from matched half experiments (etching on both the (010)

and  $(0\bar{1}0)$  surfaces). However, from these studies, there was no quantitative deduction of kinetics or the characterisation of dissolution features from a crystallographic perspective, thereby limiting the insights gained.

Since then, the development of the AFM and application of interferometry has transformed our understanding of crystal surfaces and their behaviour during dissolution. Recent *in situ* AFM studies by Bosbach and Rammensee<sup>119,120</sup> and Hall and Cullen<sup>162</sup> on the basal (010) plane of gypsum suggested that formed etch pits were constrained in the [101], [001] and [100] directions laterally and in the [010] direction normal to the cleavage plane. These etch pits were very shallow with a height of only a few monolayers ( $\sim 0.8$  nm), suggesting that they nucleated at point or line defects. In addition, etch pit evolution was found to be instantaneous (nucleation of new etch pits later in the process is rare) and exhibited similar behaviour to that observed in crystal growth studies, in that step displacement velocities was highly anisotropic, with the trend:  $v_{[100]} \ll v_{[001]} \approx v_{[101]}$ .

A later AFM study by Fan and Teng<sup>4</sup> corroborated these earlier AFM studies and postulated that the observed anisotropy was due to the drastically different atomic stacking along the [001] and [100] directions (Figure 1.2). However, they suggested that etch pit morphology was constrained only in the [100] and [001] directions, with the earlier mentioned [101] direction being the result of imaging the mirror surface, i.e. the  $(0\bar{1}0)$  plane. In addition, they observed progressive nucleation, i.e. nucleation of etch pits occurring throughout the etching experiment which is compatible with nucleation at point defects sites.

Colombani applied holographic interferometry to gypsum dissolution,<sup>40,132</sup> and deduced the intrinsic dissolution rate of gypsum crystal under surface controlled conditions to be  $5 \pm 2 \times 10^{-9} \text{ mol cm}^{-2} \text{ s}^{-1}$ .<sup>40</sup> As mentioned earlier, he reviewed various earlier works and reconciled the discrepancies in the mass transport conditions, by estimating the diffusion layer thickness for each study, and comparing these values to the saturation state. From these comparisons Colombani deduced an average gypsum dissolution rate of  $7 \times 10^{-9} \text{ mol cm}^{-2} \text{ s}^{-1}$ .<sup>40</sup>

## **1.8. Analysis and Characterisation Techniques**

This section describes the experimental techniques used throughout this thesis and the significance of investigating gypsum growth/dissolution studies from both local and bulk approaches.

### **1.8.1 Multi-Scale Approach**

The mineral-water interface is at the heart of any exchange between the crystal and the solution and it is important to take note of the prevailing conditions in the bulk solution as well as the nature of the bulk crystal lattice which governs surface processes.<sup>47</sup> As mentioned above, one of the most important challenges in crystal growth and dissolution studies is quantitatively relating macroscopically observed events to the local processes on the crystal surface from which they originate. Monitoring changes in the bulk solution may not reflect developments on the surface and as such, large discrepancies arise in otherwise internally consistent data.<sup>47</sup> To this end, growth/dissolution studies on specific systems can be carried out at different length and time scales. For

instance, dissolution occurring in a powder suspension may be thought of as representing a bulk study. A closer look at a single micro-crystal in this suspension reveals a dynamic surface morphology with numerous parallel events such as displacement of steps from various sources (kinks and steps) which collectively result in the overall dissolution of the crystal (Figure 1.16). Further magnification leads us to a molecular/atomistic view of processes involving individual species (ion-pairs, simple ions) with bond breaking and formation. It is therefore important to probe these crystal growth and dissolution studies from a multi-scale approach with the aim of reconciling perceived differences. The relationship between analytical techniques and the time and length scale they fall under is illustrated in Figure 1.18.<sup>163</sup>

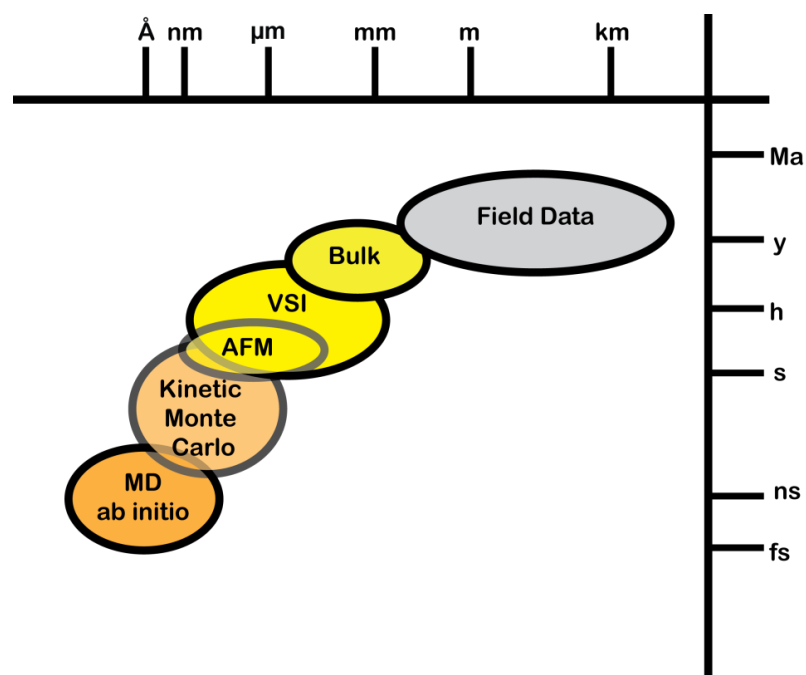


Figure 1.18: Relationship between different analytical techniques and the time (y-axis) and length (x-axis) scale under which crystal growth/dissolution is accessible.<sup>163</sup>

### 1.8.2 Bulk Techniques – The Channel Flow Cell (CFC)

To understand mineral/liquid reaction kinetics, experimental techniques need to be able to quantitatively separate mass transport and surface kinetic effects<sup>155,164</sup> and ideally allow the study of well-defined surfaces.

The channel flow cell (CFC) method (Figure 1.19) has proven particularly powerful for studying growth/dissolution processes.<sup>165-176</sup> This technique typically involves locating the crystal substrate of interest flush in the base wall of a rectangular duct through which solution flows under laminar conditions. Well-defined flow allows accurate modelling of mass transport within the flow cell chamber. Furthermore, because mass transport rates are controllable over a wide range, their influence on reaction rates can be elucidated quantitatively.<sup>165-176</sup> The CFC method permits rate laws governing a reaction to be proposed and tested by comparing experimental data to the predictions from mass transport-chemical reactivity models.<sup>165-177</sup> Hitherto, dissolution reactions in the CFC method have typically been monitored by the use of local electrochemical measurements<sup>165-177</sup> to provide in-situ detection of the dissolution process. However, some types of electrodes e.g. Ca<sup>2+</sup> ion selective electrodes are rather fragile and difficult to deploy in such cells.<sup>178</sup>

Due to current innovations in CFC design and fabrication (*vide infra*), the dimensions of a CFC unit can be accurately defined thus facilitating a well defined parabolic hydrodynamic regime (laminar flow). As a result, the CFC lends itself to theoretical modelling. Important issues to account for in hydrodynamic systems include determining whether solution flow follows a laminar profile above the exposed substrate region, and the mass transfer coefficient,  $k_t$  under varying flow rate conditions. For the CFC, these factors are

dependent on the cell dimensions. Laminar flow in CFCs is typically described with a Reynolds number,  $Re < 2000$ <sup>179</sup> and;

$$Re = \frac{\bar{U}l}{\nu} \quad (1.5)$$

where  $\bar{U}$  is the characteristic fluid velocity ( $\text{cm s}^{-1}$ ),  $l$  is a characteristic length (cm) and  $\nu$  is the kinematic viscosity (typically  $10^{-2} \text{ cm}^2 \text{ s}^{-1}$  for aqueous solution at standard conditions). The mass transfer coefficient can be approximated by applying the Levich equation<sup>180</sup>:

$$k_t = 0.925 D^{2/3} h^{-2/3} d^{-1/3} x^{-1/3} V_f^{1/3} \quad (1.6)$$

where  $D$  is the diffusion coefficient ( $\text{cm}^2 \text{ s}^{-1}$ ),  $h$  is the channel height (cm),  $d$  is the channel width (cm),  $x$  is the channel length and  $V_f$  is the volume flow rate ( $\text{cm}^3 \text{ s}^{-1}$ ).

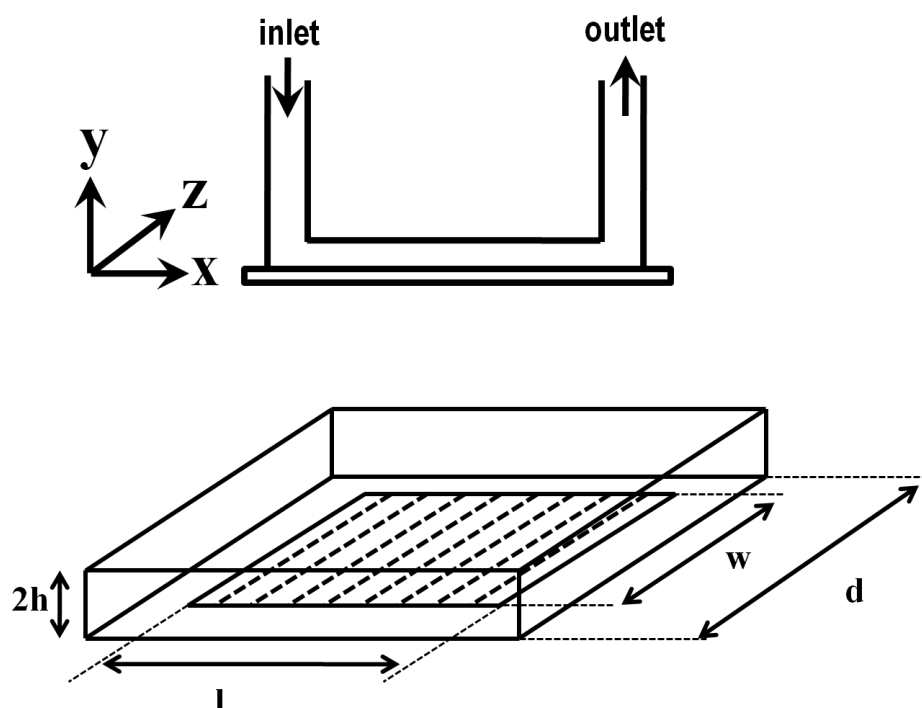


Figure 1.19: Typical channel flow cell schematic

### 1.8.3 Local Techniques

#### Atomic Force Microscopy (AFM)

The AFM technique was first developed by Binnig *et al.*,<sup>181</sup> based on scanning tunnelling microscopy (STM),<sup>182</sup> and belongs to a family of techniques under the banner of scanned probe microscopy (SPM). The technique operates by employing a sharp force sensing cantilever tip which rasters across the substrate surface and is deflected to correspond with the surface. Cantilever deflections are detected by a laser beam which reflects these changes to a photodiode, and this information is electronically translated into topographical information. AFM is typically applied in three main imaging modes: contact, tapping (intermittent) and non-contact. Using all imaging modes, AFM has been used extensively in crystal growth and dissolution studies.

More recently a new imaging mode known as Peak Force Quantitative Nanomechanical Tapping (Peak force QNM)<sup>TM</sup> has been developed by the commercial SPM suppliers, Veeco.<sup>183</sup> This technique improves on tapping mode AFM by first performing a fast force curve at every point of contact between the AFM tip and the substrate (Figure 1.20). The peak force obtained from the curve is then used as the feedback signal such that the force applied by the tip to the surface is controlled. In addition, by using auto-optimisation protocol (ScanAsyst) of scan parameters (such as scan rate, setpoint and gains) topographical images at very high resolution can be obtained.

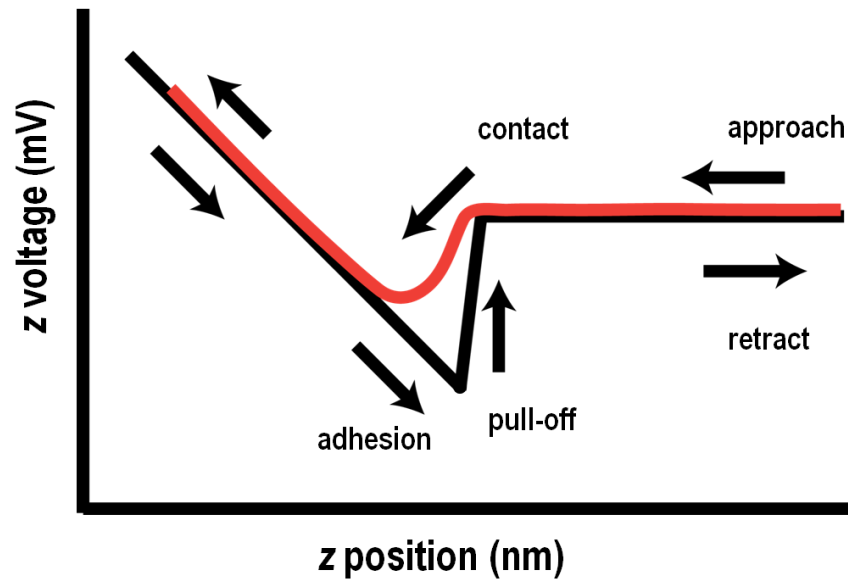


Figure 1.20: Typical force curve illustrating deflection of the cantilever as a function of distance from the substrate.

### White Light Interferometry (WLI)

WLI is a non-invasive optical profiling technique based on optical microscopy which utilises white light (broad band). Typically, a white light beam passing through the objective lens towards the sample. This beam is split into two whereby one beam reflects off a reference sample while the other reflects off of the test sample. The two beams recombine to form interference fringes from which surface topography can be mapped. Surface height information is obtained by controlled vertical scanning through the focal point as a camera (typically CCD) captures interference data.<sup>184,185</sup> For each point on the surface, the local surface height as well as lateral displacement information is extracted from the corresponding peak of the interference signal. WLI has a wide range in the direction normal to the substrate ( $z$ -axis) with an upper limit of up to  $\sim 100 \mu\text{m}$ , while the lower limit is comparable to AFM, at few nanometres.<sup>186</sup> However, WLI allows for a much larger scan area than AFM,

with a lateral range of up to  $\sim 1 \text{ mm}^2$ . A typical interferometer is illustrated in Figure 1.21(a).

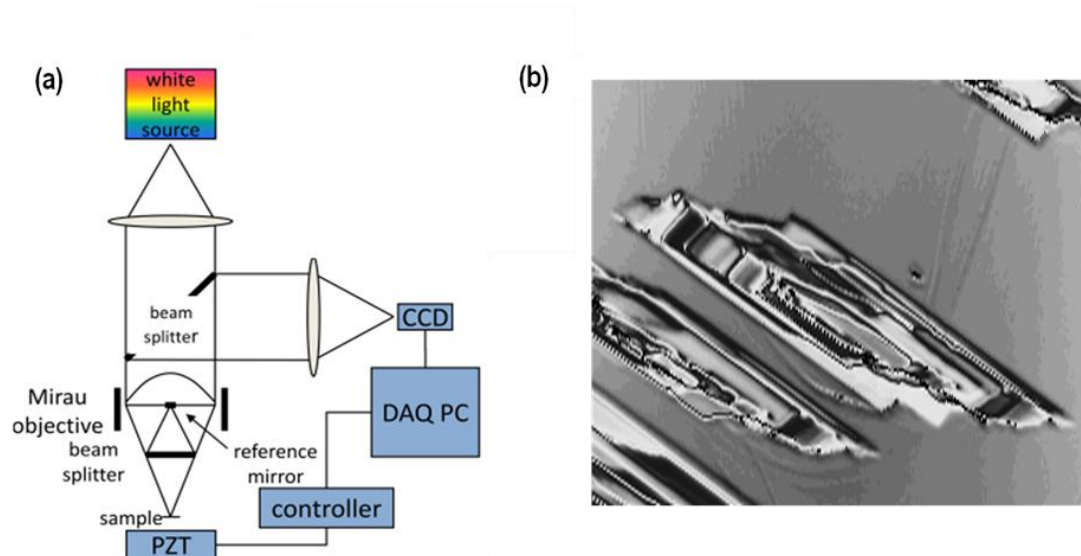


Figure 1.21: (a) Schematic of typical WLI.<sup>163</sup> and (b) interference fringes on an etched gypsum surface

## **1.9. Thesis Aims**

As a ubiquitous mineral with wide ranging industrial applications, the growth and dissolution processes of gypsum have attracted a significant amount of attention. However, as described in the introduction, dissolution processes are less well understood than growth processes and much remains to be done in this area.

To this end, the main aim of this thesis is to bridge the gap between the various experimental length-scales in crystal growth/dissolution studies. To achieve this, both local scale (Chapter 4) and bulk scale (Chapters 5 and 6) dissolution studies were carried out, and attempts were made to reconcile the apparent differences between these two approaches. The insights gained from these studies were then applied to local crystal growth of isolated gypsum micro-crystals (Chapter 7), and the approach validated by comparing to bulk studies in the literature.

At the most basic level, the reliable elucidation of intrinsic kinetics requires determination of the relative contributions of mass transport (diffusion to/from bulk media) and surface reactions (processes resulting in the generation/adsorption of species at the crystal/solution interface). The studies herein aim to address this important issue by limiting investigations to conditions of high (and quantifiable) mass transport rates in order to 'outrun' the typically fast surface processes thereby allowing for the study of intrinsic rates. At the local scale (Chapters 4 and 7), studies were limited to the analysis of isolated microscopic active features which are known to exhibit fast mass transport rates. For bulk scale studies (Chapters 5 and 6), the CFC technique was applied where varying flow rates ensured high mass transfer rates.

Another important aspect of this work was to compare experimental insights with theoretical considerations. For all experimental investigations, computer simulations were developed with the aim of accurately predicting spatially resolved local fluxes, and interfacial concentrations, by solving the diffusion-reaction problem at the surface/solution interface. In the case of CFC studies, this was done by formulating convective-diffusive equations which describe mass transport in the CFC, coupled to a boundary condition for dissolution of the crystal surface. In this way, reaction rate laws may be tested and validated against experimental data.

While bulk studies provide significant insights into reaction kinetics, these observations are typically the result of average surface reactivity, which 'masks' the contribution of individual crystal faces. An important feature of local studies is that it is possible to distinguish between the reactivity of different crystal faces, and, as the reaction (dissolution/growth) progresses, emerging trends leading to bulk scale observations can be identified. Furthermore, such an investigation can be expanded to explore the effects of impurities/additives, particularly those known to be industrially significant in influencing reaction kinetics. This approach is applied in Chapter 5 where the CFC technique is coupled with a local study with the aim of determining the influence of impurities at specific crystal faces, based on observations made at the macroscopic level. In Chapter 7, it is shown that face-specific kinetics, and consequently the crystal habit, are strongly affected by growth media stoichiometry.

In addition to this main theme, the work herein explores the importance of image processing packages, typically used to analyse topographical images

produced via visualisation techniques such as AFM and WLI. Chapter 3 describes the development of a custom-designed image processing package with the aim of, expediting image analysis and extracting vital quantitative data. The relative merits of this approach compared to using a commercial package are explored, with the aim of highlighting the need for more sophisticated image processing methods, to meet the increasingly specialised needs in crystal-surface science.

Finally, the themes explored in this thesis are summarised in Chapter 8 with a brief discussion of potential future directions for crystal growth and dissolution studies.

## References

- (1) Ford, D. C.; William, P. W. *Karst Geomorphology and Hydrology*; Unwin Hyman, 1989.
- (2) Atoji, M.; Rundle, R. E. *J. Chem. Phys.* **1958**, *29*, 1306.
- (3) Cole, W. F.; Lancucki, C. J. *Acta Crystallogr., Sect. B: Struct. Sci.* **1974**, *B 30*, 921.
- (4) Fan, C.; Teng, H. H. *Chem. Geol.* **2007**, *245*, 242.
- (5) Gera, F.; Mancini, O.; Mecchia, M.; Sarrocco, S. In *Studies in Environmental Science*; J.J.J.M. Goumans, H. A. v. d. S., Th, G. A., Eds.; Elsevier: 1991; Vol. Volume 48, p 433.
- (6) Peris Mora, E.; Monzó, J.; Paya, J.; Borrachero, M. V. In *Studies in Environmental Science*; J.J.J.M. Goumans, G. J. S., Slood, H. A. v. d., Eds.; Elsevier: 1997; Vol. Volume 71, p 581.
- (7) Yan, T. Y. *Energy* **1984**, *9*, 265.
- (8) Founie, A. *Gypsum: Statistics and Information*, 2011.
- (9) Notholt, A. J. G.; Highley, D. E. *Gypsum and Anhydrite*; H.M.S.O: London, 1975.
- (10) Khalil, A.-A. A. *Thermochim. Acta* **1982**, *53*, 59.
- (11) Khalil, A.-A. A. *Thermochim. Acta* **1980**, *38*, 329.
- (12) Molony, B.; Ridge, M. J. *Aust. J. Chem.* **1968**, *21*, 1063.
- (13) Cave, S. R.; Holdich, R. G. *Chem. Eng. Res. Des.* **2000**, *78*, 971.
- (14) Coquard, P.; Boistelle, R. *Int. J. Rock Mech. Min.* **1994**, *31*, 517.
- (15) Kovler, K. *Cem. Concr. Res.* **1998**, *28*, 523.
- (16) Kovler, K. *Cem. Concr. Res.* **1998**, *28*, 423.
- (17) O'Rourke, B.; McNally, C.; Richardson, M. G. *Constr. Build. Mater.* **2009**, *23*, 340.
- (18) Gartner, E. M. *Cem. Concr. Res.* **2009**, *39*, 289.
- (19) Chappuis, J. *Colloid Surf. A-Physicochem. Eng. Asp.* **1999**, *156*, 223.
- (20) Badens, E.; Veesler, S.; Boistelle, R. *J. Cryst. Growth* **1999**, *198-199*, 704.
- (21) Finot, E.; Lesniewska, E.; Mutin, J. C.; Goudonnet, J. P. *Surf. Sci.* **1997**, *384*, 201.
- (22) Finot, E.; Lesniewska, E.; Mutin, J. C.; Goudonnet, J. P. *Langmuir* **2000**, *16*, 4237.
- (23) Kim, D. H.; Jenkins, B. M.; Oh, J. H. *Desalination* **2011**, *265*, 140.
- (24) Sohnel, O.; Garside, J. *Precipitation*; Butterworth-Heinemann: Oxford, 1992.
- (25) Bott, T. R. *Fouling of Heat Exchangers*; Elsevier: Amsterdam, 1995.
- (26) Cowan, J. C.; Weintritt, D. J. *Water-formed Scale Deposits*; Gulf Publishing Company, 1976.
- (27) Hoang, T. A.; Ang, M.; Rohl, A. L. *Chem. Eng. Technol.* **2011**, *34*, 1003.
- (28) El Dahan, H. A.; Hegazy, H. S. *Desalination* **2000**, *127*, 111.
- (29) Sangwal, K. *Additives and Crystallization Processes: From Fundamentals to Applications*; John Wiley & Sons Ltd: Chichester, 2007.
- (30) Salman, M.; Qabazard, H.; Moshfeghian, M. J. *Petrol. Sci. Eng* **2007**, *55*, 48.
- (31) Bader, M. S. H. *J. Petrol. Sci. Eng* **2007**, *55*, 93.
- (32) www.statoil.com.
- (33) Goudie, A. S.; Viles, H. A. *Salt Weathering Hazards*; John Wiley & Sons, Ltd: Chichester, 1997.
- (34) Kloppmann, W.; Bromblet, P.; Vallet, J. M.; Vergès-Belmin, V.; Rolland, O.; Guerrot, C.; Gosselin, C. *Sci. Total Environ.* **2011**, *409*, 1658.
- (35) Irassar, E. F.; Di Maio, A.; Batic, O. R. *Cem. Concr. Res.* **1996**, *26*, 113.
- (36) Liu, Z.; Deng, D.; Schutter, G. D.; Yu, Z. *Cement Concrete Comp.* **2011**, *33*, 179.
- (37) Liu, Z.; De Schutter, G.; Deng, D.; Yu, Z. *Constr. Build. Mater.* **2010**, *24*, 2052.
- (38) Klimchouk, A. *Int. J. Speleol.* **1996**, *25*, 9.
- (39) Mbogoro, M. M.; Snowden, M. E.; Edwards, M. A.; Peruffo, M.; Unwin, P. R. *J. Phys. Chem. C* **2011**, *115*, 10147.

- (40) Colombani, J. *Geochim. Cosmochim. Acta* **2008**, 72, 5634.
- (41) Jeschke, A. A.; Vosbeck, K.; Dreybrodt, W. *Geochim. Cosmochim. Acta* **2001**, 65, 27.
- (42) Klimchouk, A. *Int. J. Speleol.* **1996**, 25, 21.
- (43) Klimchouk, A.; Andrejchuk, V. *Int. J. Speleol.* **1996**, 25, 145.
- (44) James, A. N. *Soluble materials in civil engineering*; Ellis Horwood: Chichester, 1992.
- (45) Cooper, A. H.; Calow, R. C. *Avoiding gypsum geohazards: Guidance for planning and constriction*, 1998.
- (46) [www.bgs.ac.uk/science](http://www.bgs.ac.uk/science).
- (47) Brantley, S. L.; Kibicki, J. D.; White, A. F. *Kinetics of Water-rock Interaction*; Springer Science: New York, 2008.
- (48) Lasaga, A. C. *Kinetic Theory and applications in Earth Sciences*; Princeton Press: Princeton, 1998.
- (49) Chakreverty, B. K. *Crystal Growth: An Introduction*; North-Holland Publishing Company, 1973.
- (50) Frenkel, J. J. *Chem. Phys.* **1939**, 7, 538.
- (51) Turnbull, D.; Fisher, J. C. *J. Chem. Phys.* **1949**, 17, 71.
- (52) Becker, D.; Doring, W. *Ann. Phys-Berlin* **1935**, 24, 719.
- (53) Volmer, M.; Weber, A. Z. *Phys. Chem.* **1925**, 119, 277.
- (54) Sangwal, K. *Etching of Crystals, Theory, Experiment and Application*; North Holland: Amsterdam, 1987.
- (55) Merikanto, J.; Zapadinsky, E.; Lauri, A.; Vehkamäki, H. *Phys. Rev. Lett.* **2007**, 98, 145702.
- (56) Cölfen, H.; Antonietti, M. *Langmuir* **1998**, 14, 582.
- (57) Rieger, J.; Thieme, J.; Schmidt, C. *Langmuir* **2000**, 16, 8300.
- (58) Meldrum, F. C.; Cölfen, H. *Chem. Rev.* **2008**, 108, 4332.
- (59) Banfield, J. F.; Welch, S. A.; Zhang, H.; Ebert, T. T.; Penn, R. L. *Science* **2000**, 289, 751.
- (60) Navrotsky, A. *Proc. Natl. Acad. Sci. U. S. A.* **2004**, 101, 12096.
- (61) Gebauer, D.; Völkel, A.; Cölfen, H. *Science* **2008**, 322, 1819.
- (62) Mutaftschiev, B. In *Handbook on Crystal Growth*; Hurle, D. T. J., Ed.; North-Holland: Amsterdam, 1993, p 187.
- (63) De Yoreo, J. J.; Velikov, P. In *Biom mineralization*; Weiner, S., Ed.; Mineralogical Society of America: Washington DC, 2003; Vol. 54, p 57.
- (64) Chernov, A. A. *Modern Crystallography III: Crystal Growth*; Springer: Berlin, 1984.
- (65) Nielsen, A. E.; Toft, J. M. *J. Cryst. Growth* **1984**, 67, 278.
- (66) Nielsen, A. E. *J. Cryst. Growth* **1984**, 67, 289.
- (67) Kossel, W. *Nachr. Ges. Wiss. Göttingen. Math.-Phys. Klasse* **1927**, 135.
- (68) Stranski, I. N. *Z. Phys. C* **1928**, 136, 259.
- (69) Brandes, H.; Volmer, M. *International journal of research in physical chemistry and chemical physics* **1931**, 155, 466.
- (70) Burton, W. K.; Cabrera, N. *Discuss. Faraday Soc.* **1949**, 5, 33.
- (71) Cabrera, N.; Burton, W. K. *Discuss. Faraday Soc.* **1949**, 5, 40.
- (72) Hull, D.; Bacon, D. J. *Introduction to dislocations*; Butterworth-Heinemann: Oxford, 2001.
- (73) Burton, W. K.; Cabrera, N.; Frank, F. C. *Philos. Trans. R. Soc. Lond. Ser. A* **1951**, 243, 299.
- (74) Okabe, Y.; Kyu, T.; Saito, H.; Inoue, T. *Macromolecules* **1998**, 31, 5823.
- (75) Dobson, P. S.; Bindley, L. A.; Macpherson, J. V.; Unwin, P. R. *Langmuir* **2005**, 21, 1255.
- (76) Larsen, K.; Bechgaard, K.; Stipp, S. L. S. *Geochim. Cosmochim. Acta* **2010**, 74, 2099.
- (77) Larsen, K.; Bechgaard, K.; Stipp, S. L. S. *Geochim. Cosmochim. Acta* **2010**, 74, 558.

- (78) Cubillas, P.; Holden, M. A.; Anderson, M. W. *Cryst. Growth Des.* **2011**, *11*, 3163.
- (79) Kuvadia, Z. B.; Doherty, M. F. *Cryst. Growth Des.* **2011**, 2780.
- (80) Jung, T.; Sheng, X.; Choi, C. K.; Kim, W.-S.; Wesson, J. A.; Ward, M. D. *Langmuir* **2004**, *20*, 8587.
- (81) Markov, I. V. *Fundamentals of Nucleation, Crystal Growth and Epitaxy*; World Scientific: Singapore, 2003.
- (82) Pethrick, R. A. *Polymer structure Characterization*; RSC Publishing: Cambridge, 2007.
- (83) Bravais, A. *Memoire sur les systemes formes par des points distribute regulierement sur un plan ou dans l'espace*, 1850.
- (84) Hartman, P.; Perdok, W. G. *Acta Cryst.* **1955**, *8*, 49.
- (85) Hartman, P.; Perdok, W. G. *Acta Cryst.* **1955**, *8*, 521.
- (86) Welch, F. C. *Industrial & Engineering Chemistry* **1924**, *16*, 238.
- (87) Felsing, W. A.; Potter, A. D. *J. Chem. Educ.* **1930**, *7*, 2788.
- (88) Davis, C. F. *Industrial & Engineering Chemistry* **1935**, *27*, 1016.
- (89) Schierholtz, O. J. *Can. J. Chem.* **1958**, *36*, 1057.
- (90) Liu, S.-T.; Nancollas, G. H. *Talanta* **1973**, *20*, 211.
- (91) Liu, S. T.; Nancollas, G. H. *J. Colloid Interface Sci.* **1975**, *52*, 593.
- (92) Prisciandaro, M.; Lancia, A.; Musmarra, D. *AIChE J.* **2001**, *47*, 929.
- (93) Prisciandaro, M.; Lancia, A.; Musmarra, D. *Ind. Eng. Chem. Res.* **2001**, *40*, 2335.
- (94) Doğan, Ö.; Akyol, E.; Öner, M. *Cryst. Res. Technol.* **2004**, *39*, 1108.
- (95) Liu, S.-T.; Nancollas, G. H. *J. Cryst. Growth* **1970**, *6*, 281.
- (96) Nancollas, G. H.; Reddy, M. M.; Tsai, F. J. *Cryst. Growth* **1973**, *20*, 125.
- (97) Nancollas, G. H. *Adv. Colloid Interface Sci.* **1979**, *10*, 215.
- (98) Smith, B. R.; Sweett, F. J. *Colloid Interface Sci.* **1971**, *37*, 612.
- (99) Ching, W.; McCartney, E. R. *J. Appl. Chem. Biotechn.* **1973**, *23*, 451.
- (100) Ching, W.; McCartney, E. R. *J. Appl. Chem. Biotechn.* **1973**, *23*, 441.
- (101) Tadros, M. E.; Mayes, I. J. *Colloid Interface Sci.* **1979**, *72*, 245.
- (102) Christoffersen, M. R.; Christoffersen, J.; Weijnen, M. P. C.; Van Rosmalen, G. M. *J. Cryst. Growth* **1982**, *58*, 585.
- (103) Gunn, D. J. *Faraday Discuss. Chem. Soc* **1976**, *61*, 133.
- (104) Klepetsanis, P. G.; Koutsoukos, P. G. *J. Cryst. Growth* **1989**, *98*, 480.
- (105) Witkamp, G. J.; Van der Eerden, J. P.; Van Rosmalen, G. M. *J. Cryst. Growth* **1990**, *102*, 281.
- (106) Van Rosmalen, G. M.; Daudey, P. J.; Marchée, W. G. J. *J. Cryst. Growth* **1981**, *52*, 801.
- (107) Zhang, J.; Nancollas, G. H. *J. Cryst. Growth* **1992**, *118*, 287.
- (108) Klepetsanis, P. G.; Dalas, E.; Koutsoukos, P. G. *Langmuir* **1999**, *15*, 1534.
- (109) Goto, M.; Ridge, M. J. *Geol. Mineral.* **1967**, *4*, 349.
- (110) Kagawa, M.; Sheehan, M. E.; Nancollas, G. H. *J. Inorg. Nucl. Chem.* **1981**, *43*, 917.
- (111) Bosbach, D.; Junta-Rosso, J. L.; Becker, U.; Hochella Jr, M. F. *Geochim. Cosmochim. Acta* **1996**, *60*, 3295.
- (112) Van Rosmalen, G. M.; Marche'e, W. G. J.; Bennema, P. *J. Cryst. Growth* **1976**, *35*, 169.
- (113) McCartney, E. R.; Alexander, A. E. *J. Coll. Sci.* **1958**, *13*, 383.
- (114) Amjad, Z. *J. Colloid Interface Sci.* **1988**, *123*, 523.
- (115) Weijnen, M. P. C.; van Rosmalen, G. M.; Bennema, P. *J. Cryst. Growth* **1987**, *82*, 528.
- (116) Bosbach, D.; Hochella Jr, M. F. *Chem. Geol.* **1996**, *132*, 227.
- (117) El-Shall, H.; Rashad, M. M.; Abdel-Aal, E. A. *Cryst. Res. Technol.* **2002**, *37*, 1264.
- (118) Weijnen, M. P. C.; van Rosmalen, G. M. *Desalination* **1985**, *54*, 239.
- (119) Bosbach, D.; Rammensee, W. *Geochim. Cosmochim. Acta* **1994**, *58*, 843.

- (120) Bosbach, D.; Jordan, D. G.; Rammensee, W. *Eur. J. Mineral.* **1995**, *7*, 267.
- (121) Van Driessche, A. E. S.; Garcia-Ruiz, J. M.; Delgado-Lopez, J. M.; Sazaki, G. *Cryst. Growth Des.* **2010**, *10*, 3909.
- (122) Dove, P. M.; Platt, F. M. *Chem. Geol.* **1996**, *127*, 331.
- (123) Lüttge, A. *J. Electron Spectrosc. Relat. Phenom.* **2006**, *150*, 248.
- (124) Tang, R.; Nancollas, G. H.; Orme, C. A. *J. Am. Chem. Soc.* **2001**, *123*, 5437.
- (125) Schott, J.; Brantley, S.; Crerar, D.; Guy, C.; Borcsik, M.; Willaime, C. *Geochim. Cosmochim. Acta* **1989**, *53*, 373.
- (126) Cabrera, N.; Levine, M. M.; Plaskett, J. S. *Physical Review* **1954**, *96*, 1153.
- (127) Cabrera, N.; Levine, M. M. *Philos. Mag.* **1956**, *1*, 450
- (128) Lasaga, A. C.; Lüttge, A. *Science* **2001**, *291*, 2400.
- (129) Lasaga, A. C.; Lüttge, A. *Am. Mineral.* **2004**, *89*, 527.
- (130) Wang, L.; Nancollas, G. H. *Chem. Rev.* **2008**, *108*, 4628.
- (131) Cama, J.; Zhang, L.; Soler, J. M.; Giudici, G. D.; Arvidson, R. S.; Lüttge, A. *Geochim. Cosmochim. Acta* **2010**, *74*, 4298.
- (132) Colombani, J.; Bert, J. *Geochim. Cosmochim. Acta* **2007**, *71*, 1913.
- (133) Barton, A. F. M.; Wilde, N. M. *Transactions of the Faraday Society* **1971**, *67*, 3590.
- (134) Raines, M. A.; Dewers, T. A. *Chem. Geol.* **1997**, *140*, 29.
- (135) Dewers, T.; Raines, M. *Chem. Geol.* **2000**, *168*, 275.
- (136) Liu, S.-T.; Nancollas, G. H. *J. Inorg. Nucl. Chem.* **1971**, *33*, 2311.
- (137) Christoffersen, J.; Christoffersen, M. R. *J. Cryst. Growth* **1976**, *35*, 79.
- (138) Lebedev, A. L.; Lekov, A. *Geochem. Int.* **1990**, *27*, 85.
- (139) Bolan, N. S.; Syers, J. K.; Sumner, M. E. *J. Sci. Food Agric.* **1991**, *57*, 527.
- (140) Kuechler, R.; Noack, K.; Zorn, T. *Ecological Modelling* **2004**, *176*, 1.
- (141) Truesdale, V. *Aquatic Geochemistry* **2011**, *17*, 141.
- (142) Truesdale, V. *Aquatic Geochemistry* **2011**, *17*, 21.
- (143) Schachter, O.; Lev, C. *Isr. J. Chem.* **1968**, *6*, 51.
- (144) Gobran, G. R.; Miyamoto, S. *Soil Sci.* **1985**, *140*, 89.
- (145) Kemper, W. D.; Olsen, J.; deMooy, C. J. *Soil Sci. Soc. Am. J.* **1975**, *39*, 458.
- (146) Keisling, T. C.; Rao, P. S. C.; Jessup, R. E. *Soil Sci. Soc. Am. J.* **1978**, *42*, 234.
- (147) Keren, R.; Shainberg, I. *Soil Sci. Soc. Am. J.* **1981**, *45*, 103.
- (148) Keren, R.; O'Connor, G. A. *Soil Sci. Soc. Am. J.* **1982**, *46*, 726.
- (149) Jones, C. E.; Macpherson, J. V.; Unwin, P. R. *J. Phys. Chem. B* **2000**, *104*, 2351.
- (150) Malkin, A. J.; Kuznetsov, Y. G.; Glantz, W.; McPherson, A. *J. Phys. Chem.* **1996**, *100*, 11736.
- (151) Macpherson, J. V.; Unwin, P. R. *J. Phys. Chem.* **1994**, *98*, 1704.
- (152) Macpherson, J. V.; Unwin, P. R. *J. Phys. Chem.* **1994**, *98*, 11764.
- (153) Macpherson, J. V.; Unwin, P. R.; Hillier, A. C.; Bard, A. J. *J. Am. Chem. Soc.* **1996**, *118*, 6445.
- (154) McGeouch, C.-A.; Edwards, M. A.; Mbogoro, M. M.; Parkinson, C.; Unwin, P. R. *Anal. Chem.* **2010**, *82*, 9322.
- (155) Unwin, P. R.; Macpherson, J. V. *Chem. Soc. Rev.* **1995**, *24*, 109.
- (156) Vinson, M. D.; Arvidson, R. S.; Lüttge, A. *J. Cryst. Growth* **2007**, *307*, 116.
- (157) Beig, M. S.; Lüttge, A. *Geochim. Cosmochim. Acta* **2006**, *70*, 1402.
- (158) Kasai, J.; Kondo, H.; Takagi, H.; Sakuma, M.; Nakahara, M. *Gypsum and Lime* **1965**, *75*, 325.
- (159) Raju, K. S. *Bull. Mater. Sci.* **1980**, *2*, 139.
- (160) Raju, K. S. *Bull. Mater. Sci.* **1981**, *3*, 67.
- (161) Raju, K. S. *J. Mater. Sci.* **1985**, *20*, 756.
- (162) Hall, C.; Cullen, D. C. *AIChE J.* **1996**, *42*, 232.
- (163) Lüttge, A.; Arvidson, R. S. *J. Am. Ceram. Soc.* **2010**, *93*, 3519.

- (164) Macpherson, J. V.; Unwin, P. R. *J. Chem. Soc., Faraday Trans.* **1993**, *89*, 1883.
- (165) Compton, R. G.; Pritchard, K. L.; Unwin, P. R.; Grigg, G.; Silvester, P.; Lees, M.; House, W. A. *J. Chem. Soc., Faraday Trans. 1* **1989**, *85*, 4335.
- (166) Compton, R. G.; Pritchard, K. L.; Unwin, P. R. *J. Chem. Soc.-Chem. Commun.* **1989**, 249.
- (167) Compton, R. G.; Unwin, P. R. *Philos. Trans. R. Soc. Lond. Ser. A* **1990**, *330*, 1.
- (168) Compton, R. G.; Walker, C. T.; Unwin, P. R.; House, W. A. *J. Chem. Soc.-Faraday Trans.* **1990**, *86*, 849.
- (169) Barwise, A. J.; Compton, R. G.; Unwin, P. R. *J. Chem. Soc., Faraday Trans.* **1990**, *86*, 137.
- (170) Wilkins, S. J.; Compton, R. G.; Taylor, M. A.; Viles, H. A. *J. Colloid Interface Sci.* **2001**, *236*, 354.
- (171) Thompson, M.; Wilkins, S. J.; Compton, R. G.; Viles, H. A. *J. Colloid Interface Sci.* **2003**, *259*, 338.
- (172) Orton, R.; Unwin, P. R. *J. Chem. Soc.-Faraday Trans.* **1993**, *89*, 3947.
- (173) Brown, C. A.; Compton, R. G.; Narramore, C. A. *J. Colloid Interface Sci.* **1993**, *160*, 372.
- (174) Hong, Q.; Suarez, M. F.; Coles, B. A.; Compton, R. G. *J. Phys. Chem. B* **1997**, *101*, 5557.
- (175) Booth, J.; Sanders, G. H. W.; Compton, R. G.; Atherton, J. H.; Brennan, C. M. *J. Electroanal. Chem.* **1997**, *440*, 83.
- (176) Peltonen, L.; Liljeroth, P.; Heikkilä, T.; Kontturi, K.; Hirvonen, J. *Eur. J. Pharm. Sci.* **2003**, *19*, 395.
- (177) Compton, R. G.; Unwin, P. R. *Comprehensive chemical Kinetics*; Elsevier: New York, 1989; Vol. 29.
- (178) Compton, R. G.; Pritchard, K. L. *Philos. Trans. R. Soc. Lond. Ser. A* **1990**, *330*, 47.
- (179) Nakayama, Y. *Introduction to Fluid Mechanics*; Arnold: London, U.K, 1999.
- (180) Brett, C. M. A.; Brett, A. M. O. *Electrochemistry Principles, Methods, and applications*; OUP: Oxford, 2005.
- (181) Binnig, G.; Quate, C. F.; Gerber, C. *Phys. Rev. Lett.* **1986**, *56*, 930.
- (182) Binnig, G.; Rohrer, H. *Helv. Phys. Acta* **1982**, *55*, 726.
- (183) Pittenger, B.; Erina, N.; Su, C. *Quantitative Mechanical Property Mapping at the Nanoscale with Peak Force QNM*; Veeco Instruments Inc.: New York, 2010.
- (184) Creath, K. *An introduction to Phase-measurement Interferometry.*, WYKO Corporation Application Note: 87-004., 1987.
- (185) Caber, P. J. *Appl. Opt.* **1993**, *32*, 19.
- (186) Lüttge, A.; Bolton, E. W.; Lasaga, A. C. *Am. J. Sci.* **1999**, *299*, 652.

# Chapter 2

## Experimental Procedures

This chapter describes the experimental procedures, reagents used and analytical techniques employed in the studies carried out within this thesis.

### 2.1. Chemicals

All solutions used were prepared using Milli-Q reagent Water (Millipore) with a typical resistivity of 18.2 M $\Omega$  at 25 ( $\pm 1$ ) °C. All ionic strength and chemical speciation data were calculated using the numerical code MINEQL+ (Environmental Research Software Version 4.5).<sup>1</sup> Using this method, the solubility of gypsum,  $C_{sat}$  (total concentration of dissolved calcium at equilibrium) was found to be ~16.2 mM in pure H<sub>2</sub>O which compares well to the value reported experimentally (~15.2 mM).<sup>2</sup> The Davies equation was used to calculate the activity coefficients for each solution.<sup>3</sup> The solubility products ( $K_{sp}$ ) of gypsum and anhydrite were  $2.45 \times 10^{-5}$  and  $4.93 \times 10^{-5}$ , respectively.<sup>2</sup>

Chemical	Purity/Grade	Supplier
Calcium nitrate tetrahydrate (Ca(NO <sub>3</sub> ) <sub>2</sub> ·4H <sub>2</sub> O)	99%	Sigma
Sodium sulphate (Na <sub>2</sub> SO <sub>4</sub> )	≥ 99.0%	Fisher Scientific
Sodium nitrate (NaNO <sub>3</sub> )	≥ 99.0%	Aldrich

Potassium nitrate (KNO <sub>3</sub> )	≥ 99.0%	Sigma-Aldrich
Calcium chloride dihydrate (CaCl <sub>2</sub> .2H <sub>2</sub> O)	≥ 99.0%	Sigma-Aldrich
Dimethyl dichlorosilane (DMDCS)	≥ 99 %	ACROS Organics
Isopropanol (IPA)	Reagent grade	Fisher Chemicals
DL-Tartaric acid	99%	Sigma-Aldrich
Tri-sodium trimetaphosphate (STMP)	Reagent grade	Sigma-Aldrich
3,4,5,-trihydroxybenzoic acid monohydrate (gallic acid)	≥ 98.0%	Sigma-Aldrich
Boric acid (H <sub>3</sub> BO <sub>3</sub> )	≥ 99.5%	Fisher scientific
Ca <sup>2+</sup> ICP Standard (1 g dm <sup>-3</sup> )	≥ 99.0%	Fluka
P <sup>3+</sup> ICP Standard (1 g dm <sup>-3</sup> )	≥ 99.0%	Fluka
Aluminium dihydrogen phosphate monohydrate (AlH <sub>2</sub> PO <sub>4</sub> .H <sub>2</sub> O)	Reagent grade	Sigma-Aldrich
Orthophosphoric acid (H <sub>3</sub> PO <sub>4</sub> )	Reagent grade	Fisher scientific
α-plaster	Reagent grade	Saint-Gobain Formula

---

## 2.2. Etching of Crystal Surfaces

Large natural gypsum (St Gobain Gyproc) samples were broken into manageable pieces (area  $\sim 2 \text{ cm}^2$ ) and then cleaved along the (010) plane with a sharp razor blade, to produce clean fresh surfaces largely devoid of macrosteps. In some cases, the two surfaces produced were both studied and considered to be mirrors. The samples were cleaned with a strong burst of ultrapure  $\text{N}_2$  gas (BOC) to remove any adhered micro fragments. Next, they were mounted onto a holder with the (010) plane flush to the solution. In order to minimise contamination, samples were handled with tweezers at all times and only fresh cleavages were used.

Etching of individual crystals was carried out in approximately 100 ml of quiescent solution in a glass beaker. Experiments were performed at  $24 \pm 1^\circ\text{C}$ . The mounted crystal sample was submerged into the solution of interest to achieve complete surface wetting. After a set time, the sample was withdrawn and immediately dried with a strong burst of  $\text{N}_2$  gas (BOC). For the dissolution experiments in salt solutions, etched samples were quickly rinsed in water before drying with  $\text{N}_2$  gas. This was done to minimise the precipitation of salts on the crystal surface, upon drying with  $\text{N}_2$  gas. Dissolution experiments were carried out for times in the range between  $30 \pm 3$  and  $110 \pm 5$  s. Occasionally, extensive etching was carried out (*vide infra*) but these etched surfaces were not used to extract kinetic data.

It was important to determine the significance, if at all, of kinematic stepwaves,<sup>4</sup> on the timescale of the measurements herein, because this could alter the apparent depths and dimensions of pits measured. To this end, a section of a prepared sample was masked off and protected with tape (Pressure

Sensitive Tape Scotch <sup>TM</sup> Klebeband) which was carefully removed after dissolution.

To locate the region of interest, the surfaces were visualized via DIC, from which it was found that dissolution features stopped abruptly at the boundary between the masked-off region and the exposed crystal surface. The surfaces were visualized via WLI (NT 2000 Surface Profiler, WYKO systems) at a number of places across this boundary so as to measure any global recession of the basal plane. Figure 2.1(a), shows a VSI micrograph of the gypsum (010) basal surface after etching for 180 s (longer than the studies in the chapter) in pure H<sub>2</sub>O. The irregular elevated region between the masked and reactive areas is residue left after removal of the masking tape. Due to the low rates of global dissolution under the conditions applied, the residue allowed for a clear demarcation between the active and inactive regions over the surface. Figure 2.1(b) is a plot of the cross section shown in Figure 2.1(a), and highlights a negligible change in global height between the two regions. The average difference in height across between the two regions was found to be < 15 nm after etching for 180 s. Since the maximum etching time for dissolution experiments was ~ 100 s, we could therefore conclude that for the time scale chosen, dissolution was essentially limited to pits.

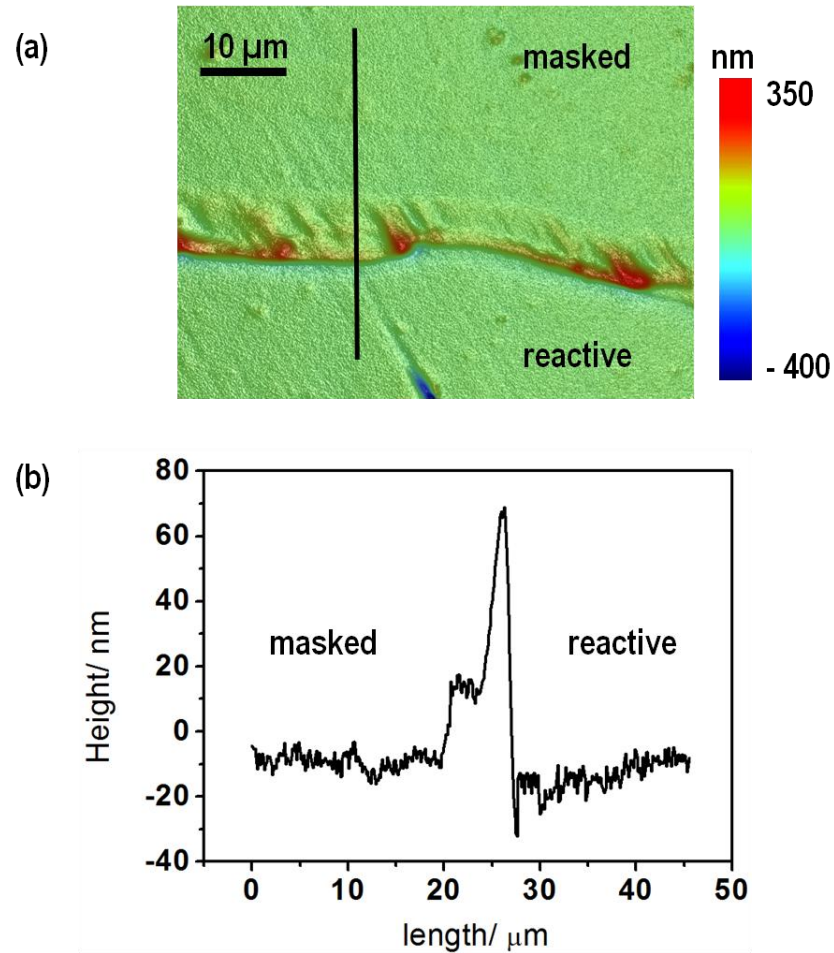


Figure 2.1: (a) WLI micrograph of gypsum (010) surface after etching for 180 sec and (b) plot of cross-section across the surface between masked and reactive regions.

### 2.2.1 Etch Pit Visualisation and Analysis

After etching, samples were sputtered with gold (Sputter Coater Quorum Technologies) producing a uniform coating  $\sim 12$  nm thick across the surface, which was negligible compared to the dimensions of the etch features. The resulting surfaces were visualized routinely via DIC optical microscopy (Leica DM 4000, Leica Microsystems) and AFM (AFM-tapping mode <sup>TM</sup>, using RFESP tips on a Veeco Multimode V with Nanoscope V Controller). Topographical images produced via these techniques were analysed via a Matlab program designed in-house (Chapter 3).

## 2.3. Channel Flow Cell (CFC) Studies

### 2.3.1 Preparation of Natural Samples

Natural gypsum single crystal samples (St Gobain Gyproc) were prepared by breaking large selenite crystals into manageable pieces ( $\sim 5 \text{ cm}^2$ ) and cleaving along the (010) plane with a sharp razor blade. Careful cleavage on this plane produced clean, fresh surfaces largely devoid of macro steps. Polycrystalline anhydrite (UKGE Limited) and (001) edge plane gypsum samples (exposed surface  $\sim 8 \text{ cm}^2$ ) were embedded in epoxy resin moulds (Delta Resins Ltd). These samples (anhydrite and edge plane gypsum) were first polished with silicon carbide 4000 grit paper (Buehler) and further on a pad with  $6 \mu\text{m}$  diamond spray (Kemet Int Ltd) followed by thorough rinsing in ultrapure  $\text{H}_2\text{O}$ . For each experiment, a fresh surface was fashioned by polishing the surface of the embedded crystal. Surfaces were etched before studies (*vide infra*) to ensure a contaminant-free surface.

### 2.3.2 Polycrystalline Materials Modified with Humid-Creep Additives

DL-tartaric acid (Sigma-Aldrich), trisodium trimetaphosphate (STMP) (Sigma-Aldrich), 3,4,5-trihydroxybenzoic acid monohydrate (gallic acid, Sigma-Aldrich) and boric acid (Fisher Scientific) were dissolved in Milli-Q reagent grade water (Millipore) with a typical resistivity of *ca.*  $18.2 \text{ M}\Omega \text{ cm}$  at  $25^\circ\text{C}$ , to yield solutions of  $1 \text{ mM}$ . This concentration was chosen to compare the effectiveness of humid creep inhibitors in quantities similar to those reported in industrial applications.<sup>5-8</sup> Gypsum samples were cast by mixing  $\alpha$ -plaster (94% calcium sulfate hemihydrate by thermo-gravimetric analysis (TGA) with these humid creep solutions, such that water: plaster = 0.7:1 by weight. A control

sample of similar ratio as the humid creep samples was also made where the plaster was mixed with pure water. Gypsum samples were produced by pouring the mixture into silicone moulds (12 mm diameter and 24 mm height), which were left for 1.5 hours to hydrate (conversion of  $\text{CaSO}_4 \cdot 0.5\text{H}_2\text{O}$  into  $\text{CaSO}_4 \cdot 2\text{H}_2\text{O}$ ). The cylindrical samples were then dried in an oven at  $40^\circ\text{C}$  for 12 hrs, after which samples were impregnated under vacuum with low viscosity grade epoxy resin (Epofix) and allowed to cure. The compositions, by weight, of samples prepared in this way are summarized in Table 2.1.

Table 2.1: Composition of humid creep additive samples in 1mM solution

Sample	Humid creep additive/ %	$\lambda$
Gypsum control	0	$1.5 \pm 0.1$
STMP	0.021	$1.4 \pm 0.3$
Tartaric acid	0.011	$1.4 \pm 0.2$
Boric acid	0.011	$1.8 \pm 0.2$
Gallic acid	0.013	$1.3 \pm 0.1$

### 2.3.3 Composite Phosphate Materials

Composite samples made with gypsum, aluminum dihydrogen phosphate and phosphoric acid in varying molar ratios were prepared by impregnating dry porous gypsum under vacuum; table 2.2. The samples were then dried at  $40^\circ\text{C}$  for 12 hr after which they were crushed and pressed (10 MPa, 1 min) before heating up to  $500^\circ\text{C}$  at  $5^\circ\text{C min}^{-1}$  and holding there for 2hrs. All samples processed in this way were polished with silicon carbide 4000 grit paper (Buehler) as well as on a pad with 6  $\mu\text{m}$  diamond spray (Kemet Int Ltd), after

which they were rinsed (1-2 s) in ultrapure H<sub>2</sub>O. For each dissolution experiment, a fresh surface was fashioned by polishing the surface as described below.

Table 2.2: Nominal compositions of composite samples.

Mole fraction				Al: P	$\lambda$
Ca	S	P	Al		
0.40	0.40	0.21	0.00	0	1.8 ± 0.2
0.40	0.40	0.19	0.02	0.1	1.9 ± 0.2
0.40	0.40	0.17	0.03	0.2	1.6 ± 0.3
0.40	0.40	0.15	0.05	0.33	1.8 ± 0.5

### 2.3.4 Surface Roughness Normalisation for CFC Studies

An important consideration in dissolution studies is the initial surface morphology or roughness and how this changes during the course of the reaction. Several studies have attempted to establish a consensus on an appropriate way to normalize dissolution rates for studies where the surface area changes.<sup>9-11</sup> In order to account for possible changes in surface roughness between different substrates and over the course of dissolution reactions, surface area measurements were carried out via WLI (WYKO NT-2000 Surface Profiler, WYKO Systems), typically using a 10 × or 20 × objective (*vide infra*).

### Natural Crystals

For samples used for the study in Chapter 5, surface roughness was addressed by initially etching samples with the expectation (validated, *vide infra*) that they would maintain a constant specific surface area during the course of dissolution. Thus, prior to CFC experiments, each sample was etched in a large volume (> 500 cm<sup>3</sup>) of ultrapure H<sub>2</sub>O at 22 ± 1 °C in a beaker stirred with a magnetic flea. After ~30 min, the sample was withdrawn and immediately dried

with a strong burst of N<sub>2</sub> gas (BOC). By etching the surface before CFC studies, we produced surfaces with a roughness factor,  $\lambda$  defined as the ratio between the specific surface area of the crystal due to dissolution and a smooth geometric area of similar lateral dimensions without fluctuations in the z-direction. This issue is further discussed in Chapter 5. In most cases,  $\lambda$  was found to be close to unity, but occasionally several times larger, depending on the sample (*vide infra*). An early study by Bruckenstein<sup>12</sup> found that mass transport to a rotating disk electrode (RDE) for a large dynamic range of rotation speeds was unaffected by values up to 7.5. Since the RDE and the CFC have similar mass transport rates,<sup>13,14</sup> it was reasonable to assume that the sample preparation procedure used would not significantly perturb mass transport in the CFC. To determine  $\lambda$  for the different etched substrates, surface area measurements were made using WLI and the images produced, and analyzed via SPIP.

### **Polycrystalline Surfaces**

For the polycrystalline samples embedded in a resin matrix (Chapter 6), the surface roughness measurements were carried out on the substrates both prior to, and immediately after, CFC experiments. The topographical images were analysed via WYKO (Figure 2.2). From these measurements,  $\lambda$  could be determined and used to normalize dissolution data obtained from ICP analysis, by the exposed surface area of the dissolving substrate, thereby providing reliable dissolution rates.<sup>15,16</sup>

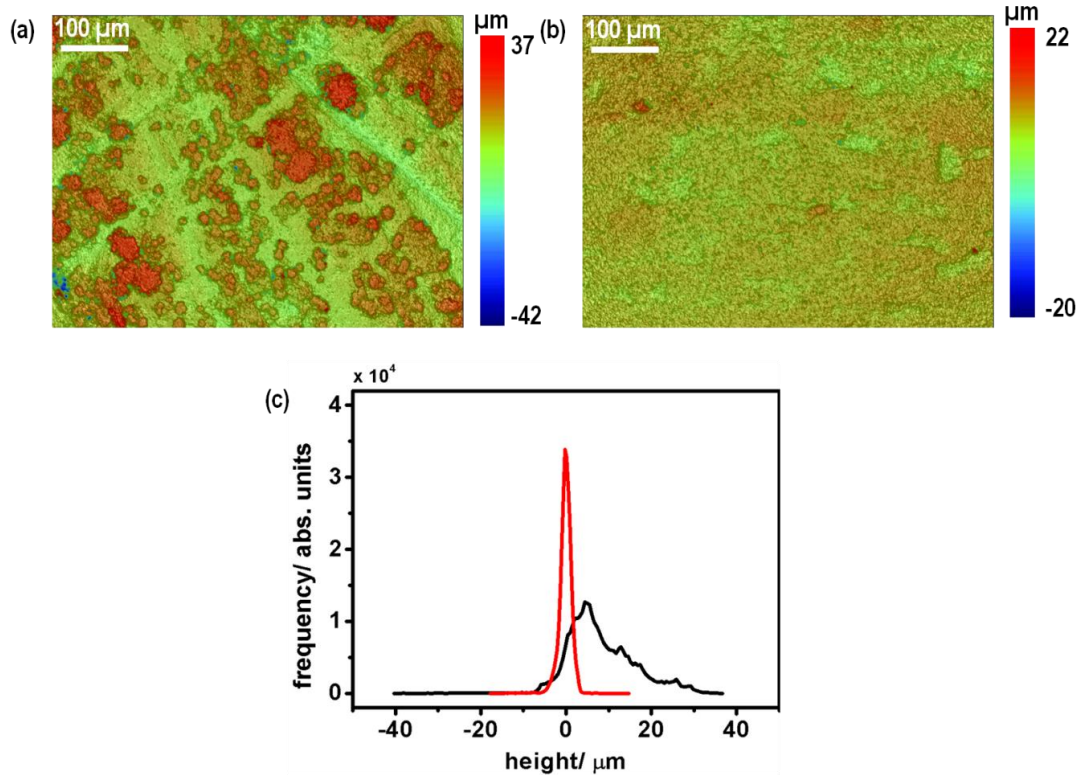


Figure 2.2: WLI height images displaying the surface topography of polycrystalline gypsum samples before (a) and after (b) polishing. A plot of the height of surface data points is also shown (c) where the rougher surface exhibits a wider spread (black) compared to the smoother polished one (red).

Polycrystalline samples were further visualised via scanning electron microscopy by Robin Fisher (Warwick University Dept. Chemistry) using SEM (EVO 50 XVP Zeiss Supra 55-VP) at 20 keV. Prior to SEM analysis, each sample was coated with a thin layer of carbon and a copper strip was attached to provide a conductive path to ground. Quantitative analysis of surface composition was carried out using energy dispersive X-ray analysis (EDXA) (Inca X-sight, Oxford Instruments) to determine the relative amount of resin and gypsum crystal on the surface using the backscattered electron detector, and then binarizing with ImageJ, a commercial IP package. This process was carried out to first, determine the nature of surface heterogeneity in order to

validate the approach used, and second, to estimate the relative proportion of active (crystalline) regions on the surface.

### **2.3.5 Design of The CFC Unit**

This group has recently introduced a new CFC design and fabrication procedure using micro-stereo lithography (MSL) to produce radically miniaturised one-part CFC units.<sup>17</sup> Briefly, the CFC unit is drawn using 3D graphical design software, SolidWorks (Dassault Systèmes, France) after which the design is used as input for a Micro-Stereo Lithography (MSL) system (Envisiontec PerFactory Mini Multi-Lens, Germany). The in-built MSL software then digitally slices the input design into 25  $\mu\text{m}$  horizontal slices for use as lithography masks to cure a single layer of photosensitive resin.<sup>18</sup> The first 'slice' is fabricated by lowering the build platform into a reservoir containing the resin, where a digital projector focuses the 3D design onto the plane sandwiched between the build platform and the resin stock. After curing this layer, the platform raises by the thickness of one layer (25  $\mu\text{m}$ ) to facilitate the fabrication of the next contiguous lateral 'slice'.<sup>17</sup> Subsequent layers are fabricated by repeating this process.

Most CFC designs comprise of two-part or three-part assemblies typically held together with nuts and bolts, to produce channels, typically 40 mm in length, 6-10 mm across and 0.2-1 mm high.<sup>19</sup> Such cells place some restrictions on sample size and the way in which crystal materials are presented for study. CFC units as described above eliminate awkward assembly (nuts, bolts or adhesive sealants) and greatly reduce the cell volume, without compromising mass transport. Indeed, a much wider range of mass transport rates can be

implemented. The MSL-CFC is assembled by simply placing a CFC unit on the substrate of interest and securing with light pressure or even a thread!

The CFC units used in Chapters 5 and 6, incorporated an in-built mixer in the outlet which ensured solution exiting the CFC was homogeneous. Figure 2.3 shows (a) the CFC unit schematically in cross-section with the mixer in the outlet with (b) a photo of the finished CFC unit and (c) perspective drawings of the CFC unit. The geometric area of the crystal exposed to solution was determined by the internal channel dimensions: the width,  $w$ , was 4 mm and length,  $l$ , was 10 mm. The channel height ( $2h$ ) was determined via WLI to be  $210 \pm 10 \mu\text{m}$ .

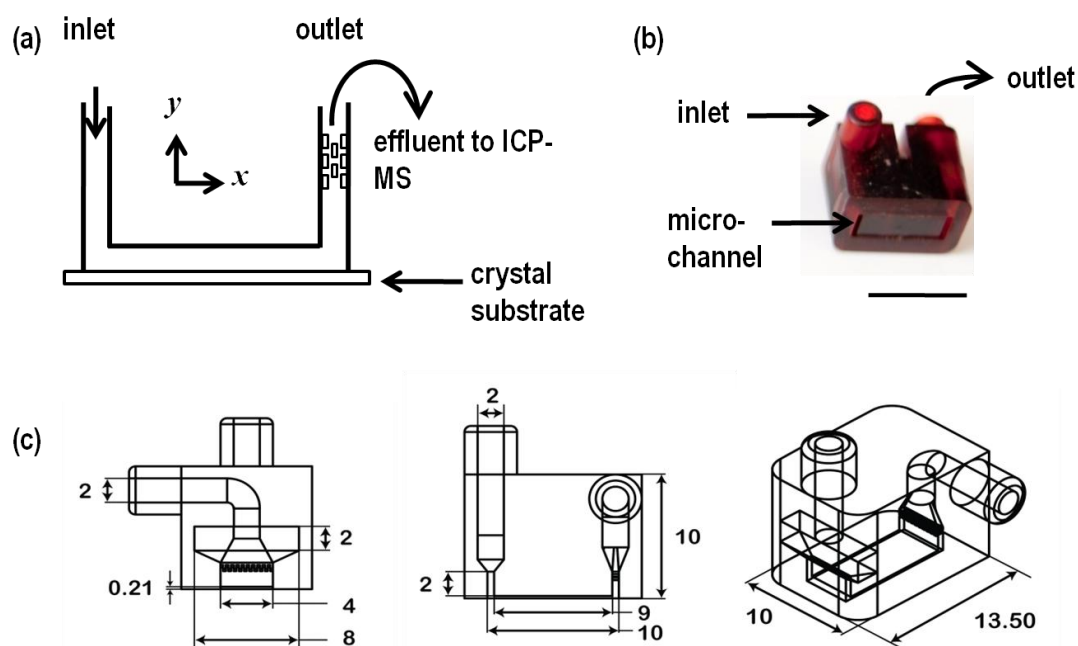


Figure 2.3: Illustration of (a) the two dimensional cross-section of the flow cell (not to scale), highlighting the crystal substrate which forms the base of the channel and the mixer in the outlet, (b) a photograph of a finished CFC unit where the scale bar is 10 mm and (c) schematic of the CFC design from several viewpoints, where the cell dimensions are in mm.

The channel was assembled by simply applying light pressure on the channel unit, placed on the crystal substrate of interest. Inlet and outlet pipes (PVC, 0.318 cm inner diameter and 0.635 cm outer diameter, St Gobain Plastics) were connected directly to the cell by push-fitting to a syringe pump using Omni-fit adapters (Bio-Chem Fluidics). The complete experimental set up is shown in Figure 2.4.

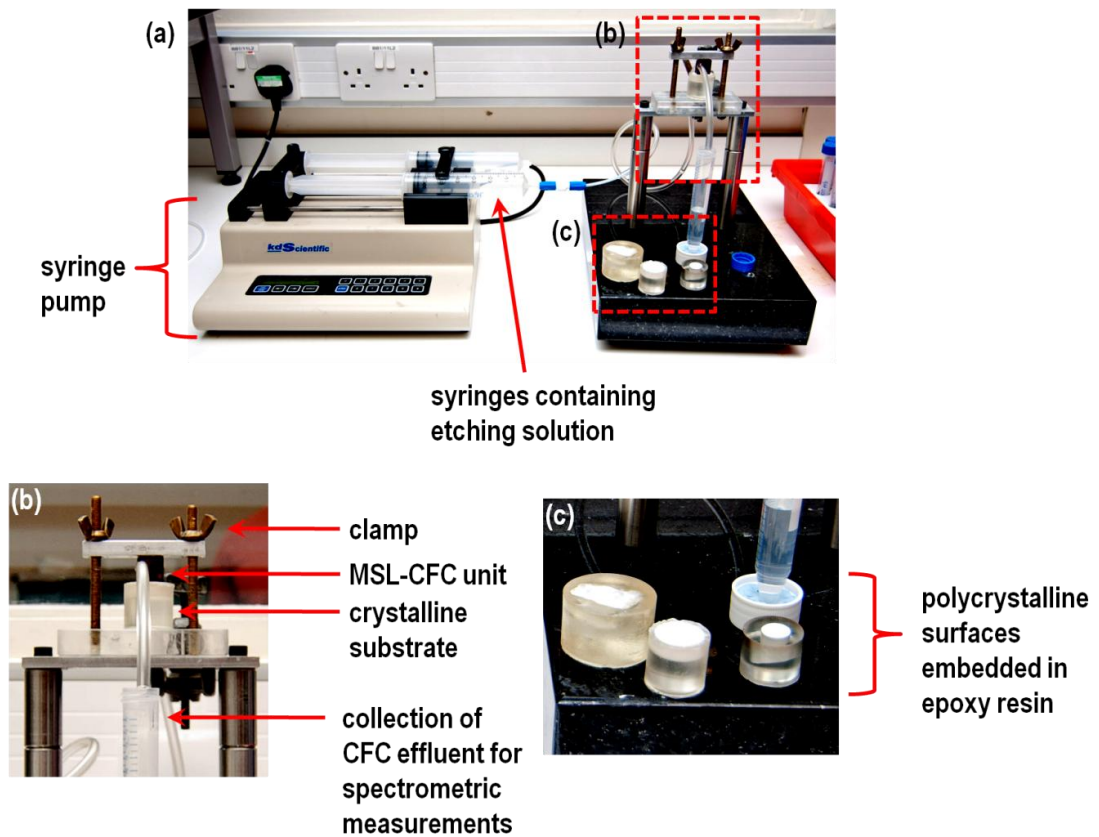


Figure 2. 4: Experimental set up used for CFC dissolution experiments.

### 2.3.6 CFC Dissolution Procedure

A syringe pump (KD Scientific) was equipped with a 50 ml syringe (BD Plastipak, luer-Lok) with a 22 mm inner diameter. This was used to drive solution into the assembled cell. Dissolution experiments took place at flow rates ( $V_f$ ) in the range  $0.008 - 0.167 \text{ cm}^3 \text{ s}^{-1}$ , corresponding to  $Re \sim 8 - 16$  which is significantly below the critical value of 2000<sup>20</sup> thus denoting well-defined

laminar flow profile within the CFC channel. This corresponds to a maximum contact time of  $\sim 1$  s for solution within the part of the channel above the crystal at the lowest flow rate. Furthermore, the mass transfer coefficients,  $k_t$ , for the lowest and highest flow rates were deduced to be  $0.004 \text{ cm s}^{-1}$  and  $0.01 \text{ cm s}^{-1}$ , respectively. Thus, it was possible to change flow rate and make measurements very easily over a wide range. All CFC measurements were made at standard conditions. Aliquots ( $5 \text{ cm}^3$ ) of the effluent were collected at intervals for the range of flow rates used. Trace element analysis of dissolved  $\text{Ca}^{2+}$  was carried out on the aliquots via ICP-MS (7500 Agilent) and ICP-OES (Perkin-Elmer Optima 5300 DV) for natural (Chapter 5) and polycrystalline (Chapter 6) samples, respectively. The former has a lower limit of detection of 1ppm compared to 100 ppm for the latter. This allowed for the extraction of flow-rate dependent output concentrations, from which dissolution fluxes were determined. For spectrometric analysis, standards for Ca and P were prepared from  $1 \text{ g dm}^{-3}$  stock solutions.

## **2.4. Micro-Crystal Growth Studies**

### **2.4.1 Crystal Seeding Process**

Glass cover-slips (47 mm diameter, 0.17 mm thick) were silanised using dimethyl dichlorosilane (DMDCS, ACROS Organics) for 20 min, followed by washing thoroughly in isopropanol (IPA, Fisher) for 10 min after which they were dried under a stream of compressed nitrogen (BOC). In this way, the cover-slips were rendered hydrophobic (Figure 2.6). Typically, silanising procedures aim to fashion a homogeneously hydrophobic surfaces. However, in our case, the process was designed to render a majority of the surface  $-\text{OH}$

groups inactive by bonding to DMDCS, while leaving a few unmodified -OH groups available as sites for crystal nucleation and growth.

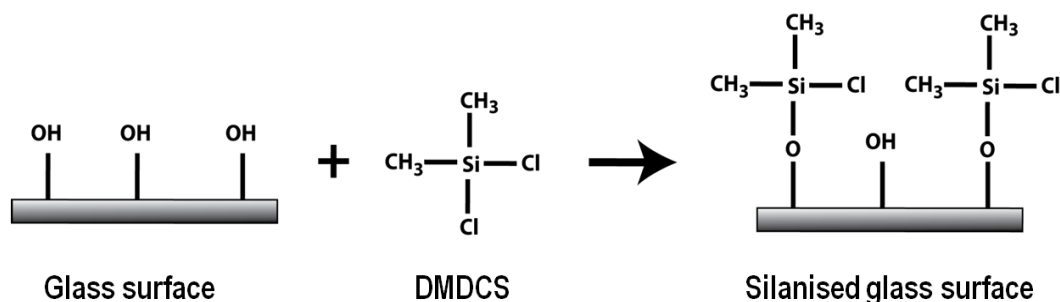


Figure 2.5: Silanisation of a glass substrate

A small aliquot (10 ml) of stock solution was syringed into a petri-dish and the silanised glass cover-slip was placed flush against this solution and visualised via DIC optical microscopy (Leica DM 4000, Leica Microsystems). After ~15 min the resulting surfaces grown gypsum seed crystals were quickly rinsed (1-3 s) in ultra pure H<sub>2</sub>O and immediately dried with a strong burst of nitrogen gas. This ensured that no residue from the growth solution was left on the surface and that only the seed crystals which strongly adhered to the surface remained for use in growth experiments. A typical surface with gypsum seed crystals is shown in figure 2.6. The glass substrate was then attached to a petri-dish rim (Willco) to fashion an *in-situ* AFM cell, with the seed crystals on the basal surface. These cells were then kept in a dry environment for ~3 weeks prior to use in crystal growth experiments.

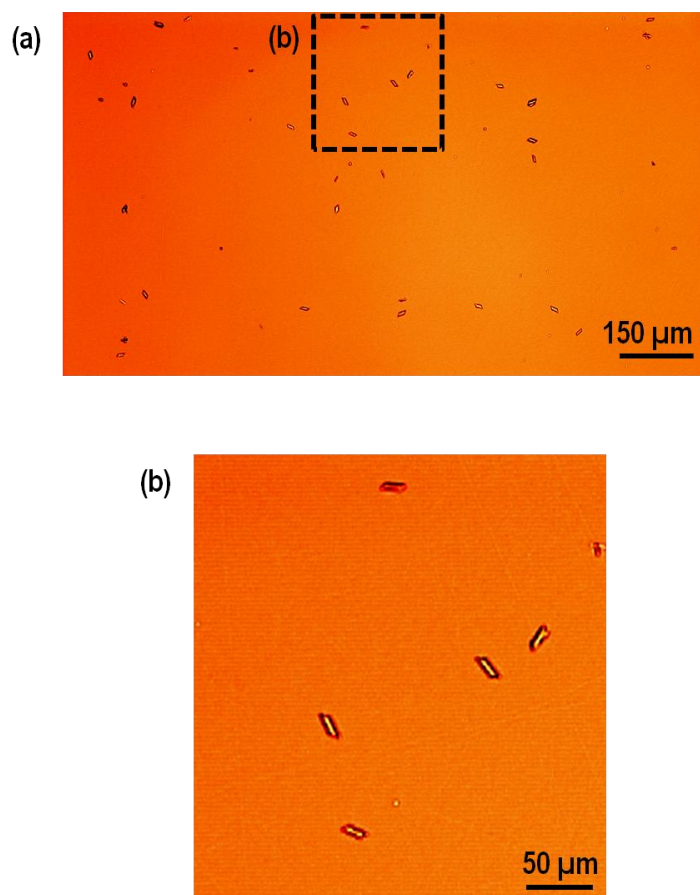


Figure 2.6: DIC image of a silanised glass surface after a seeding process ( $\sim 30$  min) showing numerous crystals randomly distributed across the surface. The magnification of a small section (b) reveals well defined gypsum crystals exhibiting a monoclinic structure. Note that the formed crystals are of similar size (within  $\sim 10\%$ ), indicating an instantaneous nucleation process.

#### 2.4.2 Crystal Growth Experiments

Following the seeding process, the grown gypsum crystals were characterised via Micro-Raman spectrometry to verify their identity. All growth experiments were conducted at room temperature ( $23 \pm 1$  °C) under conditions open to the atmosphere. MINEQL+ simulations conducted for a closed system revealed a negligible change in speciation between a closed and an open system. Individual crystals for imaging purposes were selected based on their size, (maximum initial dimension  $10 \pm 3$  μm), morphology (monoclinic structure

devoid of macroscopic steps and defects) and isolation, (distance between adjacent crystals  $\geq \times 10$  the characteristic length of a crystal under observation). The imposed restrictions satisfied the conditions necessary for a microscopically active surface to be diffusionally isolated while maintaining high mass transfer rates which work to minimise the influence of the AFM tip on diffusion to the crystal surface.

A small aliquot (4 ml) of growth solution (Table 7.1) as prepared, (*vide supra*) was transferred to the *in-situ* AFM cell, using a 10 ml syringe (Becton Dickinson S.A. Plastipak, Spain) after filtering (0.20  $\mu\text{m}$  pore, Sartorius Ministart High-Flow, UK) to prevent the introduction of dust and other impurities from the growth solution into the AFM cell. After a period of equilibration, ( $\sim 10$  min), the growth of gypsum crystals was visualised via *in-situ* AFM, under Peak Force Quantitative Nanomechanical Tapping mode (Peak Force QNM<sup>TM</sup>, Bruker AXS, Bioscope Catalyst, UK). This imaging mode performs a fast force curve at every point of contact and by using auto-optimisation protocol of scan parameters, (Scan Asyst<sup>TM</sup>, Bruker AXS) topographical images at very high resolution can be obtained. All measurements were carried out using silicon nitride AFM tips (SNL-type, Bruker AFM Probes) with a nominal spring constant of  $k = 0.35 \text{ Nm}^{-1}$ , and tip sharpness of 2 – 3 nm.

The AFM system was equipped with an inverted Differential Interference Contrast (DIC) optical microscope (Leica Microsystems DMI 4000) which was used to locate crystals for imaging and allow positioning of the AFM tip on the crystal surface. Typically, the growth of a crystal was tracked for a period between 60 - 90 min and for each value of  $r$ , at least three crystals were imaged

for each solution (subject to conditions described above) in at least two replicate experiments.

In addition, nanoscopic step motion measurements were conducted, on steps nucleating from 2D islands on the (010) basal plane. Using DIC microscopy, the AFM tip was positioned on the crystal surface such that the scan direction was perpendicular to step movement, and one could track both nanoscale step propagation (AFM) and overall lateral growth of the crystal (DIC). All topographical images produced were analysed via WYKO Vision Software (Veeco Instruments, Inc, Vision 4.10).

## **2.5. Finite Element Method**

In addition to experimental methods, computer simulations were designed to support the insights gained from empirical studies. To this end, experiments were extensively modelled using the finite element method (FEM) (Comsol Multiphysics).

FEM is a numerical technique used to approximate numerical solutions to partial differential equations (PDE) and ordinary differential equations (ODEs). Other similarly powerful methods exist, such as the finite difference, boundary element and finite volume element techniques,<sup>21</sup> that can accommodate very complex geometries. FEM allows various physical phenomena such as chemical kinetics and complex mass transport processes to be addressed.

Typically, the approach used (and applied herein) is to simplify the problem to a steady-state situation where the differential equation is eliminated. The primary challenge is to define the physical geometry of the

problem via a system of nodes (mesh elements) which together form the simulation domain (called a mesh), with specific properties (boundary conditions) which describe how the structure (or specific parts) behaves under certain situations. Typically, the more elements used to define the domain, the more accurate the solution is and in areas of interest (*vide infra*) a higher density of nodes is applied compared to other regions, in order to accommodate the anticipated 'stress'.<sup>22</sup> For 2D problems triangular nodes are used while for more complex 3D situations, tetrahedral nodes are employed.

FEM numerically solves the PDEs at each node in the domain. The solution at each node can be combined to generate a representation (2D or 3D for more intricate geometries) of the solution. One significant advantage of using FEM is the capacity to compute solutions of complex geometries. A simple example is shown in Figure 2.7 below.

A dissolving isolated etch pit with a triangular profile is simulated (Figure 2.7(a)). The domain walls 1-3 represent a bulk environment (in this case pure water) where the concentration,  $C = 0$ , while boundaries 4 and 6 represent an inert surface in the vicinity of the evolving etch pit. Boundary 5 represents the etch pit, from which a fixed flux emanates, and is described by  $K(C-1)$ . A mesh is generated (Figure 2.7 (b)) as described above, with a higher density in the active region (boundary 5). For the conditions applied, FEM is used to solve the PDE problem that describes the reaction-diffusion and a concentration profile (Figure 2.7 (c)) is generated. It is clear that in the region of the etch pit, the concentration is predictably higher due to generation of dissolution products into the interfacial region. Furthermore, the hemispherical diffusion profile

shown to extend some distance into the bulk solution and is characterised by a decrease in concentration the further away from the etch pit you go.

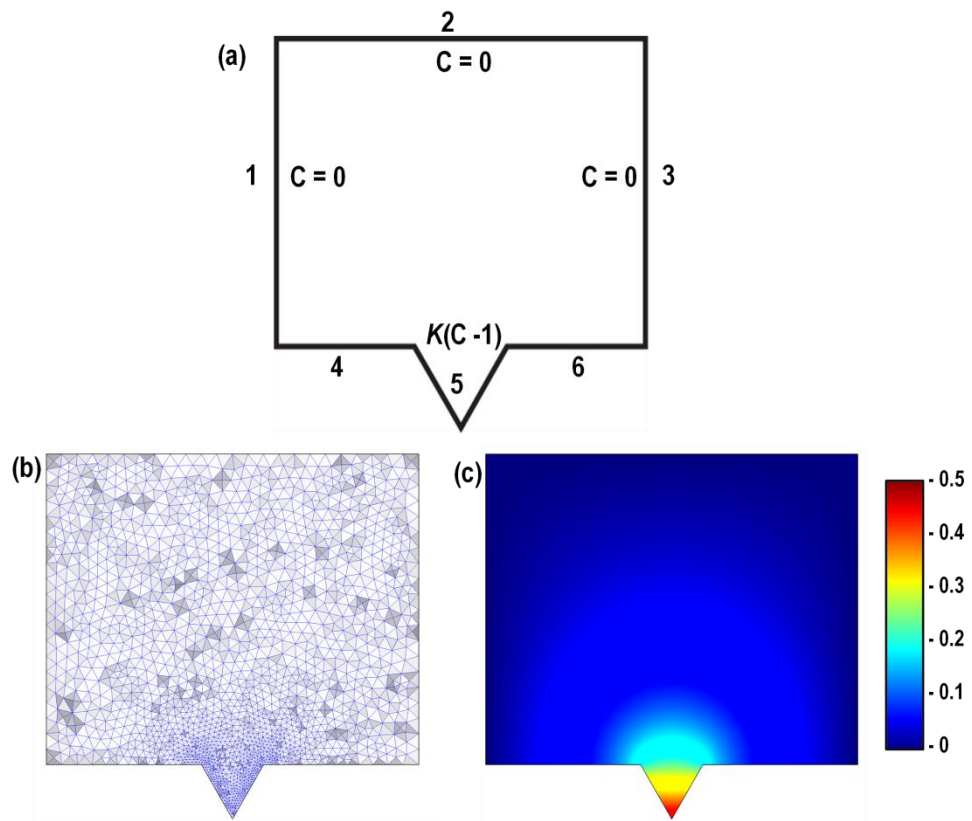


Figure 2.7: A single etch pit undergoing a dissolution process is modelled by (a) describing the physical domain in the vicinity of the pit, where the numbers represent boundaries each governed by specific conditions, (b) a mesh made up of triangular nodes is generated over the entire domain with higher densities close to the active etch pit and (c) the FEM solution of the reaction-diffusion problem illustrated as a concentration profile.

## References

- (1) Schecher, W. D. *A chemical Equilibrium Modelling System*; Hallowell: Maine, 2003.
- (2) Christoffersen, J.; Christoffersen, M. R. *J. Cryst. Growth* **1976**, *35*, 79.
- (3) Davies, C. W. *Ion Association*; Butterworths: London, 1962.
- (4) Lasaga, A. C.; Lutge, A. *Science* **2001**, *291*, 2400.
- (5) Arese, R.; Martin, D.; Rigaudon, M. **2003**, *Process for reducing creep in a gypsum plaster-based element, gypsum plaster-based composition and method for making a gypsum plaster-based element with reduced creep. US Patent 2006/0048680*
- (6) Muller, R. E.; Henkels, P. L.; O' Kelly, B. M. **1965**, *Gypsum board. US Patent 3,190,787.*
- (7) Yu, Q.; Sucech, S.; Groza, B.; Mlinac, R.; Jones, F.; Boehnert, F. **2003**, *Process for reducing creep in a gypsum plaster-based element, gypsum plaster-based composition and method for making a gypsum plaster-based element with reduced creep. US Patent 6,632,550.*
- (8) Wilson, B. K.; Jones, K. W. **1977**, *Production of shaped gypsum articles. GB 1,481,788.*
- (9) White, A. F.; Brantley, S. L. *Rev. Mineral.* **1995**, *31*, 1.
- (10) Brantley, S. L.; Mellot, N. R. *Am. Mineral.* **2000**, *85*, 1767.
- (11) Lutge, A. *Am. Mineral.* **2005**, *90*, 1776.
- (12) Bruckenstein, S.; Sharkey, J. W.; Yip, J. Y. *Anal. Chem.* **1985**, *57*, 368.
- (13) Unwin, P. R.; Compton, R. G. *J. Electroanal. Chem. Interfacial Electrochem.* **1988**, *245*, 287.
- (14) Compton, R. G.; Unwin, P. R. *Comprehensive chemical Kinetics*; Elsevier: New York, 1989; Vol. 29.
- (15) Colombani, J. *Geochim. Cosmochim. Acta* **2008**, *72*, 5634.
- (16) Jeschke, A. A.; Vosbeck, K.; Dreybrodt, W. *Geochim. Cosmochim. Acta* **2001**, *65*, 27.
- (17) Snowden, M. E.; King, P. H.; Covington, J. A.; Macpherson, J. V.; Unwin, P. R. *Anal. Chem.* **2010**, *82*, 3124.
- (18) Leigh, S. J.; Pursell, C. P.; Bowen, J.; Hutchins, D. A.; Covington, J. A.; Billson, D. R. *Sensors and Actuators A: Physical* **2011**, *168*, 66.
- (19) Cooper, J. A.; Compton, R. G. *Electroanalysis* **1998**, *10*, 141.
- (20) Nakayama, Y. *Introduction to Fluid Mechanics*; Arnold: London, U.K, 1999.
- (21) Morton, K. W.; Mayers, D. F. *Numerical solution to Partial Differential Equations, An Introduction*; CUP: Cambridge, 2005.
- (22) Reddy, J. N. *An Introduction to the Finite Element Method*; McGraw Hill, 1984.

# Chapter 3

## Image Processing with Matlab

### **Abstract**

This chapter describes the development of various user-defined computer routines written in the commercial Matlab technical computing interface. Individually, they were designed to perform specific tasks on images and, collectively, these routines form a highly specialised image processing (IP) package designed to extract quantitative information from 3D images obtained from various studies, including the analysis of crystal dissolution data obtained in Chapter 4. Common challenges associated with commercial IP software are discussed briefly with a view to highlight the benefits of a user-designed approach.

### **3.1. Introduction**

Image processing (IP), involves manipulating an image in order to facilitate the extraction of important information. In science and technology, IP has wide ranging applications in areas such as law enforcement (fingerprint analysis), medicine (MRI, CAT scans) and surface science (microscopy).<sup>1</sup>

In surface science, the development of scanning probe microscopy and other surface profiling techniques such as interferometry has induced a great interest in developing image processing and analysis software which complement these techniques, in order to extract both qualitative and quantitative information from the surfaces under analysis. <sup>2,3</sup> IP in the context of these techniques involves manipulating the topographical (3D) images produced in order to facilitate the extraction of important surface information.

Commercial IP software is traditionally supplied by the manufacturers of microscopy systems where they offer a number of options to the user when processing images. However, they are typically designed to cater for broad IP issues and often, lack the flexibility required for more specialised image analysis. In addition, most software only allow processing of a narrow range of image formats and for researchers who use a wide variety of imaging techniques each with a unique set of image analysis issues to resolve, this presents an inconvenient limitation. However, these software packages normally allow image data to be stored either as simple matrices (text files) or in widely used formats such as TIFF, JPEG and PNG among others, therefore facilitating more specialised image analysis. The subject of image storage format is of particular importance in image analysis due to the role it plays in the preservation of spatial calibration information which facilitates the conversion

of image data (pixels) to real dimensions ( $\mu\text{m}$ ).<sup>2</sup> For images produced in one IP package and subsequently analysed in another, the parameters used in image acquisition significantly influence the validity of results.

Some free-standing commercial IP software such as scanning probe image processor (SPIP, Image metrology)<sup>4</sup> have attempted to bridge the gap between increasingly diverse image analysis requirements and the limited options currently available. In addition, various free software packages such as ImageJ<sup>5</sup> and Image SXM<sup>6</sup> have been developed with a view to encourage user contribution to software development, thus making image analysis options more versatile.

A further pertinent issue in IP is batch processing, which is the process by which a sequence of tasks or operations are performed on large sets of images, without manual/user intervention. This is particularly crucial for some studies, such as, real-time visualisation of dynamic processes on a surface (such as growth and dissolution). Typically, large sets of images are produced from time-lapse sequences, and therefore, an efficient and convenient method of processing them in order to extract time-dependent information, is required.<sup>7</sup> Unfortunately most IP software either lack this option or, when available, offer options that are limited to a very narrow range of operations.

In this chapter, an IP package written and executed in Matlab (Mathworks, Inc., Cambridge, U. K.) computing language was designed for the purposes of analysing images acquired in crystal dissolution studies. The sequence of image analysis operations applied is summarised in Figure 3-1. The use of Matlab allows the integration of a vast array of commands called functions, through which various tasks can be performed. These include data acquisition and

analysis, modeling and simulations as well as the development of graphical user interfaces (GUIs) which provide a user-friendly environment for image analysis. This software is typically equipped with an IP Toolbox which contains a large set of in-built functions designed to perform specific image processing tasks. These tasks include image restoration and enhancement (contrast, de-blurring, and noise removal) as well as image segmentation (isolation of shapes), in addition, to the in-built functions available in the Matlab environment, which allow the user to write new commands using the computing language. In addition, the Matlab environment is uniquely designed to cater for batch processing operations, thereby providing an expedient tool for addressing unique image analysis problems.

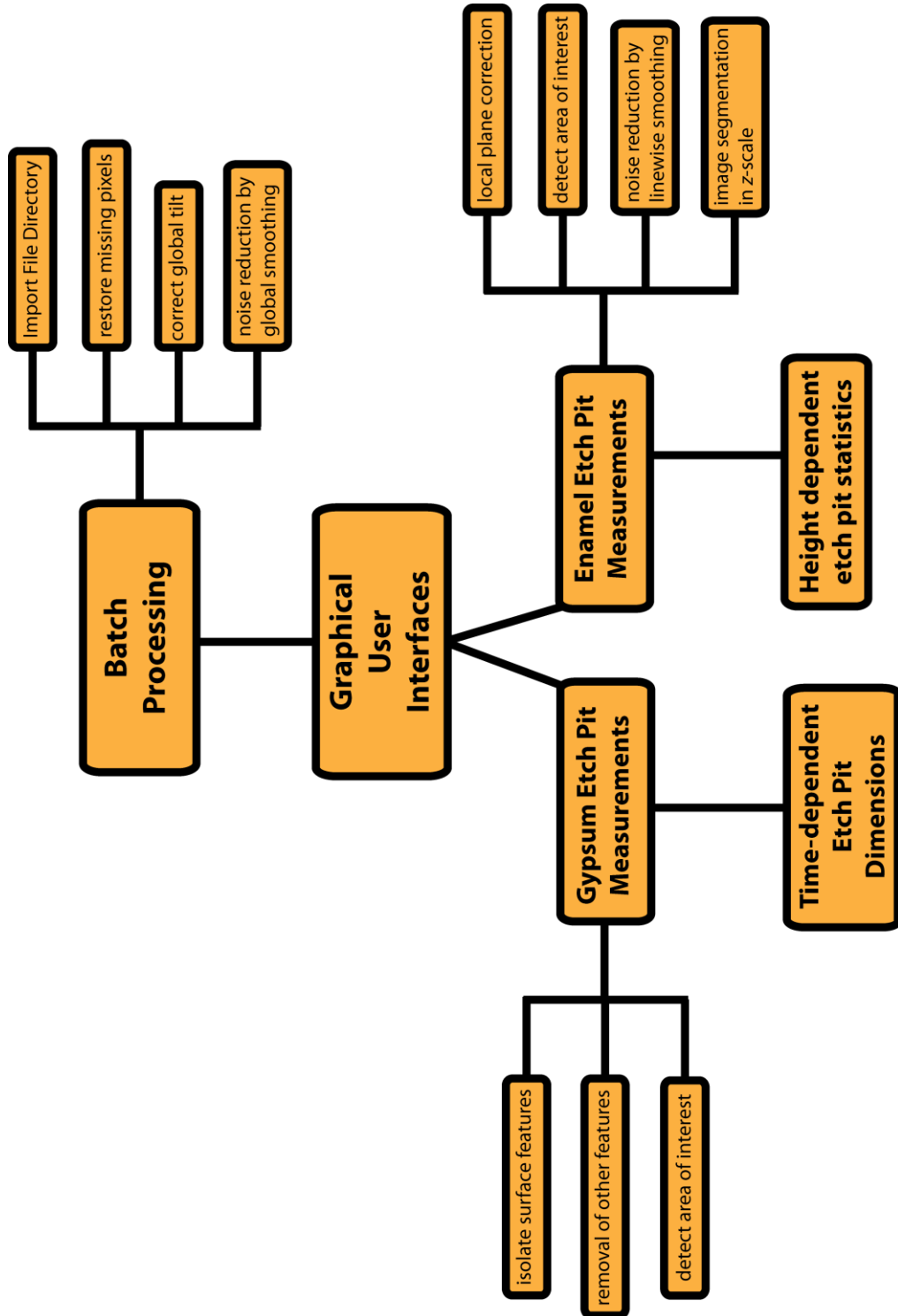


Figure 3.1: Sequence of operations performed on 3D images.

## **3.2. Method**

Images processed via the Matlab IP package were acquired from crystal dissolution studies from experiments carried out on etched surfaces, such as those described in chapter 3 below and other works.<sup>8,9</sup>

### **3.2.1 Visualised Surfaces**

Local scale dissolution of a crystalline surface was carried out to produce characteristic etch pits. The application of different experimental conditions (such as a large range of saturation states and/or the use of additives) yielded etch features with characteristic morphologies and sizes. Figure 3.2 shows WLI height images of (a) a cylindrical etch pit on the surface of enamel and (b) characteristic etch pits produced after etching the (010) surface of single crystal gypsum.

In order to monitor the dissolution reaction, the resulting surfaces (after dissolution experiments) were visualised, via WLI and AFM. Topographical (3D) images produced via these techniques were saved as simple matrices, with image acquisition parameters and spatial calibration information stored in the header of each image file. These files were then quantitatively analysed with the in-house Matlab IP package, for the determination of dissolution kinetics.

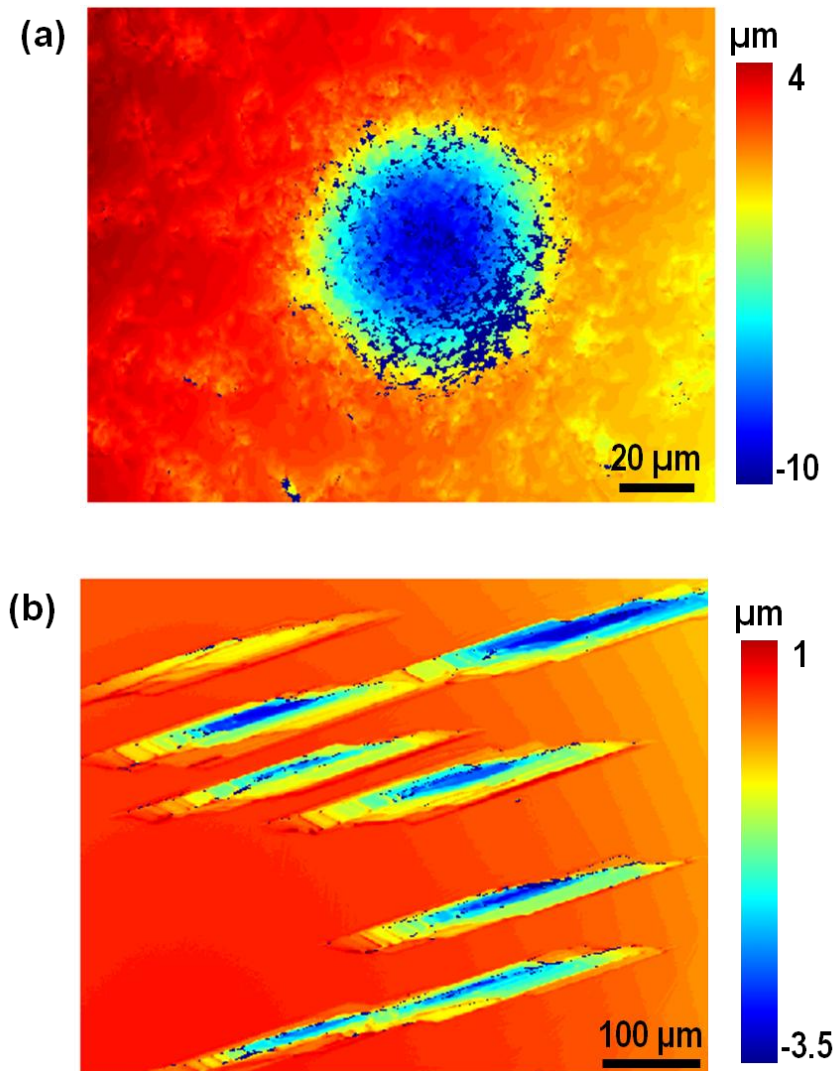


Figure 3.2: Typical WLI images reproduced using the in-house designed image processing package. (a) Etch pit on enamel surface and (b) etch pits on gypsum (010) surface. Note the tilt on the surface as denoted by the drastic colour change from the right-hand-side to the left-hand-side of the images as well as the missing pixels highlighted by the dark irregular areas close to the etch pit edges.

### 3.2.2 Image Restoration via Batch Processing

In each of the studies described (*vide supra*), a very large number of images was produced, typically  $\geq 100$  images per study and at times much higher depending on the experimental variables applied. With such large data sets, the task of manually processing each individual image would take an

inordinate amount of time and thus a more efficient batch processing approach was desirable.

Batch processing allows for a sequence of operations to be performed on an image file (or a set of images) without the need for manual intervention. A batch processing function was performed on a file directory containing all raw images pertaining to a particular study. For each image file, the 3D image was imported into Matlab where the unique image acquisition parameters were extracted and applied to the loaded image matrix. In this way, further image analysis could be carried out on real image data. Batch processing was employed to expedite numerous other operations (*vide infra*).

Once imported the images underwent a series of restoration routines designed to correct various imaging artifacts such as image tilt and missing pixels.

### **Missing Pixels**

In some cases, imported image matrices contained pixels with missing values. This is a typical problem observed with some topographic images produced via interferometry as a consequence of low reflectivity at points on the surface exhibiting high aspect ratio features. For instance, the etch pits produced in the studies analysed here exhibited steep tapering profiles (etch pit walls) with a flat base in the direction normal to the surface. To correct this, user-written functions were designed to scan the entire image matrix for the coordinates of pixels with missing values. Once found, a plane was fitted to the pixels surrounding these coordinates and the missing value was replaced with the corresponding value from the fitted plane, in effect, assigning a local average value to the empty pixel position. This is shown clearly in Figure 3.4(a) where

the height image of an etched gypsum (010) surface is shown with a cross-section through a series of etch pits on the surface. The plot shown in Figure 3.3 (b) shows an overlap between the raw cross-section highlighting missing values (red line) and the restored cross-section (green line). Figure 3.4 shows a 3D surface plot of an etch pit on enamel surface (a) highlighting areas with missing pixel values and (b) the restored image. In this case it is clear that the extraction of quantitative information from the etch pit data prior to image restoration would significantly affect the results obtained.

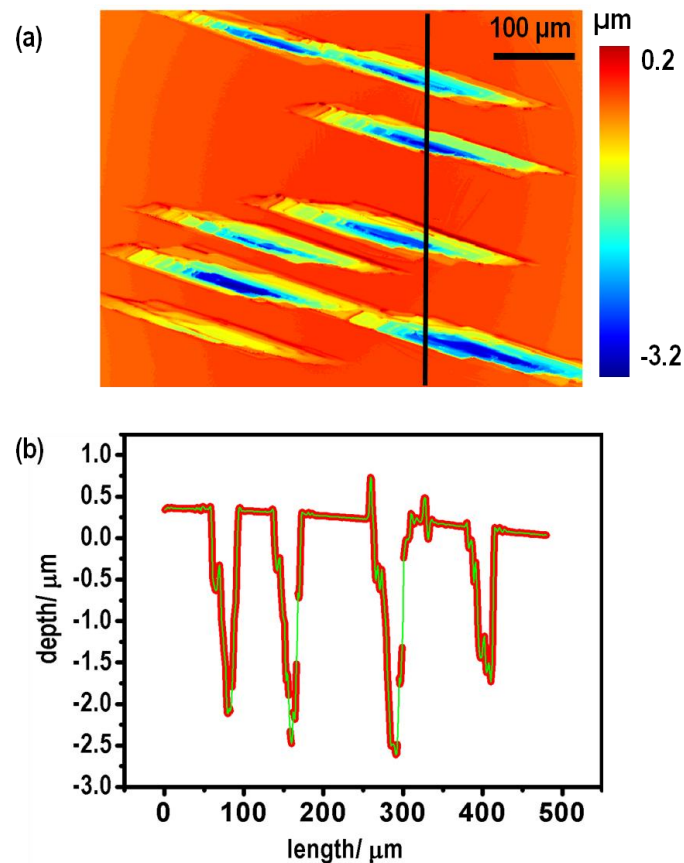


Figure 3.3: (a) WLI micrograph of etch pits with (b) original cross-section (red) with missing pit data overlaid with a cross-section from a restored image where missing pixel values were replaced with a local average (green).

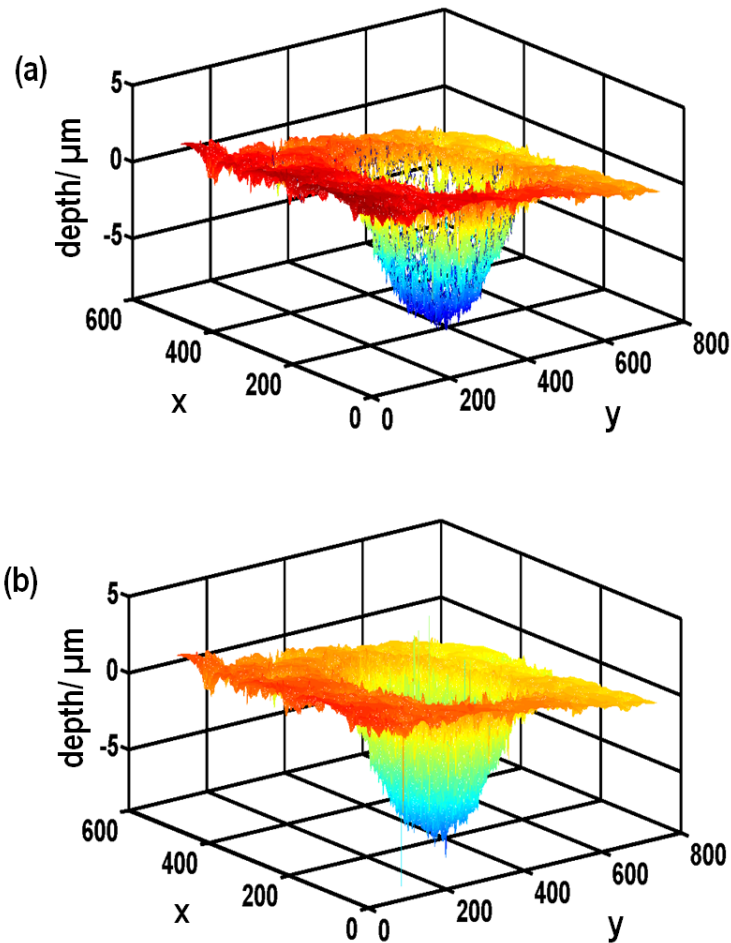


Figure 3.4: (a) 3D image of etch pit on enamel surface showing missing pixels and (b) etch pit after image restoration

### Tilt and Curvature

Typical of microscopy images, background tilt and curvature were common occurrences. These and other sources of imaging artifacts have been documented extensively particularly in the case of AFM.<sup>10-13</sup> For the case of the enamel etch pit images, characterised by a large central etch pit, the tilted image was restored by first isolating a  $10 \times 10$  pixel box at the corner of each image matrix. This was carried out to ensure that the area selected was at the furthest possible distance from the etch pit boundaries. Collectively, these corner pixels represented a reasonable approximation of the tilted plane. In order to restore

the tilted image to a geometrically flat plane, a least-squares plane was subtracted from the tilted image fashioned from these corner pixels. In this way, the extraction of  $z$ -scale data (heights) could be carried out from a baseline where the highest point on the image was at  $z = 0$ . As a simple operation, this task was employed in a batch process. A typical example of plane correction is shown in Figure 3.5 where a cross-section through a tilted etch pit (black line) is overlaid with the plane-corrected cross-section (red line).

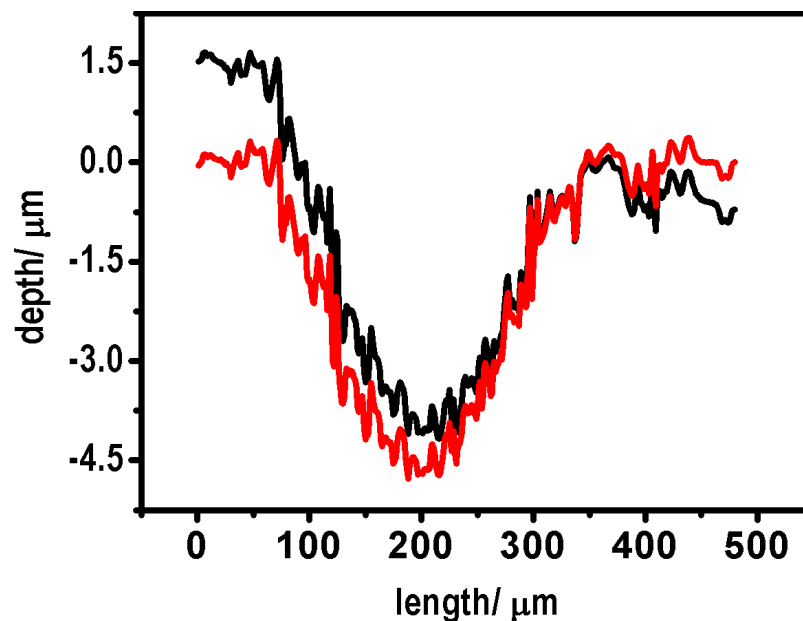


Figure 3.5: Overlay of original (black) and tilt corrected (red) cross-section.

For images with numerous regions of interest, such as the etch pits produced after etching a gypsum crystal surface (Figure 3.2(b)) the method applied above would be inappropriate since some etch features traverse the border of the image and a global plane correction would therefore be erroneous. In this case, a local level plane fit was carried out for each etch pit on the image. First, etch pit outlines were determined via a series of operations. Using an in-built Matlab function (*edge*), the boundaries of an etch pit were

deduced. This customisable function works by finding areas on an image where the gradient between adjacent pixels changes dramatically (such as at the edge of an etch pit) and outputs an image showing only the areas where these gradient changes exist and in our case, it returned the etch pit outlines. In this way, pixels inside the etch pit could be isolated. In addition, this outline could be expanded (whenever necessary) using a dilation operation in order to encompass some of the plateau surrounding the etch pit. The pixels corresponding to the etch pit were subtracted and a plane fitted to the remaining pixels (only the plateau surrounding the etch pit). This approach ensured that etch pit properties were not compromised or modified by tilt correction in a significant way.

### **3.3. Graphical User Interfaces (GUIs)**

After general image restoration operations, the task of extracting quantitative information from etched surfaces was performed by developing graphical user interfaces (GUIs) which provide the user with real-time views of any changes applied to the image by executing user-written functions. Two GUIs were developed and are described below.

#### **3.3.1 Images of Etched Gypsum Surfaces**

The first GUI was designed to determine the time-dependent dimensions of etch pits on gypsum (010) surfaces. Figure 3.6 shows a 'screen dump' of the GUI, where in (a), images are imported after the image restoration batch processes described (*vide supra*). By applying contour thresholds similar to the edge finder operations (*vide supra*), features at a specific height were isolated

(Figure 3.6 (b)) after which small surface fragments were subtracted (Figure 3.6 (c)). The etch pit outlines were then slightly dilated to encompass the entire etch pit (Figure 3.6 (d)) and the resulting image superimposed on the original imported image to compare etch pit edge approximation (Figure 3.6 (a)). In addition, complete user control was afforded by the use of built-in sliders (e) for all tasks. Specific details of each operation are described below.

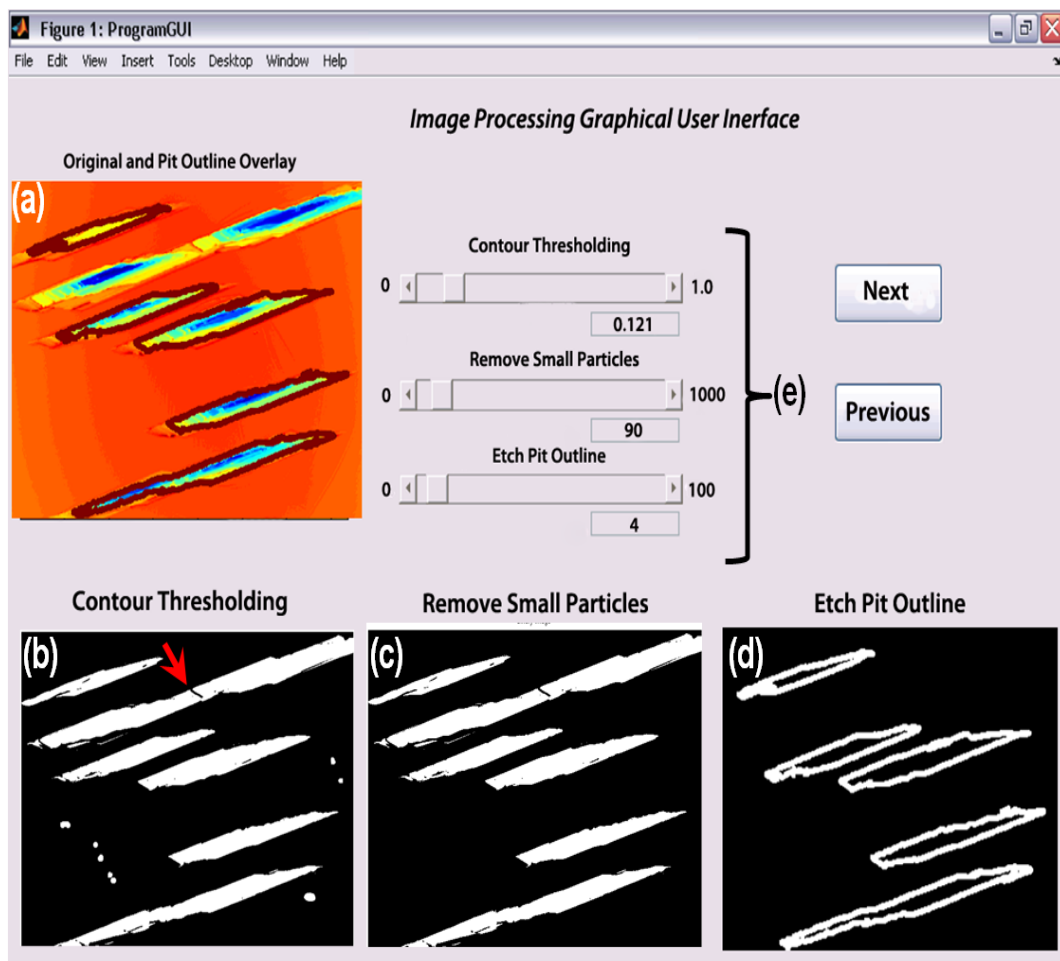


Figure 3.6: Graphical User Interface (GUI) designed to isolate the etch pits from the image background and determine etch pit measurements.

### Etch Pit Isolation

First, etch pit isolation was carried out by applying a depth threshold to the imported image by scanning through the z-scale (pixel values) and finding

the edges of objects at each contour level. The objective was to find the edge of the pit close to the surface ( $\sim z = 0$ ) and isolate it from the image background. In the surface image analysed in Figure 3.6, it was observed that this GUI feature was robust enough to isolate etch pits which were very close together as shown by the arrow in part (b). The output from this operation was a simple binary image file (all pixels are either 1 or 0) which easily highlighted areas on the surface found at the same height. As shown in part Figure 3.6(b) in addition to the large etch pits, small particles were found on the surface, although they were not clearly discernible from the imported colour image Figure 3.6(a).

### **Removal of Small Surface Features**

Since this GUI was designed to analyse all isolated surface features and after the pit isolation operation (*vide supra*), the numerous small particles may complicate data analysis and thus had to be eliminated. This command was designed to remove these small particles from the main image by thresholding the output from part (b) on the basis of particle size. The function once again finds all surface features with the use of the user-controlled slider, and disregards features below a certain size (number of pixels). For instance, if a typical etch pit on the surface was made up of 100 connected pixels, particles below this value (100) may then be selected and removed by creating an additional binary image without the small particles (Figure 3.6 (c)).

### **Pit Outlines and Etch Pit Statistics**

At this point, only the areas of interest (etch pits) remained on the image. The last operation eliminated any surface feature which was connected to the image border to ensure that etch pit statistics were extracted from whole etch

pits only. Additionally, from the resulting binary image, the outlines of surface features were isolated and overlaid onto the original input image, so as to allow a direct comparison between the user-defined pit size approximations and the original image (Figure, 3.6(a)). Additionally, a dilation operation was performed by applying a user defined morphological structural element (using the slider at the bottom of the series, Figure 3.6 (e)) to each pixel in the binary pit outline image. This has the effect of gradually enlarging the boundaries of each pixel. All results were shown to the user to ensure the chosen pit area enclosed the entire pit. This chosen pit area erred to the side of caution, and frequently a fringe containing some of the plateau surrounding the pit was chosen, however, this did not cause any inaccuracies, (*vide infra*).

Once this has been achieved, the function selected the etch pit pixels from the rest of the image matrix and measured a set of features for each etch pit on the image. This operation was carried out by applying an in-built Matlab function (*regionprops*) which measures specific properties for object on an image (features with connected pixels). These measurements include, etch pit area, centre of mass (centroid), length, width, perimeter and orientation, among others. These values were used as the input to a function which calculated the etch pit volume and surface area using the area of each pit pixel and its corresponding value (which denotes the height at that point). The quantitative information gathered facilitated the deduction of time-dependent etch pit volumes and surface areas culminating in a deduction of dissolution rates.

### 3.3.2 Images of Etched Enamel Surfaces

The second GUI was designed to process electrochemically etched enamel surfaces with the aim of extracting height dependent pit measurements. In a similar way to the GUI for etched gypsum surfaces, the imported images had previously undergone image restoration operations.

For large features, in high resolution images, analysis naturally takes longer than it does for smaller low aspect ratio features due to the large amount of information that has to be processed. Therefore, the purpose of this GUI was, first, to simplify the process of image analysis by reducing the amount of data processed without compromising the quality of information deduced and second, perform various operations on these simplified data to determine etch pit dimensions at different heights. Figure 3.7 shows a screen dump of the GUI.

Cross-sections taken at user defined intervals (every 10 rows/columns) spanning the entire image were considered to be representative of the dominant surface profile of the etch pit and were plotted in Figure 3.7 (b). From these data, the image centroid (centre of mass) was determined by using the Matlab function, *regionprops*. Briefly, the function calculates the coordinates of centre of mass based on the shape and size of surface features. In the case of the images analysed here, the large (central) cylindrical shape indicates that the coordinates of the image centroid are likely to be at the centre of the pit close to the deepest point. Once the centroid coordinates had been deduced, a cross-section through these coordinates was plotted as shown on Figure 3.7(c). It was assumed that the line through the centroid (in most cases), was representative of the overall pit geometry and changes observed to this profile (due to varying experimental conditions) could therefore be used to monitor the dissolution reaction.

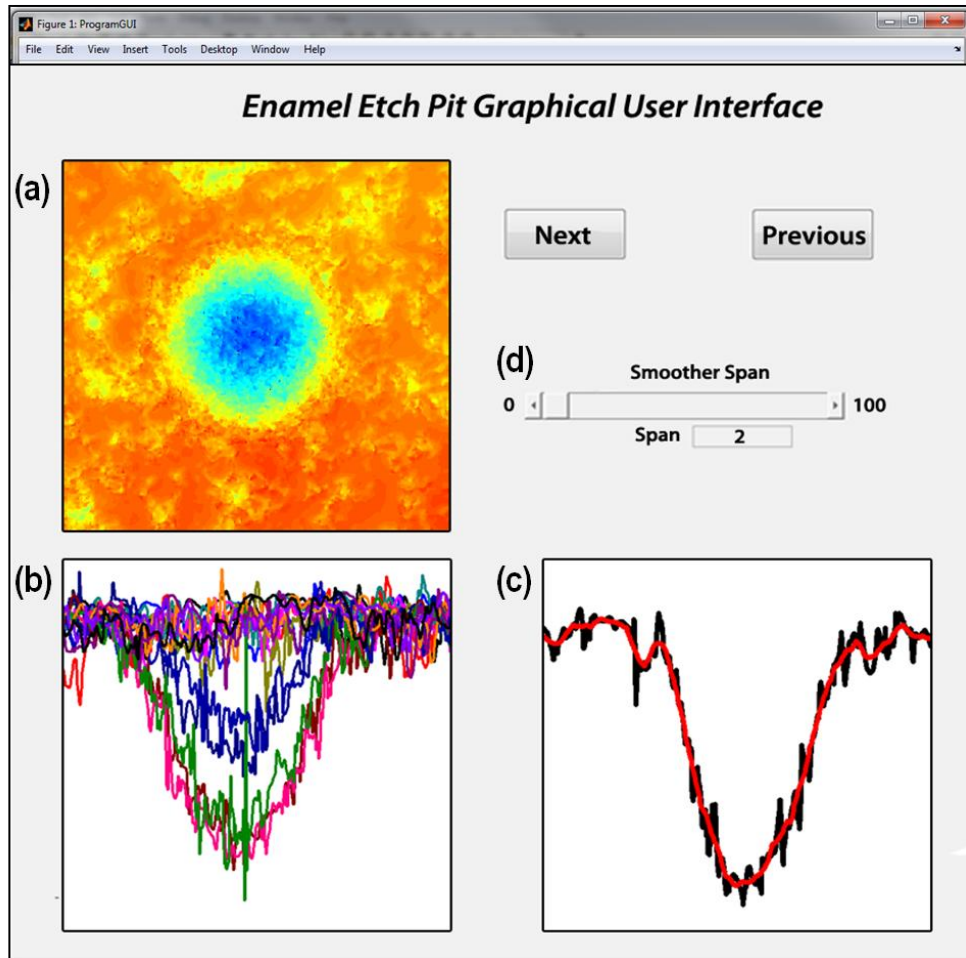


Figure 3.7: GUI image designed to extract height dependent etch pit dimensions where (a) is the input 3D image, (b) cross-sections across the surface and (c) cross-section through the image centroid.

In order to reveal the underlying pit profile, which was at times masked by random variations due to imaging artifacts and noise, a simple moving average smoothing function was applied to each column of the input image and the result was shown via changes in plots on Figure 3.7 (b) and (c). In this method, a series of averages are calculated for an array, computed by averaging a user-defined block of elements (span). For example, the cross-section through the centroid,  $M$  where:

$$M = m_1, m_2, m_3, \dots, m_n \tag{3.1}$$

and  $m_n$  is the value of the  $n^{\text{th}}$  element, averaged with a span of 3 elements yields;

$$MM = \left( \frac{m_1 + m_2 + m_3}{3}, \frac{m_2 + m_3 + m_4}{3}, \dots, \frac{m_{n-2} + m_{n-1} + m_n}{3} \right) \quad (3.2)$$

where  $MM$  is the smooth array and  $mm$  is an element in this array. Figure 3.7(d) shows a slider used to define the span and therefore control the extent of smoothing applied to the image cross-sections. The higher span, the larger the block of elements used to determine the moving average, resulting in a smoother line. Changes in the etch pit profile due to smoothing were monitored by real-time overlaying the original (blue) and smoothed (red) cross-sections as shown in Figure 3.7(c). When large span values are used, smoothing in this way can give rise to a significant modification of the image, consequently leading to flawed measurements and to avoid this, low span values (< 10) were used throughout for all images analysed.

The smooth etch pit image was stored for the deduction of etch pit measurements. Figure 3.8 shows 3D surface plots of (a) the original input etch pit surface image after batch processes but prior to GUI operations and (b) the etch pit surface profile after smoothing. Note that the general pit geometry does not change in a significant way so as to compromise the validity of etch pit dimensions deduced from the smoothed image.

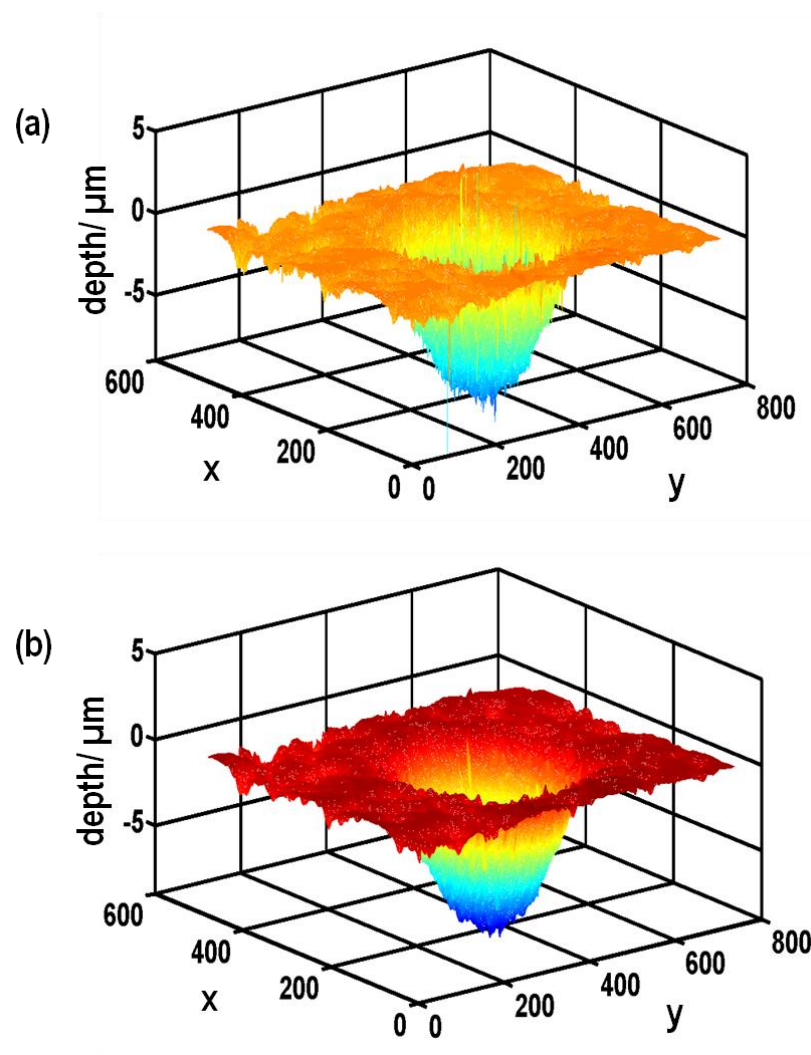


Figure 3.8: 3D surface plots of (a) a pre-processed etched enamel surface with a large central pit and (b) the result of user-defined smoothing to eliminate 'noise' while maintaining image integrity

Etch pit characterisation was carried out by taking x-y cross-sections of the etch pit over a range of depths ( $z$ ) and measuring features (diameters, areas, etc) at these user-defined contour levels. Further analysis of these contiguous contours aided the discrimination between lateral and longitudinal etch pit expansion rates. Figure 3.9 illustrates typical contours viewed from (a) direction normal to etch pit depth and (b) contour plots through the image

topography. Note that the contours observed were reasonably regular in shape, highlighting uniform lateral dissolution of the enamel surface at a particular height. When related to the prevailing experimental conditions, the information extracted from the image analysis approach used here, facilitated the deduction of dissolution kinetics.

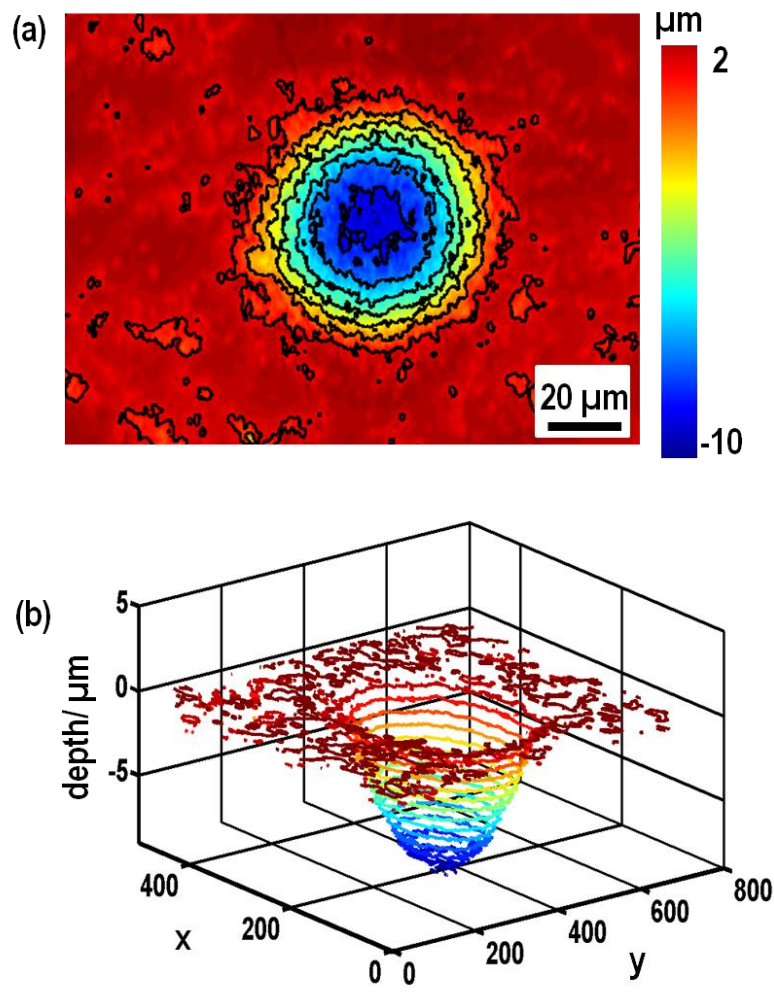


Figure 3.9: Etch pit measurements at different pit depths.

### 3.4. Discussion

The image processing package designed in-house was proven to offer significant advantages over commercial IP software (from manufacturers of microscopy equipment) as well as stand-alone packages. Figure 3.10 shows a typical plot of pit length as a function of etching time, calculated from dissolution etch features produced on a gypsum crystal surface, where the results from commercial SPIP software are compared to those from the user-written Matlab IP package.

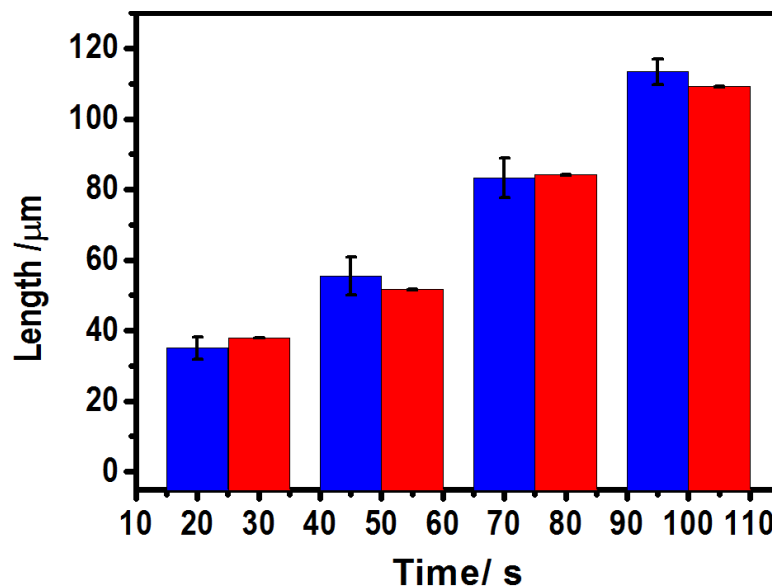


Figure 3.10: Typical plot of etch pit length as a function of time, comparison between the Matlab IP package designed in-house (blue bars) and commercial IP software SPIP (red bars).

It was found that for simple tasks, the in-house designed package worked as well as commercial software. However, for more challenging operations such as those involving the extraction of etch pit dimensions at varying depths, no direct comparisons could be made since commercial software typically do not

provide such specialised image analysis options and furthermore, some do not allow users to customise the IP source code to facilitate these operations.

A significant advantage of the Matlab IP package over others is the customisable batch processing capability which facilitates the extraction of statistically robust information and saves valuable time. Figure 3.10 illustrates the limitations of most commercial IP software compared to the options available when using a custom built IP package. It is evident that by using the latter method, the information extracted can be readily assessed for statistical robustness.

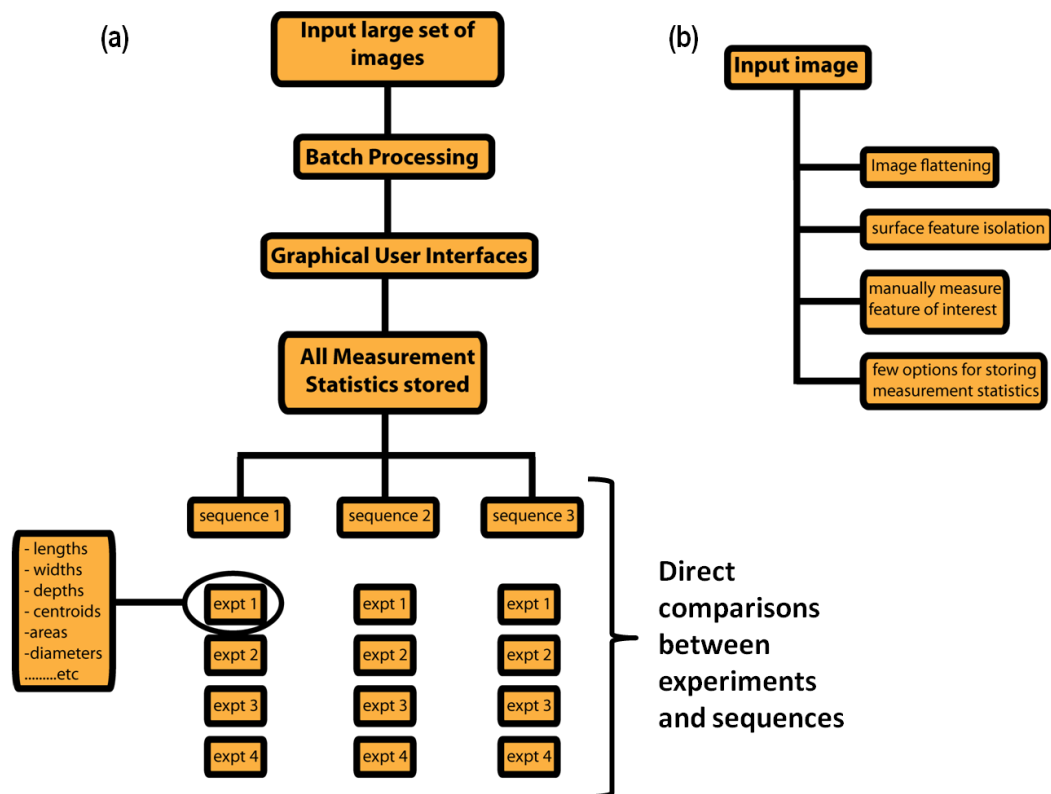


Figure 3.11: Comparisons between options and output from image analysis using (a) user-designed Matlab IP package and (b) typical commercial software

### **3.5. Conclusions**

An image processing package has been developed using the Matlab computing language and used to analyse topographical images produced from crystal dissolution studies. The Matlab environment has been shown to be incredibly versatile, offering numerous in-built functions which perform various operations on images. Furthermore, the interface allows users to readily customise in-built functions as well as design new specialised commands. The limitations of commercial software with regards to meeting the diverse needs of specialised image analysis options have also been highlighted.

The benefits of automating simple tasks has been described, in particular, regarding the improved efficiency with which large data sets can be processed with little or no manual intervention, thereby freeing the researcher to test a wide range of variables.

Two graphical user interfaces were developed for separate crystal dissolution studies. In the first case, etch pits produced on gypsum (010) crystal surface were characterised in order to extract time-dependent etch pit dimensions and aid in the determination of dissolution rates. In the second GUI, the images analysed showed large central etch pits formed on the surface of enamel. These images were analysed with the aim of separating lateral and longitudinal dissolution rate information.

In both cases, the user designed IP package proved to be a versatile and expedient approach to image processing. For simple tasks such as calculating some etch pit dimensions (lengths, widths etc), image analysis results from the Matlab IP package compared well with stand-alone commercial software.

However, the options available in the latter for more specialised operations were limited, thereby highlighting the benefits of a user-designed approach.

## References

- (1) González, R. C.; Woods, R. E. *Digital Image Processing*; 2nd ed.; Prentice-Hall: New Jersey, 2001.
- (2) Barrett, S. D. *Proceedings RMS* **2008**, *37*, 167.
- (3) Barrett, S. D.; de Carvalho, C. R. *Chromosome Res.* **2003**, *11*, 83.
- (4) [www.imagemet.com](http://www.imagemet.com).
- (5) <http://rsbweb.nih.gov/ij/index.html>.
- (6) [www.liv.ac.uk/~sdb/ImageSXM](http://www.liv.ac.uk/~sdb/ImageSXM).
- (7) Wang, D. D.; Bourke, D.; Domanski, D.; Vallotton, P. In *18th World IMACS/MODSIM Congress Cairns, Australia, 2009*.
- (8) McGeouch, C.-A.; Edwards, M. A.; Mbogoro, M. M.; Parkinson, C.; Unwin, P. R. *Anal. Chem.* **2010**, *82*, 9322.
- (9) Bawazeer, T.; McGeouch, C.-A.; Peruffo, M.; Mbogoro, M. M.; Unwin, P. R. *in preparation*.
- (10) Westra, K. L.; Mitchell, A. W.; Thomson, D. J. *J. Appl. Phys.* **1993**, *74*, 3608.
- (11) Magonov, S. N.; Whangbo, M.-H. In *Surface Analysis with STM and AFM*; Wiley-VCH Verlag GmbH: 2007, p I.
- (12) Méndez-Vilas, A.; González-Martín, M. L.; Labajos-Broncano, L.; Nuevo, M. J. *Appl. Surf. Sci.* **2004**, *238*, 42.
- (13) Bowen, W. R.; Doneva, T. A. *Journal of Membrane Science* **2000**, *171*, 141.

# **Chapter 4**

## **Bridging the Length Scales in Dissolution Kinetics: Macroscopic Fluxes, Mass Transport Effects & Direction-Specific Rates from Gypsum Etch Pit Analysis**

### **Abstract**

Dissolution processes at single crystals often involve the formation and expansion of localised characteristic etch pits. Using natural gypsum single crystal as an example, a simple but powerful morphological analysis of characteristic etch pit features is proposed. First, the high and quantitative mass transport associated with micro-scale interfaces (well known in the field of electrochemistry at ultramicroelectrodes) allows the relative importance of diffusion compared to surface kinetics to be assessed. For the case of gypsum, surface processes dominate the kinetics at early stages in the dissolution process (small etch pits) on the cleaved (010) surface. However, the contribution from mass transport increases with time, with spatial heterogeneities in both surface kinetics and mass transport effects identified. Directional dissolution velocities of the main basal face and lateral steps were in the order;  $v_{(010)} < v_{[001]} \ll v_{[100]}$ . Inert supporting electrolyte enhances dissolution velocities in all directions (salting in), but to different degrees. Studies of common ion effects reveal that  $\text{Ca}^{2+}$  has a much greater impact in reducing dissolution rates compared to  $\text{SO}_4^{2-}$ , most likely due to preferential adsorption of  $\text{Ca}^{2+}$  on the negatively charged gypsum surface. With the approach reported here, these new microscopic observations can be further interpreted to obtain macroscopic dissolution rates, which are found to be wholly consistent with previous bulk measurements. The studies thus bridge the gap between microscopic phenomena and macroscopic measurements and allow the most important features in the dissolution process to be deduced.

## **4.1. Introduction**

This chapter introduces a simple, but powerful, approach for elucidating the rate of crystal dissolution, a process driven by interfacial undersaturation.<sup>1,2</sup> In comparison to crystal growth, for which a wide body of experimental and theoretical data is available,<sup>3-7</sup> it is recognised that the kinetics and mechanisms of crystal dissolution are less well understood and new features continue to emerge.<sup>8-16</sup>

Traditional methods for the study of crystal dissolution have tended to be macroscopic, such as batch and column experiments on particulates,<sup>17,18</sup> as well as techniques that deliver well-defined mass transport to (well-defined) surfaces, such as the rotating disk method,<sup>19-24</sup> and channel flow cells.<sup>21,25-31</sup> More recently, microscopic techniques such as AFM,<sup>17,32-35</sup> scanning electrochemical microscopy (SECM)<sup>36-40</sup> and WLI<sup>4,7,41</sup> have been used to probe dissolution processes at the local level. While undoubtedly having a significant impact in terms of phenomenological observation, *in-situ* AFM has the disadvantage of limiting dissolution studies to either very slow processes or close to equilibrium conditions (for fast processes) so that the reaction is compatible with the AFM timescale, thereby restricting the range of intrinsic kinetics accessible.<sup>33</sup> Furthermore, transport in AFM (convective) fluid cells is rather complicated,<sup>42,43</sup> which may make the separation of transport and surface kinetic effects difficult. It has typically proved difficult to link nanoscale kinetics from AFM to macroscopic flux measurements,<sup>12</sup> and this is an issue which needs to be addressed generally.

Dissolution is often manifested on a crystal surface through the formation of etch pits at defect sites, giving rise to a heterogeneously active surface.<sup>17,44,45</sup>

The morphologies of such etch features have been analysed to reveal information about the mode of action of crystal habit modifiers and dissolution/growth inhibitors,<sup>2,46,47</sup> and work has shown that for slow surface-controlled processes etch pits reveal information on dissolution kinetics,<sup>7,48,49</sup> including complex processes where pits coalesce.<sup>20</sup>

In this chapter, a simple quantitative analysis of dissolution kinetics is introduced by tracking the evolution of individual characteristic etch pits at defined times during the course of a dissolution reaction and coupling these observations to a diffusion model. This approach allows the significance of mass transport to be elucidated, along with the evaluation of interfacial concentrations and the deduction of direction-dependent kinetics. The inspiration for the analysis of microscopic features in this way comes from the field of ultramicroelectrodes<sup>50,51</sup> and ultramicroelectrodes arrays<sup>52</sup> which have shown that fast kinetics and the relative importance of diffusion can be measured simply and effectively by shrinking the length scale of the reactive interface.

Figure 4.1 illustrates the conceptual approach used, where the evolution of a characteristic etch pit on a surface, undergoing the initial stages of dissolution, is tracked over time. With the time-dependent etch pit dimensions as an input, a simulation is developed which predicts local fluxes, diffusion processes and interfacial concentrations accurately. The approach yields molecular-level dissolution kinetics that may be linked readily to macroscopic fluxes, providing self-consistent hierarchical kinetics that closes the gap between the nanoscale and macroscale.

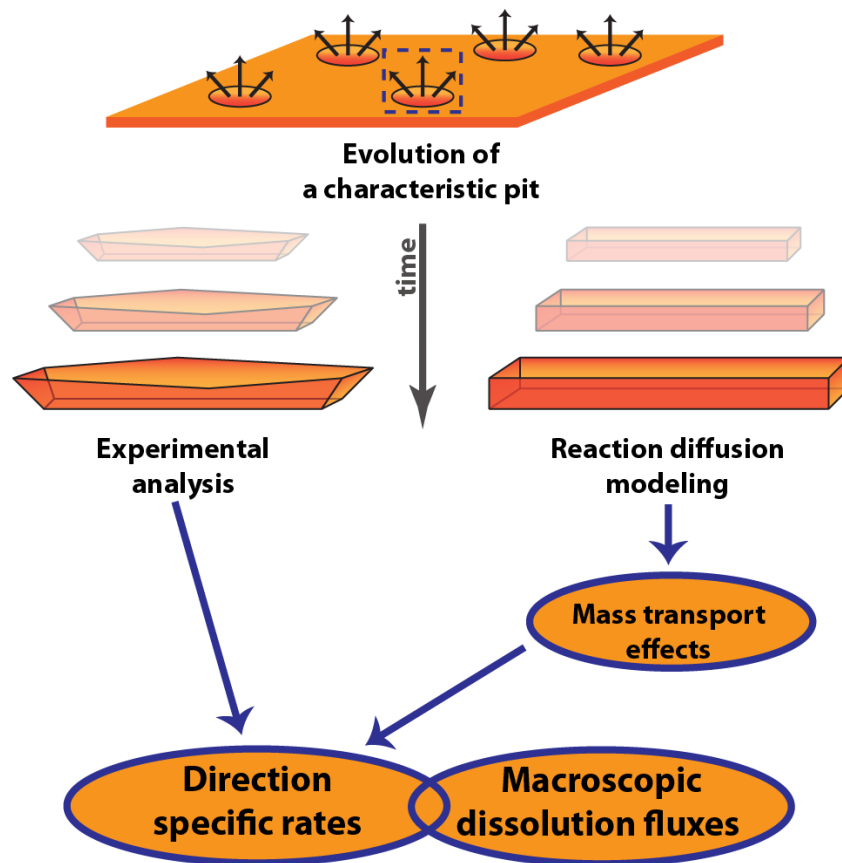


Figure 4.1: Schematic for etch pit analysis, in which a flat crystal surface is etched and dissolution is monitored by tracking the expansion of a characteristic etch pit and using complementary computer simulations to deduce dissolution kinetics, surface concentrations and mass transport effects.

Gypsum single crystal was chosen, as an example of an abundant sedimentary mineral<sup>53</sup> with extensive applications.<sup>54-57</sup> In its optically transparent form (selenite), gypsum exhibits a perfect cleavage with near atomic scale flatness along the (010) plane, which makes it particularly attractive for initial investigations with the proposed method. Various studies have explored gypsum dissolution at the macroscale<sup>58-61</sup> and nanoscale,<sup>62-65</sup> in some cases under close to equilibrium conditions.<sup>62</sup> Most nanoscale studies have reported the formation of shallow pits (pit depth  $\sim 8\text{\AA}$ ) which typically

emerge from point or line defects. Despite this body of work, there is debate on the rate determining step at an early stage in the dissolution process, with some studies highlighting the importance of mass transport<sup>54,55</sup> while others indicate surface kinetic control.<sup>56</sup> Furthermore, neither elementary direction (or plane)-specific dissolution rates nor common ion effects have been reported. Consequently, it has not been possible to relate step velocity measurements (typically lateral displacement), e.g. from AFM, to bulk dissolution rates (volumetric removal of material from crystal surface). As will be shown, (Chapter 5) the intrinsic dissolution kinetics of the basal (010) surface are accessible, but the edge planes dissolve at a diffusion-controlled rate, even with the high mass transport rates accessible from a CFC.<sup>60</sup> The approach herein addresses these missing features and is shown to provide an holistic view of dissolution kinetics.

## **4.2. Numerical Theory and Simulations**

Finite element simulations were developed to probe the internal pit surface as a function of time, and predict spatially-resolved dissolution fluxes from which local interfacial concentrations were determined. This allowed the deduction of the kinetic regime (mass transport control, surface kinetic control, or mixed kinetics) and the elucidation of the contributions of dissolution rates in specific directions and their relative importance in macroscopic measurements.

Numerical simulations were executed on a Dell Intel core™ 2 Quad 2.49 GHz computer equipped with 8 GB of RAM and running Windows XP Professional X64 bit 2003 edition. Modeling was performed using the

commercial finite element modeling package Comsol Multiphysics 3.4 (Comsol AB, Sweden), using the Matlab interface. Simulations were carried out with >27 000 tetrahedral mesh elements and mesh resolution was defined to be finest in the vicinity of the etch pit. Simulations with finer meshes were carried out (not reported) to confirm that the mesh was sufficiently fine to ensure that the predicted solutions were accurate.

#### **4.2.1 Model for Direction-Specific Dissolution Kinetics**

A finite element domain shown schematically in Figure 4.2 (a, b) was used to approximate the pit, based on the monoclinic geometry of the gypsum unit cell and the dimensions of a typical pit at a specific time (Figure 4.3). Due to the steep tapering of the pit walls, of the experimental etch pits (Figure 4.2 (c)), the lateral pit dimensions used for simulations were approximated to a cuboid using lateral pit dimensions taken at 50% pit depth, while pit depth was taken from average depth of the pit (010) face. This was a very reasonable approximation for the purpose herein, which was to determine the relative importance of mass transport. The distance between etch pits on the surface was sufficiently large to avoid overlap of concentration boundary fields generated due to the accumulation of dissolution products. This assumption is reasonable for the time scale chosen for analysis, coupled with the fact that it was found that the reaction was far from diffusion-controlled. The model could easily be developed to allow for diffusional interaction of material from neighbouring pits if it was needed in the future.

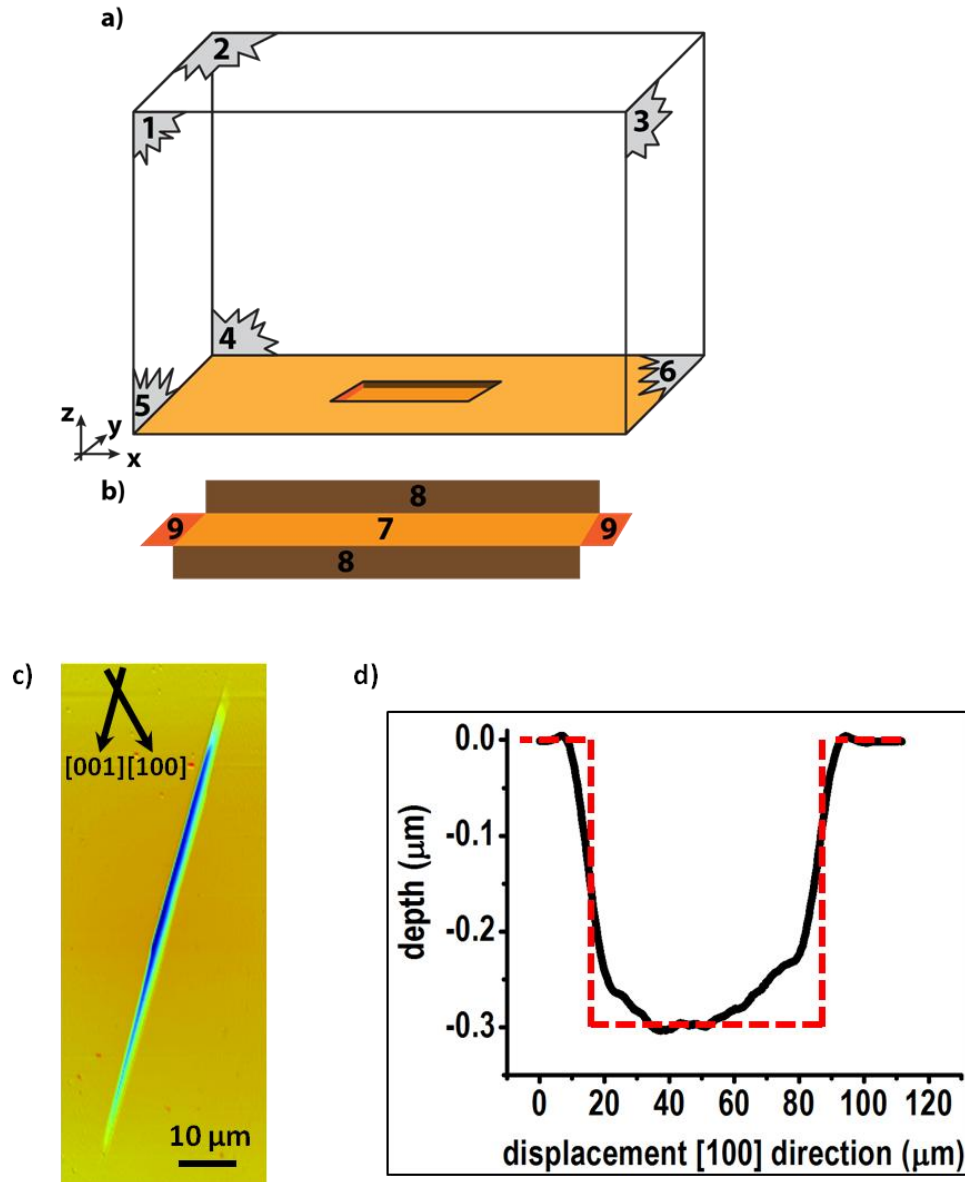


Figure 4.2: (a) Simulation domain used for finite element simulations of plane (direction)-specific dissolution fluxes where the numbers represent the boundaries used in simulations (not to scale). (b) The simulated etch pit whose walls have been opened up for clarity, and (c) a typical etch pit with (d) the cross section along the pit length ([001] direction). The dashed line represents the approximation used for the pit geometry.

The mass transport of ions from the crystal surface to bulk solution was described by the stationary diffusion equation (eq 4.1) solved under fixed boundary conditions:

$$D_i \nabla^2 C_i = 0 \quad (4.1)$$

where  $D_i$  is the diffusion coefficient of species  $i$ , where  $i$  is  $\text{Ca}^{2+}$  or  $\text{SO}_4^{2-}$ , and  $C_i$  is the concentration of species  $i$ . The use of equation 4.1 assumes that the expansion of the pit geometry is slow compared to the characteristic diffusion times,  $t_{diff} \sim l_p^2/D$ , where  $l_p$  is the characteristic pit dimension. For all of the cases herein, this condition was satisfied. Dissolution of ions from the crystal surface was considered to be a stoichiometric process so that electroneutrality was maintained. Consequently, the diffusion equation was solved only for the  $\text{Ca}^{2+}$  ion, with  $D_{\text{Ca}^{2+}} = 0.79 \times 10^{-5} \text{ cm}^2 \text{ s}^{-1}$ ,<sup>66</sup> which was reasonable because  $\text{SO}_4^{2-}$  has a similar diffusion coefficient to  $\text{Ca}^{2+}$ .

The walls of the cubic domain (Figure 4.2) numbered **1-5**, define bulk solution conditions governed by equation 4.2:

$$C_i = C_{i,b} \quad (4.2)$$

where  $C_{i,b}$  is the bulk concentration of species  $i$ . and the numbers used represent boundary numbers described in the text to define boundary conditions. Boundary **6** represents the inert basal plane and therefore satisfies a no normal flux as described by:

$$\underline{n} \cdot (D_i \nabla C_i) = 0 \quad (4.3)$$

where  $\underline{n}$  is the inward pointing unit normal to the surface. Boundaries **7-9** represent the etch pit walls in the [010], [001] and [100] directions, respectively (Figure 4.2 (b)) and their corresponding experimentally determined fluxes normal to specific planes,  $J_{(hkl)}$ , ( $\text{mol m}^{-2} \text{ s}^{-1}$ ) were used as inputs for predicting concentration profiles, mass transport effects and the interfacial concentration (of  $\text{Ca}^{2+}$ ) ions at each plane, as governed by:

$$\underline{n} \cdot D_i \nabla C_i = J_{(hkl)} \quad (4.4)$$

### 4.3. Results and Discussion

#### 4.3.1 Morphological Etch Pit Analysis

Figure 4.3 shows typical AFM images of etch pits produced after etching the (010) plane of gypsum in 0.2 M NaNO<sub>3</sub> for (a) 30 s, (b) 55 s, (c) 80 s and (d) 105 s. The images show etch pit evolution over time with no significant change in morphology. In this and all cases, the etch pit shape resembles a parallelogram elongated along the [001] direction, with well-defined edges of the etch pit embracing the main [100] and [001] crystallographic directions (Figure 1.1). This trend in pit growth was typical, and the major time-dependent pit dimensions were used to produce direction-dependent dissolution rates (*vide infra*) and as inputs in simulations.

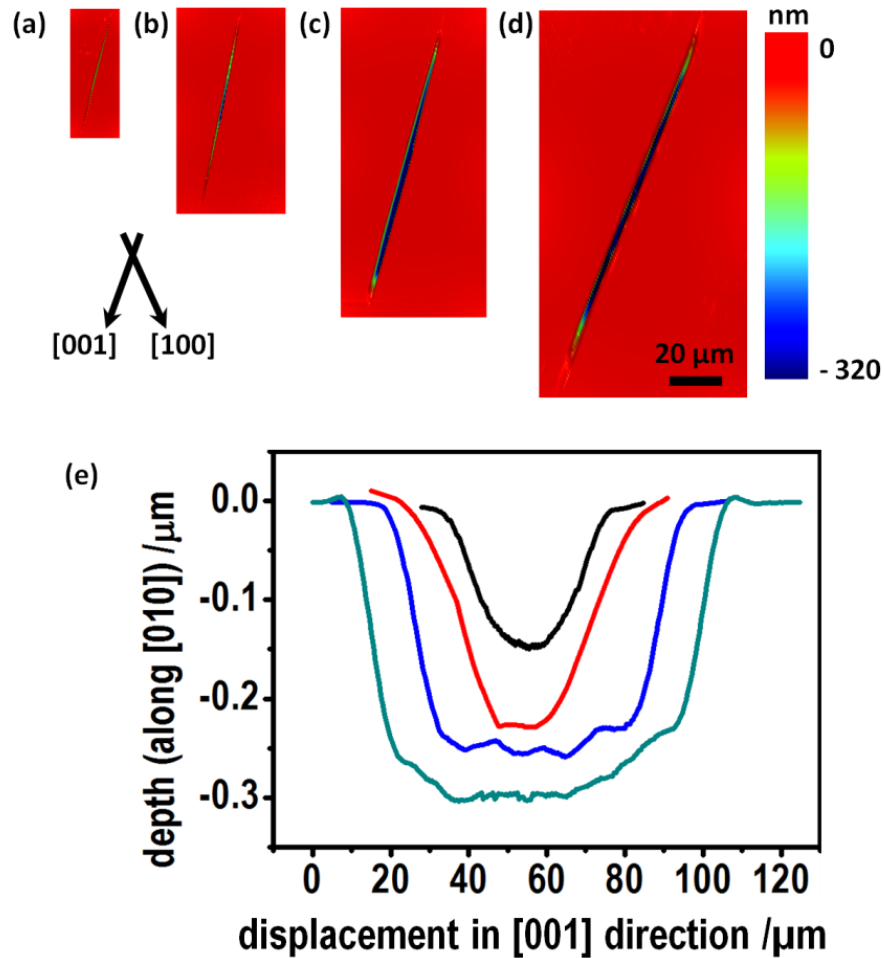


Figure 4.3: Typical AFM micrographs of etch pits produced after etching the (010) gypsum surface in 0.2 M  $\text{NaNO}_3$  solution for (a) 30 s, (b) 55 s, (c) 80 s, (d) 105 s and (e) the corresponding cross sectional profiles along the [001] direction for 25 s (black), 50 s (red), 75 s (blue) and 100 s (cyan). Note the evident anisotropy of step kinetics which results in etch pit elongation along the [001] direction. Pit depth corresponds to expansion in the [010] direction.

The initially isolated pits tended to coalesce typically at times  $> 15$  min in pure  $\text{H}_2\text{O}$  and  $> 10$  min at  $\text{IS} = 0.2$  M (in inert salt solution), which was well beyond the maximum duration used experimentally ( $\leq 110 \pm 5$  s) for quantitative etch pit analysis. By focusing on short times, the development of non-interacting etch pits can be considered and, moreover, on this length scale

mass transport is strongly diffusional with negligible contribution from (natural) convective effects (*vide infra*).

Etch pit depth, due to dissolution in the [010] direction, perpendicular to the (010) plane, was typically in the range 50 - 530 nm (in pure H<sub>2</sub>O), increasing as the etch time increased. The dimension of a characteristic repeat layer in this direction, comprising one CaSO<sub>4</sub> layer (Figure 1.1 (a)) is ~ 0.4 nm,<sup>67</sup> which suggests that even for the shortest dissolution period (30±3 s), the pits analysed were at least 120 monolayers deep. Occasionally, some very shallow etch pits were observed, but their occurrence was not common under the experimental conditions. By contrast, previous *in-situ* AFM studies<sup>62-65</sup> have reported only the formation of such shallow pits with depths of just a few monolayers. However, these latter measurements were made close to equilibrium and shallow etch features of this sort most likely emerge from surface/point defects. The consensus is that these shallow pits do not contribute to gypsum dissolution rates in a significant way.<sup>62-65</sup>

The relatively deep pits observed by in this work, indicates that they nucleate at dislocation sites emerging at the surface.<sup>44,68,69</sup> This is evident from Figure 4.4 which depicts DIC micrographs of matched cleavages. The etch pits nucleate at the same location on each surface and exhibit similar dimensions. The correspondence of the etch pits is good evidence that they emerge from defects which run through the crystal (essentially perpendicular to the (010) plane), such as dislocations.<sup>44</sup> For any specific etching duration and solution, etch pits of this type were formed across the entire surface and were found to exhibit similar dimensions to each other (within ≤ 10%). This indicated that pit formation for the (010) gypsum surface occurred via an essentially

instantaneous process and that any particular pit is characteristic of the dissolution process. Such characteristic etch features occur generally in the dissolution of many crystalline materials<sup>7,12,44,69</sup> making the approach advocated here widely applicable.

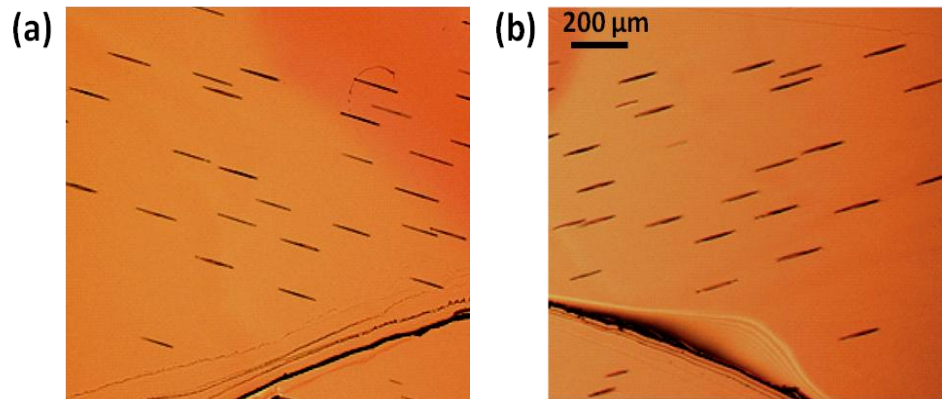


*Figure 4.4: DIC micrographs of the (010) surface of gypsum showing matched halves after a 7 min etch in pure H<sub>2</sub>O. Note the correspondence of etch pits on the same mirror positions and that the area selected had a macroscopic scratch (bottom section) chosen deliberately to allow correlation of the mirror surfaces.*

### **4.3.2 Step Displacement Kinetics**

Figure 4.5 shows summary plots of etch pit displacement for the (010) face (a), [001] steps (b) and [100] steps (c) as a function of time, based on direct measurement of pits via AFM, for all etching solutions used. Lateral measurements of pit expansion of the [001] and [100] steps were taken from close to the top of the etch pit while pit depths (dissolution of the (010) face) were calculated from cross sections taken across the pit width and length, from the basal floor of the pit to the crystal basal surface. For each etching time, at least three surfaces were etched and, from these, at least three characteristic etch pits were analysed, n=9. The displacements plotted in Figure 4.5 are average values and the error bars represent two standard deviations. A

reasonably linear relationship of step displacement versus time was found for all directions for these relatively short time durations. Step velocity values,  $v_{[uvw]}$ , calculated from each of the slopes in Figure 4.5 are summarised in Table 4.1. It is evident that there is a significant trend:  $v_{(010)} < v_{[001]} \ll v_{[100]}$ .

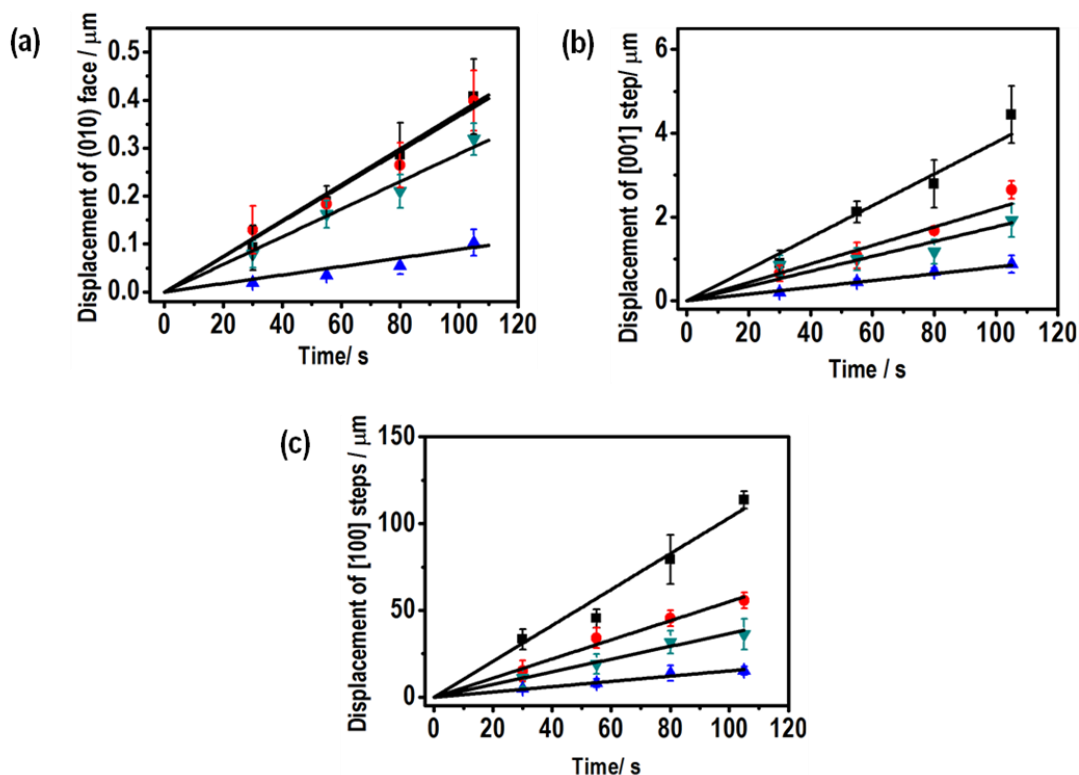


Figure 4.5: Etch pit displacement as a function of etching time for the (010) gypsum surface ( $n=9$ ) in solutions of 0.2 M  $\text{NaNO}_3$  (black), 0.075 M  $\text{Na}_2\text{SO}_4$  (red),  $\text{Ca}(\text{NO}_3)_2 \cdot 4\text{H}_2\text{O}$  (blue) and pure  $\text{H}_2\text{O}$  (green) for the (a) (010) face, (b) [001] and (c) [100] steps and the solid lines are linear fits to the experimental data.

For etching in pure  $\text{H}_2\text{O}$ , the dissolution velocities were:  $330 \pm 30 \text{ nm s}^{-1}$ ,  $17 \pm 3 \text{ nm s}^{-1}$  and  $3.0 \pm 0.4 \text{ nm s}^{-1}$  for the [100], [001] steps and the (010) face, respectively. This order can be rationalised to some extent by reference to bonding in the crystal, particularly within the  $\text{CaSO}_4$  bilayer (Figure 1.1 (a)), as outlined by Teng and Fan,<sup>62</sup> using periodic bond chain arguments.<sup>70,71</sup> There is

a staggered conformation of neighbouring like-ions (e.g. from one  $\text{Ca}^{2+}$  ion to another) along the [001] direction, while along the [100] direction, like-ions are eclipsed. With respect to bonding to neighbouring  $\text{SO}_4^{2-}$  groups, a more densely packed arrangement is formed in the [100] direction compared to the [001] direction. Step movement is likely to be faster along the less densely packed direction, and consequently, etch pits are elongated along the [001] direction, *vide supra* (Figure 4.3 (a)). In the [010] direction, a  $\text{H}_2\text{O}$  layer is sandwiched between the  $\text{CaSO}_4$  layers through H-bonding <sup>67</sup> (Figure 1.1 (b)) thereby disrupting the continuity of the periodic bond chain in this direction, and consequently, facilitating the lower displacement velocities along [010] relative to the [100] and [001] directions for all etching solutions.

Table 4.1: Measured displacement velocities obtained from dissolution studies.

Etching Solution	Displacement velocities ( $\text{nm s}^{-1}$ )		
	[100] step	[001] step	(010) face
$\text{H}_2\text{O}$	$330 \pm 30$	$17 \pm 3$	$3.0 \pm 0.4$
$\text{NaNO}_3$	$1030 \pm 60$	$31 \pm 4$	$4.1 \pm 0.6$
$\text{Na}_2\text{SO}_4$	$550 \pm 30$	$20 \pm 3$	$3.7 \pm 0.5$
$\text{Ca}(\text{NO}_3)_2 \cdot 4\text{H}_2\text{O}$	$160 \pm 10$	$8.5 \pm 1.2$	$0.9 \pm 0.2$

Compared to dissolution in pure H<sub>2</sub>O, etching in 0.2 M NaNO<sub>3</sub> was found to enhance step velocities (salting-in)<sup>34,72,73</sup> by factors of ~3, ~2 and ~1.4 for the [100], [001] steps and (010) face, respectively. The enhanced dissolution rates are expected since gypsum solubility increases by a factor of 2 from 16.2 mM in pure H<sub>2</sub>O to 32.3 mM (MINEQL+) with 0.2 M NaNO<sub>3</sub>. However, it is evident that the salt effect is strongly direction-dependent, impacting dissolution in the [100] direction in particular.

Conversely, dissolution in solutions containing common ions (Na<sub>2</sub>SO<sub>4</sub> and Ca(NO<sub>3</sub>)<sub>2</sub>·4H<sub>2</sub>O solutions) yielded strikingly different step velocity trends despite having similar IS values. Naturally, compared to etching at the same IS with an inert supporting electrolyte (NaNO<sub>3</sub>), step velocities in all directions are predictably lower for both Na<sub>2</sub>SO<sub>4</sub> and Ca(NO<sub>3</sub>)<sub>2</sub>·4H<sub>2</sub>O (common ion effect). However, from Figure 4.6 and Table 4.1, it is evident that step velocities in the presence of SO<sub>4</sub><sup>2-</sup> ions are significantly higher than values obtained in the Ca<sup>2+</sup>-rich solution for all directions. This observation is particularly striking for dissolution of the (010) face of the pit (Figure 4.5 (a)) where dissolution velocities are more than 4 times faster when etching occurs in the presence of SO<sub>4</sub><sup>2-</sup> ion compared to Ca<sup>2+</sup>. These effects can be rationalised generally, because gypsum crystal exhibits a negative ζ- potential in pure H<sub>2</sub>O under standard conditions and over a wide pH range, due to the preferential adsorption of anions relative to cations on the crystal surface.<sup>74,75</sup> Thus, in a Ca<sup>2+</sup>-rich solution, the back reaction, characterised by the adsorption of Ca<sup>2+</sup> (and SO<sub>4</sub><sup>2-</sup>) on the crystal surface, appears to be enhanced compared to the situation in the SO<sub>4</sub><sup>2-</sup>-rich solution.

When comparisons can be made to previous studies, the step displacement velocities deduced in this work are much higher than those deduced by *in-situ* AFM. For example, at a relative saturation,  $S = C/C_{sat} = 0.65$ , where  $C$  is the bulk solution concentration, Bosbach and Rammensee<sup>63,64</sup> measured velocities of steps running parallel to the [100] and [001] directions of  $\leq 30.0 \text{ nm s}^{-1}$  and  $\leq 2.5 \text{ nm s}^{-1}$ , respectively. These values were later corroborated by others using AFM<sup>65</sup> but, more recently, for the range of  $S = 0.34$  to 0.96, Fan and Teng<sup>62</sup> deduced much slower step velocities for steps parallel to [100], of  $\sim 2 - 7 \text{ nm s}^{-1}$  while steps parallel to [001] moved at  $\sim 0.2 - 1.2 \text{ nm s}^{-1}$ . Of course, one reason for the difference between the measurements reported in this work and these previous studies, is that AFM has to be conducted at medium to low driving force to deliberately slow the step movement (*vide supra*). It is non-trivial to extrapolate between these previous results and our measurements conducted at high driving force, but if one considers common rates laws such as first or higher order dependences of dissolution on (interfacial) undersaturation, then the rates measured here are significantly higher than one might expect. This can be rationalised because, as shown below, dissolution in the [001] direction (that is the movement of steps parallel to [100]) show that mass transport slows down at longer times. Thus, surfaces studied by AFM in stagnant solutions, which involve necessarily lengthy periods and extensively etched surfaces, are very likely subject to severe diffusional limitations, which would serve to slow the step movement. Such effects would provide a plausible explanation for differences between different AFM studies: diffusion-limited dissolution will not only be sensitive to mass transport conditions in the AFM cell but also the topography (density of steps) on the

crystal surface. In contrast, the studies herein provide true intrinsic step velocities and allow those velocities to be related faithfully to interfacial saturation levels that can be predicted by solution of a well-posed mass transport problem..

#### **4.4. Direction-Specific Dissolution Kinetics**

Dissolution fluxes normal to specific crystal faces,  $J_{(hkl)}$ , ( $\text{mol cm}^{-2} \text{ s}^{-1}$ ) were calculated as the product of experimentally deduced step motion velocities, and the molar density ( $13400 \text{ mol m}^{-3}$ ) of the crystal.<sup>76</sup> These values are summarised in Table 4.2 and predictably mirror the trend seen in the displacement velocity measurements (*vide supra*) such that;  $J_{(010)} < J_{(001)} \ll J_{(100)}$ . These direction-specific dissolution fluxes were used in conjunction with the etch pit dimensions as inputs for the finite element model. This model predicted the corresponding ( $\text{Ca}^{2+}$  and  $\text{SO}_4^{2-}$ ) concentration profiles around the pits, and in particular, the interfacial concentration of dissolved  $\text{Ca}^{2+}$  and  $\text{SO}_4^{2-}$  at reactive pit faces. From these profiles, the relative importance of mass transport and surface kinetics could be elucidated, from which the kinetic (rate-determining) regime could be determined.

Table 4.2: Summary of plane specific fluxes under different etchants.

Etching Solution	Flux ( $\text{mol cm}^{-2} \text{s}^{-1}$ ) normal to plane		
	(100)	(001)	(010)
H <sub>2</sub> O	$5.1 (\pm 0.5) \times 10^{-7}$	$2.5 (\pm 0.4) \times 10^{-8}$	$4.0 (\pm 0.5) \times 10^{-9}$
NaNO <sub>3</sub>	$1.6 (\pm 0.1) \times 10^{-6}$	$4.7 (\pm 0.5) \times 10^{-8}$	$5.5 (\pm 0.8) \times 10^{-9}$
Na <sub>2</sub> SO <sub>4</sub>	$8.4 (\pm 0.4) \times 10^{-7}$	$3.1 (\pm 0.4) \times 10^{-8}$	$5.0 (\pm 0.7) \times 10^{-9}$
Ca(NO <sub>3</sub> ) <sub>2</sub> ·4H <sub>2</sub> O	$2.4 (\pm 0.2) \times 10^{-8}$	$1.3 (\pm 0.2) \times 10^{-8}$	$1.2 (\pm 0.3) \times 10^{-9}$

Figure 4.6 illustrates a section of the overall simulated pit, approximated reasonably well as a cuboid. The pit profile is shown at times of (a) 50 s and (b) 100 s in pure H<sub>2</sub>O. For each specific time, it is evident that the surface concentration profile is heterogeneous over the pit surface, with the highest concentration arising from the fast moving (100) face. At the mid- time in the process (50 s, Figure 4.6 (a)), it was found that the total average interfacial concentration was 0.17 mM, 0.18 mM and 0.88 mM for the basal (010), (001) and (100) faces, respectively. The highest interfacial concentration (on the (100) face) equates to  $\sim 5.4\%$   $C_{sat}$  which indicates, that on this scale, dissolution is essentially controlled by surface kinetics. This is a consequence of high mass transport from a microscopically active surface as seen, for example, with amperometric ultramicroelectrodes in electrochemistry.<sup>52</sup>

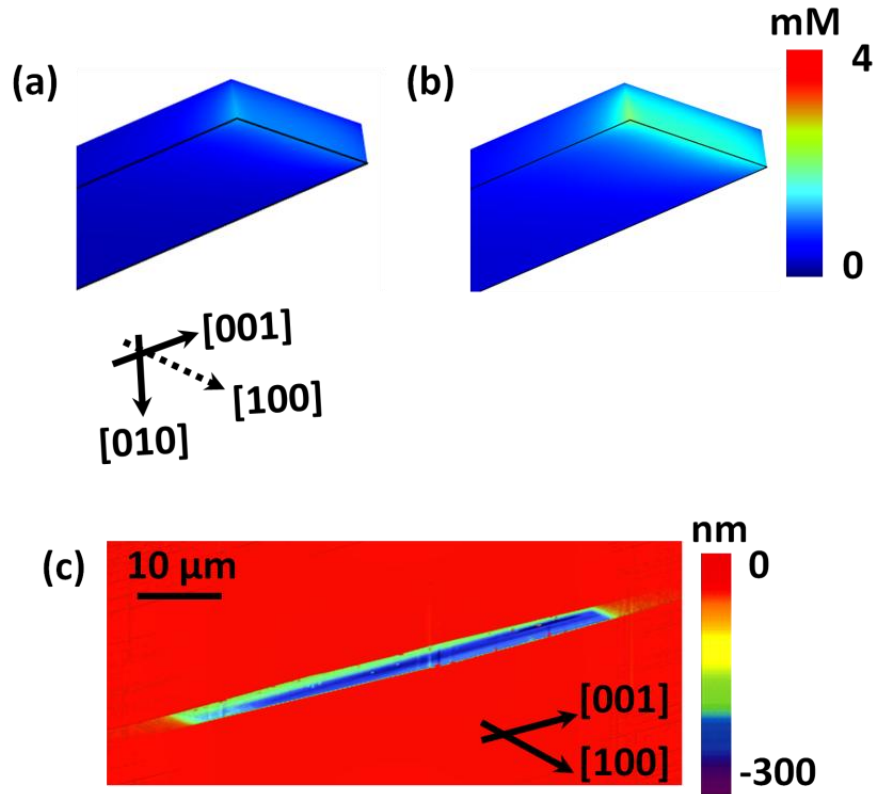


Figure 4.6: Typical simulated interfacial  $\text{Ca}^{2+}$  and  $\text{SO}_4^{2-}$  concentration profile over the pit from a section of the overall pit (not to scale) close to the (100) face, after (a) 50 and (b) 100 s etches in pure  $\text{H}_2\text{O}$ , and for comparison (c) an experimental etch pit formed after 100 s etch in pure  $\text{H}_2\text{O}$ , acute angle ( $\sim 62^\circ$ ). The magnification (a-b) highlights the change in surface concentration on the fast moving (100) face.

At later times in the dissolution process (100 s, Figure 4.6 (b)), the surface concentration values increase (as the pit dimensions increase) to such an extent that diffusion becomes more important, particularly for dissolution of the (100) face. Figure 4.7 illustrates the change in diffusion fields due to the evolution of etch pits as a function of time. It is clear that at early times, the diffusion field above the etch pit is isolated from neighbouring pits. However, with time, these fields start to interact and eventually (longer times) establish a

planar field where there is significant diffusional overlap between neighbouring etch pits.

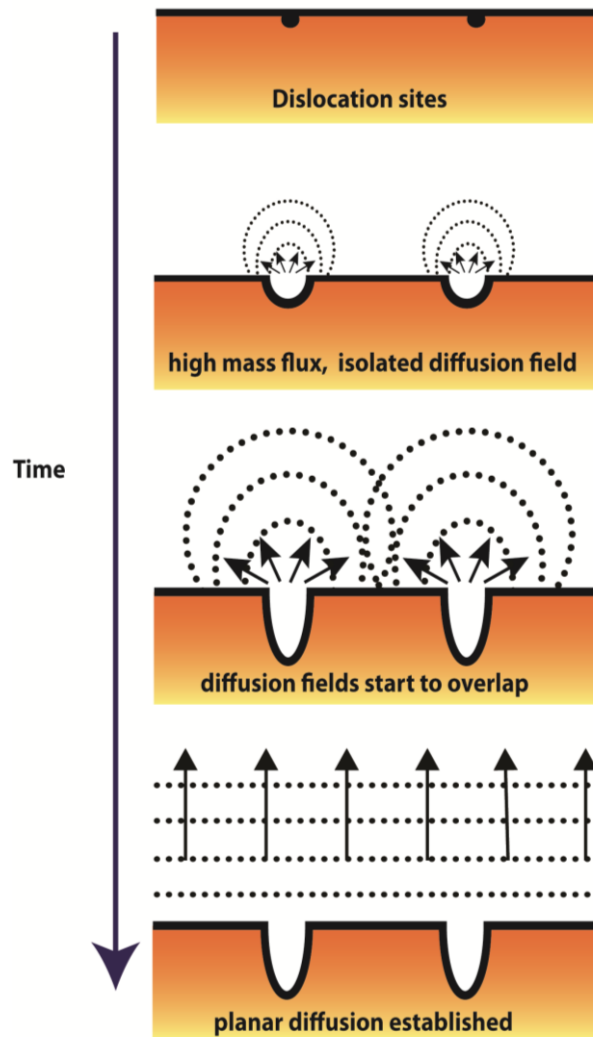


Figure 4.7: Illustration describing the onset of dissolution at defect sites, where initially, the formed etch pits are isolated from their neighbours and show evidence of unimpeded high mass flux. With time, these pits grow to an extent that diffusional cross-talk is exhibited, with the consequence of establishing a planar diffusion profile at the inter-facial region.

#### 4.5. Linking Microscopic and Macroscopic Dissolution Kinetics

The average intrinsic rate (in pure H<sub>2</sub>O) of dissolution from the entire etch pit was predicted from simulations to be  $J = 1.34 \times 10^{-8} \text{ mol cm}^{-2} \text{ s}^{-1}$  and  $J = 1.27$

$\times 10^{-8}$  mol cm<sup>-2</sup> s<sup>-1</sup> for dissolution after 50 s and 100 s, respectively. When the relative surface area of individual faces,  $A_{(hkl)}$  is considered, these rates suggest that gypsum dissolution at early times ( $\leq 100$  s) is dominated by the edge (100) and (001) planes relative to the basal (010) surface. These average rates decrease with time as a consequence of pit expansion such that  $A_{(100)} / A_{(010)}$  (and similarly  $A_{(001)} / A_{(010)}$ ), decrease significantly as a function of etching duration and, consequently, the contribution from these high flux faces diminishes over time. Eventually, at longer times (where the surface is fully reactive) dissolution will be dominated by the basal plane. Indeed, the flux from the basal plane was predicted to be  $J_{(010)} = 4.0 (\pm 0.5) \times 10^{-9}$  mol cm<sup>-2</sup> s<sup>-1</sup> which compares reasonably to values suggested by Colombani<sup>61</sup> who reviewed various previous bulk studies and deduced  $J = 5 (\pm 2) \times 10^{-9}$  mol cm<sup>-2</sup> s<sup>-1</sup> <sup>77</sup> by extrapolation of many different techniques. However, it is important to point out, in light of our work that the overall flux deduced from macroscopic measurements will necessarily be very sensitive to the nature of the surface exposed. The studies reported here, with the deduction of plane (direction)-specific dissolution kinetics, provides a framework for the construction of accurate dissolution models for complex (polycrystalline) materials and single crystal surfaces with an abundance of different features. Most importantly, these intrinsic rates can be used to predict when mass transport will become important for different planes and faces.

#### **4.6. Conclusions**

A simple but powerful method has been described, with which the time-dependent analysis of characteristic etch pits formed by dissolution of crystal

surfaces, allows microscopic and macroscopic fluxes to be linked in a self-consistent manner. The methodology allows a determination of the relative importance of surface processes compared to mass transport in controlling dissolution kinetics at different crystal facets (steps, planes).

A particularly striking aspect of the analysis is that direction-specific reaction rates are deduced directly. For the case of gypsum, at early times in the process, dissolution in all measured directions was predominantly surface-controlled, but the fast moving steps parallel to the [100] direction yielded higher interfacial local concentrations, indicating relatively more contribution from mass transport. The etch pit morphology was dominated by the large flat (010) pit base for which the dissolution flux was  $J_{(010)} = 4.0 (\pm 0.5) \times 10^{-9} \text{ mol cm}^{-2} \text{ s}^{-1}$ . This value compares well with previous macroscopic flux measurements of this face. Past attempts to measure intrinsic fluxes from other faces (edge planes) have been unsuccessful due to their fast rates. Herein, these fluxes have been measure for the first time, yielding  $J_{(001)} = 2.5 (\pm 0.4) \times 10^{-8} \text{ mol cm}^{-2} \text{ s}^{-1}$  and  $J_{(100)} = 5.1 (\pm 0.5) \times 10^{-7} \text{ mol cm}^{-2} \text{ s}^{-1}$ . The associated step velocities are much faster than can be measured by *in-situ* AFM studies which have clearly been shown to be highly susceptible to impacted by mass transport effects, making kinetic/mechanistic interpretations of such data difficult.

Studies of salt effects have yielded two important new observations for gypsum. In the presence of an inert salt ( $\text{NaNO}_3$ ) faster dissolution velocities have been found for all crystal directions compared to dissolution in pure water, but the magnitude of the effect is direction-specific. Second, a brief exploration of common ion effects ( $\text{Ca}^{2+}$  vs.  $\text{SO}_4^{2-}$  in bulk solution) has revealed

a significant retardation effect of  $\text{Ca}^{2+}$  ion compared to  $\text{SO}_4^{2-}$  and this has been rationalised based on the known (negative)  $\zeta$ -potential of gypsum.

## References

- (1) Unwin, P. R.; Macpherson, J. V. *Chem. Soc. Rev.* **1995**, *24*, 109.
- (2) Lasaga, A. C. *Kinetic Theory and applications in Earth Sciences*; Princeton Press: Princeton, 1998.
- (3) Tang, R.; Nancollas, G. H.; Orme, C. A. *J. Am. Chem. Soc.* **2001**, *123*, 5437.
- (4) Lüttge, A. *J. Electron Spectrosc. Relat. Phenom.* **2006**, *150*, 248.
- (5) Nancollas, G. H. *Biological Mineralization and Demineralization*; Springer-Verlag: Berlin, 1982.
- (6) Stumm, W. *Chemistry of the Solid-Water Interface*; Wiley: New York, 1992.
- (7) Lasaga, A. C.; Luttge, A. *Science* **2001**, *291*, 2400.
- (8) Arvidson, R. S.; Collier, M.; Davis, K. J.; Vinson, M. D.; Amonette, J. E.; Lüttge, A. *Geochim. Cosmochim. Acta* **2006**, *70*, 583.
- (9) Arvidson, R. S.; Luttge, A. *Chem. Geol.* **2010**, *269*, 79.
- (10) Jones, C. E.; Macpherson, J. V.; Unwin, P. R. *J. Phys. Chem. B* **2000**, *104*, 2351.
- (11) Jones, C. E.; Unwin, P. R.; Macpherson, J. V. *ChemPhysChem* **2003**, *4*, 139.
- (12) Morse, J. W.; Arvidson, R. S. *Earth-Sci. Rev.* **2002**, *58*, 51.
- (13) Tang, R. *Prog. Chem.* **2005**, *17*, 368.
- (14) Tang, R.; Orme, C. A.; Nancollas, G. H. *ChemPhysChem* **2004**, *5*, 688.
- (15) Wang, L.; Tang, R.; Bonstein, T.; Orme, C. A.; Bush, P. J.; Nancollas, G. H. *J. Phys. Chem. B* **2004**, *109*, 999.
- (16) Jeschke, A. A.; Dreybrodt, W. *Geochim. Cosmochim. Acta* **2002**, *66*, 3055.
- (17) Zhang, J. W.; Nancollas, G. H. *Rev. Mineral.* **1990**, *23*, 365.
- (18) Singh, H.; Bajwa, M. *Soil Research* **1990**, *28*, 947.
- (19) Burns, K.; Wu, Y.-T.; Grant, C. S. *Langmuir* **2003**, *19*, 5669.
- (20) MacInnis, I. N.; Brantley, S. L. *Chem. Geol.* **1993**, *105*, 31.
- (21) Brown, C. A.; Compton, R. G.; Narramore, C. A. *J. Colloid Interface Sci.* **1993**, *160*, 372.
- (22) Compton, R. G.; Daly, P. J. *J. Colloid Interface Sci.* **1987**, *115*, 493.
- (23) Liu, S.-T.; Nancollas, G. H. *J. Inorg. Nucl. Chem.* **1971**, *33*, 2311.
- (24) Svensson, U.; Dreybrodt, W. *Chem. Geol.* **1992**, *100*, 129.
- (25) Compton, R. G.; Pritchard, K. L.; Unwin, P. R.; Grigg, G.; Silvester, P.; Lees, M.; House, W. A. *J. Chem. Soc., Faraday Trans.* **1989**, *85*, 4335.
- (26) Compton, R. G.; Pritchard, K. L.; Unwin, P. R. *J. Chem. Soc.-Chem. Commun.* **1989**, 249.
- (27) Unwin, P. R.; Barwise, A. J.; Compton, R. G. *J. Colloid Interface Sci.* **1989**, *128*, 208.
- (28) Compton, R. G.; Unwin, P. R. *Philos. Trans. R. Soc. Lond. Ser. A* **1990**, *330*, 1.
- (29) Orton, R.; Unwin, P. R. *J. Chem. Soc.-Faraday Trans.* **1993**, *89*, 3947.
- (30) Hong, Q.; Suárez, M. F.; Coles, B. A.; Compton, R. G. *J. Phys. Chem. B* **1997**, *101*, 5557.
- (31) Peltonen, L.; Liljeroth, P.; Heikkilä, T.; Kontturi, K.; Hirvonen, J. *Eur. J. Pharm. Sci.* **2003**, *19*, 395.
- (32) Binnig, G.; Quate, C. F.; Gerber, C. *Phys. Rev. Lett.* **1986**, *56*, 930.
- (33) Dove, P. M.; Platt, F. M. *Chem. Geol.* **1996**, *127*, 331.
- (34) Ruiz-Agudo, E.; Urosevic, M.; Putnis, C. V.; Rodríguez-Navarro, C.; Cardell, C.; Putnis, A. *Chem. Geol.* **2011**, *281*, 364.
- (35) Jordan, G.; Rammensee, W. *Geochim. Cosmochim. Acta* **1998**, *62*, 941.
- (36) Macpherson, J. V.; Unwin, P. R. *J. Phys. Chem.* **1995**, *99*, 14824.
- (37) Macpherson, J. V.; Unwin, P. R. *J. Phys. Chem.* **1996**, *100*, 19475.
- (38) Macpherson, J. V.; Unwin, P. R.; Hillier, A. C.; Bard, A. J. *J. Am. Chem. Soc.* **1996**, *118*, 6445.

- (39) Macpherson, J. V.; Unwin, P. R. *J.Phys.Chem.* **1995**, *99*, 3338.
- (40) Macpherson, J. V.; Unwin, P. R. *J. Phys. Chem.* **1994**, *98*, 1704.
- (41) Lüttge, A.; Bolton, E. W.; Lasaga, A. C. *Am. J. Sci.* **1999**, *299*, 652.
- (42) Gasperino, D.; Yeckel, A.; Olmsted, B. K.; Ward, M. D.; Derby, J. J. *Langmuir* **2006**, *22*, 6578.
- (43) Burt, D. P.; Wilson, N. R.; Janus, U.; Macpherson, J. V.; Unwin, P. R. *Langmuir* **2008**, *24*, 12867.
- (44) Sangwal, K. *Etching of Crystals, Theory, Experiment and Application*; North Holland: Amsterdam, 1987.
- (45) Blum, A. E.; Lasaga, A. C. *Aquatic Surface Chemistry*; John Wiley: New York, 1987.
- (46) Brantley, S. L.; Kibicki, J. D.; White, A. F. *Kinetics of Water-rock Interaction*; Springer Science: New York, 2008.
- (47) Blum, A. E.; Yund, R. A.; Lasaga, A. C. *Geochim. Cosmochim. Acta* **1990**, *54*, 283.
- (48) Arvidson, R. S.; Ertan, I. E.; Amonette, J. E.; Luttge, A. *Geochim. Cosmochim. Acta* **2003**, *67*, 1623.
- (49) Cama, J.; Zhang, L.; Soler, J. M.; Giudici, G. D.; Arvidson, R. S.; Lüttge, A. *Geochim. Cosmochim. Acta* **2010**, *74*, 4298.
- (50) Cortés-Salazar, F.; Momotenko, D.; Girault, H. H.; Lesch, A.; Wittstock, G. *Anal. Chem.* **2011**, *83*, 1493.
- (51) Heinze, J. *Angew. Chem.* **1993**, *32*, 1268.
- (52) Forster, R. J. *Chem. Soc. Rev.* **1994**, *23*, 289.
- (53) Ford, D. C.; William, P. W. *Karst Geomorphology and Hydrology*; Unwin Hyman, 1989.
- (54) Van Rosmalen, G. M.; Daudey, P. J.; Marchée, W. G. J. *J. Cryst. Growth* **1981**, *52*, 801.
- (55) Alonso-Azcárate, J.; Bottrell, S. H.; Tritlla, J. *Chem. Geol.* **2001**, *174*, 389.
- (56) Alonso-Azcárate, J.; Bottrell, S. H.; Mas, J. R. *Chem. Geol.* **2006**, *234*, 46.
- (57) Bosbach, D.; Hochella Jr, M. F. *Chem. Geol.* **1996**, *132*, 227.
- (58) Christoffersen, J.; Christoffersen, M. R. *J. Cryst. Growth* **1976**, *35*, 79.
- (59) Jeschke, A. A.; Vosbeck, K.; Dreybrodt, W. *Geochim. Cosmochim. Acta* **2001**, *65*, 27.
- (60) Mbogoro, M. M.; Snowden, M. E.; Edwards, M. A.; Peruffo, M.; Unwin, P. R. *J. Phys. Chem. C* **2011**, *115*, 10147.
- (61) Colombani, J.; Bert, J. *Geochim. Cosmochim. Acta* **2007**, *71*, 1913.
- (62) Fan, C.; Teng, H. H. *Chem. Geol.* **2007**, *245*, 242.
- (63) Bosbach, D.; Jordan, D. G.; Rammensee, W. *Eur. J. Mineral.* **1995**, *7*, 267.
- (64) Bosbach, D.; Rammensee, W. *Geochim. Cosmochim. Acta* **1994**, *58*, 843.
- (65) Hall, C.; Cullen, D. C. *AIChE J.* **1996**, *42*, 232.
- (66) Vanysek, P. *CRC Handbook of Chemistry and Physics: Diffusion coefficients and ionic conductivities*; 91st ed.; CRC Press Taylor & Francis: Boca Raton, FL, 2010-2011.
- (67) Schofield, P. F.; Knight, K. S.; Stretton, I. C. *Am. Mineral.* **1996**, *81*, 847.
- (68) White, A. F.; Brantley, S. L. *Rev. Mineral.* **1995**, *31*, 1.
- (69) Luttge, A. *Am. Mineral.* **2005**, *90*, 1776.
- (70) Hartman, P.; Perdok, W. G. *Acta Cryst.* **1955**, *8*, 49.
- (71) Hartman, P.; Perdok, W. G. *Acta Cryst.* **1955**, *8*, 521.
- (72) Kowacz, M.; Putnis, A. *Geochim. Cosmochim. Acta* **2008**, *72*, 4476.
- (73) Ruiz-Agudo, E.; Kowacz, M.; Putnis, C. V.; Putnis, A. *Geochim. Cosmochim. Acta* **2010**, *74*, 1256.
- (74) Buchanan, A. S.; Heymann, E. *J. Coll. Sci.* **1949**, *4*, 137.
- (75) Titiz-Sargut, S.; Sayan, P.; Avci, B. *Cryst. Res. Technol.* **2007**, *42*, 119.
- (76) Olhoeft, G. R.; Johnson, G. R. In *Practical Handbook of Physical Properties of Minerals*; Carmichael, R. S., Ed.; CRC Press: Boca Raton, Florida, 1989.

- (77) Colombani, J. *Geochim. Cosmochim. Acta* **2008**, 72, 5634.

# Chapter 5

## Intrinsic Kinetics of Gypsum and Calcium Sulphate Anhydrite Dissolution: Surface Selective Studies Under Hydrodynamic Control and the Effect of Additives

### Abstract

In this chapter, the intrinsic dissolution activity of the basal (010) and edge (001) surfaces of gypsum; and polycrystalline calcium sulphate anhydrite ( $\text{CaSO}_4$ ) crystals has been investigated, under far from equilibrium conditions, via the channel flow cell (CFC) method with off-line inductively coupled plasma-mass spectrometry (ICP-MS) for the measurement of dissolved  $\text{Ca}^{2+}$  from the crystal surface. This approach allows measurements to be made over a wide range of flow rates, so that the importance of mass transport vs. surface kinetics can be elucidated. Complementary quantitative modelling of the dissolution process was carried out to complement experimental studies. linear rate law applied and intrinsic dissolution fluxes were deduced. The following dissolution fluxes,  $J_o = k_{diss} \times c_{eq}$  were measured, where  $k_{diss}$  is the dissolution rate constant and  $c_{eq}$  the calcium sulphate concentration in saturated solution:  $5.7 (\pm 1.4) \times 10^{-9}$  mol  $\text{cm}^{-2}$   $\text{s}^{-1}$  for basal plane gypsum and  $4.1 (\pm 0.7) \times 10^{-9}$  mol  $\text{cm}^{-2}$   $\text{s}^{-1}$  for calcium sulphate anhydrite. Edge (001) plane gypsum, under the experimental conditions applied, dissolved at a mass transport-controlled rate. The effects of l- and d-tartaric acid, and STMP as important potential additives of the dissolution process of basal plane gypsum were investigated. It was found that the tartaric acids had little effect but that STMP significantly retarded gypsum dissolution with  $J_o = 1.6 (\pm 0.6) \times 10^{-9}$  mol  $\text{cm}^{-2}$   $\text{s}^{-1}$  (5 mM STMP solution). The mode of action of STMP was further elucidated via etch pit morphology studies.

## **5.1. Introduction**

Among the rock forming minerals, gypsum ( $\text{CaSO}_4 \cdot 2\text{H}_2\text{O}$ ) and related calcium sulphate materials such as the hemi-hydrate ( $\text{CaSO}_4 \cdot 0.5\text{H}_2\text{O}$ ) and anhydrite ( $\text{CaSO}_4$ ), are abundant in nature, with extensive deposits underlying an estimated 25% of the global surface.<sup>1</sup>  $\text{CaSO}_4$  minerals play an important role in the evolution of karst systems,<sup>2</sup> and in numerous geochemical phenomena;<sup>3,4</sup> they are also utilised extensively in metallurgical processes,<sup>5</sup> and in construction and manufacturing.<sup>6,7</sup> Furthermore, the formation of these minerals causes significant scaling problems, particularly in petroleum technology.<sup>8,9</sup> Studies of dissolution/growth kinetics and mechanisms are pertinent to all these areas in order to develop knowledge and understanding of natural systems, and to optimize the use of  $\text{CaSO}_4$  minerals in technological applications.<sup>10-13</sup>

The dissolution of gypsum has been studied by many techniques, ranging from macroscopic kinetic measurements on particulate systems,<sup>14-17</sup> to high resolution microscopic studies using AFM.<sup>18-20</sup> A recent review by Colombani<sup>21</sup> sought to correlate various macroscopic kinetic measurements of gypsum dissolution in order to extract a unified surface dissolution rate, by estimating the likely mass transport rates associated with different techniques. An intrinsic *surface dissolution rate constant* into free solution (maximum undersaturation at the crystal/solution interface) was deduced to be  $J_o = 5 \pm 2 \times 10^{-9} \text{ mol cm}^{-2} \text{ s}^{-1}$ , as the intercept of a reciprocal rate – reciprocal mass transport plot. Some confidence in this assignment comes from the fact that the techniques surveyed included the RD method which delivers well-defined mass transport. However, in many cases, the techniques used previously have been characterised by

poorly defined and/or low mass transport conditions making it difficult to assign surface kinetics from individual studies. Furthermore, many previous investigations have employed polycrystalline material, so that different crystal faces, edges and corners are exposed to solution, which are likely to have different dissolution characteristics. To further improve our understanding of dissolution kinetics, surface-selective studies under well-defined mass transport conditions are imperative. Such studies are the focus of this chapter.

Calcium sulphate anhydrite dissolution has also been investigated, but not as extensively as gypsum. Because the solubility of gypsum is less than that of anhydrite,<sup>22</sup> reliable anhydrite dissolution data may only be obtained under far from equilibrium conditions where the concentration of dissolved products near the crystal surface, is below the saturation level with respect to gypsum.<sup>23</sup> Higher surface concentration may lead to precipitation of gypsum on the surface of the dissolving anhydrite crystal, thereby forming a protective layer which inhibits further dissolution.<sup>3,23</sup> An early RD study on polycrystalline anhydrite found a rather high intrinsic dissolution flux of  $J_o = 2 \pm 1 \times 10^{-8} \text{ mol cm}^{-2} \text{ s}^{-1}$ .<sup>15</sup> However, subsequent free drift batch investigations on particulates<sup>23</sup> deduced much lower rates,  $J_o = 5 \pm 1 \times 10^{-9} \text{ mol cm}^{-2} \text{ s}^{-1}$  which have been corroborated by other studies.<sup>1</sup>

A further important aspect of crystal dissolution is the role of additives. This is of particular relevance for  $\text{CaSO}_4$  minerals used in construction, where additives are used to passivate dissolution, so as to retard physico-chemical deterioration by processes such as humid creep, caused by environmental factors such as rain water and atmospheric pollutants.<sup>24,25</sup> However, in contrast to calcium carbonate minerals, for example, where the role of additives has

been explored extensively,<sup>26-34</sup> relatively few gypsum dissolution studies have considered the influence of additives. Such studies would be valuable to elucidate the effect of additives on the durability and versatility of CaSO<sub>4</sub>-based materials,<sup>35,36</sup> and so a further aspect of this chapter is to examine the mode of action of key additives on gypsum dissolution.

As highlighted herein, to understand mineral/liquid reaction kinetics, experimental techniques need to be able to quantitatively separate mass transport and surface kinetic effects<sup>37,38</sup> and ideally allow the study of well-defined surfaces.

Herein, we couple the CFC technique with off-line ICP-MS for the measurement of dissolved Ca<sup>2+</sup> from the crystal surface, collected from the CFC effluent, over a wide range of flow rates. This is effective because of the miniaturised flow cell unit and short wash-out time of the cell (*vide infra*). For the purposes of quantitative modelling, we formulate convective-diffusive equations for mass transport in the CFC, coupled to a boundary condition for the crystal surface, which describes the dissolution process. In this way, we are able to predict the outlet Ca<sup>2+</sup> concentration for analysis of experimental data. Using this approach we provide intrinsic rates for the dissolution of the basal cleavage (010) and edge (001) plane surfaces of gypsum, in order to elucidate any differences in magnitude for the first time. Furthermore, we elucidate the effect of key additives on dissolution from basal plane gypsum, in order to identify any kinetic influences and morphological effects. Finally, we investigate the dissolution of natural polycrystalline anhydrite, to resolve the discrepancy in kinetics highlighted above, and to further demonstrate the capability of the methodology.

## 5.2. Experimental

Most experiments were run in ultrapure water, but some measurements were made in 5 mM solutions of the additives of interest (Figure 5.1); these were STMP, *d*-tartaric acid and *l*-tartaric acid (all from Sigma). In addition, a solution of 0.03 M KNO<sub>3</sub> (Sigma) was used as an ionic strength match in some experiments for comparison to the 5 mM STMP solution. Table 5.1 summarizes all additive solutions used, with the input concentrations, and resulting pH and ionic strength values.

*Table 5.1: Additives used for CFC dissolution studies on basal plane gypsum crystal*

<b>Additive</b>	<b>Concentration (mM)</b>	<b>pH</b>	<b>Ionic strength (mM)</b>
<i>l</i> -tartaric acid	5	2.71	19
<i>d</i> -tartaric acid	5	2.70	19
STMP	5	5.88	30
KNO <sub>3</sub>	30	5.63	30

### **5.3. Mass Transport and Kinetic Modelling**

Numerical simulations were performed on a Dell Intel core™ 2 Quad 2.49 GHz computer equipped with 8GB of RAM and running Windows XP Professional X64 bit 2003 edition. Modelling was performed using the commercial finite element modelling package Comsol Multiphysics 3.5a (Comsol AB, Sweden), using the Matlab interface (Release 2009b) (MathWorks Inc., Cambridge, UK). Simulations were carried out with >51,000 triangular mesh elements. Mesh resolution was defined to be finest around the bottom plane of the channel, i.e. in the vicinity of the surface of the crystal substrate where the concentration gradient was steepest. Simulations with finer meshes were carried out (not reported) to confirm the mesh was sufficiently fine to ensure the predicted solutions were accurate (better than 0.01% variance).

#### **5.3.1 Theory**

The channel was simulated as a 2D cross-section along the channel length ( $l$ ) as illustrated in Figure 5.1(a). Because  $w \gg h$ , edge effects in the  $w$  direction were neglected, to render a 3D model unnecessary.

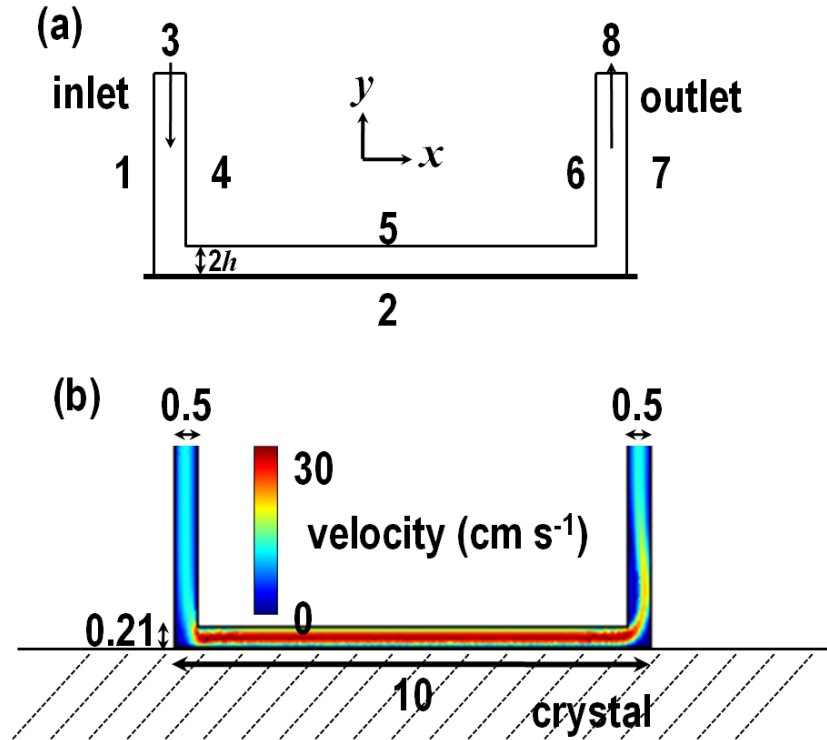


Figure 5.1: 2D representation of (a) the channel geometry used for finite element modelling simulations where the numbers represent the boundaries (edges) used in simulations (not to scale) and are described by equations 5.3 – 5.5, and (b) the velocity profile of solution within the flow cell for the case of  $V_f = 0.167 \text{ cm}^3 \text{ s}^{-1}$ . The cell dimensions in (b) are in mm and were used throughout.

### 5.3.2 Hydrodynamics

The incompressible Navier-Stokes equations for momentum balance (eq 1) and continuity (eq 2) were solved under steady-state conditions for the cross-sectional domain shown in Figure 5.1(a).

$$\rho \mathbf{V} \cdot \nabla \mathbf{V} = -\nabla p + \eta \nabla^2 \mathbf{V} \quad (5.1)$$

$$\nabla \cdot \mathbf{V} = 0 \quad (5.2)$$

where  $\rho$  is the density of the solution ( $1.00 \text{ g cm}^{-3}$  was used, as for water),  $\mathbf{V}$  is the velocity vector (with components  $u$  and  $v$  in the  $x$  and  $y$  directions, respectively),  $p$  is the pressure,  $\eta$  is the dynamic viscosity assumed to be 1.00

mPa s,  $\nabla$  is the vector differential operator and  $\nabla^2$  is the vector laplacian operator.

The hydrodynamic behaviour within the channel cell, as described by the incompressible Navier-Stokes equations, was solved for the following boundary conditions, where the boundaries are defined in Figure 5-3(a):

boundaries 1, 2 and 4 – 7: 
$$u = 0, v = 0 \quad (5.3)$$

boundary 3: 
$$u = 0, v = -\frac{v_f}{wx_{ch}} \quad (5.4)$$

boundary 8: 
$$n \cdot \eta \nabla^2 \mathbf{V} = 0 \quad (5.5)$$

where  $x_{ch}$  is the channel height at the inlet (length of boundary 3, 0.5 mm),  $n$  is the vector normal to a particular boundary. The condition on boundary 3 (eq 4) is plug flow into the cell.

### 5.3.3 Convective-Diffusive Mass Transport

Once the velocity components  $u$  and  $v$  within the CFC had been determined, the local velocity vectors were used in the solution of the convective-diffusion equations, to predict the concentration distribution in the cell, and especially in the region of the outlet. The convective-diffusion equation was solved under steady-state conditions:

$$D_i \nabla^2 c_i - \mathbf{V} \cdot \nabla c_i = 0 \quad (5.6)$$

where  $D_i$  is the diffusion coefficient of the species of interest,  $i$ , and  $c_i$  is the concentration of species  $i$ . Since the two dissolving species have similar diffusion coefficients ( $0.792 \times 10^{-5} \text{ cm}^2 \text{ s}^{-1}$  for  $\text{Ca}^{2+}$  at infinite dilution), the mean diffusion coefficient was used for the purposes of simulations, thereby facilitating the solution for one species only. This is appropriate given that the

studies were for stoichiometric dissolution into a medium comprising little or no additional electrolyte. The following boundary conditions applied to the flow cell:

$$\text{boundaries 1, 4 - 7:} \quad \mathbf{n} \cdot \mathbf{N} = 0 \quad (5.7)$$

$$\text{boundary 2:} \quad \mathbf{n} \cdot \mathbf{N} = k_{diss} (c_{eq} - c_i) \quad (5.8)$$

$$\text{boundary 3:} \quad c_i = 0 \quad (5.9)$$

$$\text{boundary 8:} \quad \mathbf{n} \cdot (-D_i \nabla c_i) = 0 \quad (5.10)$$

where  $\mathbf{n}$  is the vector normal to a particular boundary,  $\mathbf{N}$  is the outward vector flux of species,  $k_{diss}$  is a heterogeneous rate constant and  $c_{eq}$  is the equilibrium concentration for the solid/saturated solution (free  $\text{Ca}^{2+}$ ), when bulk ionic strength effects due to any added dissolved salts are taken into account. Herein, we used  $c_{eq} = 11$  mM (gypsum) and 16 mM (calcium sulphate anhydrite) as calculated by MINEQL<sup>+</sup>; the gypsum value is close to that deduced from experiments.<sup>15</sup> For gypsum experiments with 0.03 M added electrolyte  $c_{eq} = 14$  mM was used. Mass transport across boundary 8 is due to convection only. Because the dissolution fluxes for most of the systems of interest were relatively low, we did not model any spatial variations in ionic strength as these effects would be relatively minor. For simplicity, we chose a first order rate law (eq 8): this has been used previously for gypsum and related materials<sup>3,14,28</sup> and, further, was reasonable because the reaction was generally very far from equilibrium under the conditions of the experiments.

## **5.4. Results and Discussion**

### **5.4.1 Insights from Simulations**

The finite element simulations provide information on the processes occurring in the cell. In particular, the approach described yields: (i) the hydrodynamic behaviour within the CFC chamber, from which velocity profiles, in regions of interest, can be extracted; (ii) concentration profiles of dissolved species within the cell which informs on the kinetic/mass transport regime; and (iii) the flow rate-dependent outlet concentration which is the variable used to analyze experimental data. We use the simulations to highlight briefly some of the main features of the techniques for the case of gypsum ( $C_{eq} = 11$  mM). Figure 5.1(b) shows a typical example of the velocity profile of solution in the flow cell ( $2h = 0.21$  mm) at  $V_f = 0.1649$  cm<sup>3</sup> s<sup>-1</sup>. A steady laminar Poiseuille profile is established and maintained along the channel length, after a short lead-in length.

Figure 5.2 shows: (a) a typical concentration profile in the CFC for  $V_f = 0.0083$  cm<sup>3</sup> s<sup>-1</sup> and  $k_{diss} = 1 \times 10^{-3}$  cm s<sup>-1</sup> and (b) plots of the concentration of the dissolved species at the crystal/solution interface along the length of the channel for  $V_f = 0.0083$  cm<sup>3</sup> s<sup>-1</sup> and  $0.1649$  cm<sup>3</sup> s<sup>-1</sup>, which correspond to the lower and higher  $V_f$  limits of those used herein. The  $k_{diss}$  value is typical of that found in the experimental studies (*vide infra*). A consequence of the high mass transport rates that can be generated in the channel is that the concentration boundary layer above the dissolving substrate is relatively thin, allowing fast surface kinetics to be investigated. This is evident from Figure 5.2(b) which shows that the interfacial concentration is considerably lower than the equilibrium value at the extreme limits of typical flow rates, indicating

substantial surface kinetic control of the reaction for these parameters. The non-uniform concentration profiles along the channel length are a consequence of the non-uniform accessibility of the channel system<sup>39,40</sup> between 0.5 and 9.5 mm, coupled with stagnation zones which develop at the chamber edges. This leads to higher interfacial concentration values between 0 – 0.5 mm (upstream portion of the crystal) and 9.5 – 10 mm (downstream portion). However, these stagnation zones make a very minor contribution to the total surface flux from the entire exposed crystal.

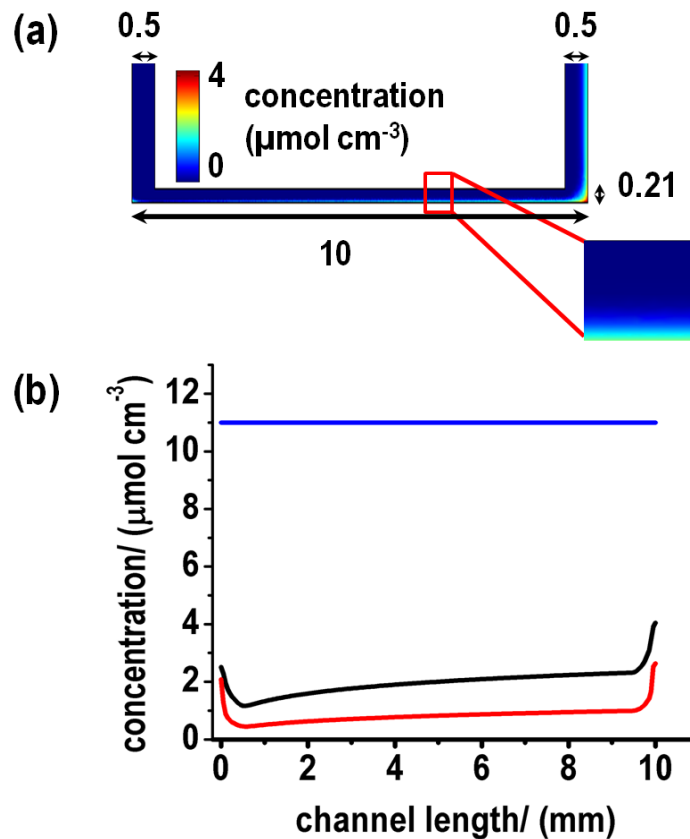


Figure 5.2: Illustration of (a) the CFC cross-section depicting the concentration for  $V_f = 0.0083 \text{ cm}^3 \text{ s}^{-1}$  and  $k_{diss} = 1 \times 10^{-3} \text{ cm s}^{-1}$  where dimensions are in mm, and (b) the corresponding interfacial concentration along the length of the channel for  $V_f = 0.0083 \text{ cm}^3 \text{ s}^{-1}$  (black) and  $V_f = 0.1649 \text{ cm}^3 \text{ s}^{-1}$  (red), with an applied rate constant  $k_{diss} = 1 \times 10^{-3} \text{ cm s}^{-1}$  in each case. For comparison, the saturated solution concentration is shown (blue).

Figure 5.3 shows 3D plots of the outlet concentration (a) and average surface flux (b) as a function of the kinetic constant,  $k_{diss}$ , and flow rate,  $V_f$ . For any particular flow rate, an increase in  $k_{diss}$  results in an increase in the surface flux and outlet concentration, as a consequence of increasing generation of dissolution products from the crystal surface up to a maximum ( $k_{diss}$ -independent value) where the reaction becomes transport-controlled. In addition, it can be seen that for any rate constant, the highest outlet concentration is predicted at low flow rates, essentially because the duration of interaction between the crystal surface and solution in the cell is then longer, thereby allowing dissolution products to accumulate more readily in the solution. In the regime  $k_{diss} > 0.1 \text{ cm s}^{-1}$ , for the range of  $V_f$  shown, the reaction becomes transport-limited. Below this value, surface kinetic determination is possible.

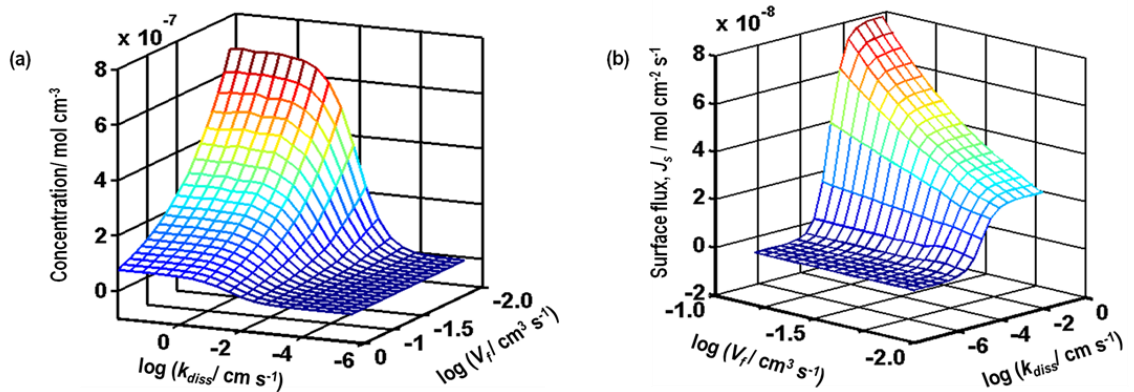


Figure 5.3: (a) Simulated outlet concentrations and (b) mean surface flux,  $J_s$ , as a function of  $k_{diss}$  and  $V_f$ . The channel cell was characterised by the parameters shown in Figure 5.1(b).

## **5.4.2 Dissolution Kinetics**

### **Surface Analysis**

WLI measurements were made to determine the surface topography of the crystal surfaces before and after CFC studies, with the aim of determining the specific surface area of the crystal surface exposed to the solution. This was primarily to confirm that the surface area was constant over the duration of a CFC experiment and to determine the roughness factor ( $\lambda$ ) with which flux values predicted by simulations could be normalised to allow comparison between different materials and to obtain intrinsic dissolution rates.

Figure 5.4 depicts typical DIC micrographs of the basal plane gypsum surface after etching in ultrapure H<sub>2</sub>O, for: (a) 90 s, (b) 10 min, (c) 30 min; and (d) a WLI micrograph after a 30 min etch. The micrographs clearly show an alteration in surface topography, from early times in the dissolution process (Figure 5.4(a)), where small etch features are isolated on the (010) cleavage surface. With time, these features grow and achieve complete coalescence by ~ 30 min (Figure 5.4(c)) and the surface topology and  $\lambda$  essentially remains similar for times thereafter.  $\lambda$  was found to be in the range of 1.1-1.2, 1.9- 3.3 and 1.6-4.4 for (010) gypsum, edge plane gypsum and anhydrite, respectively. The highest  $\lambda$  value (roughest sample used for experiments) yielded an rms roughness value of 4.5  $\mu\text{m}$  constituting ~2.3 % of the channel height ( $2h$ ) which was considered unlikely to disrupt the cell hydrodynamics describes above, as evidenced by the fact that electrodes deployed in channels are only slightly smoother than this and conform well to predictions for a smooth surface.<sup>39,40</sup> In addition,  $\lambda$  values for each sample were within  $\pm 10\%$  when examined before and after CFC studies.

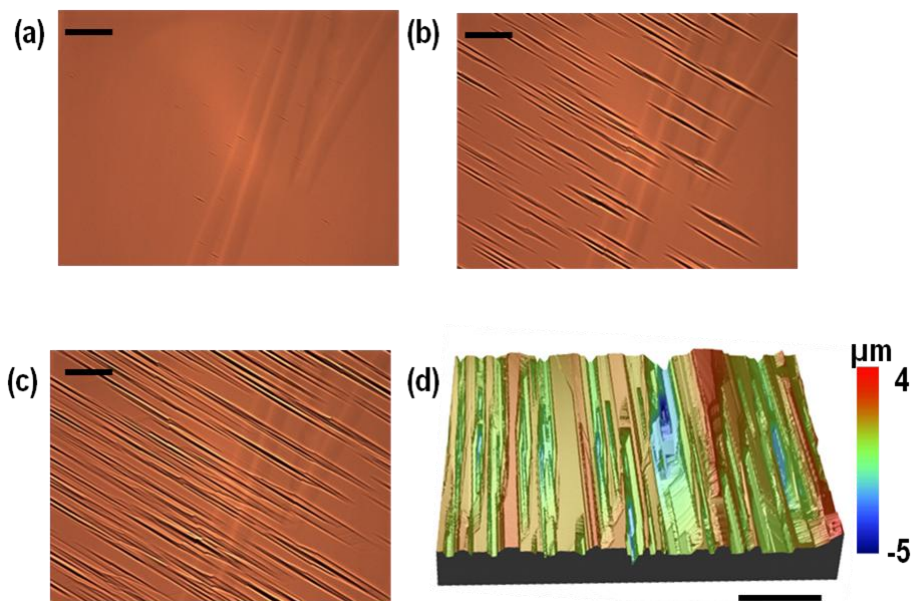


Figure 5.4: Typical DIC micrographs (scale bars 100  $\mu\text{m}$ ) of the (010) cleaved gypsum surface after etching in pure  $\text{H}_2\text{O}$  for (a) 90 s, (b) 10 min, (c) 30 min, and (d) the corresponding WLI micrograph after a 30 min etch, where the scale bar is 30  $\mu\text{m}$ .

### **CFC Dissolution Measurements**

As mentioned above, the dissolution reaction was monitored via flow rate-dependent off-line ICP-MS analysis on CFC effluent for  $\text{Ca}^{2+}$  at each flow rate. At least four replicate runs were made for each flow rate. These data were then analysed, using the model described, to obtain values for the heterogeneous rate constant ( $k_{diss}$ ) for the dissolution of each substrate.

Figure 5.5 shows typical experimental data, of outlet  $\text{Ca}^{2+}$  concentration as a function of flow rate for the three different crystal substrates. The error bars in this plot and that in Figure 5.6 reflect 2 standard deviations calculated from four replicate runs from ICP-MS data at each flow rate shown. The solid lines represent the best fit of  $k_{diss}$  for each substrate, as predicted from simulations. The etched surface of basal plane gypsum exhibited the lowest value of  $k_{diss} = 6.0 (\pm 1.5) \times 10^{-4} \text{ cm s}^{-1}$  while that of anhydrite was slightly higher at  $k_{diss} = 7.8$

$(\pm 1.3) \times 10^{-4} \text{ cm s}^{-1}$ . The excellent agreement between experiments and predictions from simulations observed here, particularly in the high flow rate range, justifies the choice of a first-order rate law for basal plane gypsum and anhydrite dissolution in pure  $\text{H}_2\text{O}$ . At lower flow rate, the model tends to overestimate the outlet concentrations. Under these conditions, the interfacial concentrations move closer to equilibrium and the small deviation between theory and experiment may indicate a change in the reaction order. Notably, edge plane gypsum yielded a rate constant of  $k_{diss} > 0.1 \text{ cm s}^{-1}$  indicating a mass-transport controlled dissolution process under the experimental conditions.

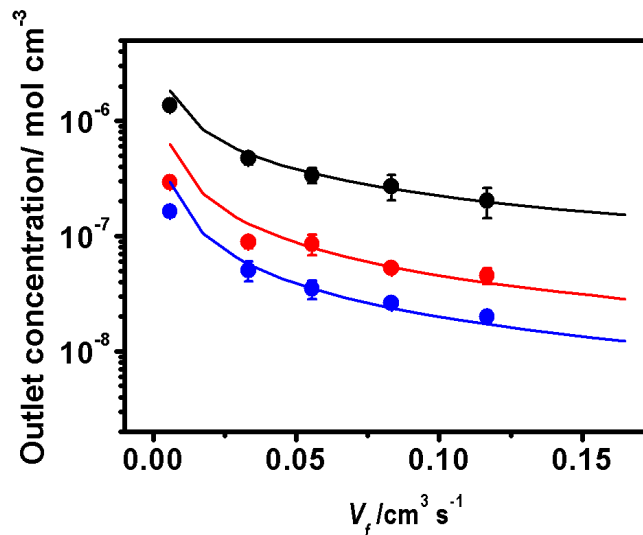


Figure 5.5: Cell outlet concentration as a function of flow rate for the dissolution of etched basal plane gypsum (red), edge plane gypsum (black) and anhydrite (blue). The solid lines correspond to the best fits to the model with rate constant,  $k_{diss}$  ( $\text{cm s}^{-1}$ ) of  $6.0 (\pm 1.5) \times 10^{-4} \text{ cm s}^{-1}$ ,  $> 0.1 \text{ cm s}^{-1}$  and  $7.8 (\pm 1.3) \times 10^{-4} \text{ cm s}^{-1}$ , for basal plane gypsum, edge plane gypsum ( $c_{eq} = 11 \text{ mM}$  for gypsum) and anhydrite ( $c_{eq} = 16 \text{ mM}$ ) respectively. The simulation used other parameters stated in the text.

With these rate constants, the associated intrinsic dissolution fluxes  $J_o$  ( $\text{mol cm}^{-2} \text{ s}^{-1}$ ) =  $k_{diss} \times c_{eq}$  taking into account  $\lambda$  in the calculation of the area, were deduced to be  $5.7 (\pm 1.4) \times 10^{-9} \text{ mol cm}^{-2} \text{ s}^{-1}$  and  $4.0 (\pm 0.7) \times 10^{-9} \text{ mol cm}^{-2}$

$s^{-1}$  for basal plane gypsum (010) and anhydrite, respectively. The kinetics found for gypsum compare favourably with the values deduced by Colombani<sup>21</sup> of  $J_o = 5 (\pm 2) \times 10^{-9} \text{ mol cm}^{-2} \text{ s}^{-1}$ . The intrinsic dissolution flux for anhydrite crystal compares well with recent values from Jeschke and Dreybrodt<sup>23</sup> who obtained  $J_o = 5 (\pm 1) \times 10^{-9} \text{ mol cm}^{-2} \text{ s}^{-1}$ . However, these values are much smaller than the value of  $J_o = 2 \pm 1 \times 10^{-8} \text{ mol cm}^{-2} \text{ s}^{-1}$  deduced from anhydrite polycrystalline pellets.<sup>71</sup> It is important to point out that we have analysed natural polycrystalline anhydrite samples which have been deposited over geological time scales such that the crystalline deposits are compacted to an extent that porosity is negligible. In contrast, anhydrite pellets such as those used in some previous studies<sup>71</sup> are typically formed by dehydrating gypsum pellets, a process which exposes the sample to thermal shock, possibly further weakening sample structure. This typically results in samples with high specific surface areas which would naturally produce higher dissolution fluxes defined in terms of the geometric area of the sample.

It is further important to note that, with the CFC method, we eliminate the possibility of surface concentrations (from generation of dissolution products) approaching the gypsum saturation point, by probing anhydrite dissolution under far from equilibrium conditions via the high rates of mass transport that can be generated.

### **Effect of Additives**

The influence of key additives on gypsum dissolution were considered next. Figure 5.6 shows plots of outlet concentration as a function of flow rate for etched basal plane gypsum in the presence of STMP, l-tartaric acid and d-tartaric acid, with H<sub>2</sub>O also shown. These additives were chosen because of

their extensive use as inhibitors of humid creep, in the production of  $\text{CaSO}_4$  based materials.<sup>35,36</sup> In each case, there is good agreement between the experimental data and the first-order model proposed (which takes into account the ionic strengths of the different solutions in calculating  $c_{eq}$ , Table 5.1). Rate constants for dissolution in the presence of d-tartaric and l-tartaric acids were found to be similar (within experimental error) and close to that for pure  $\text{H}_2\text{O}$ , with  $k_{diss} = 7.3 (\pm 2.0) \times 10^{-4} \text{ cm s}^{-1}$ , which shows that d- and l-tartaric acid have relatively little effect on gypsum dissolution under the experimental conditions. However, in the presence of STMP, the rate constant was much lower,  $k_{diss} = 1.3 (\pm 0.5) \times 10^{-4} \text{ cm s}^{-1}$ , indicating a significant retardation of the dissolution process.

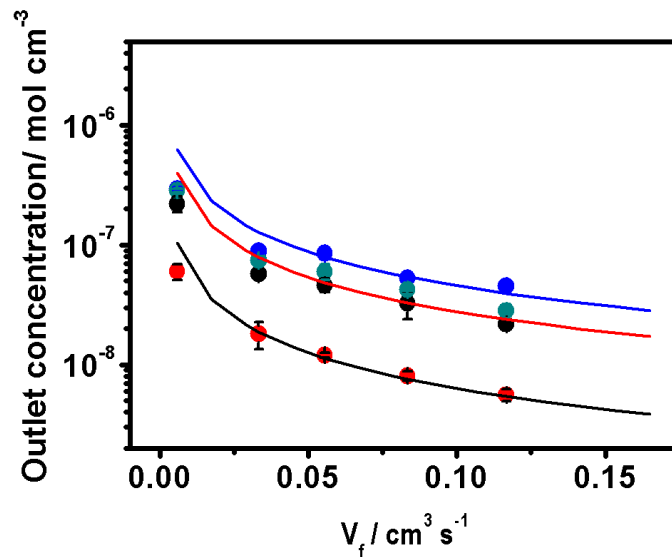


Figure 5.6: Outlet concentration as a function of flow rate for dissolution of the etched basal plane of gypsum in 5 mM solutions of l-tartaric acid (blue points), d-tartaric acid (green points), and STMP (black) and in pure  $\text{H}_2\text{O}$  (red). The solid lines correspond to the best fit rate constant,  $k_{diss}$  ( $\text{cm s}^{-1}$ ) predicted by simulations with values of  $6.0 (\pm 1.5) \times 10^{-4} \text{ cm s}^{-1}$  and  $1.3 (\pm 0.5) \times 10^{-4} \text{ cm s}^{-1}$  for pure  $\text{H}_2\text{O}$  and STMP, respectively, while l-tartaric and d-tartaric acids exhibit a similar rate constant of  $7.3 (\pm 2.0) \times 10^{-4} \text{ cm s}^{-1}$  (blue solid line).

To elucidate and explain the mode of action of STMP on the process of gypsum dissolution, we carried out etch pits studies for dissolution in quiescent solution for a period of 20 min. By careful cleaving along the (010) gypsum plane, mirror surfaces were produced. One half, was etched in STMP while the other was etched in ultrapure H<sub>2</sub>O. There is almost complete dissociation of STMP, yielding a solution ionic strength *ca.* 0.03 M. In order to investigate ionic strength effects, etching was also carried out in 0.03 M KNO<sub>3</sub>.

Figure 5.7 shows DIC micrographs of the resulting etch pits, where (a) is the surface after etching in H<sub>2</sub>O, (b) the mirror surface when etched in STMP, (c) superimposition of (a) and (b), and (d) a gypsum surface after etching in KNO<sub>3</sub>. When the two microstructures in (a) and (b) are superimposed (c), it is clear that there is exact correspondence between the positions of etch pits, and therefore, both pit types emerge from the same defect sites which presumably run through the crystal. Notably, however, there is a drastic difference in the pit sizes, with STMP retarding dissolution compared to water. This effect is even more striking when one considers that the higher ionic strength of the STMP solution would be expected to promote dissolution if it simple acted as an inert salt, as evidenced by the KNO<sub>3</sub> data (Figure 5.7(d)).

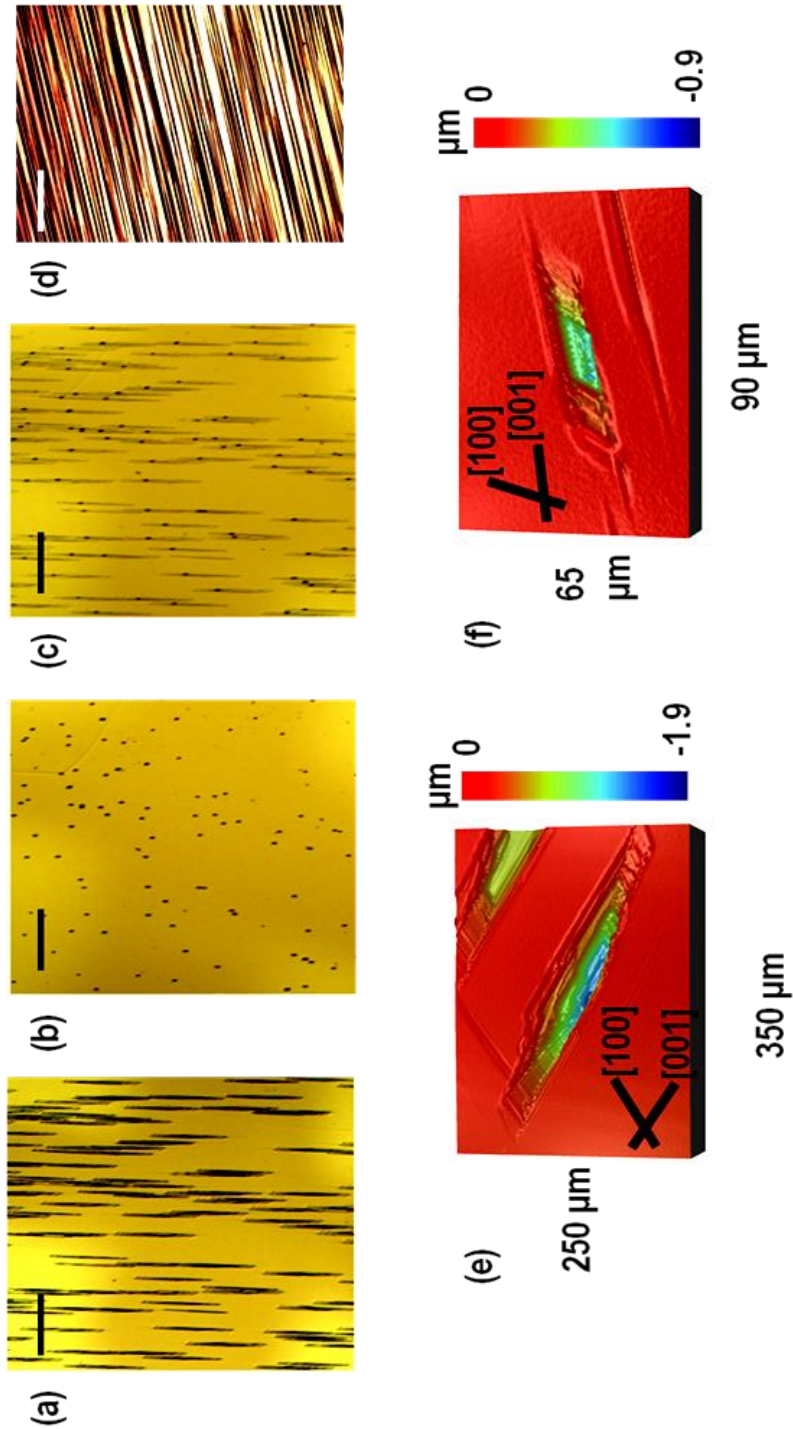


Figure 5.7: DIC micrographs of the (010) surface of gypsum (matched halves) after a 20 min etch in (a)  $H_2O$  and (b) 5 mM STMP. The two surfaces (a and b) are superimposed in (c) to show correspondence of etch pits on the surfaces. A cleaved gypsum surface etched for 20 min in 0.03 M  $KNO_3$  is shown in (d) for comparison. The scale bars are 300  $\mu m$ . WLI micrographs of pit morphology after etching for 20 min in (e)  $H_2O$  and (f) 5 mM STMP are also shown. The main crystallographic directions with respect to the etch pits formed on the (010) surface are indicated and the [010] direction normal to the surface.

Figure 5.7 also shows isolated pits that result from etching in water (e) and STMP (f). In the case of H<sub>2</sub>O, the pits are irregular hexagons with two parallel edges aligned along the [001] and [100] directions and one poorly defined edge (Figure 5.7(e)); see Figure 1.1 for the gypsum unit cell. The pits were found to exhibit typical dimensions of 350 ±30 μm, 62 ±14 μm and 1.9 ±0.5 μm in [001], [100] and [010] directions, respectively, after etching for 20 min. In contrast, etching in the presence of STMP produced pits with the shape of a parallelogram, laterally embracing the [001] and [100] directions only (Figure 5.7(f)). The etch pits were also relatively small compared to those produced when etching in pure water, with typical dimensions of 90 ±10 μm, 36 ±6 μm and 1.4 ±0.5 μm in [001], [100] and [010] directions, respectively. The elongated etch pit morphologies indicate preferential dissolution in the [001] direction relative to the [100] etching in pure H<sub>2</sub>O. Indeed much faster dissolution along the [001] direction relative to the [100] direction may be responsible for the development of the irregular pit edge (Figure 5.7(e)). In the presence of STMP, dissolution in [001] and [100] directions were retarded to different extents so that the rates became closer in magnitude resulting in the parallelogram pit shape observed. Since STMP dissociates to P<sub>3</sub>O<sub>9</sub><sup>3-</sup>,<sup>41,42</sup> under the experimental conditions, it is likely that STMP will have a binding affinity with surface calcium ion sites, inhibiting dissolution. The anion has a chair configuration with the phosphate groups facing outwards from the ring, giving it the capacity to adsorb onto several positively charged sites on the crystal surface and form surface complexes.<sup>43,44</sup>

For both etchants (H<sub>2</sub>O and STMP), dissolution in the [010] direction (etch pit depth) was much slower than in the other directions analysed. However, the

values obtained with and without STMP were similar, indicating little effect of STMP on dissolution in this direction. Dissolution in the [010] direction involves periodic removal of the water layer interspaced between CaSO<sub>4</sub> bilayers in the gypsum crystal. The fact that STMP has little influence suggests that detachment of the water layer may be rate-limiting in this direction.

## **5.5. Conclusions**

The dissolution kinetics of gypsum and anhydrite have been obtained and analysed via the CFC method, coupled with off-line ICP-MS for the measurement of dissolved Ca<sup>2+</sup> from the crystal surface. It has been possible to distinguish between the dissolution kinetics for the basal (010) and edge plane (001) surfaces of gypsum: radically different dissolution characteristics have been observed. The basal surface exhibited an intrinsic flux,  $J_o = 5.7 (\pm 1.4) \times 10^{-9}$  mol cm<sup>-2</sup> s<sup>-1</sup> into pure water ( $k_{diss} = 6.0 (\pm 1.5) \times 10^{-4}$  cm s<sup>-1</sup>), whereas the edge plane exhibited high rate constant values,  $k_{diss} > 0.1$  cm s<sup>-1</sup> indicating a transport-controlled process under the experimental conditions applied. Anhydrite crystals, exhibited fluxes of  $J_o = 4.0 (\pm 0.7) \times 10^{-9}$  mol cm<sup>-2</sup> s<sup>-1</sup> into pure water ( $k_{diss} = 7.8 (\pm 1.3) \times 10^{-4}$  cm s<sup>-1</sup>).

The effect of additives on dissolution of the basal gypsum surface considered molecules which have been used industrially as inhibitors of humid creep in CaSO<sub>4</sub>-based building materials. It was observed that tartaric acid (d- and l-) had little influence on dissolution kinetics with rates similar to those observed when dissolution was carried out in pure water. In the presence of STMP, dissolution rates were much lower,  $J_o = 1.6 (\pm 0.6) \times 10^{-9}$  mol cm<sup>-2</sup> s<sup>-1</sup> ( $k_{diss} = 1.3 (\pm 0.5) \times 10^{-4}$  cm s<sup>-1</sup>), despite the high ionic strength associated with the

additive which would be expected to promote dissolution (salting-in). Etching studies revealed that STMP significantly inhibits gypsum dissolution across the basal surface, but has a lower inhibitory effect in the [010] direction (normal to the basal surface). The mode of action is likely to involve surface complexation of SMTP anions on the crystal surface. The lack of any significant effect in the [010] tentatively suggests that the loss of the water layer may be the rate limiting process in this direction for which STMP would have little influence.

The studies herein illustrate how the CFC method is particularly powerful in elucidating surface kinetics and the role of mass transport in the interfacial processes. The methodology is flexible and allows the study of particular crystal faces and the introduction of inhibitors. When coupled with simple etching methods, one can obtain a good level of information on kinetics, mechanisms and the mode of action of inhibitors on dissolution.

## References

- (1) Ford, D. C.; Williams, P. W. *Karst hydrogeology and geomorphology*; John Wiley & Sons, 2007.
- (2) Klimchouk, A.; Andrejchuk, V. *international Journal of Speleology* 1996, 25, 145.
- (3) Klimchouk, A. *International Journal of Speleology* 1996, 25, 9.
- (4) Bosbach, D.; Junta-Rosso, J. L.; Becker, U.; Hochella Jr, M. F. *Geochim. Cosmochim. Acta* 1996, 60, 3295.
- (5) Van Rosmalen, G. M.; Daudey, P. J.; Marchée, W. G. J. *J. Cryst. Growth* 1981, 52, 801.
- (6) Livingston, R.; Wolde-Tinsae, A.; Chaturbahai, A. *Comput. Mech.* 1991, 1, 157.
- (7) Charola, A. E.; Puhlinger, J.; Steiger, M. *Comput. Mech. Publ.* 2007, 1, 157.
- (8) Cowan, J. C.; Weintritt, D. J. *Water-formed Scale Deposits*; Gulf Publishing Company, 1976.
- (9) Vetter, O. J. G.; Philips, R. C. *J. Petrol. Technol.* 1970, 22, 1299.
- (10) Lasaga, A. C.; Blum, A. E. *Geochim. Cosmochim. Acta* 1986, 50, 2363.
- (11) Schott, J.; Pokrovsky, O. S.; Oelkers, E. *Rev. Mineral.* 2009, 70, 207.
- (12) Lasaga, A. C.; Luetge, A. *Eur. J. Mineral.* 2003, 15, 603.
- (13) Lüttge, A. *J. Electron Spectrosc. Relat. Phenom.* 2006, 150, 248.
- (14) Liu, S.-T.; Nancollas, G. H. *J. Inorg. Nucl. Chem.* 1971, 33, 2311.
- (15) Barton, A. F. M.; Wilde, N. M. *Transactions of the Faraday Society* 1971, 67, 3590.
- (16) Singh, H.; Bajwa, M. *Soil Research* 1990, 28, 947.
- (17) Svensson, U.; Dreybrodt, W. *Chem. Geol.* 1992, 100, 129.
- (18) Bosbach, D.; Rammensee, W. *Geochim. Cosmochim. Acta* 1994, 58, 843.
- (19) Bosbach, D.; Jordan, G.; Rammensee, W. *Eur. J. Mineral.* 1995, 7, 267.
- (20) Fan, C.; Teng, H. H. *Chem. Geol.* 2007, 245, 242.
- (21) Colombani, J. *Geochim. Cosmochim. Acta* 2008, 72, 5634.
- (22) Vanysek, P. *CRC Handbook of Chemistry and Physics: Diffusion coefficients and ionic conductivities*; 91st ed.; CRC Press Taylor & Francis: Boca Raton, FL, 2010-2011.
- (23) Jeschke, A. A.; Dreybrodt, W. *Chem. Geol.* 2002, 192, 183.
- (24) Coquard, P.; Boistelle, R. *Int. J. Rock Mech. Min.* 1994, 31, 517.
- (25) Gartner, E. M. *Cem. Concr. Res.* 2009, 39, 289.
- (26) Orme, C. A.; Noy, A.; Wierzbicki, A.; McBride, M. T.; Grantham, M.; Teng, H. H.; Dove, P. M.; DeYoreo, J. J. *Nature* 2001, 411, 775.
- (27) Morse, J. W.; Arvidson, R. S. *Earth-Sci. Rev.* 2002, 58, 51.
- (28) Arvidson, R. S.; Collier, M.; Davis, K. J.; Vinson, M. D.; Amonette, J. E.; Lüttge, A. *Geochim. Cosmochim. Acta* 2006, 70, 583.
- (29) Vavouraki, A. I.; Putnis, C. V.; Putnis, A.; Koutsoukos, P. G. *Chem. Geol.* 2008, 253, 243.
- (30) Ruiz-Agudo, E.; Kowacz, M.; Putnis, C. V.; Putnis, A. *Geochim. Cosmochim. Acta* 2010, 74, 1256.
- (31) Freij, S. J.; Godelitsas, A.; Putnis, A. *J. Cryst. Growth* 2005, 273, 535.
- (32) Gledhill, D. K.; Morse, J. W. *Geochim. Cosmochim. Acta* 2006, 70, 5802.
- (33) Harstad, A. O.; Stipp, S. L. S. *Geochim. Cosmochim. Acta* 2007, 71, 56.
- (34) Xu, M.; Higgins, S. R. *Geochim. Cosmochim. Acta* 2011, 75, 719.
- (35) Arese, R.; Martin, D.; Rigaudon, M. 2003, *Process for reducing creep in a gypsum plaster-based element, gypsum plaster-based composition and method for making a gypsum plaster-based element with reduced creep. US, Patent 2006/0048680*
- (36) Yu, Q.; Sucech, S.; Groza, B.; Mlinac, R.; Jones, F.; Boehnert, F. U.S., 2003.
- (37) Unwin, P. R.; Macpherson, J. V. *Chem. Soc. Rev.* 1995, 24, 109.
- (38) Macpherson, J. V.; Unwin, P. R. *J. Chem. Soc., Faraday Trans.* 1993, 89, 1883.

- (39) Compton, R. G.; Unwin, P. R. *J. Electroanal. Chem.* 1986, 205, 1.
- (40) Compton, R. G.; Pilkington, M. B. G.; Stearn, G. M.; Unwin, P. R. *J. Electroanal. Chem.* 1987, 238, 43.
- (41) Jones, H. W.; Monk, C. B.; Davies, C. W. *Journal of the Chemical Society (Resumed)* 1949, 2693.
- (42) Jones, H. W.; Monk, C. B. *Journal of the Chemical Society (Resumed)* 1950, 3475.
- (43) Liu, S. T.; Nancollas, G. H. *J. Colloid Interface Sci.* 1975, 52, 593.
- (44) Rashchi, F.; Finch, J. A. *Miner. Eng.* 2000, 13, 1019.

# Chapter 6

## Dissolution Kinetics of Polycrystalline Calcium Sulfate-Based Materials: Influence of Chemical Modification

### Abstract

Using a CFC system the dissolution kinetics of polycrystalline gypsum-based materials have been examined with the aim of understanding their interaction with water, a property that limits the applications of the material in many situations. ICP analysis of elemental concentrations in solution as a function of time yields surface fluxes by using a finite element modelling approach to simulate the hydrodynamic behaviour within the CFC. After correction for surface roughness, a value for the intrinsic dissolution flux into water of pure polycrystalline gypsum,  $\text{CaSO}_4 \cdot 2\text{H}_2\text{O}$ , of  $1.1 (\pm 0.4) \times 10^{-8} \text{ mol cm}^{-2} \text{ s}^{-1}$  has been obtained. The addition of known humid-creep inhibitors to the gypsum samples, including boric acid, tartaric acid and 3,4,5-trihydroxybenzoic acid (gallic acid), was found to have little measurable effect on the dissolution kinetics of gypsum: all yielded dissolution fluxes of  $1.4 (\pm 0.6) \times 10^{-8} \text{ mol cm}^{-2} \text{ s}^{-1}$ . However, STMP was found to have a small detectable inhibitory effect relative to pure gypsum yielding a flux of  $7.4 (\pm 2.0) \times 10^{-9} \text{ mol cm}^{-2} \text{ s}^{-1}$ . The data strongly suggest that models for humid-creep inhibition that involve dissolution-crystallization of gypsum crystallites are less likely than those that involve a hindered ingress of water into the gypsum matrix. For comparison, composite materials that comprised of calcium sulfate anhydrite ( $\text{CaSO}_4$ ) crystallites bound by a polyphosphate matrix were also studied. For some of these samples,  $\text{Ca}^{2+}$  surface fluxes were observed to be  $\sim 1$  order of magnitude lower than values for polycrystalline gypsum control substrates, suggesting a useful way to impart water resistance to gypsum-based materials.

## **6.1. Introduction**

Gypsum,  $\text{CaSO}_4 \cdot 2\text{H}_2\text{O}$ , has been used since antiquity to line the interiors of buildings owing to its many attractive properties such as ease of application, good thermal insulation, fire resistance and its favourable processing conditions, requiring only moderate temperatures.<sup>1</sup> There is renewed interest in utilizing gypsum for exterior and load bearing applications given its availability as an industrial by-product and the much lower processing temperatures compared to traditional silicate cements.<sup>2</sup> The property that restricts the wider use of gypsum is its poor water resistance. Gypsum materials are produced by the hydration of calcium sulfate hemi-hydrate to yield an interlocking mass of polycrystalline, needle-shaped gypsum particles.<sup>3</sup> A small amount of water, present as atmospheric humidity, is enough to cause a dramatic reduction in mechanical properties such as Young's modulus,<sup>4</sup> flexural strength,<sup>5</sup> compressive strength<sup>6</sup> and hardness.<sup>5</sup> Gypsum can also deflect or creep under an applied stress in the presence of water over long periods of time, a process that has been suggested to be responsible for the instability of old gypsum mines.<sup>7</sup> A similar phenomenon is also seen in industrial products where preformed shapes of polycrystalline gypsum, such as ceiling tiles, can deflect in high humidity environments, in a process known as 'humid creep' or 'sag', causing aesthetic as well as mechanical defect.<sup>8</sup>

A consensus on the exact mechanisms responsible for the humid creep of gypsum with moisture contact has not been reached. Badens *et al.* suggest that the bonds between crystals are weakened by the ingress of water at grain boundaries,<sup>4</sup> whereas Chappuis proposed a model involving local dissolution and recrystallization of gypsum in the surface water layers at the contact points

between interlocking crystals.<sup>9</sup> Chemical additives, including tartaric acid,<sup>10</sup> boric acid,<sup>11</sup> STMP<sup>12</sup> and gallic acid,<sup>13</sup> have been reported in the patent literature as means of inhibiting the macroscopic effect of humid creep. The mechanism of their mode of action is unclear, although in separate studies the presence of carboxylic acids, including tartaric acid, has been found to have an effect on the rate of crystal growth of gypsum.<sup>4,14</sup> From that work, it was proposed that carboxylate anions are able to bind to the surface of gypsum crystals, thus potentially modifying crystal habit as well as crystallization rate.<sup>4</sup> <sup>14</sup> It is interesting to note that previous studies on other calcium minerals have shown that tartaric acid can also inhibit dissolution.<sup>15</sup>

In this chapter we study the dissolution of various modified gypsum materials to provide experimental values for the kinetics of dissolution. The effective dissolution rate is reliant on the interplay between surface reactivity of the substrate under investigation and mass transport conditions.<sup>16,17</sup> Reliable dissolution rates can be elucidated when the experimental techniques employed distinguish quantitatively between surface kinetic effects and mass transport.

Herein, the CFC technique (as described in Chapter 5) is combined with ICP-OES for the determination of concentrations of dissolved  $\text{Ca}^{2+}$  (and  $\text{PO}_4^{3-}$  in some of the modified materials) originating from the substrate materials collected in the CFC effluent. Mass transport in the CFC is modelled by formulating convective-diffusion equations and defining a boundary condition for the dissolving substrate so as to predict the concentration of dissolved  $\text{Ca}^{2+}$  (and  $\text{PO}_4^{3-}$ ) at a specific flow rate. By using this approach, a comparison can be made between experimental data and predictions from theory; ultimately

offering mechanistic insights into the dissolution reaction and the ability to test the validity of rate equations. We have compared the effect of proprietary humid creep additives on gypsum, with an alternative approach to moisture inhibition which uses composite phosphate-bound gypsum crystallites. Aluminium phosphate has previously been used to bind SiC and AlN,<sup>18</sup> and glass fiber<sup>19</sup> to make high temperature stable composites. Consequently, this represents an interesting prospect for improving the durability of gypsum-based materials. Our aim was to provide direct experimental data that might allow the various models proposed for the interaction between gypsum-based materials and water to be distinguished.

## **6.2. Theory and Kinetic Modelling**

The theory and kinetic modeling was described in Chapter 5 however, note that the condition on boundary 2 (the exposed crystal surface, equation 5.8) introduces a simple dissolution flux (rate constant,  $k$ );

$$\mathbf{n} \cdot \mathbf{N} = k \quad (6.1)$$

This contrasts with the work on single crystal gypsum described in Chapter 5, where we considered a rate law that was first-order in interfacial undersaturation.<sup>20</sup>

The approach herein is reasonable because first, we study the dissolution reaction far from equilibrium (approaching zero saturation levels across the entire crystal surface) at the crystal/solution interface in the case of gypsum and second, we do not know the solubility of these modified substrates explicitly, so a straightforward flux approach is optimal. We were able to

confirm the veracity of this simple model by virtue of the fact that measurements are made over a wide range of mass transport rates in the CFC method, and by the fact that intrinsic fluxes deduced are consistent with earlier work (where comparisons can be made)<sup>16,17</sup> and our own recent CFC studies.<sup>20</sup>

### **6.3. Results and Discussion**

It is important to note that the length scale of the heterogeneity in the surface presented to solution is relatively small and comparable to the size of the concentration boundary layer over much of the surface, for all of the flow rates (Figure 6.1(b)), so that the surface can be treated as uniformly active for the purposes of the dissolution model. The heterogeneity was quantitatively assessed to validate this assertion (*vide infra*).

#### **6.3.1 Insights from Simulations**

Mass transport in the CFC utilized has been described in detail in Chapter 5. Briefly: after a short lead-in length, a steady laminar Poiseuille velocity is established and maintained along the channel.<sup>20</sup> Figure 6.1(b), shows a typical concentration profile of dissolved  $\text{Ca}^{2+}$  at a flow rate of  $0.008 \text{ cm}^3 \text{ s}^{-1}$ , and  $k = 7 \times 10^{-9} \text{ mol cm}^{-2} \text{ s}^{-1}$ . The concentration distribution near the reactive substrate becomes more diffuse with increasing distance downstream. Over much of the substrate, the concentration boundary thickness is less than or of the order of the surface heterogeneity of the samples, confirming the validity of the model utilized which treats the surface as uniformly active with subsequent correction for the exposed active substrate surface area (*vide infra*).

Figure 6.2 is a 3D plot of the outlet concentration as a function of applied rate constant  $k$  ( $\text{mol cm}^{-2} \text{s}^{-1}$ ) and volume flow rate,  $V_f$  ( $\text{cm}^3 \text{s}^{-1}$ ) predicted from simulations. It is evident that an increase in  $k$  results in an increase of outlet concentrations for any flow rate. This is a consequence of the increase in the rate of generation of dissolution products from the crystal surface. Furthermore, the highest outlet concentrations are seen for the lowest  $V_f$  ( $0.008 \text{ cm}^3 \text{s}^{-1}$ ) values, because of the longer interaction between the crystal surface and etching solution, resulting in an accumulation of dissolved species.

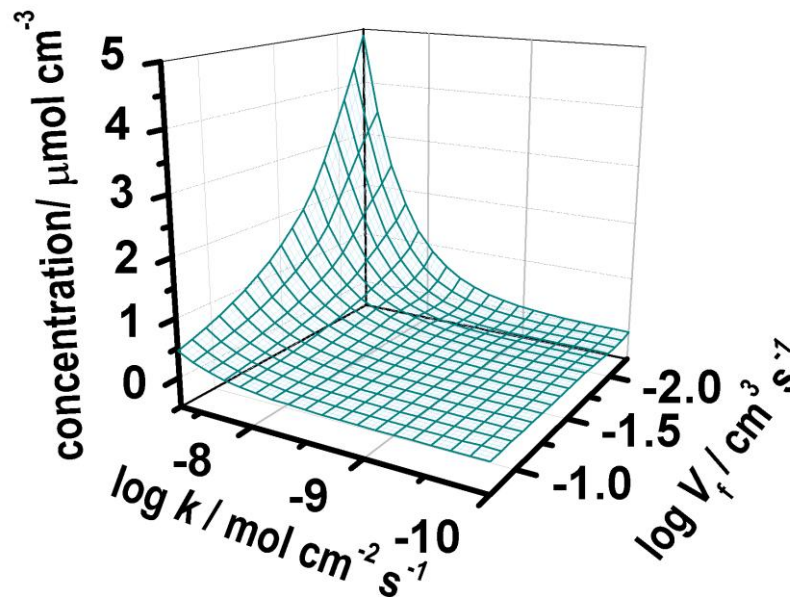


Figure 6.2: Simulated outlet concentrations as a function of applied rate constant,  $k$ , and flow rate as predicted from finite element simulations, which are based on the parameters in Figure 6.1(a)).

### 6.3.2 Surface Area Analysis

WLI measurements were carried out in order to determine the surface roughness factor,  $\lambda$  of all substrates. This technique is powerful, with a lateral resolution of  $0.5\text{-}1.2 \mu\text{m}$  (at  $10 \times$  magnification) and a vertical resolution of  $\sim 5 \text{ nm}$ . Significant changes to surface roughness could influence the hydrodynamic

character along the CFC channel, as well as affect the value of the reactive surface area exposed to solution during dissolution. To this end,  $\lambda$  was determined both prior to and after CFC experiments, to establish the extent of any surface roughening due to dissolution. Prior to dissolution, it was found that,  $\lambda$  ranged from 1.1 - 1.8 and 1.2 - 1.8 for the humid creep and composite surfaces, respectively. After dissolution measurements,  $\lambda$  remained largely within the pre-etching range at values of 1.2 - 2.1 and 1.5 - 2.8 for the humid creep and phosphate binder surfaces, respectively. For the purposes of normalizing dissolution data, the mean  $\lambda$  value obtained from the two measurements (before and after dissolution) was used and these values are summarised in Table 6.2.

*Table 6.2: WLI surfaces area ratio ( $\lambda$ ) prior to and after CFC measurements*

<b>Substrate</b>	<b>Surface area ratio</b>		<b>% change due to dissolution</b>
	<b>Before CFC measurements</b>	<b>After CFC measurements</b>	
Gypsum reference	1.22 ± 0.2	1.78± 0.1	46.9
STMP	1.22 ± 0.3	1.56± 0.3	29.3
Tartaric acid	1.11 ± 0.1	1.49± 0.4	35.1
Boric acid	1.55 ± 0.2	2.05± 0.1	32.1
Gallic acid	1.17 ± 0.1	1.43± 0.3	22.8

The impact of surface recession on CFC hydrodynamics was determined by estimating the relative change in the channel height due to dissolution. The roughest surface (highest  $\lambda = 2.8$ ) yielded an rms roughness value of 4.6  $\mu\text{m}$ , which equates to  $\sim 2\%$  of the channel height (210  $\mu\text{m}$ ).

While the intrinsic surface dissolution fluxes ( $J_s$ ,  $\text{mol cm}^{-2} \text{s}^{-1}$ ) can be obtained by normalizing the theoretical rate constants ( $k$ ,  $\text{mol cm}^{-2} \text{s}^{-1}$ ) values obtained from computer simulations by dividing by  $\lambda$ , this treatment of data was adequate for the composite sample set. Due to the presence of the inert resin matrix in the case of samples impregnated with humid creep additives, the flux measured was further normalized to account for the fraction of the surface which was active, i.e.  $J_s = k / (\lambda \times \varphi)$ , where  $\varphi$  is the fraction of exposed surface area (crystalline gypsum) across the sample.

### **6.3.3 Surface Heterogeneity**

SEM analysis of the samples (Figure 6.3) yielded binary images which were analysed to determine the relative amount of resin and gypsum crystal on the surface. Heavier elements (higher atomic number) back scatter electrons more strongly than lighter (lower atomic number).<sup>21</sup> Consequently, the resulting image exhibits bright regions in regions composed of heavier elements, and darker zones where lighter elements may be found, thus allowing different elements to be distinguished based on the contrast of the image. By increasing the contrast in these images using ImageJ, and IP software package, a quantitative analysis of the surface composition could be carried out.

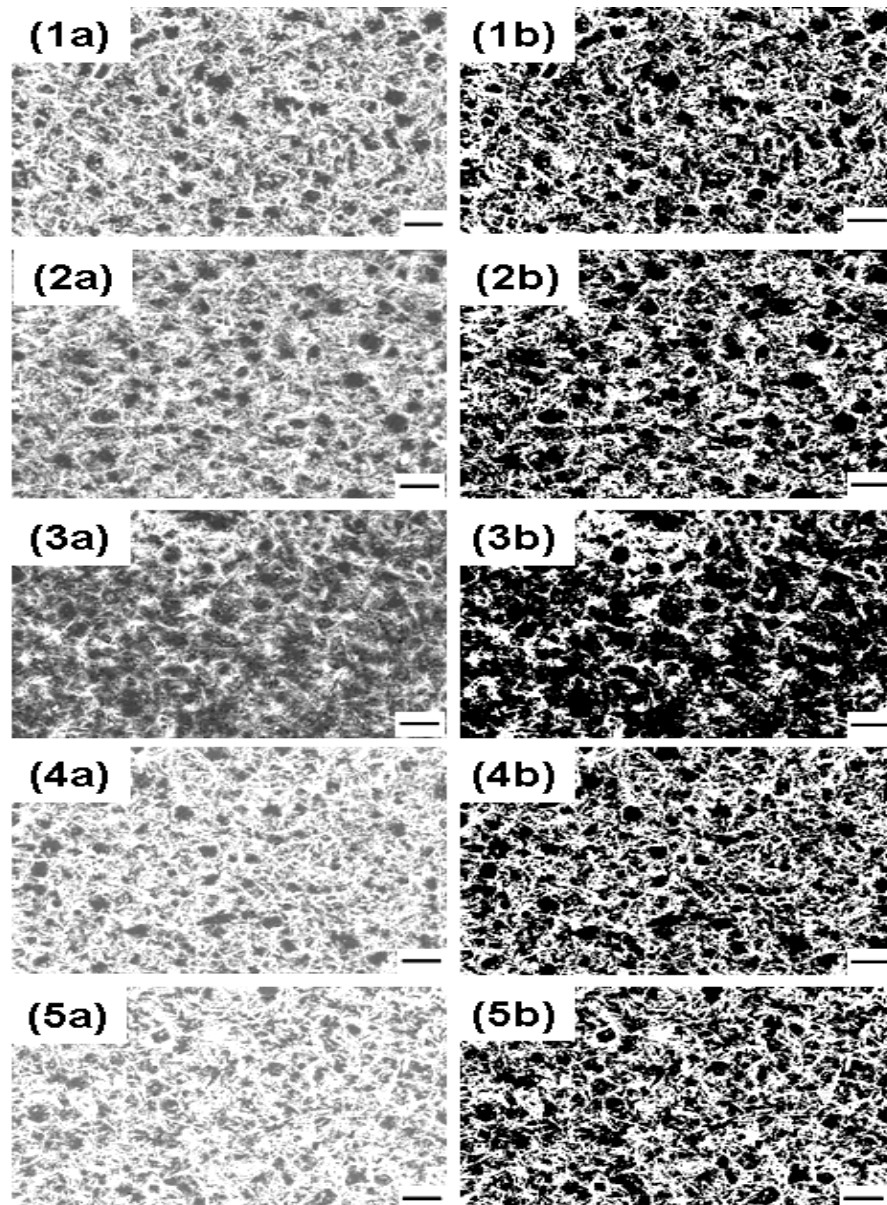


*Figure 6.3: Typical SEM images from the backscattered electron detector (a) with the corresponding binarised image (b) of the gypsum control sample (1) and those impregnated with humid creep the additives: STMP (2), tartaric acid (3), boric acid (4) and gallic acid (5).the scale bar represents 50  $\mu\text{m}$ .*

The relative amount of exposed crystal relative to resin as obtained from SEM studies is summarised in Figure 6.4. It is evident from this figure that on average, crystal: resin ratio was  $\sim 1:1$  apart from samples treated with tartaric resin where the ratio was 1: 1.5.

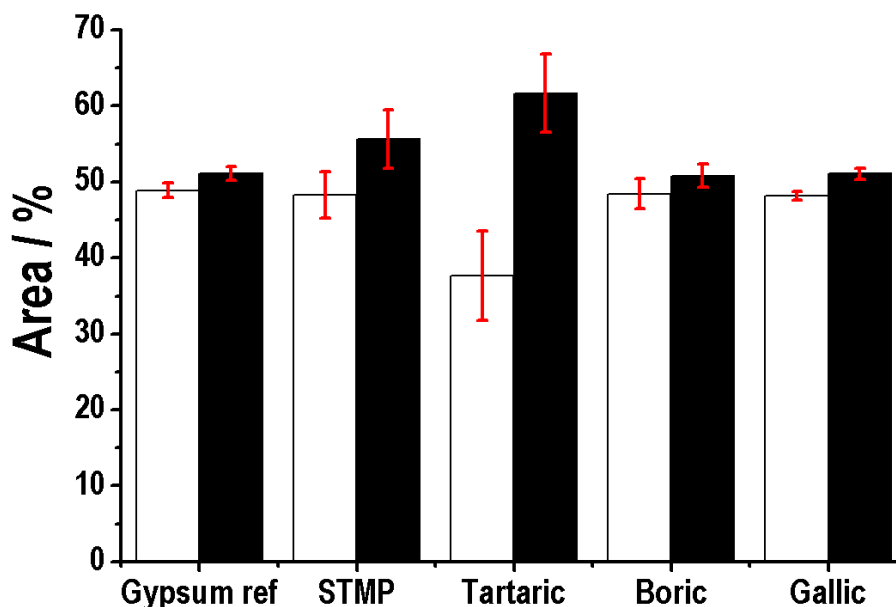


Figure 6.4: reactive surface area result from SEM image analysis, showing gypsum crystal (white) and resin (black). Error bars are based on 1 standard deviation.

The SEM images were further analysed via the user-defined Matlab IP package (Chapter 3) to investigate the nature of surface heterogeneity, i.e. the distance between active sites on the resin impregnated gypsum samples, and allow comparisons to the diffusional layer thickness under particular flow rates. In this way, it was possible to verify the significance of surface heterogeneity on the elucidation of dissolution kinetics. Figure 6.5 shows plots of the distance between contiguous active sites (exposed crystal) across the substrate surface for all chemically modified gypsum samples. From this figure, it is evident that for most of the surface, active regions were within  $\sim 5 \mu\text{m}$  from each other, with very few ( $\leq 5\%$ ) exceeding this value. In addition, there was no significant variation between samples, suggesting that all samples exhibited similar heterogeneity.

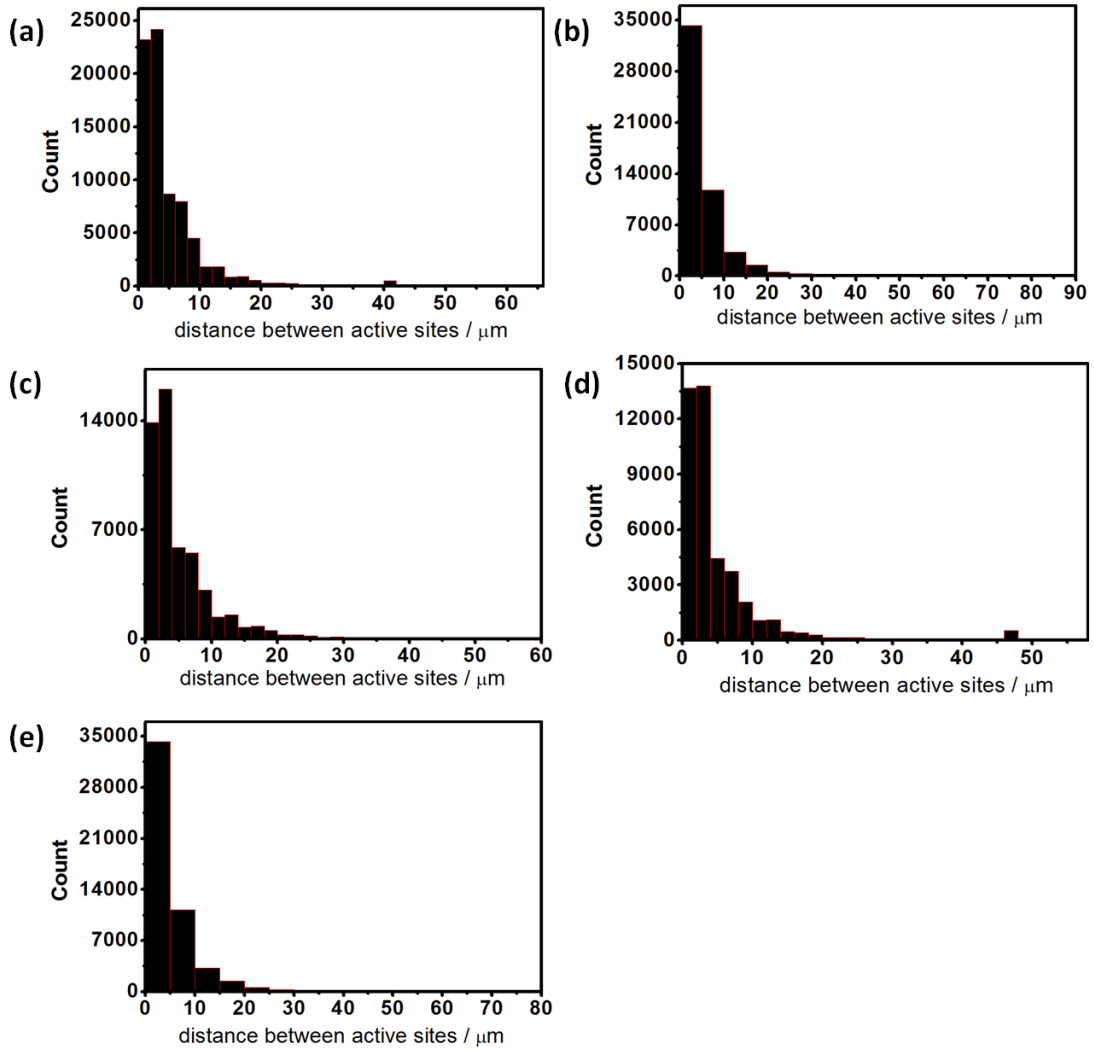


Figure 6.5: Distance between active regions as a function of frequency on (a) gypsum control, and samples modified with; (b) STMP, (c) gallic acid, (d) tartaric acid and (e) boric acid

### 6.3.4 Diffusion Layer Thickness

The concentration profile into the CFC channel height varied both as a function of distance along the channel (more diffuse further downstream) and applied flow rate ( $V_f$ ). Figure 6.6 illustrates the change in  $\text{Ca}^{2+}$  concentration within the channel height under (a)  $V_f = 0.008 \text{ cm}^3 \text{ s}^{-1}$  and (b)  $V_f = 0.167 \text{ cm}^3 \text{ s}^{-1}$ . From these plots, the average diffusion boundary thickness was estimated to range between 25 and 90  $\mu\text{m}$  for the highest and lowest flow rates used for CFC experiments, respectively.

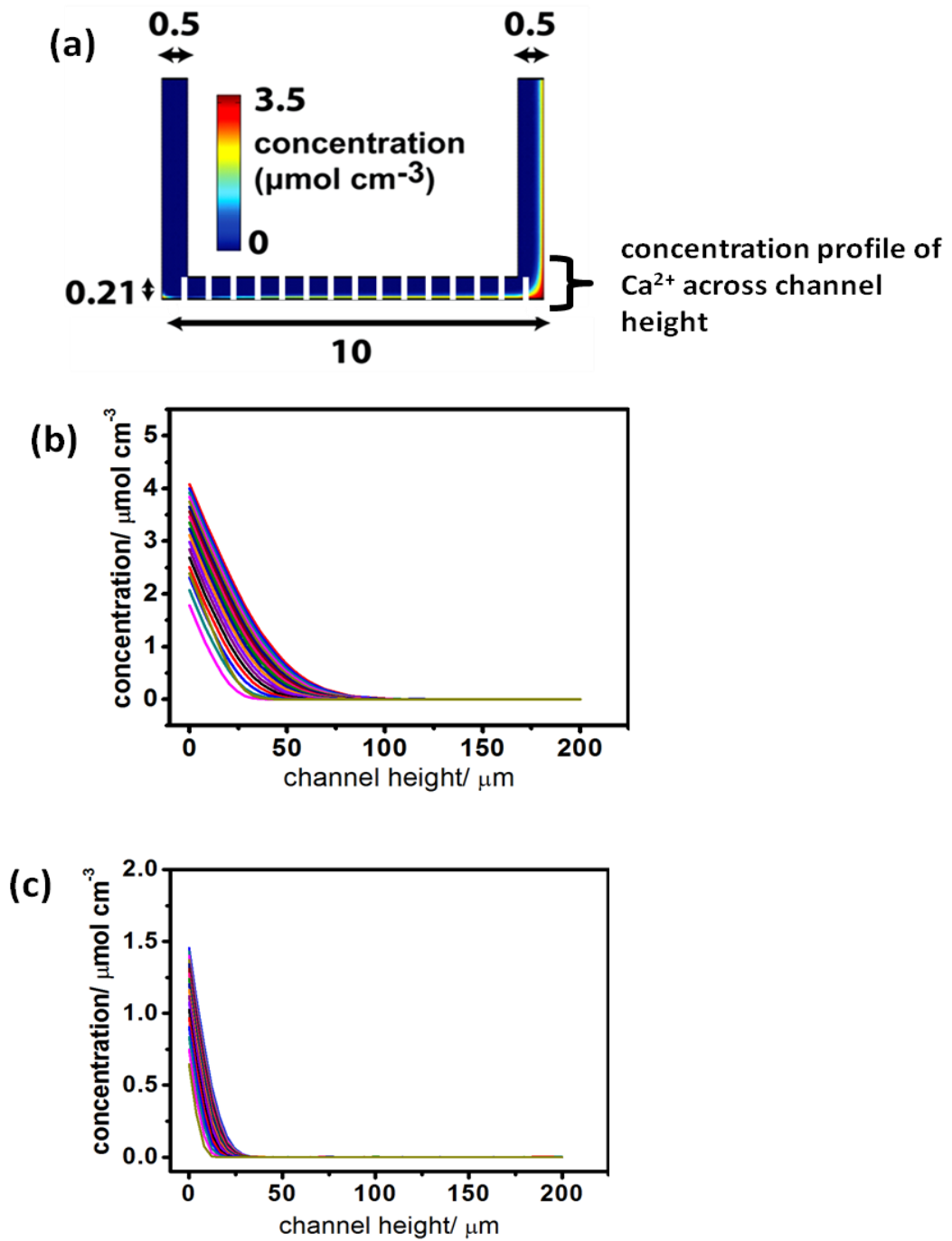


Figure 6.6: (a) Concentration profile within CFC highlighting cross sections taken across the channel height to measure the concentration profile of  $\text{Ca}^{2+}$  ions at a fixed flux of  $7 \times 10^{-9} \text{ mol cm}^{-2} \text{ s}^{-1}$  and (b)  $V_f = 0.008 \text{ cm}^3 \text{ s}^{-1}$  and (c)  $V_f = 0.167 \text{ cm}^3 \text{ s}^{-1}$ .

### **6.3.5 Dissolution Kinetics of Gypsum Modified with Humid-Creep Inhibitors**

The effluent from CFC experiments was analysed via ICP-OES to obtain flow rate-specific concentrations of  $\text{Ca}^{2+}$ . For each sample, at least four replicate runs were made. Figure 6.7(a) shows typical plots of average outlet concentrations as a function of flow rate; and the solid line corresponds to the best fit of applied  $k$  ( $\text{mol cm}^{-2} \text{s}^{-1}$ ) obtained from the complementary simulations described above. The error bars are the result of two standard deviations calculated from at least four data sets. Once the theoretical rate constant,  $k$ , had been determined, average surface fluxes,  $J_s$  ( $\text{mol cm}^{-2} \text{s}^{-1}$ ) were deduced by normalizing predicted data with respect to the exposed surface area and  $\lambda$ , *vide supra*.

The values of  $J_s$  for all chemically-modified samples are summarised in Figure 6.7(b), in which polycrystalline gypsum was observed to exhibit  $J_s = 1.1 (\pm 0.4) \times 10^{-8} \text{ mol cm}^{-2} \text{ s}^{-1}$ . Colombani recently reviewed various gypsum dissolution studies with the goal of reconciling discrepancies between them in the rates derived, along with newly measured values using holographic interferometry, and showed that when properly normalised for surface area effects ( $\lambda$ ), all studies gave a consistent value of  $J_s = 7 \times 10^{-9} \text{ mol cm}^{-2} \text{ s}^{-1}$  compared to  $J_s = 5 (\pm 2) \times 10^{-9} \text{ mol cm}^{-2} \text{ s}^{-1}$  obtained from new measurements.<sup>16</sup> The values obtained in the current work are in reasonable agreement with those previously reported, giving confidence in the surface area normalization and allowing meaningful comparisons to be made with the modified samples. That the values are slightly higher can be attributed to the polycrystalline

nature of the substrates used, as well as the exposure of highly reactive planes on dissolving crystallites.

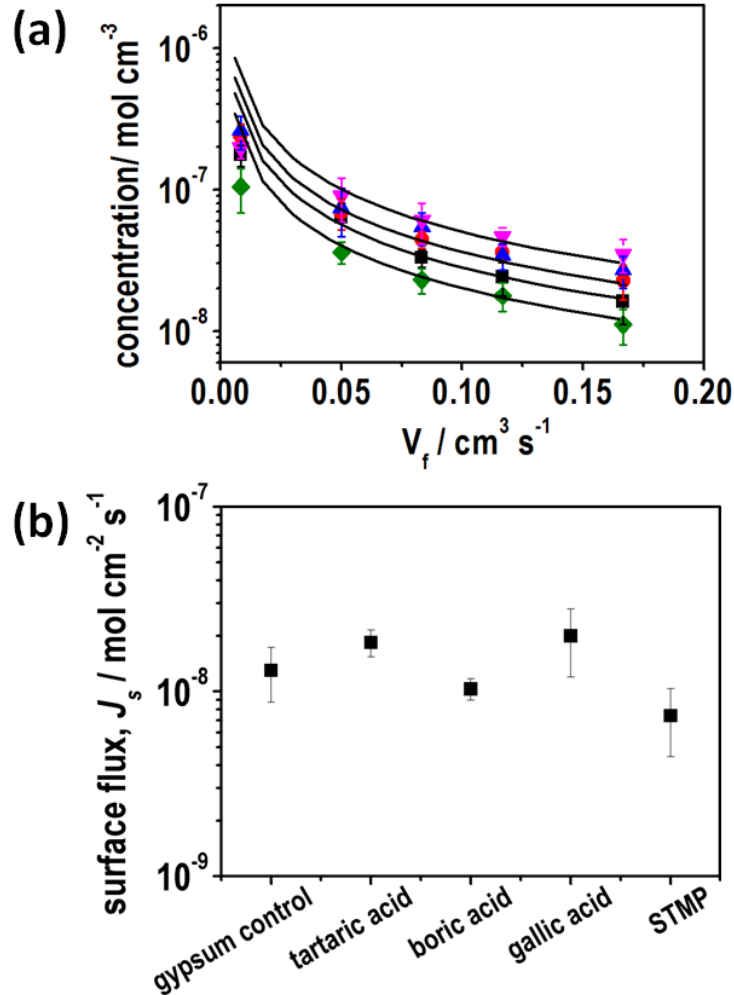


Figure 6.7: Plots of (a)  $\text{Ca}^{2+}$  outlet concentration as a function of flow rate for the dissolution of polycrystalline gypsum impregnated with humid creep inhibitors. The solid lines correspond to best fits to the model with rate constants in  $k$  ( $\text{mol cm}^{-2} \text{s}^{-1}$ ) in the range of  $8.6 (\pm 3.6) \times 10^{-9} \text{ mol cm}^{-2} \text{ s}^{-1}$  for all humid creep samples, and the samples were, gypsum control (black), STMP (green), tartaric acid (red), boric acid (blue), 3,4,5-trihydroxybenzoic acid (gallic acid) (pink) and STMP (green). These values were normalised with respect to surface area ( $\lambda$ ), to yield (b) the average surface fluxes  $J_s$  of  $1.3 (\pm 0.4) \times 10^{-8} \text{ mol cm}^{-2} \text{ s}^{-1}$  for the gypsum control, and  $1.8 (\pm 0.3) \times 10^{-8} \text{ mol cm}^{-2} \text{ s}^{-1}$ ,  $1.0 (\pm 0.1) \times 10^{-8} \text{ mol cm}^{-2} \text{ s}^{-1}$  and  $2.0 (\pm 0.6) \times 10^{-8} \text{ mol cm}^{-2} \text{ s}^{-1}$  and  $7.4 (\pm 0.4) \times 10^{-9} \text{ mol cm}^{-2} \text{ s}^{-1}$  for the humid creep samples impregnated with tartaric acid, boric acid, 3,4,5-trihydroxybenzoic acid (gallic acid) and STMP, respectively.

For gypsum materials modified with humid creep modifiers,,  $J_s$  was found to be relatively similar, in the range  $1.4 (\pm 0.6) \times 10^{-8} \text{ mol cm}^{-2} \text{ s}^{-1}$  with STMP exhibiting a small retarding effect on gypsum dissolution compared to the other inhibitors, yielding  $J_s = 7.4 (\pm 2.0) \times 10^{-9} \text{ mol cm}^{-2} \text{ s}^{-1}$ . The influence of STMP on gypsum dissolution kinetics corroborates our recent work, where STMP in solution was found to retard the dissolution kinetics of the (010) basal plane of gypsum, particularly in the [010], [001] and [100] directions.<sup>20</sup> The inhibitory effect measured here is somewhat less because there is no inhibitor in the solution; rather there is a finite (small amount) in the material which will be released during dissolution. The lack of a discernible retardation of dissolution due to the presence of humid creep additives (except from the small effect of STMP noted), casts some doubt on the dissolution-precipitation theory proposed by Chappuis to explain the mode of action of humid creep inhibition in industrial gypsum products.<sup>9</sup> Another proposal is that the additives alter crystal habit and therefore the faces in contact with each another;<sup>22</sup> however, no additive produced a significant crystal habit modifying effect from SEM results. The net effect of crystal habit modification may be to increase the total adhesion between crystals according to Finot *et al.* who determined that the adhesion between crystal faces was dependent on the combination in contact.<sup>23</sup> Indeed, Kato *et al.* found that other polar liquids such as ethanol also reduced the mechanical properties, to an extent in correlation with the liquid polarity.<sup>24</sup> Reynauld *et al.* used internal friction measurements to later postulate a visco-elastoplastic rheological model to describe the plastic flow of gypsum, where the absorbed liquid layer shields the electrostatic interactions between crystals and they slide past one-another under stress.<sup>25</sup>

Badens *et al.* proposed that tartaric acid adsorbs on the (120) and (111) faces of gypsum, based on the most stable conformations of the molecule and the inter-atomic distances of calcium ions in the gypsum lattice.<sup>14</sup> Through molecular modeling, it has been predicted that the surface energy of most faces of gypsum (apart from the most stable (010) plane)<sup>25</sup> decreases when calcium tartrate is formed.<sup>26</sup> It follows from our results, and this discussion, that the mode of action of humid creep inhibition may be to reduce the amount of water present in the inter-crystal region, thereby preventing loss of mechanical strength. Indeed Badens *et al.* also proposed that the humid creep inhibitors reduce the thickness of the absorbed water film on the crystallite surface,<sup>4</sup> which could be by the displacement of water molecules, as proposed by van der Voort and Hartman for gypsum crystallizing in the presence of organic impurities.<sup>27</sup> Based on our dissolution studies, this appears to be the most plausible explanation for the mode of action of humid-creep inhibitor additives.

### **6.3.6 Composite Materials**

Figure 6.8 shows typical plots of the average outlet concentration values for calcium and phosphate as a function of flow rate for the gypsum-composite materials, where the Al: P ratio was (a) 0, (b) 0.1, (c) 0.2 and (d) 0.33, and the solid lines correspond to the best fit  $k$  ( $\text{mol cm}^{-2} \text{s}^{-1}$ ) as predicted from simulations, with the values shown in Table 6.3. For all samples, it was found that outlet concentrations of calcium were higher than those of phosphate, due to the sample composition (Ca: P ratio) as seen in Figure 6.8. However, the outlet concentration values in sample Al: P = 0.33 showed an apparently larger difference between calcium and phosphate.

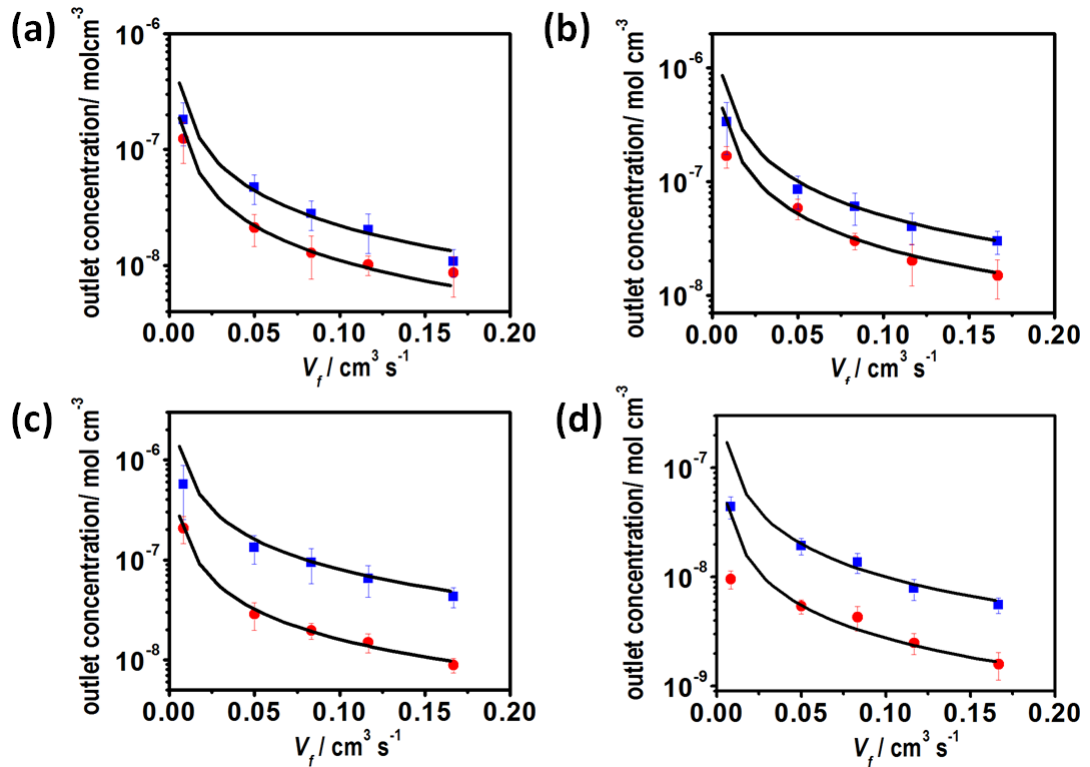


Figure 6.8: Plots of outlet concentrations of calcium (blue) and phosphorous (red) as a function of flow rate for the phosphate binder samples where the Al: P ratio was (a) 0, (b) 0.1, (c) 0.2 and (d) 0.33. The solid lines correspond to the best fit to the model with fixed flux  $k$  ( $\text{mol cm}^{-2} \text{s}^{-1}$ ). Values for  $k$  are shown in Table 4.

Surface-area normalised fluxes,  $J_s$  for the dissolution of calcium and phosphate ions from the composite materials are shown in Figure 6.9(a), along with the corresponding value obtained for the polycrystalline gypsum control sample, for comparison. These data highlight the difference between the release rates of  $\text{PO}_4^{3-}$  and  $\text{Ca}^{2+}$  from the phosphate bound materials upon dissolution, and clearly show how the dissolution of these composites vary significantly depending on the Al: P ratio used, as well as the morphology of the samples.

*Table 6.3: Theoretical flux predictions from simulations for composite binder materials*

Sample		Theoretical Flux, $k$ (mol cm <sup>-2</sup> s <sup>-1</sup> )	
Al: P	Ca: P	Ca <sup>2+</sup>	PO <sub>4</sub> <sup>3-</sup>
0	1.9	$5.4 (\pm 2.0) \times 10^{-9}$	$2.8 (\pm 1.5) \times 10^{-9}$
0.1	2.1	$1.3 (\pm 0.2) \times 10^{-8}$	$6.5 (\pm 0.9) \times 10^{-9}$
0.2	2.4	$1.5 (\pm 0.7) \times 10^{-8}$	$8.0 (\pm 1.5) \times 10^{-9}$
0.33	2.67	$2.5 (\pm 0.7) \times 10^{-9}$	$6.9 (\pm 1.5) \times 10^{-10}$

At Al: P = 0, surface fluxes were found to be  $J_s = 2.9 (\pm 1.1) \times 10^{-9}$  mol cm<sup>-2</sup> s<sup>-1</sup> and  $J_s = 1.5 (\pm 0.7) \times 10^{-9}$  mol cm<sup>-2</sup> s<sup>-1</sup> for Ca<sup>2+</sup> and PO<sub>4</sub><sup>3-</sup>, respectively, which were ~1 order of magnitude lower than polycrystalline gypsum control ( $J_s = 1.1 (\pm 0.4) \times 10^{-8}$  mol cm<sup>-2</sup> s<sup>-1</sup>). In this case, the anhydrite crystallites in the composite matrix can be envisaged as being protected by a phosphate coating. As Al: P content increased to 0.1 and 0.2, Ca<sup>2+</sup> dissolution rates approached values similar to the gypsum control (Figure 6.9 (a)) with  $J_s = 7.1 (\pm 1.1) \times 10^{-9}$  mol cm<sup>-2</sup> s<sup>-1</sup> and  $J_s = 9.1 (\pm 0.6) \times 10^{-9}$  mol cm<sup>-2</sup> s<sup>-1</sup> for the Al: P = 0.1 and 0.2 substrates, respectively. These higher rates may have resulted due to the crystalline Al(PO<sub>3</sub>)<sub>3</sub> as determined via FTIR, (not shown) creating heterogeneity within the coating and, therefore less protective of the calcium sulfate from contact with impinging water in the channel. The Al: P = 0.33, which has the stoichiometric quantity of elements for Al(H<sub>2</sub>PO<sub>4</sub>)<sub>3</sub>, is substantially amorphous and chemically stable<sup>28</sup> and seemed to provide the most protection of the coating for the anhydrite crystallites.

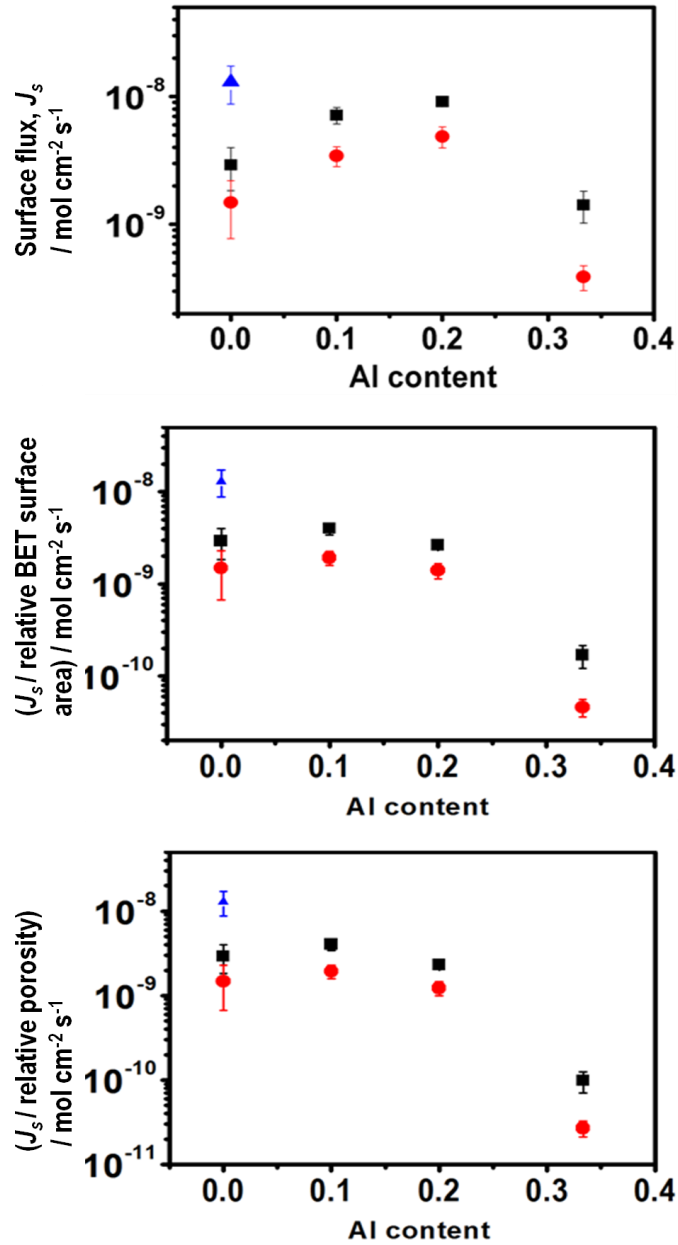


Figure 6.9: Plots of (a) dissolution fluxes, (b) dissolution fluxes normalised with respect to relative BET surface area and (c) dissolution fluxes normalised with respect to relative sample porosity. The rates of  $\text{Ca}^{2+}$  (black) and  $\text{PO}_4^{3-}$  (red) as a function of Al content for all binder composites are shown. The calcium fluxes from polycrystalline gypsum control (blue) are also shown. The relative porosity and BET surface areas are defined with respect to the values for the gypsum control.

This conclusion is further supported by the lower surface fluxes obtained at this Al: P ratio compared to corresponding values at lower Al content and, furthermore, by the pronounced discrepancy in  $\text{Ca}^{2+}$  and  $\text{PO}_4^{3-}$  surface fluxes

with  $J_s = 1.4 (\pm 0.4) \times 10^{-9} \text{ mol cm}^{-2} \text{ s}^{-1}$  and  $J_s = 3.9 (\pm 0.8) \times 10^{-10} \text{ mol cm}^{-2} \text{ s}^{-1}$  for  $\text{Ca}^{2+}$  and  $\text{PO}_4^{3-}$  ions, respectively. The release rates for calcium and phosphate were a factor of 2-3 slower than in the case where Al: P = 0 and, moreover,  $\sim 1$  order of magnitude lower than the gypsum reference sample.

#### **6.4. Conclusions**

We have shown how a novel channel flow cell technique can be applied to study the dissolution behaviour of industrially relevant materials. We find that the simple flux rate law applied herein describes adequately the dissolution kinetics of unmodified polycrystalline gypsum and yields intrinsic dissolution flux values that compare well to values obtained in literature. Modification of polycrystalline gypsum with a variety of established humid-creep inhibitors has a minimal influence on dissolution kinetics under the experimental conditions applied, suggesting that a simple dissolution-precipitation model of moisture interaction with gypsum does not explain the mode of action of humid creep inhibitors. Models involving the surface binding of additives that reduce water adsorption in the inter-crystal region are more reasonable.

## References

- (1) Arpe, H.-J. In *Ullmans Encyclopaedia of Industrial Chemistry*; 5th ed.; VCH: Weinheim, 1985; Vol. A4, p 555.
- (2) Escalante-Garcia, J. I.; Magallanes-Rivera, R. X.; Gorokhovskiy, A. *Constr. Build. Mater.* **2009**, *23*, 2851.
- (3) Gartner, E. M. *Cem. Concr. Res.* **2009**, *39*, 289.
- (4) Badens, E.; Veesler, S.; Boistelle, R.; Chatain, D. *Colloid Surf. A-Physicochem. Eng. Asp.* **1999**, *156*, 373.
- (5) Coquard, P.; Boistelle, R. *Int. J. Rock Mech. Min.* **1994**, *31*, 517.
- (6) Russell, J. *Zement Kalk Gips* **1960**, *13*, 345.
- (7) Hoxha, D.; Homand, F.; Auvray, C. *Eng. Geol.* **2006**, *86*, 1.
- (8) Saadaoui, M.; Meille, S.; Reynaud, P.; Fantozzi, G. *J. Eur. Ceram. Soc.* **2005**, *25*, 3281.
- (9) Chappuis, J. *Colloid Surf. A-Physicochem. Eng. Asp.* **1999**, *156*, 223.
- (10) Arese, R.; Martin, D.; Rigaudon, M. **2003**, *Process for reducing creep in a gypsum plaster-based element, gypsum plaster-based composition and method for making a gypsum plaster-based element with reduced creep. US Patent 2006/0048680*
- (11) Muller, R. E.; Henkels, P. L.; O' Kelly, B. M. **1965**, *Gypsum board. US Patent 3,190,787.*
- (12) Yu, Q.; Sucech, S.; Groza, B.; Mlinac, R.; Jones, F.; Boehnert, F. **2003**, *Process for reducing creep in a gypsum plaster-based element, gypsum plaster-based composition and method for making a gypsum plaster-based element with reduced creep. US Patent 6,632,550.*
- (13) Wilson, B. K.; Jones, K. W. **1977**, *Production of shaped gypsum articles. GB 1,481,788.*
- (14) Badens, E.; Veesler, S.; Boistelle, R. *J. Cryst. Growth* **1999**, *198*, 704.
- (15) Barwise, A. J.; Compton, R. G.; Unwin, P. R. *J. Chem. Soc.-Faraday Trans.* **1990**, *86*, 137.
- (16) Colombani, J. *Geochim. Cosmochim. Acta* **2008**, *72*, 5634.
- (17) Jeschke, A. A.; Vosbeck, K.; Dreybrodt, W. *Geochim. Cosmochim. Acta* **2001**, *65*, 27.
- (18) Chung, D. D. L. *J. Mater. Sci.* **2003**, *38*, 2785.
- (19) Deng, S. F.; Wang, C. F.; Zhou, Y.; Huang, F. R.; Du, L. *Mater. Sci. Eng. A-Struct. Mater. Prop. Microstruct. Process.* **2008**, *477*, 96.
- (20) Mbogoro, M. M.; Snowden, M. E.; Edwards, M. A.; Peruffo, M.; Unwin, P. R. *J. Phys. Chem. C* **2011**, *115*, 10147.
- (21) Pye, K.; Krinsley, D. H. *J. Sediment. Res.* **1984**, *54*, 877.
- (22) Singh, N. B.; Middendorf, B. *Prog. Cryst. Growth Charact. Mater.* **2007**, *53*, 57.
- (23) Finot, E.; Lesniewska, E.; Mutin, J. C.; Goudonnet, J. P. *Langmuir* **2000**, *16*, 4237.
- (24) Kato, Y., Matsui, M and Umeya, K *Gypsum Lime* **1980**, *166*, 83.
- (25) Reynaud, P.; Saadaoui, M.; Meille, S.; Fantozzi, G. In *ICIFMS-14*; Elsevier Science Sa: Kyoto, JAPAN, 2005, p 500.
- (26) Hill, J. R.; Plank, J. J. *Comput. Chem.* **2004**, *25*, 1438.
- (27) van der Voort, E.; Hartman, P. *J. Cryst. Growth* **1991**, *112*, 445.
- (28) Tricot, G.; Coillot, D.; Creton, E.; Montagne, L. *J. Eur. Ceram. Soc.* **2008**, *28*, 1135.

# Chapter 7

## Quantitative 3-D Visualisation of Gypsum Micro-Crystal Growth Kinetics Using AFM

### Abstract

Crystal growth processes typically involve a complex interplay between the macroscopically observed events and processes occurring at the crystal surface. In this chapter, the growth of isolated gypsum micro-crystals is monitored via in-situ AFM under quiescent conditions. The process is investigated under a wide range of non-stoichiometric conditions, while maintaining a constant supersaturation, in order to elucidate the influence of constituent ions ( $\text{Ca}^{2+}$  and  $\text{SO}_4^{2-}$ ) on plane-specific growth behaviour. The separation of mass transport effects and surface kinetics is achieved by focusing on a microscopically active surface which exhibits high mass transfer rates. Additionally complementary computer models which predict the interfacial concentrations are designed and developed, thus deducing the dominant kinetic regime. It is found that growth kinetics are controlled by surface reactivity, with the 'edge' planes, (100) and (001), dominating the process at early times. Deviation from equimolar concentrations (of reagent ions,  $\text{Ca}^{2+}$  and  $\text{SO}_4^{2-}$ ) is found to depress plane-specific growth rates in the lateral directions ([100] and [001]), while the basal (010) surface growth showed a small decrease with increasing  $\text{SO}_4^{2-}$  concentration. Furthermore, it is found to dramatically affect the morphology of grown crystals with large plate-like geometries forming in  $\text{SO}_4^{2-}$ -rich solutions, while in  $\text{Ca}^{2+}$ -rich conditions, a needle-like morphology is observed. Analysis of the basal surface topography during growth reveals the formation of 2D layers which exhibit complex propagation kinetics, with steps velocities following the order:  $v_{[100]} \gg v_{[001]}$ .

## **7.1. Introduction**

The elucidation of crystal growth mechanisms requires an intimate knowledge of thermodynamic factors such as supersaturation, temperature etc., and, the relationship between the macroscopically observed rates and the local microscopic events on the crystal surfaces which manifest them.<sup>1,2</sup> In addition, reliable determination of the kinetic regime demands a demarcation between the prevailing mass transport conditions which facilitate the diffusion of species to the crystal surface, and, the surface processes which allow the incorporation of these species into the crystal lattice.

Early attempts to study crystal growth and address these issues were bulk studies such as batch crystallizers using seeded suspensions.<sup>3</sup> While significant insights have been gained from these studies, determination of the dominant kinetic regime for the growth process was found to be complicated due to inherent difficulties in the separation of mass transport and surface processes when using such techniques. With the focus being on macroscopic observations, the reactivity of individual crystal faces has only recently been tackled and subsequently, there is much to be done to understand the relative contribution of specific crystal faces to overall 'average' growth behaviour.

Powerful local techniques such as AFM<sup>4</sup> and various electrochemical methods<sup>5-9</sup> have proved useful in probing crystal growth processes at the microscopic level. However, as seen for crystal dissolution studies,<sup>10</sup> a high thermodynamic driving force induces rates which are inaccessible via AFM, therefore limiting the range which can be probed. In addition, recent studies on the mass transport condition in AFM fluid cells suggest that not only are the hydrodynamics in these cells complicated,<sup>11,12</sup> the AFM probe can pose a

significant influence on diffusion to the crystal surface.<sup>13,14</sup> The issue has been addressed in some studies, by probing the growth of isolated micro-crystals ( $\leq 20 \mu\text{m}$  characteristic dimension) under quiescent conditions.<sup>15,16</sup> It has been shown that mass transport to an isolated microscopic active surface is typically very high and well defined, as seen for example with ultramicroelectrodes in electrochemistry.<sup>17</sup> In this chapter, we track the growth of an isolated micro-crystal over time, and develop a complementary diffusion model which predicts the prevailing kinetic regime.

Traditional approaches to crystal growth (bulk and local) have tended to focus on growth where the ratio of the activity of reagent ions, ( $r$ ) matches the ion ratio in the crystal lattice. For instance, for an  $A_xB_y$  crystal, in most cases, stoichiometry in the growth solution:  $r = (a_{A^{y+}} / a_{B^{x-}}) = 1$ . While this approach is useful, it neglects the environments likely to exist in geochemical systems, such as sea brines,<sup>18,19</sup> and brackish waters,<sup>20</sup> where non-stoichiometric conditions ( $r \neq 1$ ) often prevail, and therefore highlights an area that needs further exploration. A comprehensive treatment of crystal growth kinetics should not only accommodate the dependence of growth behaviour on thermodynamic considerations (saturation, temperature, etc), but also probe the influence of varying growth solution stoichiometry ( $r$ ). It has been suggested that the integration kinetics of cations vary considerably to those of anions, due to their different dehydration rates with cations exhibiting much lower rates relative to anions.<sup>21-25</sup> Some studies<sup>26-28</sup> have found that varying solution composition in this way has dramatic effects on crystal nucleation and growth kinetics and in addition, the morphology of grown crystals. In addition, other works suggest that the adsorption of background electrolyte ions and  $\text{H}_2\text{O}$  molecules may act

as a barrier to the surface integration of reagent ions.<sup>29</sup> Herein, the relative influence of varying reagent ion activity on plane-specific crystal growth rates is investigated over a wide range of  $r$  not only to probe the influence on overall growth kinetics, but also to elucidate plane specific effects.

Gypsum ( $\text{CaSO}_4 \cdot 2\text{H}_2\text{O}$ ) is one of the most abundant sulphate minerals<sup>30-32</sup> with significant geological<sup>20,33,34</sup> and industrial importance.<sup>35-39</sup> Despite its importance in these fields, the mineral is less well studied than others,<sup>21,27,28,40-42</sup> particularly under non-stoichiometric growth conditions and even less so at the local level, thus lending itself as a suitable candidate for investigating crystal growth phenomena. The vast majority of bulk<sup>43-47</sup> and local<sup>2,48-52</sup> gypsum crystal growth studies have focused on growth in stoichiometric solutions ( $r = 1$ ). Most previous studies conducted on gypsum crystal growth at  $r \neq 1$  conditions have been bulk studies,<sup>18,53-57</sup> such as early work by Zhang and Nancollas<sup>54</sup> at ( $0.17 < r < 5.0$ ) who found that crystal growth rates increased with decreasing  $r$ . Recent bulk studies such as works by Abdel-Aal *et al.*<sup>57</sup> explored the influence of varying  $r$ , on crystal morphology, where they found that  $\text{SO}_4^{2-}$  rich solutions produced large plate-like crystals compared to the needle-like habit observed at  $r = 1$ . To date, gypsum crystal growth via local techniques such as AFM under non-stoichiometric conditions are scarce.

Early studies<sup>36,50-54</sup> on suspensions (bulk) suggested that gypsum growth followed 2<sup>nd</sup> order kinetics at close to equilibrium conditions and low ionic strength solutions. This body of work thus corroborated the Burton, Cabrera and Frank (BCF)<sup>58</sup> crystal growth model, characterised by advancement of spiral hillocks on the dominant  $F$ -faces of a crystal, as well as the 'layer-by-layer' growth theory,<sup>59-61</sup> which, similarly follows a 2<sup>nd</sup> order dependence. With the

development of AFM, it has been possible to discriminate between competing theories by probing the surface topography during crystal growth. Recent AFM studies<sup>48-51,62</sup> on gypsum growth (typically conducted on the cleaved basal (010) surface of natural samples at close to equilibrium conditions) have reported the existence of 2D layers with few spirals observed, thus supporting the 'layer-by-layer' growth theory. Most of these AFM studies have been concerned with tracking the movement of crystallographically constrained steps across the surface as a measure of growth kinetics with few links to macroscopic observations.

In this chapter, we visualise the surface topography of the basal (010) surface of a grown gypsum micro-crystal and probe step motion on this face. In this way, we can directly relate the growth mechanism of this surface to the microscopic growth of the overall crystal.

## **7.2. Experimental**

Crystal seeding solutions were prepared by mixing 0.04 M CaCl<sub>2</sub>H<sub>2</sub>O and 0.04 M Na<sub>2</sub>SO<sub>4</sub>. Stock solutions of 0.56 M CaCl<sub>2</sub>H<sub>2</sub>O and 0.56 M Na<sub>2</sub>SO<sub>4</sub> were made and through sequential dilutions, solutions with  $r = 7.12, 4.00, 1.01, 0.25$  and  $0.133$  were prepared. Each stock solution and subsequent growth solution was prepared immediately prior to experiments.  $S$  was maintained at  $\sim 1.9$  and solution pH was  $5.6 \pm 0.3$ . Table 1 shows a summary of all growth solutions used. Based on calculations using MINEQL+, the concentration of the ion pair, CaSO<sub>4</sub> was kept constant for all growth solutions at  $\sim 0.01$  M. The experimental set up and growth procedure are described in detail in Chapter 3.

Table 7.1: Summary of all solutions used for growth experiments.

	Free ion activity / mM		Ion pair concentration / mM	Ionic Strength/ M	S
<i>r</i>	Ca <sup>2+</sup>	SO <sub>4</sub> <sup>2-</sup>	CaSO <sub>4</sub>		
0.13	2.5	18.8	10.4	0.27	1.92
0.25	3.4	13.7	10.3	0.20	1.90
1.01	6.9	6.8	10.4	0.15	1.92
4.00	13.6	3.4	10.3	0.19	1.89
7.12	17.8	2.5	10.5	0.25	1.81

### 7.3. Characterisation of Seed Crystals

In order to confirm the identity of grown crystals, individual crystals grown were analysed via Raman spectrometry (Reinshaw inVia Raman Microscope) equipped with a 633 nm Ar<sup>+</sup> laser. The laser power was set to 100% (50 mW) with an exposure time of 20 s and for each sample, 16 accumulations were recorded. Figure 7.1, shows typical Raman spectra for two samples (superimposed) with peaks highlighted. The spectra were typical of gypsum crystal with characteristic peaks denoting SO<sub>4</sub> bending (shifts at 494 cm<sup>-1</sup>, 620 cm<sup>-1</sup> and 671 cm<sup>-1</sup>) and SO<sub>4</sub> stretching (1008 cm<sup>-1</sup> and 1136 cm<sup>-1</sup>).<sup>63</sup>

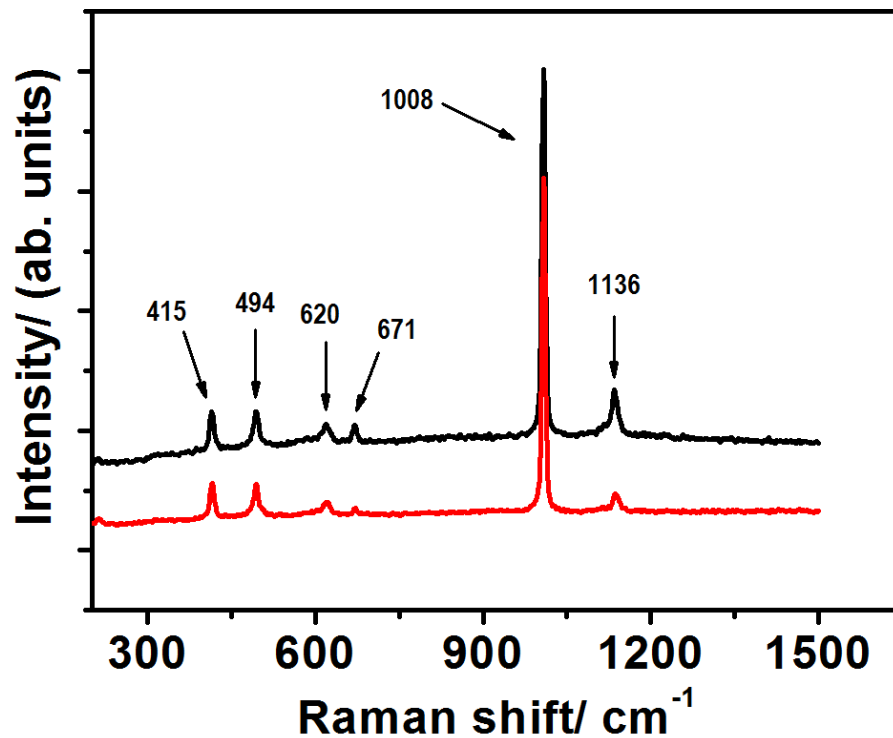


Figure 7.1: Typical Raman spectra acquired from analysing seed gypsum crystals.

Figure 7.2 shows an AFM image of a typical gypsum micro-crystal highlighting the dominant crystal faces. In this and all cases, crystal morphology was typical of gypsum crystal structure, characterised by a monoclinic geometry.<sup>64</sup> After the seeding process, a typical crystal was  $10 (\pm 3) \mu\text{m}$  long (elongation in the [001] direction) with a height of  $\sim 0.5 \mu\text{m}$  (growth in the [010] direction). In addition, they were largely devoid of macrosteps and large defects. Most formed crystals exhibited similar dimensions (within 10 %) suggesting that nucleation on the glass substrates was an instantaneous process with few new crystals forming over time. Occasionally, some of the crystals formed were twinned or in small clusters but their occurrence was not common. Furthermore, their presence was not considered to impede diffusion to the well-defined isolated crystals selected for growth experiments due to the

minimum distance restriction imposed ( $\geq 10 \times$  characteristic crystal dimension).

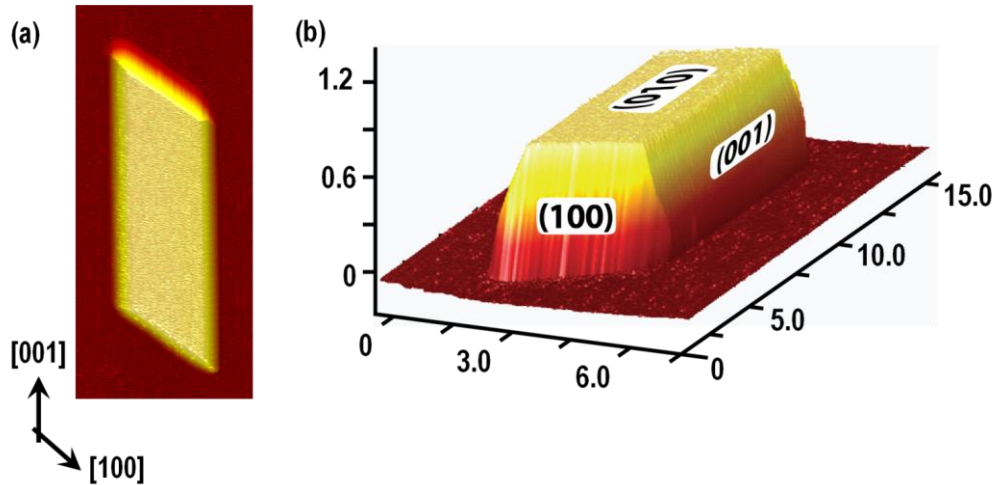


Figure 7.2: Typical AFM images of a grown gypsum crystal, (a) top view highlighting the dominant crystallographic directions and (b) showing crystal morphology.

#### 7.4. Numerical Theory and Simulations

All computer simulations were executed on a Dell Intel(R) core™ 2 Quad 2.13 GHz computer equipped with 16 GB of RAM and running Windows 7 Professional X64 bit 2010 edition. Modeling was performed using the commercial finite element modelling package Comsol Multiphysics 4.2 (Comsol AB, Sweden). Simulations were carried out with  $>10^6$  tetrahedral mesh elements and mesh resolution was defined to be finest in the vicinity of the crystal surface. Simulations with finer meshes were carried out (not reported) to confirm that the mesh was sufficiently fine to ensure that the predicted solutions were accurate.

## Theory

The following system was considered: the growth of an isolated gypsum crystal in quiescent supersaturated solution via the incorporation of species ( $\text{Ca}^{2+}$ ,  $\text{SO}_4^{2-}$  and/or  $\text{CaSO}_4$ ) to the dominant planes of the crystal. The distance between adjacent crystals was assumed to be large enough that the crystal under observation was diffusionally isolated from adjacent crystals. Plane-dependent crystal growth velocities,  $v_{(hkl)}$  ( $\text{nm s}^{-1}$ ) and the corresponding fluxes from crystal faces,  $J_{(hkl)}$  ( $\text{mol m}^{-2} \text{s}^{-1}$ ) were obtained directly from time-dependent crystal growth measurements and were used as inputs for a stationary boundary simulation which was developed to represent the growing crystal. The simulated crystal geometry was approximated to the monoclinic structure of gypsum crystal which mimicked the morphology of crystals grown experimentally (*vide infra*).

The simulation domain is shown in Figure 7.3 where the numbers used represent boundary numbers described in the text to define boundary conditions. In bulk solution, the mass transport of ions was solved under fixed boundary conditions as described by:

$$D_i \nabla^2 C_i = 0 \quad (7.1)$$

where  $D_i$  is the diffusion coefficient of species  $i$ , where  $i$  is  $\text{Ca}^{2+}$  or  $\text{SO}_4^{2-}$ , and  $C_i$  is the concentration of species  $i$ . Diffusion coefficients used for the purposes of simulations were  $0.792 \times 10^{-5} \text{ cm}^2 \text{ s}^{-1}$  and  $1.065 \times 10^{-5} \text{ cm}^2 \text{ s}^{-1}$  for  $\text{Ca}^{2+}$  and  $\text{SO}_4^{2-}$ , respectively.<sup>65</sup> Boundaries **1-3** represent the crystal planes in the (010), (001) and (100) directions, respectively (Figure 7.3) and their corresponding experimentally determined plane-specific fluxes,  $J_{(hkl)}$ , ( $\text{mol m}^{-2} \text{ s}^{-1}$ )

1) were used as input for predicting the interfacial concentration of  $\text{Ca}^{2+}$  ions at each plane, as governed by:

$$\underline{n} \cdot D_i \nabla C_i = J_{(hkl)} \quad (7.2)$$

where  $\underline{n}$  is the inward pointing unit normal to the surface. Boundary 4 represents the inert glass substrate and satisfies a no normal flux as governed by:

$$\underline{n} \cdot (D_i \nabla C_i) = 0 \quad (7.3)$$

Boundaries 5-9 define bulk solution conditions as described by equation 4:

$$C_i = C_{i,b} \quad (7.4)$$

where  $C_{i,b}$  is the bulk concentration of species  $i$ .

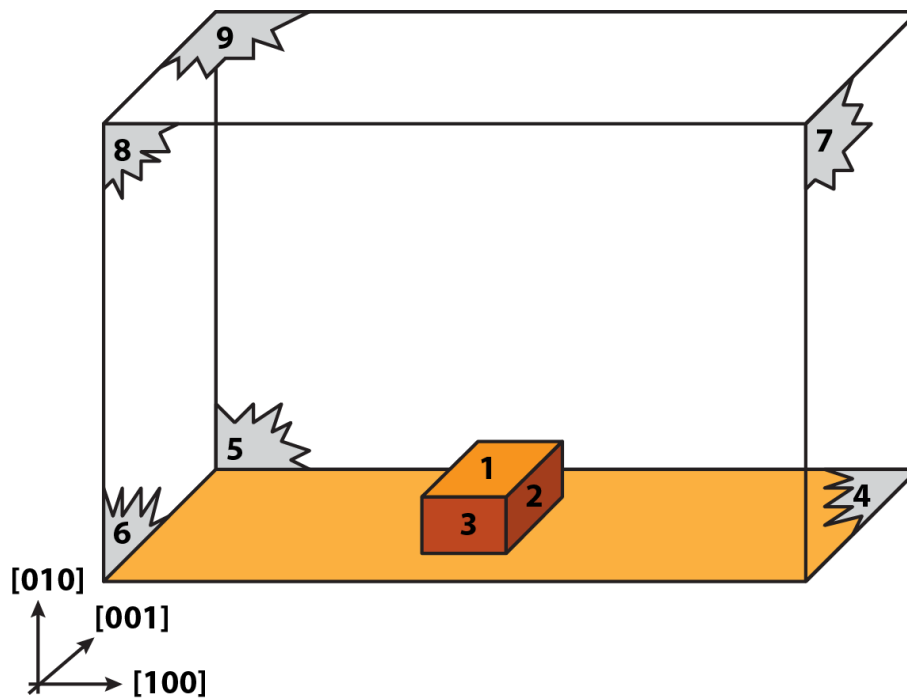


Figure 7.3: Simulation domain used for finite element simulations of plane-specific crystal growth fluxes. The numbers represent boundaries used in simulations (not to scale) and described in the text.

Table 7.2 summarises all interfacial concentrations at specific crystal faces, for the range of  $r$  used. It is evident that the surface concentration values remained essentially the same as the bulk concentration ( $\ll 1\%$  difference), for all crystal faces, thus suggesting significant surface kinetic control for the range of  $r$ . It was therefore possible to probe the relative influence of specific reagent ions on the ‘intrinsic’ growth mechanisms at specific crystal faces.

Table 7.2: Plane-specific surface concentrations for all  $r$  values.

$r$	Activity of limiting ion/ mM	Interfacial Concentration/ mM		
		(100) face	(001) face	(010) face
0.133	2.5	2.48	2.48	2.48
0.25	3.4	3.38	3.38	3.38
1.01	6.9	6.89	6.89	6.89
4.00	3.4	3.39	3.39	3.39
7.12	2.5	2.49	2.5	2.48

## 7.5. Results and Discussions

### 7.5.1 Plane Specific Growth Rates

Figure 7.4 shows typical AFM height images (top view) of a seed crystal (a) in  $r = 1$  solution, and after growth for (a) 530 s (b) 1215 s (c) 2430 and (d) 3645 s. It is evident that the imaged crystal expanded (both laterally and

longitudinally) with time and therefore facilitated tracking of both overall (average) and plane-specific growth rates. Under these conditions, the crystal was observed to elongate in the [001] direction (displacement of the (100) face) indicating anisotropy on growth kinetics. During imaging, the crystals were found to remain in position (no significant drift due to AFM tip rastering).

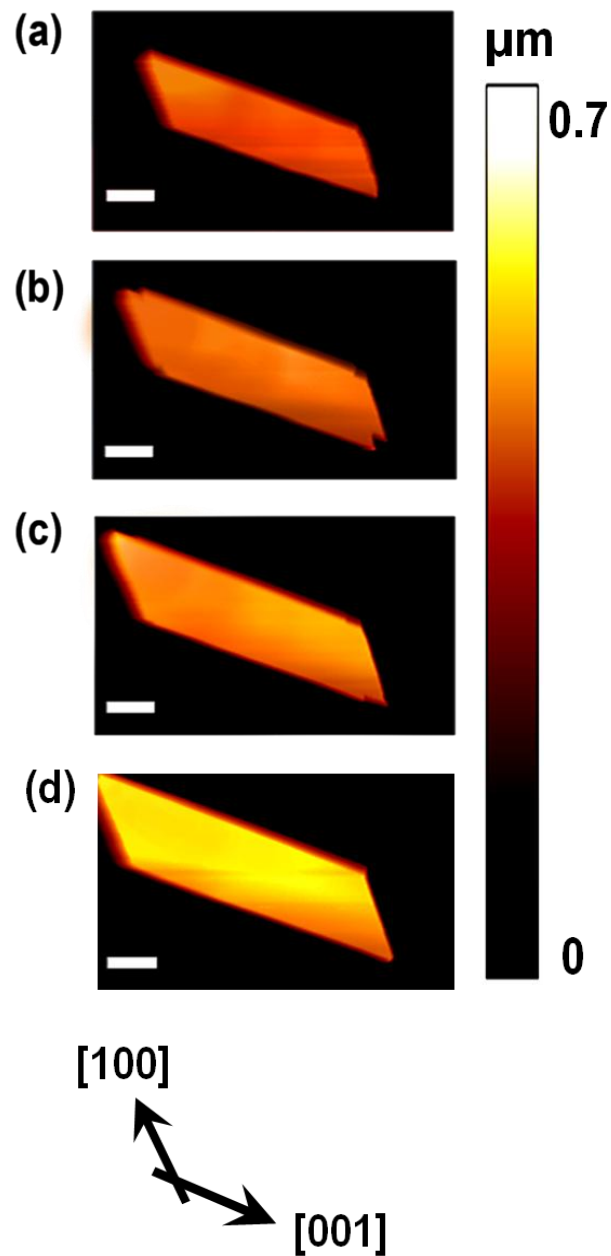


Figure 7.4: Typical AFM height images (top view) of a seed crystal in  $r = 1$  solution after growth for (a) 530 s, (b) 1215 s, (c) 2430 s and (d) 3645 s. The scale bar represents  $2 \mu\text{m}$ .

Figure 7.4 shows a summary plot of crystal expansion in the dominant planes; (100), (001) and (010) as a function of time for an  $r = 1$  solution, based on direct measurements from AFM. The growth velocities,  $v_{(hkl)}$  ( $\text{nm s}^{-1}$ ) were found to follow the trend;  $v_{(010)} < v_{(001)} < v_{(100)}$ . For these and all other cases ( $0.13 < r < 7.12$ ), the plots were found to be reasonably linear as expected for a surface controlled process.

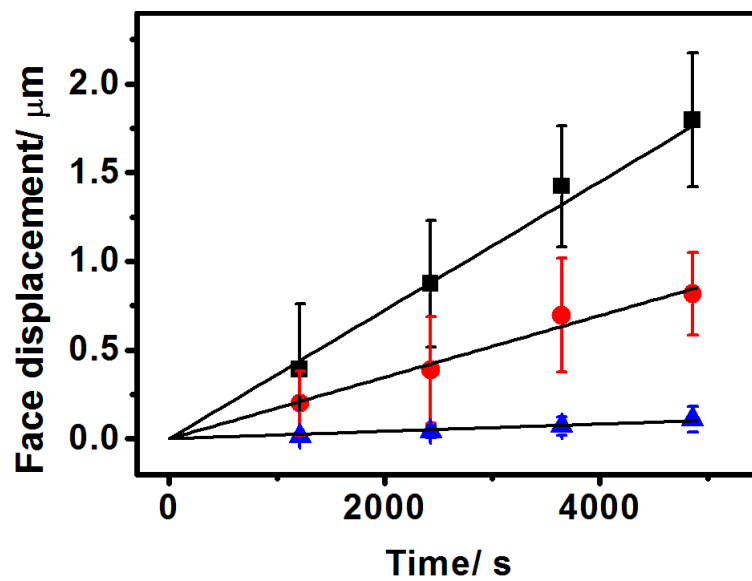


Figure 7.5: Crystal expansion of the principle planes; (100) (black), (001) (red) and the basal (010) surface (blue), as a function of time when grown in a stoichiometric ( $r$ ) growth solution.

For each AFM image, the average length of a crystal in a particular direction was determined from at least five cross sections across the entire length of the crystal. Crystal height data was determined from these cross sections also and the error bars represent two standard deviations. For each  $r$  value, at least three crystals were visualized and analyzed in this way. A summary of the plane-specific velocities is shown in Table 7.3.

Table 7.3: Summary of all plane-specific displacement velocities.

<i>r</i>	Plane-specific displacement/ nm s <sup>-1</sup>		
	(100) face	(001) face	(010) face
0.133	0.27 ± 0.12	0.39 ± 0.10	0.06 ± 0.02
0.25	0.40 ± 0.10	0.40 ± 0.06	0.08 ± 0.03
1.01	0.76 ± 0.09	0.51 ± 0.08	0.03 ± 0.01
4.00	0.60 ± 0.11	0.32 ± 0.08	0.04 ± 0.01
7.12	0.22 ± 0.07	0.07 ± 0.02	0.010 ± 0.005

From the crystal expansion measurements, plane-specific fluxes,  $J_{(hkl)}$  (mol m<sup>-2</sup> s<sup>-1</sup>) were calculated as the product of plane-specific velocities ( $v_{(hkl)}$ ) and the molar density of gypsum crystal (13400 mol m<sup>-3</sup>). Figure 7.5 shows a plot of average plane-specific growth fluxes, as a function of varying solution stoichiometry ( $r$ ).

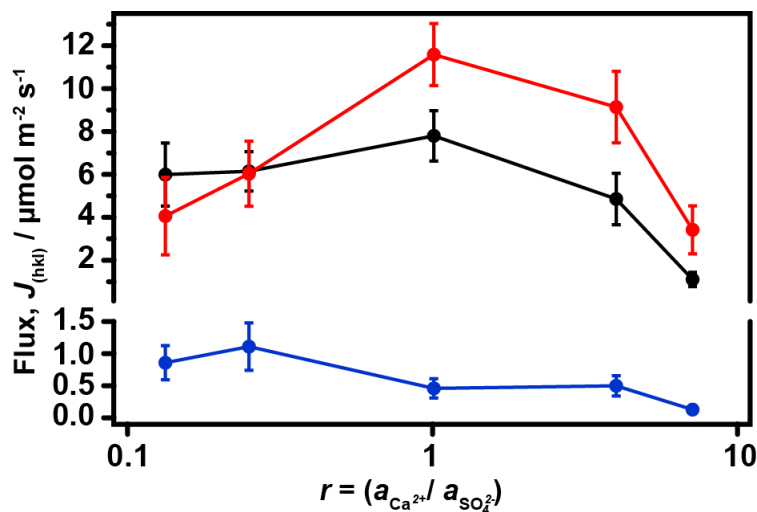


Figure 7.6: Summary plot of plane-specific growth fluxes to the (100) (black), (001) (red) faces and the basal (010) face (blue), as a function of solution stoichiometry ( $r$ ).

Maximum lateral ( $J_{(100)}$  and  $J_{(001)}$ ) rates were observed at stoichiometric growth conditions ( $r = 1$ ), highlighting a strong dependence on equimolar amounts of  $\text{Ca}^{2+}$  and  $\text{SO}_4^{2-}$  ions for lateral crystal growth. As  $r$  deviated from 1, growth rates on these faces decreased non-symmetrically with  $J_{(100)}$  diminishing more sharply in  $r < 1$  conditions than at  $r > 1$ . At  $r = 0.25$ , Flux to the (100) face decreases to values lower than those observed for the (slower moving) (001) face, indicating that low  $\text{Ca}^{2+}$  ions significantly limited growth in this direction. Conversely, under similar conditions ( $r \leq 0.25$ ), flux to the (001) face appeared to plateau indicating that further reduction of bulk  $\text{Ca}^{2+}$  concentration had a negligible effect on the growth rates of this face.

In the range of  $r > 1$ , the decrease in  $J_{(100)}$  was more gradual relative to rates observed at  $r < 1$ . However, at  $r = 7.5$  (maximum  $r$  value),  $J_{(100)}$  (growth of the (100) face) was seen to diminish to values similar to those observed at  $r = 0.133$  (minimum  $r$  value), suggesting that crystal growth on this face, is sensitive to  $\text{SO}_4^{2-}$  ion concentration in a similar way to  $\text{Ca}^{2+}$  concentration, particularly at extreme  $r$  values. At these extreme values,  $r = 0.133$  and  $r = 7.12$ ,  $J_{(100)}$  is seen to decrease by a factor of  $\sim 5$  compared to rates at stoichiometric conditions ( $r = 1$ ).

Over the entire range of  $r$ , growth of the (010) crystal surface was found to be slow relative to other measured directions. The basal surface of gypsum is known to be stable relative to the (100) and (001) faces.<sup>66</sup> In addition, there was a decrease in  $J_{(010)}$  with increasing  $r$ . The growth behaviour on this face may be rationalised based on, first, dehydrations kinetics and second, bonding in the crystal in the [010] direction. The rate of ion integration into the crystal surface

is known to be controlled by dehydration of ions and as mentioned, anion dehydration kinetics are much faster relative to cations (*vide supra*). Therefore, as  $r$  increases, integration is limited by  $\text{Ca}^{2+}$  dehydration kinetics despite ever increasing amounts of  $\text{Ca}^{2+}$  in solution. Additionally, the effect of fast anion dehydration rates is limited by low  $\text{SO}_4^{2-}$  activity ( $r > 1$ ) and therefore overall growth rates are low. In terms of bonding character in this surface, a  $\text{H}_2\text{O}$  layer is interspaced between  $\text{CaSO}_4$  bilayers, suggesting a discontinuity of the periodic bond chain in this direction.<sup>67</sup> Previous studies<sup>2,50</sup> have alluded to the  $\text{CaSO}_4$  bilayer as the repeat growth (and dissolution) unit, indicating that the exposed molecules at the crystal surface are likely to be  $\text{H}_2\text{O}$ . It is likely that adsorbed  $\text{H}_2\text{O}$  can act as a diffusive barrier to ion integration at the crystal surface and, possibly retard their dehydration kinetics as well.<sup>29</sup> Since the ion pair concentration was maintained at a constant value ( $\sim 0.1$ ), the influence of this species on crystal growth kinetics could not be fully investigated.

Direct comparisons between this work and others is difficult owing to the fact that, first, most previous studies were carried out under stoichiometric conditions ( $r = 1$ ) and second, most studies were based on growth on a cleaved basal (010) surface rather than (in our case) an isolated micro-crystal.<sup>2,48-51</sup> For cleaved surfaces, the separation of mass transport and surface processes is complex in part, due to the size of the reactive area. While an isolated micro-crystal exhibits very fast mass transport and is essentially diffusionally isolated (*vide supra*), a cleaved surface placed in a supersaturated solution may be assumed to be fully reactive, whereby all surface features (kinks, ledges, dislocations etc) contribute to observed growth rates. Due to both the density of active features and their proximity to each other, the diffusion profile to each

active feature will interact with others nearby and result in slower overall diffusion to the crystal surface. This behaviour is reminiscent of the planar diffusion profile seen for example, in the case of large electrodes in electrochemistry.<sup>17</sup> Consequently, kinetically controlled (intrinsic) crystal growth rates are difficult to elucidate.

### **7.5.2 Effect of $r = (a_{Ca^{2+}}/a_{SO_4^{2-}})$ on Crystal Morphology**

The observed trends in plane-specific velocities,  $v_{(hkl)}$  (Table 7.3) or equivalent fluxes, over a range of  $r$  (Figure 7.6) were predictably manifest in the morphology of the growing crystals. Figure 7.7 shows AFM height images of crystals grown with  $r$  values of (a-b) 0.133, (c-d) 1 and (e-f) 7.12 where (a), (c) and (e) are crystals after the initial scan and (b), (d) and (f) after growth for  $\sim 3600$  s. When grown in the  $SO_4^{2-}$  rich solution (Figure 7.7 (a-b)), the ratio of lateral rates of growth were found to be  $v_{(100)} / v_{(001)} \approx 0.7$  (Table 7.3), producing a plate-like crystal morphology with comparable dimensions in the [100] and [001] directions. As  $r$  increased to stoichiometric levels ( $r = 1$ ),  $v_{(100)} / v_{(001)} \approx 1.3$  thus producing crystals slightly elongated in the [001] direction (Figure 7.7 (d)). In  $Ca^{2+}$  rich solution ( $r = 7.12$ ), the velocity ratio,  $v_{(100)} / v_{(001)} \approx 3$  and the crystal morphology exhibits a significant elongation in the [001] direction (relatively faster displacement of the (100) face). These findings for individual micro-crystals are in agreement with previous morphological assessment of bulk gypsum crystals<sup>54,57</sup> confirming the validity of our approach, in which we are also able to quantitatively measure plane-specific growth rates, as highlighted herein.

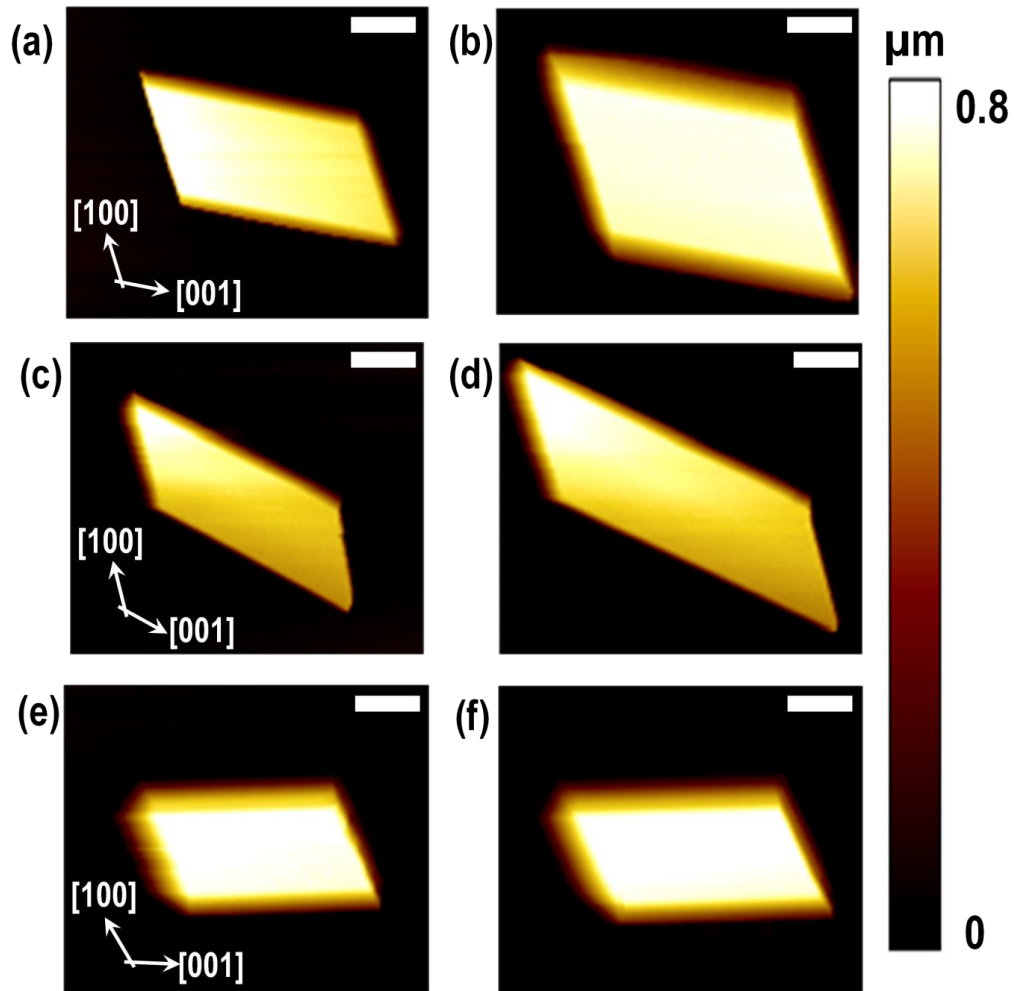


Figure 7.7: AFM height images of crystals grown with  $r$  values of (a-b) 0.133, (c-d) 1 and (e-f) 7.12 where (a), (c) and (e) are crystals initially and (b), (d) and (f) are after growth for ca. 1 hour. The scale bar represents  $2 \mu\text{m}$ .

### 7.5.3 Step Motion on the Basal (010) Surface

In addition to tracking the 3-D growth of micro-crystals, step motion on the dominant (010) basal plane was investigated to provide further information on the mechanism of crystal growth on this face. This was considered useful because, as mentioned earlier, previous AFM studies have focused on macroscopic crystals and it is useful to identify any similarities and differences between synthetically grown micro-crystals and cleaved macro-surfaces of natural crystals.

Figure 7.8 shows images of a typical crystal imaged in air on the combined AFM-optical microscope system, with (a) showing an optical image with small areas highlighted in red where AFM imaging was carried out, revealing (b) a growth hillock with a clear nucleation point where steps originate and propagate in a birth-and-spread mechanism. Steps parallel to the [100] direction are shown in (c), which is an area of the surface some distance from the nucleation point, exhibiting a large step spacing relative to the closely packed steps parallel to [001] direction, while in (d) steps parallel to the [001] direction close to the crystal edge are shown. A cross-section on Figure 7.8 (c), perpendicular to [100]-oriented steps - is plotted in Figure 7.8 (e) and reveals heights of, and spacing between, [100]-oriented steps. These steps are evidently consistent with the  $\text{CaSO}_4$  (bi)layer height in the unit cell of gypsum crystal which has a thickness of  $\sim 0.76$  nm.<sup>67</sup> Close to the crystal edge (Figure 7.8 (d)), the cross-section of slow moving steps [001]-oriented steps is plotted in Figure 7.8 (f) to reveal multilayered steps with heights of  $\leq 20$  nm. Together, these data reveal significant anisotropy between the rate of movement of slow [001]-oriented steps and much faster [100]-oriented steps.

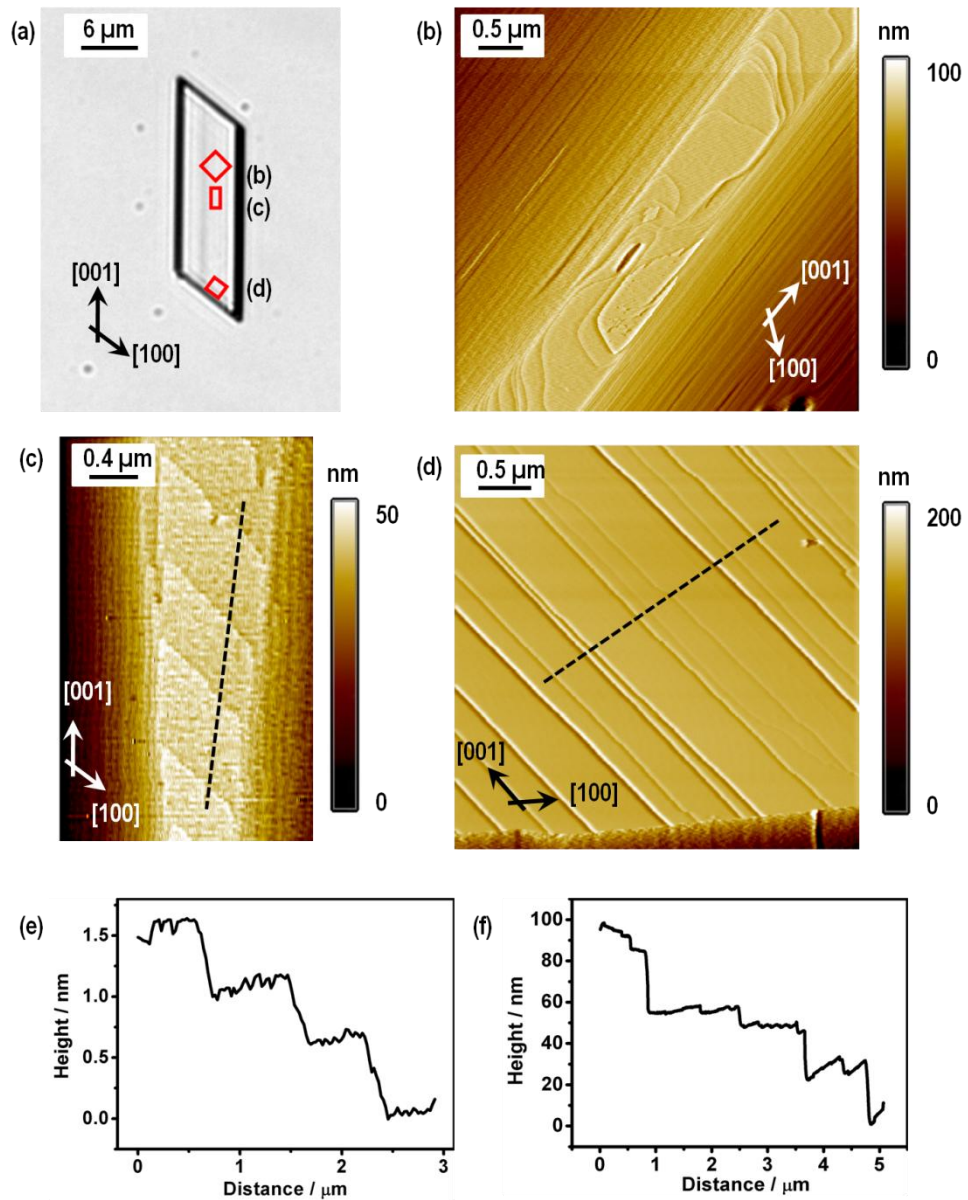


Figure 7.8: (a) DIC image depicting a typical crystal in air with small areas on the basal (010) surface magnified via AFM to reveal (b) a growth hillock with a nucleation point in the centre, which acts as a source of steps. Image (c) is an area away from the source where fast moving steps parallel to the [100] direction have a large step spacing, with much more closely packed steps parallel to the [001] direction. Image (d) is close to the crystal edge where only steps parallel to the [001] direction are evident. Cross-sections in (c) and (d) are shown in (e) and (f), respectively, and serve to highlight a difference in step heights in the different regions of the crystal surface.

Figure 7.9 shows *in-situ* AFM height data of a small area on the basal surface as a function of time after (a) 300 s, (b) 770 s, (c) 1300 s and (d) 1830 s in  $r = 1$  solution. The defect highlighted by the black arrow on the surface is gradually filled by the motion of [001]-oriented steps, and this serves as a fixed marker to obtain step velocities. The cross-section in Figure 7.9 (a) is plotted in Figure 7.9 (e), which highlights the step heights and inter-step distances. Under the growth conditions applied, steps parallel to the [100] direction were not observed on any region of the surface during *in-situ* measurements. This is consistent with the *ex-situ* data above which highlighted that [100]-oriented steps (Figure 7.8 (c)) were widely spaced and therefore fast moving. Figure 7.9 (f) plots the distance of three steps from the defect site as a function of time, from the analysis of images such as Figure 7.9 (a-d). It can be seen that (for all three steps) the step approach towards the defect is reasonably linear. A step velocity of  $0.09 (\pm 0.01) \text{ nm s}^{-1}$  was deduced and the average step height was found to be  $2.4 (\pm 0.5) \text{ nm}$ , corresponding to  $\sim 3 \text{ CaSO}_4$  bilayers.

Growth in the [010] direction (perpendicular to the (010) surface) based on the 2-D data in Figure 7.9 yields a rate of  $\sim 0.003 \text{ nm s}^{-1}$  compared to the growth rate of  $\sim 0.027 \text{ nm s}^{-1}$  measured by 3-D visualization. The difference in values, and the fact that 3-D imaging yields a higher growth rate, is not surprising because the growth process evidently involves layer-by-layer growth from numerous nucleation (polynuclear) sites across the surface and 2-D imaging captures only a small part of this. Evidently, care must be exercised in predicting bulk growth kinetics from step movement measurements in a tiny region of a crystal surface. In contrast, 3-D visualization provides accurate measurement of plane-specific growth kinetics. On the other hand, our findings

qualitatively corroborate previous microscopic work<sup>48,49,52</sup> which proposed a layer-by-layer growth process for the (010) gypsum surface. Additional scans of the (010) surface did not find any evidence for spiral hillocks which have been suggested in previous studies<sup>68</sup> as the mechanism by which gypsum crystal growth occurs.

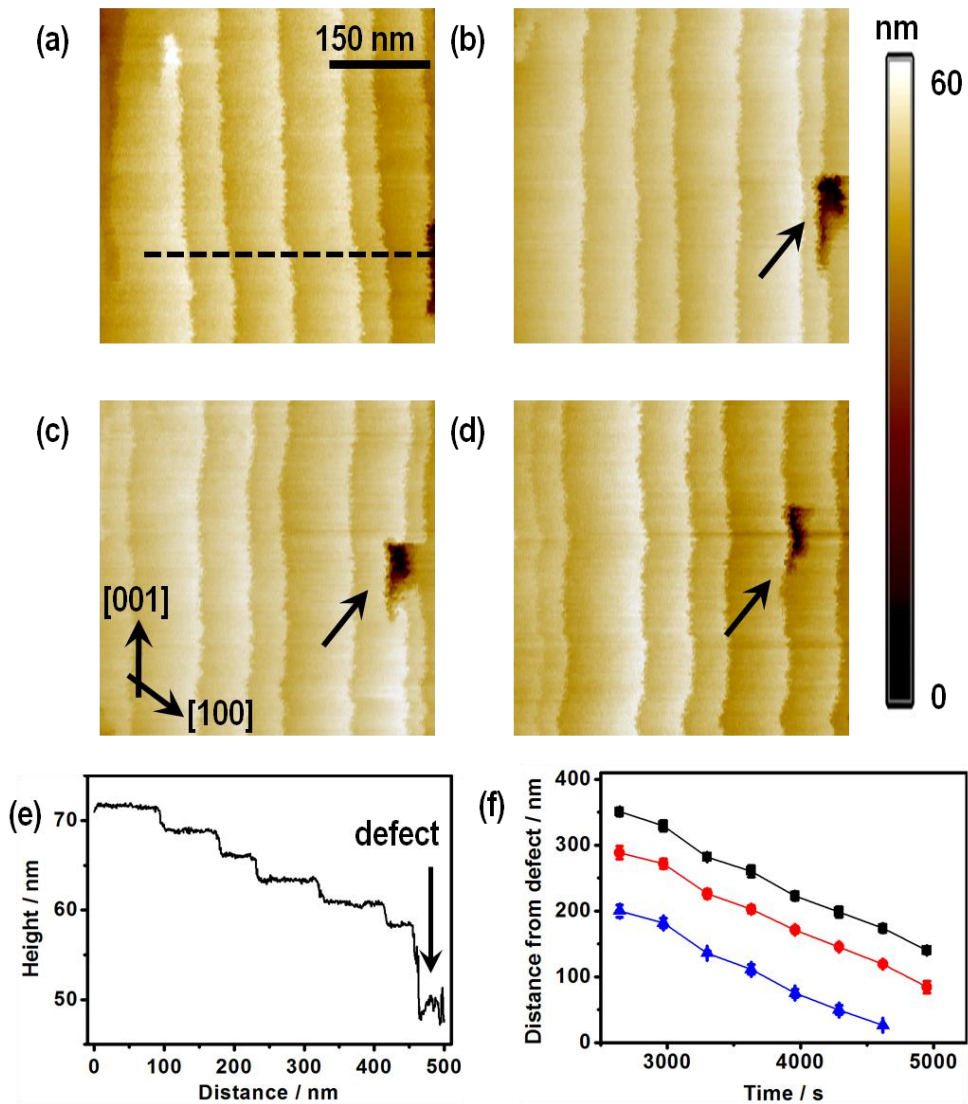


Figure 7.9: In-situ AFM height images showing steps parallel to the [001] direction on the (010) surface as a function of time, at (a) 300 s, (b) 770 s, (c) 1300 s and (d) 1830 s. A defect on the surface is also shown (black arrow) which is gradually filled in by moving steps. The cross-section in (a) is shown in (e), highlighting the step height and inter-step distance as well as the profile of the defect region. Image (f) plots the distance of three steps from the defect, as a function of time.

#### 7.5.4 Relationship Between Microscopic Fluxes, Macroscopic Growth Rates and Previous Kinetic Studies

The 3-D visualization data allow net crystal growth rates,  $J$  ( $\text{mol m}^2 \text{s}^{-1}$ ), to be deduced readily, defined as:

$$J = \frac{dV(t)}{dt} \times \frac{\rho}{A(t)} \quad (5)$$

where  $t$  is time (s),  $V(t)$  is the time-dependent crystal volume ( $\text{m}^3$ ),  $\rho$  is the molar density of gypsum crystal ( $13400 \text{ mol m}^{-3}$ ) and  $A(t)$  is the time-dependent total crystal surface area ( $\text{m}^2$ ) exposed to solution. Growth rates averaged over the time course of measurements were found to be  $1.7 (\pm 0.9) \times 10^{-6} \text{ mol m}^{-2} \text{ s}^{-1}$ ,  $2.5 (\pm 1.2) \times 10^{-6} \text{ mol m}^{-2} \text{ s}^{-1}$  and  $1.5 (\pm 0.7) \times 10^{-6} \text{ mol m}^{-2} \text{ s}^{-1}$  for  $r = 0.133$ , 1 and 7.12, respectively. In part, the trend of these values mirrors that found for plane-specific growth rates, where the highest rates were deduced at  $r = 1$ . However, the average rates determined are sensitive to the surface areas of each exposed crystal face and the corresponding reactivity of the individual faces. For instance, at  $r = 1$ , the anisotropy in plane-specific growth rates resulted in a needle-like crystal morphology, which increased the basal plane area (due to relatively fast lateral growth in the [001] direction) while the fast moving (100) plane area remained comparatively small (as a consequence of slow basal plane growth). The slowest growing face, the basal (010) plane, has significant influence on the overall (volumetric) rate of crystal growth.

The rates of growth of single isolated micro-crystals analyzed in this work can be compared to kinetic measurements in a seeded suspension. Previous studies of this type have monitored growth kinetics by tracking changes in the bulk solution via techniques such as conductivity measurements,<sup>47,69</sup>

titration,<sup>70-72</sup> potentiometry<sup>46,73</sup> and spectrometry.<sup>18</sup> A study by Zhang and Nancollas<sup>54</sup> at comparable supersaturation ( $1.54 \geq S \leq 1.84$ ) using suspensions at relatively high ionic strength (in 0.5 M KCl), determined average growth rates to be:  $3.22 \times 10^{-6} \text{ mol m}^{-2} \text{ s}^{-1}$ ,  $1.8 \times 10^{-6} \text{ mol m}^{-2} \text{ s}^{-1}$  and  $8.4 \times 10^{-7} \text{ mol m}^{-2} \text{ s}^{-1}$  for  $r = 0.1, 2$  and  $10$ , respectively. Thus, it is evident that the values in this study and previous bulk measurements correlate reasonably well, especially given the considerable differences between the *in-situ* AFM studies carried out in this work and bulk measurements on suspensions. This gives us reasonable confidence in the validity of our approach, noting that the previous work was carried out at higher ionic strength.

## **7.6. Conclusions**

In this chapter, we have described the growth behaviour of isolated gypsum micro-crystals via *in situ* 3-D AFM imaging, and determined the process to be controlled by surface-kinetics with no influence of bulk to surface diffusion. The growth kinetics for the edge-like faces, i.e. (100) and (001) faces, were found to be highly sensitive to the ratio of  $\text{Ca}^{2+}$  to  $\text{SO}_4^{2-}$  ions in the growth solution, resulting in dramatic effects on the morphology of crystals as growth progressed. In  $\text{SO}_4^{2-}$ -rich solutions, crystals adopted plate-like shapes, while in  $\text{Ca}^{2+}$ -rich solutions, they formed an elongated-plate morphology. This finding highlights an asymmetric dependence of plane-specific growth on the solution stoichiometry.

*Ex-situ* analysis of the basal (010) surface topography revealed a layer-by-layer growth process, in which steps oriented parallel to the [100] direction

propagated much faster than those parallel to the [001] direction. The considerable anisotropy of step velocities was evident during in-situ growth measurements on the (010) surface, in which only steps oriented parallel to the [001] direction could be detected and monitored. Comparison of growth rates deduced from 3-D visualization and 2-D tracking of steps highlighted potential issues with the latter approach as a means of obtain quantitative growth kinetics, as this approach typically covers only a small portion of a crystal face, which may not be representative of the entire surface. In contrast, the 3-D approach outlined allows the growth kinetics of the main exposed faces of the gypsum crystal to be determined unambiguously and quantitatively.

The approach described herein should be generally applicable to crystal growth (and dissolution); its merits being the possibility of measuring overall crystal growth rates, the ability to decouple mass transport and surface kinetic effects, and the possibility of obtaining plane-specific growth (dissolution) kinetics from the time-dependent analysis of the morphology of individual micro-crystals.

## References

- (1) Unwin, P. R.; Macpherson, J. V. *Chem. Soc. Rev.* **1995**, *24*, 109.
- (2) Van Driessche, A. E. S.; García-Ruiz, J. M.; Delgado-López, J. M.; Sazaki, G. *Cryst. Growth Des.* **2010**, *10*, 3909.
- (3) Steefel, C. I.; Maher, K. *Rev. Mineral.* **2009**, *70*, 488.
- (4) Binnig, G.; Quate, C. F.; Gerber, C. *Phys. Rev. Lett.* **1986**, *56*, 930.
- (5) Milchev, A.; Springer US: 2002, p 189.
- (6) Gabrielli, C.; Maurin, G.; Perrot, H.; Poindessous, G.; Rosset, R. *J. Electroanal. Chem.* **2002**, *538-539*, 133.
- (7) Devos, O.; Gabrielli, C.; Tribollet, B. *Electrochim. Acta* **2006**, *52*, 285.
- (8) Tian, M.; Wang, J.; Kurtz, J.; Mallouk, T. E.; Chan, M. H. W. *Nano Lett.* **2003**, *3*, 919.
- (9) Lu, X.; Zhao, Z.; Leng, Y. *J. Cryst. Growth* **2005**, *284*, 506.
- (10) Dove, P. M.; Platt, F. M. *Chem. Geol.* **1996**, *127*, 331.
- (11) Gasperino, D.; Yeckel, A.; Olmsted, B. K.; Ward, M. D.; Derby, J. J. *Langmuir* **2006**, *22*, 6578.
- (12) Fan, T.-H.; Fedorov, A. G. *Langmuir* **2003**, *19*, 1347.
- (13) Burt, D. P.; Wilson, N. R.; Janus, U.; Macpherson, J. V.; Unwin, P. R. *Langmuir* **2008**, *24*, 12867.
- (14) Leonhardt, K.; Avdic, A.; Lugstein, A.; Pobelov, I.; Wandlowski, T.; Wu, M.; Gollas, B.; Denuault, G. *Anal. Chem.* **2011**, *83*, 2971.
- (15) Dobson, P. S.; Bindley, L. A.; Macpherson, J. V.; Unwin, P. R. *Langmuir* **2005**, *21*, 1255.
- (16) Dobson, P. S.; Bindley, L. A.; Macpherson, J. V.; Unwin, P. R. *ChemPhysChem* **2006**, *7*, 1019.
- (17) Forster, R. J. *Chem. Soc. Rev.* **1994**, *23*, 289.
- (18) Reznik, I. J.; Gavrieli, I.; Antler, G.; Ganor, J. *Geochim. Cosmochim. Acta* **2011**, *75*, 2187.
- (19) Stumm, W.; Morgan, J. J. *Aquatic Chemistry*, 1996; Vol. null.
- (20) Cowan, J. C.; Weintritt, D. J. *Water-formed Scale Deposits*; Gulf Publishing Company, 1976.
- (21) Burke, E. M.; Nancollas, G. H. *Colloid Surf. A-Physicochem. Eng. Asp.* **1999**, *150*, 151.
- (22) Nielsen, A. E.; Toft, J. M. *J. Cryst. Growth* **1984**, *67*, 278.
- (23) Nielsen, A. E. *J. Cryst. Growth* **1984**, *67*, 289.
- (24) Christoffersen, J.; Christoffersen, M. R.; Johansen, T. *J. Cryst. Growth* **1996**, *163*, 304.
- (25) Dove, P. M.; Czank, C. A. *Geochim. Cosmochim. Acta* **1995**, *59*, 1907.
- (26) Ruiz-Agudo, E.; Putnis, C. V.; Wang, L.; Putnis, A. *Geochim. Cosmochim. Acta*, In Press, Corrected Proof.
- (27) Kowacz, M.; Putnis, C. V.; Putnis, A. *Geochim. Cosmochim. Acta* **2007**, *71*, 5168.
- (28) Perdikouri, C.; Putnis, C. V.; Kasiotas, A.; Putnis, A. *Cryst. Growth Des.* **2009**, *9*, 4344.
- (29) Piana, S.; Jones, F.; Gale, J. D. *J. Am. Chem. Soc.* **2006**, *128*, 13568.
- (30) Ford, D. C.; Williams, P. W. *Karst hydrogeology and geomorphology*; John Wiley & Sons, 2007.
- (31) Klimchouk, A.; Andrejchuk, V. *International Journal of Speleology* **1996**, *25*, 145.
- (32) Klimchouk, A. *International Journal of Speleology* **1996**, *25*, 9.
- (33) Sohnle, O.; Garside, J. *Precipitation*; Butterworth-Heinemann: Oxford, 1992.
- (34) Bottrell, S. H.; Newton, R. J. *Earth-Sci. Rev.* **2006**, *75*, 59.

- (35) Peris Mora, E.; Monzó, J.; Paya, J.; Borrachero, M. V. In *Studies in Environmental Science*; J.J.J.M. Goumans, G. J. S., Sloot, H. A. v. d., Eds.; Elsevier: 1997; Vol. Volume 71, p 581.
- (36) Yan, T. Y. *Energy* **1984**, *9*, 265.
- (37) Notholt, A. J. G.; Highley, D. E. *Gypsum and Anhydrite*; H.M.S.O: London, 1975.
- (38) Kovler, K. *Cem. Concr. Res.* **1998**, *28*, 423.
- (39) Bott, T. R. *Fouling of Heat Exchangers*; Elsevier: Amsterdam, 1995.
- (40) Larsen, K.; Bechgaard, K.; Stipp, S. L. S. *Geochim. Cosmochim. Acta* **2010**, *74*, 2099.
- (41) Tai, C. Y.; Chang, M.-C.; Wu, C.-K.; Lin, Y.-C. *Chem. Eng. Sci.* **2006**, *61*, 5346.
- (42) Stubicar, N.; Scrbak, M.; Stubicar, M. *J. Cryst. Growth* **1990**, *100*, 261.
- (43) Liu, S.-T.; Nancollas, G. H. *J. Cryst. Growth* **1971**, *6*, 281.
- (44) Liu, S. T.; Nancollas, G. H. *J. Colloid Interface Sci.* **1975**, *52*, 593.
- (45) Christoffersen, M. R.; Christoffersen, J.; Weijnen, M. P. C.; Vanrosmalen, G. M. *J. Cryst. Growth* **1982**, *58*, 585.
- (46) Witkamp, G. J.; Van der Eerden, J. P.; Van Rosmalen, G. M. *J. Cryst. Growth* **1990**, *102*, 281.
- (47) Amathieu, L.; Boistelle, R. *J. Cryst. Growth* **1988**, *88*, 183.
- (48) Bosbach, D.; Rammensee, W. *Geochim. Cosmochim. Acta* **1994**, *58*, 843.
- (49) Bosbach, D.; Jordan, D. G.; Rammensee, W. *Eur. J. Mineral.* **1995**, *7*, 267.
- (50) Bosbach, D.; Junta-Rosso, J. L.; Becker, U.; Hochella Jr, M. F. *Geochim. Cosmochim. Acta* **1996**, *60*, 3295.
- (51) Bosbach, D.; Hochella Jr, M. F. *Chem. Geol.* **1996**, *132*, 227.
- (52) Hall, C.; Cullen, D. C. *AIChE J.* **1996**, *42*, 232.
- (53) Reznik, I. J.; Gavrieli, I.; Ganor, J. *Geochimica et Cosmochimica Acta* **2009**, *73*, 6218.
- (54) Zhang, J.; Nancollas, G. H. *J. Cryst. Growth* **1992**, *118*, 287.
- (55) Keller, D. M.; Massey, R. E.; Hileman Jr., O. E. *Can. J. Chem.* **1980**, *58*, 2127.
- (56) Ahmi, F.; Gadri, A. *Desalination* **2004**, *166*, 427.
- (57) Abdel-Aal, E. A.; Rashad, M. M.; El-Shall, H. *Cryst. Res. Technol.* **2004**, *39*, 313.
- (58) Burton, W. K.; Cabrera, N.; Frank, F. C. *Philosophical Transactions of the Royal Society of London, Series A: Mathematical Physical and Engineering Sciences* **1951**, *243*, 299.
- (59) Kossel, W. *Nachr. Ges. Wiss. Gottigen. Math.-Phys. Klasse* **1927**, 135.
- (60) Stranski, I. *N. Z. Phys. C* **1928**, *136*, 259.
- (61) Tassev, V. L.; Bliss, D. F. *J. Cryst. Growth* **2008**, *310*, 4209.
- (62) Van Driessche, A. E. S.; Garcia-Ruiz, J. M.; Delgado-Lopez, J. M.; Sazaki, G. *Cryst. Growth Des.* **2010**, *10*, 3909.
- (63) White, S. N. *Chemical Geology* **2009**, *259*, 240.
- (64) Schofield, P. F.; Knight, K. S.; Stretton, I. C. *Am. Mineral.* **1996**, *81*, 847.
- (65) Vanysek, P. *CRC Handbook of Chemistry and Physics: Diffusion coefficients and ionic conductivities*; 91st ed.; CRC Press Taylor & Francis: Boca Raton, FL, 2010-2011.
- (66) Mbogoro, M. M.; Snowden, M. E.; Edwards, M. A.; Peruffo, M.; Unwin, P. R. *J. Phys. Chem. C* **2011**, *115*, 10147.
- (67) Fan, C.; Teng, H. H. *Chem. Geol.* **2007**, *245*, 242.
- (68) Christoffersen, M. R.; Christoffersen, J.; Weijnen, M. P. C.; Van Rosmalen, G. M. *J. Cryst. Growth* **1982**, *58*, 585.
- (69) Smith, B. R.; Sweett, F. *J. Colloid Interface Sci.* **1971**, *37*, 612.
- (70) Amjad, Z. *J. Colloid Interface Sci.* **1988**, *123*, 523.
- (71) He, S.; Oddo, J. E.; Tomson, M. B. *J. Colloid Interface Sci.* **1994**, *162*, 297.
- (72) Hamdona, S. K.; Al Hadad, U. A. *J. Cryst. Growth* **2007**, *299*, 146.
- (73) Liu, S.-T.; Nancollas, G. H. *J. Cryst. Growth* **1970**, *6*, 281.

# Chapter 8

## Conclusions

The overall aim of this thesis was to gain kinetic and mechanistic insights into processes at the mineral/solution interface, with particular emphasis on the growth and dissolution of gypsum ( $\text{CaSO}_4 \cdot 2\text{H}_2\text{O}$ ) crystal. As a ubiquitous mineral with wide ranging applications, studies carried out on gypsum are particularly relevant to the field of geochemistry and industrial areas such as building and construction. An overarching multi-scale approach has been taken for the studies herein, to facilitate a quantitative link between macroscopically observed events and the local surface processes from which they arise. With this approach, perceived discrepancies in the literature between measurements at different experimental length scales have been addressed. In addition, powerful quantitative models have been developed to describe the underlying diffusion/reaction problems, in order to complement experimental results and provide mechanistic insights.

For some of the studies carried out, visualisation techniques such as AFM, WLI and SEM, were used and, subsequently, large sets of images were produced. Typically, these images were topographical and contained vital information about the unique features formed on the surfaces under investigation. It was therefore necessary to develop a versatile and efficient way to process these images and extract important data. To this end, a highly adaptable image processing (IP) package was developed (Chapter 3). The main aim was to process 3D images produced during crystal dissolution studies, analyse surface dissolution features and collate essential structural information. In this way, the dissolution process could be monitored and direction-specific dissolution rates could be determined. The IP

package incorporated various batch processes which expedited numerous IP operations. These included operations to replace of missing pixels and correct image tilt, among others. A significant benefit to automating such tasks was that very large image sets could be processed quickly and thus allowing for a wide range of experimental variables to be probed. In addition, sophisticated graphical user interfaces (GUIs) were designed to extract specialised information in a user-defined environment. It was found that, the IP package performed comparably to stand-alone commercial software for the execution of common tasks. However, due to the limited options available in commercial packages, specialised tasks could not be performed, thus highlighting the vast benefits of a user-designed IP package.

An area in which IP methods would truly come into their own would be when they can be incorporated successfully into dynamic processes, such that quantitative kinetic information on crystal growth/dissolution can be deduced in real-time whilst eliminating the current limitations that exist with time-intensive and (surface) invasive techniques. In addition, more versatile IP packages are needed to satisfy the increasingly diverse needs of researchers, particularly since technological advances (such as Peak Force AFM and phase-shift interferometry (PSI)) are expanding the range of surfaces and processes that can be probed.

Dissolution processes typically involve the formation of characteristic etch features on crystal surfaces. In Chapter 4, a simple time-dependent analysis of etch pits formed on the cleaved basal (010) surface of gypsum was carried out, with the aim of deducing dissolution kinetics at a local scale. The study was limited to short time scales ( $\leq 100$  s) where only micro-sized etch pits form. Micro-sized active surfaces are known to exhibit very high and quantitative mass transport rates and by limiting the dissolution process to short durations, the contribution of mass transport

relative to surface processes can be determined. It was found that dissolution is controlled by surface kinetics at early times, with the ‘edge’ (100) and (001) planes dominating the process. Direction-specific dissolution velocities followed the trend:  $v_{(010)} < v_{[001]} \ll v_{[100]}$ , revealing significant anisotropy of step kinetics. The fast moving steps parallel to the [100] direction were found to yield higher interfacial concentrations, suggesting a comparatively higher contribution from mass transport for dissolution in this direction relative to both the [001] and the basal [010] directions. Analysis of direction-dependent fluxes over time revealed that the basal plane dominates the dissolution process at later times when the surface is fully reactive. The corresponding basal plane fluxes ( $J_{(010)} = 4.0 (\pm 0.5) \times 10^{-9} \text{ mol cm}^{-2} \text{ s}^{-1}$ ) are found to be consistent with previous bulk measurements, thus bridging the gap between macroscopically observed rates and microscopic phenomena. Studies of the influence of background electrolytes revealed a direction-specific enhancement (salting-in) of dissolution in the presence of inert salt, while common-ion effects ( $\text{Ca}^{2+}$  vs.  $\text{SO}_4^{2-}$ ) significantly retarded dissolution, particularly when etching in  $\text{Ca}^{2+}$  compared to  $\text{SO}_4^{2-}$ .

With striking retarding effects seen in the case of  $\text{Ca}^{2+}$  it would be worth while to investigate the influence of other ions on the dissolution process. For instance,  $\text{Mg}^{2+}$  and  $\text{Cr}^{3+}$  have been observed to significantly influence the growth and dissolution of calcite. In addition, further insight may be gained from molecular level simulations such as molecular dynamics (MD) which is capable of accommodating the energy considerations associated with these surface processes.

The dissolution process was further probed with an investigation of the reactivity of basal (010) and edge (001) surfaces of gypsum and polycrystalline anhydrite crystals, in a bulk study (Chapter 5). To probe the intrinsic dissolution

rates, the study was carried out under far from equilibrium conditions, via the CFC method, which was coupled to off-line ICP-MS for the measurement of dissolved  $\text{Ca}^{2+}$ . The dominant kinetic regime was determined by taking measurements over the wide range of flow rates accessible with the CFC technique. Using quantitative computer modelling, convective-diffusion equations were formulated, which describe mass transport in the CFC. These equations were coupled with a boundary condition for the dissolving crystal surface and it was found that a linear rate law ( $J_o = k_{diss} \times c_{eq}$ ) applies to the dissolution process.

The basal gypsum surface was found to exhibit a flux of  $J_o = 5.7 (\pm 1.4) \times 10^{-9}$  mol  $\text{cm}^{-2} \text{s}^{-1}$  into pure water and a rate constant of,  $k_{diss} = 6.0 (\pm 1.5) \times 10^{-4}$  cm  $\text{s}^{-1}$ , while polycrystalline anhydrite yielded  $J_o = 4.1 (\pm 0.7) \times 10^{-9}$  mol  $\text{cm}^{-2} \text{s}^{-1}$ . Conversely, the highly reactive edge (001) plane exhibits very high rates, yielding a lower limit for the rate constant of  $k_{diss} > 0.1$  cm  $\text{s}^{-1}$  accessible via the CFC technique. Thus the reaction is a transport-controlled process (in pure water). These observations are wholly consistent with those determined in the etch pit analysis study (Chapter 4).

The effects of common humid-creep inhibitors: STMP and tartaric acid on gypsum dissolution kinetics, are investigated and it was found that STMP significantly retards gypsum dissolution, with  $J_o = 1.6 (\pm 0.6) \times 10^{-9}$  mol  $\text{cm}^{-2} \text{s}^{-1}$ . Additional etch pit studies suggest that the STMP anion acts by preferentially adsorbing onto the edge planes (both (100) and (001)) with a smaller effect on the basal (010) plane, thus inhibiting further dissolution.

The CFC technique was further applied to the study of industrially relevant materials (Chapter 6), in order to address the mode of action of common humid creep additives. Polycrystalline gypsum samples are impregnated with

common humid creep inhibitors such as STMP, and some organic acids (tartaric acid, boric acid and gallic acid), and bound in a resin matrix. In this case, a simple flux rate law was applied and when corrected for surface roughness, all samples yielded a flux of  $1.4 (\pm 0.6) \times 10^{-8} \text{ mol cm}^{-2} \text{ s}^{-1}$ , compared to  $1.1 (\pm 0.4) \times 10^{-8} \text{ mol cm}^{-2} \text{ s}^{-1}$  from the control sample, thus indicating a negligible effect on dissolution kinetics. However, STMP showed a small inhibitory influence, yielding a flux of  $7.4 (\pm 2.0) \times 10^{-9} \text{ mol cm}^{-2} \text{ s}^{-1}$ . With the observations made in this study, current theories on the mode of action of humid creep additives were assessed. It was concluded that models that involve surface binding of additives that reduce water adsorption in the inter-crystal region, are more plausible than those proposing a dissolution-precipitation pathway. In addition, the fluxes deduced in this study are comparatively higher than those observed for the basal plane surface (Chapters 4 and 5). However, the higher reactivity can be rationalised by the fact that in this study (Chapter 6), the polycrystalline nature of the surface exposes the edge planes, which have been shown to be highly reactive (Chapters 4 and 5).

The versatility of the CFC technique is non-trivial when one considers that it can be coupled with a wide range of other techniques such as in-line electrochemical methods and others such as UV/vis. In addition, there is virtually no limit to the range of substrates (treated, synthetic) which can be investigated due to the simplicity of the CFC cell assembly. When coupled with the fact that it is just as straightforward to change the solution, this technique opens up numerous options. For instance, it may be used to quickly screen for appropriate crystal dissolution retarders for a wide range of substrates.

Using an approach reminiscent of the etch pit analysis study (Chapter 3), the growth kinetics of micro-sized gypsum crystals are determined by visualising their

growth using *in-situ* AFM. The influence of solution stoichiometry was investigated by varying the relative activities of reagent ions,  $r = (a_{\text{Ca}^{2+}}/a_{\text{SO}_4^{2-}})$  in the growth solution, while maintaining a constant driving force ( $S$ ). A robust seeding process was shown to produce well-defined isolated crystals which strongly adhered to a silanized glass substrate. In this case, the mass transport vs. surface kinetics problem was addressed by imposing restrictions on the proximity of adjacent crystals in order to ensure diffusional isolation. It was found that crystal growth was entirely controlled by surface kinetics for the entire range of  $r$ , with the edge planes dominating the process at an early time. Plane-specific velocities in the lateral directions were found to be at their highest under equimolar conditions ( $r = 1$ ), decreasing to their lowest values at  $r_{\min} = 0.13$  and  $r_{\max} = 7.12$ . These rates manifested a dramatic effect on crystal morphology yielding large plate-like geometry in  $\text{SO}_4^{2-}$ -rich solutions, while in  $\text{Ca}^{2+}$ -rich conditions, the crystals take on a needle-like shape. The basal (010) surface exhibits low rates of growth (relative to the edge planes) which are seen decrease slightly as  $r$  increases. This was due to the slow dehydration kinetics of the cation relative to the anion and the stability of the basal plane to growth (or dissolution).

The propagation of nanoscale steps on the basal (010) surface reveal only 2D islands, while spiral hillocks are not observed at any time, thus indicating a ‘layer-by-layer’ growth mechanism. However, the velocities of these steps in the lateral [001] and vertical [010] directions reveal a significant discrepancy between nanoscale (steps) and microscopic (plane-specific) growth rates with the former accounting for only a small fraction of growth in the latter. It was proposed that the basal plane is likely to grow via a complex polynuclear process. When compared to previous bulk measurements, it was found that the average rates of growth of the

crystal match relatively well, indicating the powerful insights gained from this approach.

In summary, the studies conducted in this thesis have shown that by applying approaches and techniques which successfully separate mass transport effects and surface kinetics, the prevailing kinetic regime can be determined. When effectively coupled with powerful quantitative models which complement the diffusion-reaction, intrinsic reaction kinetics can be elucidated, and under such well-defined conditions, it is possible to reliably probe crystal growth and dissolution processes. The comprehensive approach applied in this work allows for the discrimination of individual crystal planes based on their reactivity and more significantly, the deduction average macroscopic fluxes which can be compared directly to bulk studies, thus providing a powerful link between experimental length scales. Furthermore, the techniques and approaches used in this thesis are generally applicable.